Effects of Defects and Reverse Bending on Tensile Properties of Tensile Armour Wires

Kazeem Kayode, Adewole

A Thesis Submitted for the Degree of
Doctor of Philosophy

August 2011

DECLARATION

This thesis records the work carried out in the School of Chemical Engineering and Advanced Materials and the strength laboratory in the School of Mechanical Engineering of the University of Newcastle upon Tyne between September 2008 and August 2011 and is original except where acknowledged by reference to the work of others.

No portion of this work is being, nor has been submitted for a degree, diploma or any other qualification at any other University.

ACKNOWLEDGEMENT

My unreserved gratitude goes to the Almighty Allah for his continuous favour on me and for seeing me through this Ph.D programme. I equally express my profound gratitude to my supervisors, Prof Steve Bull and Dr J.M Race for their supports throughout this project, particularly for making it possible to complete my PHD on time. I also appreciate the contribution of Mr. Anua Abubakr, Mr. Kazeem Shittu, Dr. Adrian Oila, Mr. Malcom Black of the strength laboratory and Mr. Neville Dickman of the material laboratory for all the cooperation given to me during my research. I also thank my wife, my three children, my parents and other members of my extended family for given me the moral support throughout my Ph.D programme.

Abstract

Flexible pipes are used for risers and flowlines in the offshore oil and gas industry and in many other applications. As part of the construction of these pipes, tensile armour wires are incorporated to resist longitudinal stresses which arise during installation and service. Tensile armour wires also resist hoop stresses for pipes without a designated pressure armour layer.

The flexible pipeline manufacturing industry desires a better understanding of the tensile armour wire fracture mechanism, and especially the effects of defects with dimensions less than 0.2mm. Reverse bending operations (which arise due to the wire moving through paired rollers on unreeling during pipe manufacture) also affect the tensile properties of the tensile armour wires. Customarily, engineers estimate the safe load carrying capacity of defective wires solely by multiplying the ultimate strength obtained from a tension test by the original nominal area of the wire without any consideration for the fracture mechanisms of the wire. This approach may overestimate the strength of the wire. Recent research considering the fracture mechanisms of wires has employed a classical fracture mechanics approach, mainly using Linear Elastic Fracture Mechanics (LEFM) and/or Net Section Theory (NST).

Obtaining parameters for fracture mechanics analyses requires large/thick standard fracture mechanics test specimens which cannot be made out of tensile armour wires due to their small size. Also fracture mechanics analyses based on these parameters including the elastic plastic crack opening displacement (COD) and J-integral parameters are largely size and geometry dependent making transferability of the results obtained from full size specimens to actual structures questionable.

Laboratory tensile testing and tensile testing finite element simulations with mechanism-based fracture mechanics carried out on the as-received tensile armour wire and tensile armour wires with engineered defects reveal that the tensile armour wires fail by a shear mechanism. They also reveal that flat bottom scratches, pointed end scratches and dents identified from the Scanning Electron Microscope images of the as-received wire surface reduce the ultimate load and extension at fracture of the wires. In addition, denting was found to increase the wires yield load while scratching reduced the wire's yield load. The reduction in the tensile/ mechanical properties of tensile armour wires were found to depend largely on defect dimensions rather than defect locations with defects less than 0.2mm in any

of its dimensions causing less than 0.072%, 0.238% and 10.946% reduction the yield load, the ultimate load and the displacement at fracture of tensile armour wires respectively.

Laboratory and finite element simulations of reverse bending, straightening and tensile testing of the reverse bent tensile armour wires reveal that reverse bending and straightening operations reduce the ultimate load and fracture displacement of the wires. This work also reveals that the reverse bending process can only reveal near surface laminations as wires with mid depth laminations or with scratches less than 1mm deep would pass through the reverse bending process without fracturing.

List of nomenclatures

A_i	Specimen instantaneous cross sectional area
A_0	Specimen original cross sectional area
a	Notch depth or crack size
a_c	Critical crack size
b_0	Initial ligament length
D	Full width of specimen/component or full diameter
d	Width of the net section of specimen/component
E	Young Modulus
F	Deformation gradient matrix
G	Energy release rate
G_c	Critical energy release rate.
G_{Ic}	Mode I critical energy release rate.
H_α	Hardening parameters
h	Thickness
I	Identity tensor
J	Contour integral
J_Q	Provisional contour integral initiation toughness
K	Stress intensity factor
K_e	Effective stress concentration factor
K_I	Mode I stress intensity factor
K_{Ic}	Mode I critical stress intensity factor
K_t	Theoretical stress concentration factor
L_i	Instantaneous length
L_0	Specimen original gauge length
P	Applied force
p	Equivalent hydrostatic stress

List of nomenclatures continued

q	Mises equivalent stress
R	Rotation matrix.
r_p	Plastic rotation factor
s	Stress deviator
T_0	Thickness of gauge section of tensile specimen
$\bar{u}_f^{pl}$	Displacement at failure,
V	Stretch matrix
V_f	Volume occupied by a part of the body
V_p	Plastic displacement at the crack mouth
W	Rate of rotation or spin
W_e	Elastic deformation energy
w_f	Tearing energy per unit torn area
W_0	Width of the parallel length
W_p	Plastic deformation energy
W_t	Total deformation energy
w_p	Plastic energy per unit volume
X	Initial location/position of a particle in an undeformed structure
x	New position of a particle during structural deformation
Y_0	Yield stress
Y_i	Initial yield stress
α	Yield offset.
δ	Crack-tip-opening displacement (CTOD) δ
δ_{Ic}	Mode I critical value of CTOD
δ_{el}	Elastic components of CTOD
δ_{pl}	Plastic components of CTOD

List of nomenclatures continued

δ_Q	Provisional CTOD initiation toughness
Δ_c	Crosshead displacement
Δ_E	Elastic displacement in specimens
Δ_P	Plastic displacement in specimens
Δ_m	Elastic deflection of testing machines
ε	True strain
$\dot{\varepsilon}$	Total mechanical strain rate matrix
$\bar{\varepsilon}$	Equivalent strain
ε_{nom}	Engineering or nominal strain
ε_T	Strain tensor
ε_u	True uniform elongation at the ultimate tensile stress
$\dot{\varepsilon}^{el}$	Elastic strain rate
$\dot{\varepsilon}^{pl}$	Plastic strain rate
ε_f^{pl}	Equivalent plastic strain at failure
ε_D^{pl}	Equivalent plastic strain at the onset of ductile damage
ε_s^{pl}	Equivalent plastic strain at the onset of shear damage
η	Triaxiality
θ	Temperature
θ_s	Shear stress ratio
ν	Poisson's ratio
v	Velocity
ρ	Radius of curvature of the notch/defect tip
ρ'	Half the width of the “elementary structural unit”
σ	True stress
σ_c	Fracture strength

List of nomenclatures continued

σ_f	Fracture stress
σ_{fl}	Flow stress
σ_{nom}	Engineering or nominal stress
σ_0	Yield strength
σ^0	Size of the yield surface (size of the elastic range),
$\tau_{\max}$	Maximum shear stress
ϕ	backstresses,
φ	Diameter
Q_∞	Maximum increase in the elastic range

Table of figures

Table of figures continued

Table of figures continued

Table of figures continued

Table of figures continued

Table of figures continued

Table of figures continued

Table of figures continued

Table of figures continued

Table of figures continued

Table of figures continued

Table of figures continued

Table of figures continued

Table of figures continued

Table of figures continued

List of tables

List of tables continued

List of tables continued

Table of contents

Chapter 1 Introduction to thesis

1.1 Introduction

Flexible pipes are used as risers and flowlines in the offshore industry and in many other applications. As part of the construction of these pipes, tensile armour wires are incorporated to resist longitudinal stresses which arise during installation and service. Tensile armour wires also resist hoop stresses for pipes without a designated pressure armour layer and for risers in particular, the weight of the riser is carried by the tensile armours wires. Consequently, the tensile armour wires are essential to the integrity of the flexible pipes.

Prior to service, tensile armour wires inevitably contain defects arising from their manufacturing and/or from the processing they are subjected to during their transportation and during the manufacturing of flexible pipes. While in service, tensile armour wires may also develop defects, such as pitting corrosion when the external sheath of the flexible pipes is damaged and the wires get in contact with sea water. The presence of defects in the tensile armour wires can affect their expected mechanical properties and consequently affect the flexible pipes performance and integrity. Consequently, an understanding of the effects of defects on the tensile armour wire properties and the fracture mechanism of the wires is essential to be able to predict their real performance as against their ideal performance when they are defect free.

Also, tensile armour wires are subjected to routine reverse bending and straightening operations as a lamination check. The reverse bending and straightening operations subjects the wires to high bending stresses which could affect their tensile properties, and affect the behaviour of laminations and scratches present in the wires. Thus an understanding of the effects of reverse bending and straightening on the tensile armour wire properties and the combined effects of reverse bending and straightening, and defects such as laminations and scratches in the wires is essential.

Presently, in the tensile armour wire manufacturing industry, the manufacturing process has an inline eddy current defect detection system. The inline eddy current defect detection system can only detect defects that are 0.2mm and above in size. In practical terms, it means that defects that are lower than 0.2mm in depth are not detected by the in-line eddy current

defect detection system, and as such, all the tensile armour wires being currently used for flexible pipe manufacturing may have defect in them that are as deep as 0.19mm. Consequently, in the flexible pipes manufacturing industry, there is the desire to know if the present defect detection capability is adequate by knowing the effects of defects with sizes below the 0.2mm detection capability of the inline eddy current detection system on the fracture mechanisms and mechanical properties of tensile armour wires. Also the flexible pipes manufacturing industry desires to know the effects of reverse bending and straightening operations and the combined effects of reverse bending and straightening, and defects such as laminations and scratches on the tensile properties of the tensile in the wires.

The desires for a better understanding of the tensile armour wire fracture mechanism(s) and the relationships between surface defect sizes and the tensile armour wires' mechanical properties have driven this project to produce design curves for the flexible pipes quality assurance and control.

1.2 Objectives of the research

This research was undertaken to provide an understanding of the failure mechanism of tensile armour wires and the effect of the various defect types, sizes, and locations on their tensile properties. In addition, the work aims to provide an understanding of how the reverse bending and straightening operations and the combination the reverse bending and straightening operations with defects such as laminations and surface scratches affect the tensile properties of the tensile armour wires.

This research aims to ascertain if the current defect detection capability of the inline eddy current defect detection system used in the flexible pipes manufacturing industry is adequate and provide design curves. The design curves could be used to determine the reductions in the tensile properties of the tensile armour wires due to the presence of defects with given dimensions and thus be used to estimate the critical or maximum defect sizes that can be allowed in tensile armour wire and/or estimate the flexible pipe's safe working loads. This research also aims to provide data on the tensile properties of defective tensile armour wires which could serve as input into the material specifications, quality standards, and quality control of the flexible pipe tensile armour wires.

1.3 Scope of the research

This research covers the effects of the sizes and locations of flat bottom scratches, pointed end scratches, dents and laminations on the mechanical properties of tensile armour wires. These are the main defects identified from scanning electron microscopy images of the tensile armour wires surface that are of interest to flexible pipe manufacturers. The research also covers the effects of the bending, reverse bending and straightening operations on the tensile properties of the as-received wires as well as the effects of these operations on near-surface laminations, mid-depth laminations and surface scratches.

1.4 Thesis outline

Chapter 1 deals with the introduction to the research covered in this thesis, the scope of the research and the aims and objectives of the research. Chapter two covers the introduction to flexible pipes and tensile armour wires, defects in engineering materials and the damage tolerance approach to the design and assessment of structures. Chapter three introduces the finite element modelling and simulation, virtual prototyping, and verification and validation of numerical simulations. It also covers the background information and basic theories for the Abaqus Finite Element software used for the numerical investigations in this research as well as a summary of the types of the structural mechanics simulations in Abaqus. A review of the previous work on presented in the literature defects and failures in wires, tensile testing simulations, denting and its effects on steel structures and the effects of reverse bending on metal products is presented in Chapter 4.

The experimental methodology and techniques, and the test method development are covered in Chapters 5 and 6 respectively, while the effects of miniature flat bottom scratches, miniature pointed end scratches and miniature dents on the tensile properties of tensile armour wires are presented in Chapters 7, 8 and 9 respectively. Chapter 10 covers the effects of bending, reverse bending and straightening operations on the tensile properties of the tensile armour wires as well as the effects of these operations on surface scratches and laminations in the wires. The conclusions and recommendation for further work are presented in Chapter 11.

Chapter 2 Literature review: flexible pipes and damage tolerance approach to design of structures.

This chapter starts with an introduction to flexible pipes; their components, their uses, failure modes and the structural importance of tensile armour wires. Also presented in this chapter is a review of literature on: tensile testing, fracture in metals, effects of defects on engineering materials and damage tolerance approaches to design and assessment of defective structures**.** Section 2.1 covers the review on flexible pipes and their uses, failures in flexible pipeline systems and tensile armour wires. A review on tensile tests and tensile deformation processes including fracture in ductile metals; structural deformation prediction theories and equations, and the influence of testing machine on tensile properties are presented in section 2.2. A review on defects in engineering materials and their effects on the tensile properties of metals are presented in sections 2.3 and 2.4 respectively. This chapter ends with the review on defect/damage tolerance approach to design and assessment of defective structures; and fracture mechanics based design and assessment of structures with cracks, which are presented in sections 2.5 and 2.6 respectively.

2.1 Flexible pipes

A flexible pipe is a composite structure, which consists of several steel and plastic layers. The steel layers are the tensile armour layer (made of carbon steel), pressure armour layers (made of carbon steel) and internal carcass (made of corrosion resistance alloys such as stainless steel). The plastic layers are the thermoplastic outer sheath, the thermoplastic anti-wear layer and the thermoplastic pressure sheath, which are made of PVC, PP, PE (Braestrup et al, 2005). Each of these layers has an individual function but they also interact with each other (Troina et al, 2003). A flexible pipe can be bonded or unbonded. In a bonded flexible pipe, the steel reinforcement is integrated and bonded to a vulcanised elastomeric material while in an unbonded pipe shown in Figure 2.1; the polymeric and metallic layers are separate and unbonded with relative movement between layers (EN ISO 13628-2, 2006). Flexible pipes are used onshore and offshore for oil and gas production and transportation. They are used as seabed flowlines, water injection lines, horizontal and vertical jumpers, risers and as wellhead jumpers on floating dry tree units. In particular, flexible pipes are used in offshore floating production systems (FPS) where rigid pipelines are not suitable. Figure 2.2 shows the various ways in which flexible pipes are used in offshore oil and gas production.

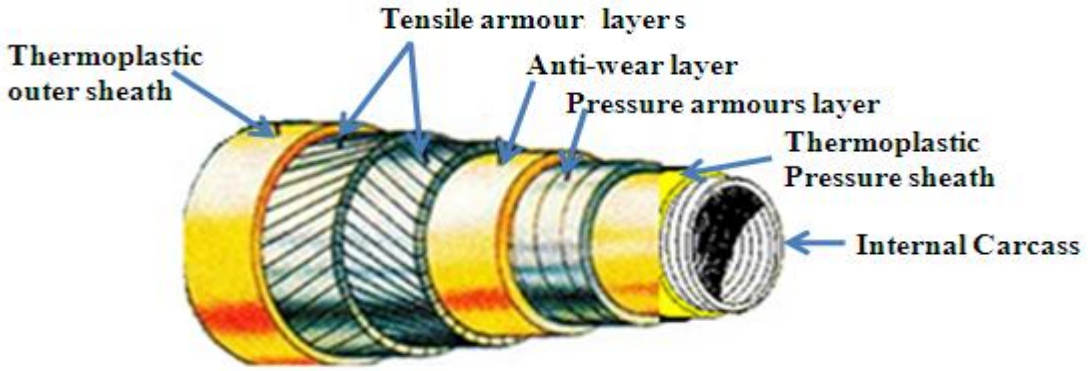

Figure 2.1: Flexible pipes components (Coutarel, 2001).

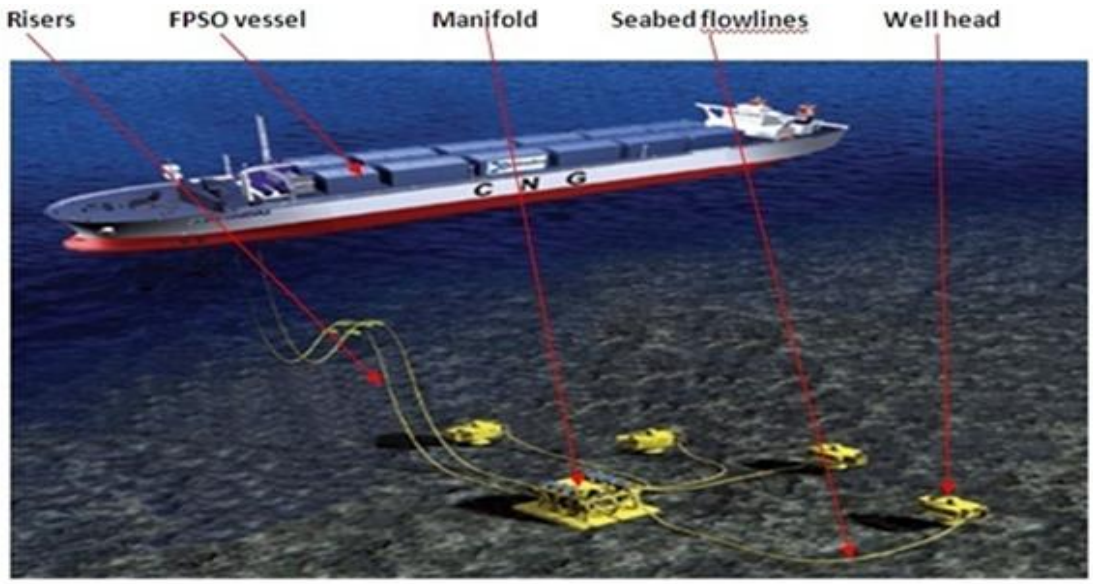

Figure 2.2: Offshore floating production system (Breastrup et al, 2005)

The use of flexible pipes within the petroleum industry to replace steel pipe as risers and flowlines is becoming popular because flexible pipes accommodate large relative motions, accommodate undulating seabed conditions, provide high corrosion resistance, reduce installation time and cost. Flexible pipes also have high damping coefficients, high resistance to dynamic loads and possibility of reuse. They also permit remote connection to subsea production equipment (Wolfe, 1991).

2.1.1 Failures in flexible pipeline system

Recently in the United Kingdom, the Health and Safety Executives (HSE) has observed an emerging trend of incidents involving the failure of flexible pipelines (HSE, 2007). The main failure modes of flexible pipes systems obtained from Pipa et al, (2010) and the HSE website are presented in Table 2.1. From Table 2.1, it is evident that many flexible pipes failures are

associated with tensile and pressure armour layer/wire failures. This is because in high-pressure applications and in ultra deepwater, the tensile armours and the pressure armours are challenged. As a matter of fact, the fatigue life of the tensile and pressure armour layers dictates the life of the flexible pipes (Troina et al, 2003). Consequently, for flexible pipes without dedicated pressure armour layer/wires, the static strength and the fatigue life of the tensile armour wires solely dictates the performance and durability of flexible pipes

Table 2.1: Flexible pipes failure modes (Pipa et al, 2010)

S/no	Failure modes	Courses of failure/potential failure manifestations
1	Collapse	Collapse of carcass and/or pressure armour due to excessive tension, excessive external pressure or installation overloads
2	Burst	Rupture of tensile or pressure armours due to excess internal pressure
3	Tensile failure	Rupture of tensile armours due to excess tension
4	Compressive failure	Birdcaging of tensile armour wires
5	Overbending	Rupture or crack of external or internal sheaths
6	Torsional failure	Failure of tensile armour wires
7	Fatigue failure	Tensile armour wire fatigue
8	Erosion	Erosion of f internal carcass
9	Corrosion	Corrosion of internal carcass or tensile/pressure armour exposed to seawater or diffused product

2.1.2 Tensile armour wires,

Tensile armour wires are carbon steel wires with sizes ranging from 4mm X 2mm to 12mm X 7mm in cross sectional dimensions and are generally produced by cold rolling or hot rolling and cold finish rolling processes (Troina et al, 2003). The two main mechanical properties of tensile armour wires that affect their suitability and ability to withstand the severe static and extreme dynamic loads (structural performance) are their tensile and fatigue properties (Troina et al, 2003). Tensile armour wires as a typical engineering material inevitably have defects such as surface markings, sharp edges, rough edges/burrs, corrosion pits, laps, dents,

cracks, and scratches. Others include: shavings, gouges, corrosion, scaling, discoloured areas (blurring, scorching, staining and the like, except at welds), distorted or buckled strip or wire profile and significant scoring (BS EN ISO 13628-2:2006).

2.2 Tensile tests

The uniaxial tension test is the fundamental mechanical test used to provide the basic information on the mechanical behaviour of materials and it is also used as an acceptance test for materials specification (Mahmudi et al, 2003). Tensile tests can be used to determine the yield strength, tensile strength, elongation, reduction in area, modulus of elasticity, and the deformation energy values consumed during the elastic and plastic deformations (Mahmudi et al, 2003). The yield strength is the stress at which a material begins to deform plastically. For materials without a conspicuous yield point, the yield strength is taken as the proof stress, which is the stress at an offset strain of 0.002 -0.005 (0.2-0.5%). Tensile tests are carried out using carefully prepared specimens which are gripped and loaded in a very controlled manner by the tensile testing machine, which provides the force-displacement curves. Stress-strain curves which provide more useful information on the mechanical properties of materials can be constructed from the load-extension curves (Mahmudi et al, 2003).

Tensile test specimens are usually substantially full size/un-machined or specimens machined to standardised dimensions (ASTM E 8M: 2009). They may be of circular, flat (square or rectangular), annular or some other uniform cross-section (BS EN ISO 6892-1:2009). The standard round test specimen shown in Figure 2.3(a) is generally used for testing metallic materials, including both cast and wrought. The standard flat test specimen shown in Figure 2.3 (b) is used for testing metallic materials in the form of sheets, plates, flat wires, strips, bands, hoops, rectangles, and shapes (ASTM E 8M: 2009). In Figure 2.3, L is the overall length, W_0 is the width of the parallel length, T_0 is the thickness of gauge section, B is the width of the grip sections/shoulders, R is the fillet radius, A is the length of the reduced section and L_0 is the gauge length (ASTM E 8M: 2009).

It is essential to know that the tensile strength results obtained from test pieces machined to standardised dimensions may not totally represent the strength and ductility properties of the end product or its behaviour while in service under different environments. Also machined specimens may not be perfectly prepared in terms of dimensional precision and may not be

completely defect free (i.e. free from all the defects listed in the last paragraph). All these could lead to obtaining unsatisfactory and incorrect test results (ASTM E 8M: 2009).

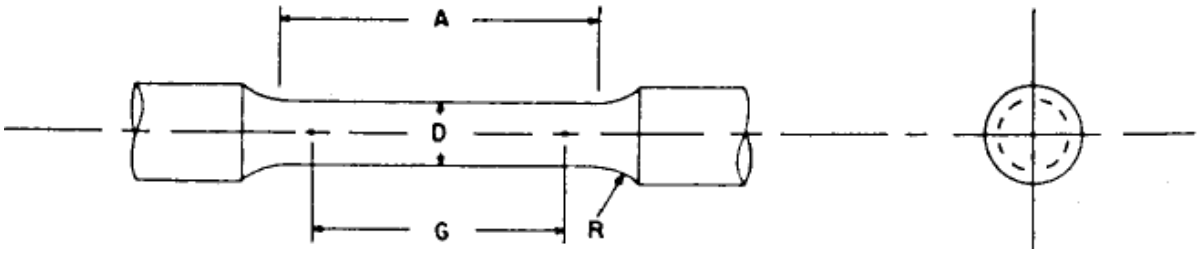

(a) Standard round tensile test specimen

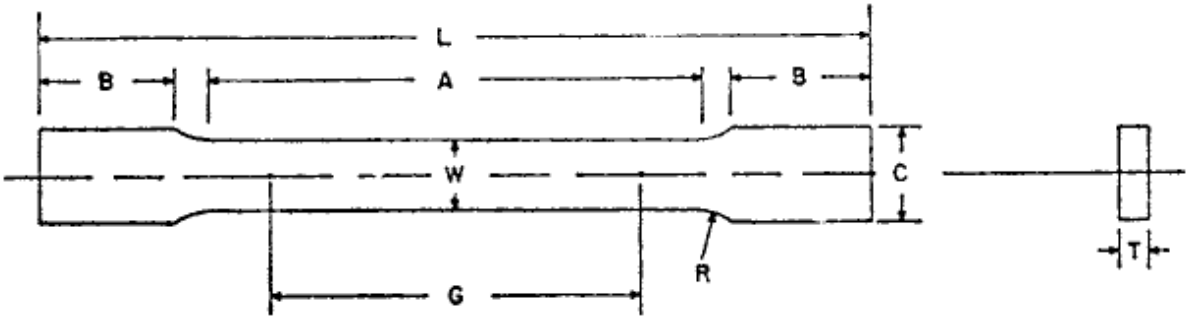

(b) Standard flat tensile test specimen

Figure 2.3: Standard machined tensile test specimens (ASTM E 8M: 2009).

2.2.1 Tensile deformation

For most ductile materials, the load-extension curve has the elastic, uniform plastic and post-necking or post-uniform deformation sections (Mahmudi et al, 2003). When a ductile material is stretched below its yield strength point A shown in Figure 2.4, the atomic and molecular bonds are merely stretched and not broken. Consequently, when the stress/applied load is removed, the material will return to its original shape. The elastic deformation energy, W_e, is usually very small and is recovered after failure. It is calculated as the area under the elastic part of the load-extension curve and is usually ignored in the calculation of the total energy, W_t (Mahmudi et al, 2003). Most metals do not have a specific yield point because the transition from elastic to plastic behaviour occurs gradually and the elastic range generally extends slightly beyond the proportional limit. The gradual transition from elastic to plastic behaviour is due to the successive yielding of the individual crystal grains (Chakrabarty, 2006).

When the material is stressed beyond its yield point, the atomic and molecular bonds begin to break and the broken bonds do not reform when the applied load/stress is removed, leading to

permanent/plastic deformation. The uniform plastic deformation energy, W_p, is the plastic energy dissipated before necking and is related to the bulk material in the gauge section (Mahmudi et al, 2003). It is significantly higher than the elastic deformation energy and it is calculated using the expression in equation 2.1 obtained from Mahmudi et al, (2003).

$$W_p = W_0 L_0 T_0 w_p \tag{2.1}$$

Where $w_p = \int_0^{\varepsilon_u} \sigma d\varepsilon$ is the plastic energy per unit volume and ε_u is the true uniform elongation at the ultimate tensile stress before necking.

Plastic deformation in metals usually involves sliding/slipping of blocks of metal crystals over one and other along defined crystallographic planes (slip planes). The slip plane usually occurs at locations of dislocations. Dislocations are defects/imperfection in the crystal lattice of metals (Dieter, 1988). During tensile plastic deformation, the strain increases faster than the stress because the specimen cross-sectional area decreases uniformly along the gauge length. In ductile materials, despite the reduction in specimen cross-sectional area, the stress/load sustained by the specimen increases in this region up to the ultimate load/tensile strength due to strain hardening/work hardening. Strain hardening is caused by dislocation storage and is proportional to the dislocation density. As the deformation continues, more dislocations are formed and stored during uniform straining as well due to gradient of strain, which occurs due to the geometry of loading or because the material is plastically inhomogeneous (such as when the material contains a non deforming phase) (Fleck et al, 1994). Dislocations stored due to trapping of dislocations by each other in a random way is termed the statistically stored dislocations and the dislocations stored due to the requirement for compatible deformation of the various parts of the crystal is termed geometrically necessary dislocations (Fleck et al, 1994). The trapping/interactions of dislocations with each other and with other barriers such as the grain boundaries impede/hinder their motion through the crystal lattice. The impedance of the motion of the dislocations leads to dislocation pile-ups/accumulation on slip planes at barriers in the crystals. The pile-ups produce a back stress which opposes the applied stress on the slip plane (Dieter, 1988).

If the strain hardened material is loaded in the reverse direction, the back stress assists the dislocation movements in the reverse direction (Takeda and Chen, 1999), thereby making them move more easily. This leads to easier plastic deformation (since plastic deformation

occurs by dislocation movement) and a reduction in the yield strength in the reverse direction. This phenomenon by which the plastic deformation of a material in one direction such as the tensile cold working of a material increases its tensile yield strength in that direction but decreases its yield strength in the opposite direction (i.e. decreases its compressive yield strength) is termed the Bauschinger effect. The Bauschinger effect is responsible for the reductions in both the fatigue strength and the static yield strength of a metal subjected to strain reversal (Takeda and Chen, 1999).

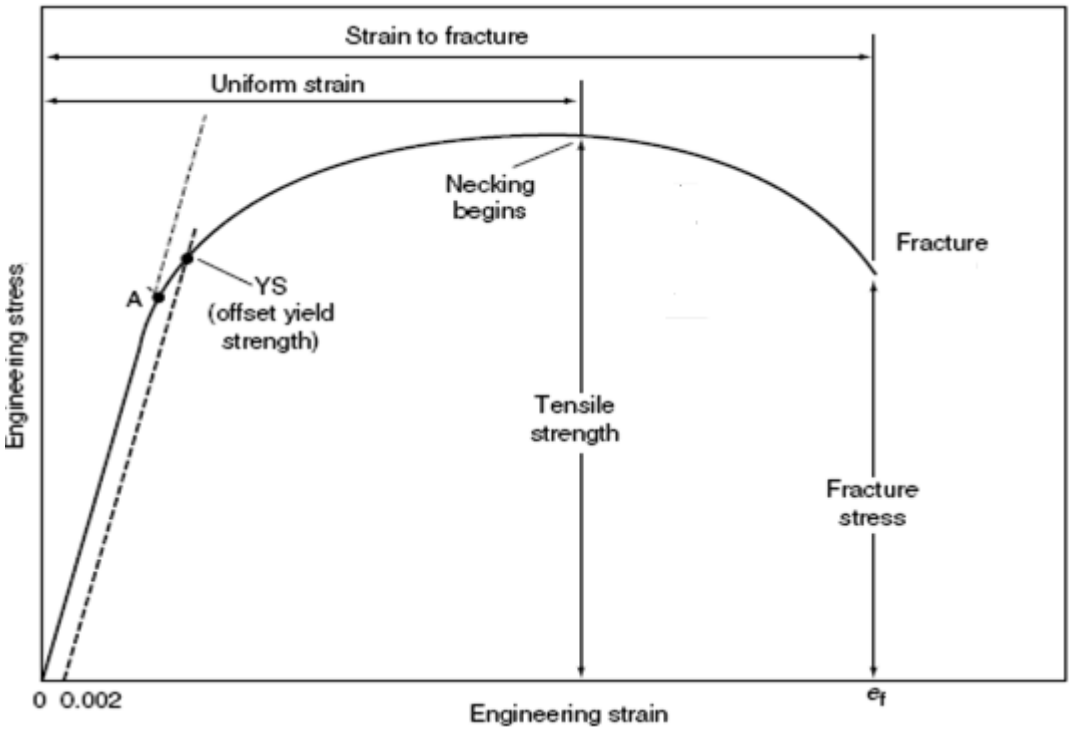

Figure 2.4: Typical experimental engineering stress-strain curve (Mahmudi et al, 2003).

Once the specimen is stressed to its ultimate load/tensile strength, the cross-sectional area of the specimen now decreases more than the increase in the deformation load due to strain hardening. Under this condition, all further plastic deformation is concentrated at a slightly weaker point in the specimen, leading to non-uniform plastic deformation, causing flow instability and making the specimen neck or thin down locally at this weaker point. For cylindrical specimens, diffused necking which involves reduction in the specimen cross sectional area over an extent that is much greater than the sample thickness as shown in Figure 2.5 occurs. Diffuse necking may terminate in fracture, but for flat specimens, especially thin strips; it is often followed by a second instability process termed localized necking of thin strips (Ling, 1996). Localized necking occurs over a narrow band inclined at

an angle to the specimen axis, as shown in Figure 2.5. Localized necking is associated with plane strain deformation with considerably increased strain and strain rate within the deformation band (Ifergane et al, 2010) and is characterized by a little contraction of the specimen in the width direction and a rapid shrinking of the specimen thickness along the necking band (Ling, 1996). Within the narrow band, the specimen cross section undergoes intense thinning leading to the thin sheet specimen fracturing with two knife-edges (Ifergane et al, 2010). As the specimen cross-sectional area is now decreasing far more rapidly than the deformation load due to strain hardening can cope with, the actual load required to deform the specimen continues to reduce (and so does the engineering stress) till fracturing of the specimen begins.

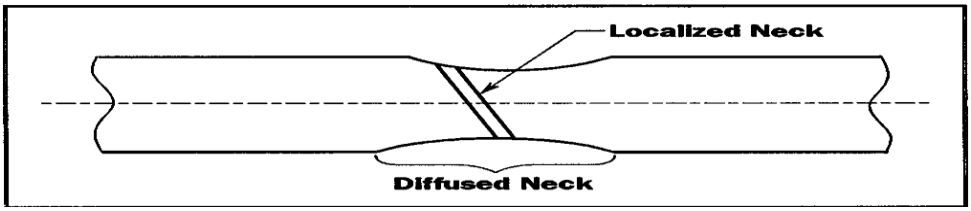

Figure 2.5: Diffused and localized necking in flat thin strips specimens (Ling Yun, 1996)

2.2.2 Fracture in metals

Fracture occurs when a homogeneous solid or a metallurgical junction separates into two parts due to one or a combination of mechanical stress, chemical influences and effect of heat (Lothian et al, 1981). The fracture of ductile materials culminates the progressive damaging process associated with the substantial plastic deformation of materials and it occurs when the materials are loaded beyond their load carrying capacities (Huang and Xue, 2009). The tearing or fracture energy W_f is related to the necked region and to the torn cross-sectional area. It is calculated in terms of the tearing energy per unit torn area w_f using the expression in equation 2.12 obtained from Mahmudi et al, (2003).

$$W_f = W_0 T_0 w_f \tag{2.2}$$

The ductile failure of structures usually begins with the accumulation of ductile plastic damage, followed by the initiation of fracture and ends with crack propagation. Microscopically, the accumulation of ductile plastic damage is associated with the void nucleation, growth and coalescence, shear band movement and the propagation of micro-

cracks. Macroscopically, fracture initiation is associated with the degradation of the material, which leads to a decrease of the material stiffness, strength and a reduction of the remaining ductility. Ductile materials may exhibit cleavage or ductile transgranular fracture mechanisms depending on the temperature (Xue, 2007).

2.2.2.1 Brittle-cleavage type fracture

For steel, the cleavage fracture mechanism often occurs at low temperatures. Cleavage fracture is nucleation controlled and the nucleation is considered a stress controlled process (Neimitz and Galkiewicz, 2006). Brittle-cleavage type fracture is characterised by separation normal to the tensile stress. It involves rapid rate of crack propagation without any appreciable plastic deformation before and during the crack propagation. Brittle fracture starts with plastic deformation which involves consecutive displacement and slipping of individual atoms of the metal to varying distances. This is followed by pile-up of dislocations along their slip planes at an obstacle. Shear stresses build-up at the head of the dislocation pile-ups leading to nucleation/initiation of a microcrack. Microcracks are initiated as a result of cracking of particles during plastic deformation or as a result of cracking/fracturing of inclusions due to high stresses associated with dislocation pile-ups at the location of inclusion or second phase particles (Dieter, 1998). The materials with these microcracks eventually fail in a brittle manner by crack propagation.

2.2.2.2 Ductile fracture

Ductile fracture process starts with micro-separation and the mechanisms by which the micro-separation is formed depend on the type of material, its microstructure, temperature, stress, strain and strain rate (Neimitz and Galkiewicz, 2006). Micro-separations in metallic polycrystalline materials that exhibit ductile fracture due to void nucleation, growth and coalescence occur after a severe local plastic flow and are thus strain controlled. However void growth depends both on the strain and hydrostatic stress. Micro-separation grows into micro-crack if the stress in front of it is high enough or grows as a void if not (Neimitz and Galkiewicz, 2006). A microcrack/microvoid is formed when a sufficient stress is applied to a material that exceeds its cohesive/bond strength σ_c, and breaks the bond between the atoms of the material at grain boundaries or interfaces between the metal and inclusions (Askeland and Phule, 2006). The cohesive/bond strength is due to the cohesive force of attraction

between the atoms per unit area and can be estimated approximately using the expression in equation (2.3) obtained from Anderson, (2005).

$$\sigma_c \approx \frac{E}{\pi} \tag{2.3}$$

Unlike brittle-cleavage type fracture, ductile fracture involves appreciable plastic deformation before and during ductile crack growth. Ductile fracture occurs by a slow tearing of the metal. Ductile fracture can take three forms. These are: a shear fracture in ductile single crystals, a cup and cone fracture in moderately ductile metals (polycrystals) and a completely ductile fracture, called rupture failure which occurs in very ductile metals (Dieter, 1998). A rupture failure occurs in high purity ductile metals. The metal necks down to a line or a point before separation.

A shear fracture occurs when shear stresses are present during plastic deformation (Lothan et al, 1981). It occurs due to extensive slip on the active slip plane. Slip occurs when the applied stress produces a resolved shear stress (the highest value of which occurs at 45° to the applied tensile stress) that equals the critical resolved shear stress. The critical resolved shear stress is the stress required to break enough metallic bond in order for slip to occur (Askeland and Phule, 2006). Applied stresses causes shear band formation and localization. This leads to the formation of cracks within shear bands and eventual failure due to fracture within shear bands (Simulia, 2007). The fracture surface of a shear fracture appears grey and fibrous and when examined using a scanning electron microscope, the dimples (the traces of the microvoids produced during fracture) on the surface are oval shaped or elongated as shown in Figure 2.9(a) (Askeland and Phule, 2006). Shear failure surface is characterised by a separation at approximately 45 degrees to the tensile stresses (Dieter, 1998).

A cup and cone fracture in moderately ductile metals begins with necking at the ultimate load as shown in Figure 2.6(a) which introduces a triaxial state of stress in the necked region. As shown in Figure 2.6(a), voids or cavities are formed in the necked region and these voids grow and coalesce into a central crack which grows in a ductile manner perpendicularly to the direction of the applied tensile stress, resulting into a flat fracture [(Anderson, 2005) and (Askeland and Phule, 2006)]. The growth of void at the center is controlled by the plastic strain and hydrostatic stress (Neimitz and Galkiewicz, 2006). The flat ductile fracture continues until it approaches the surface/edge of the specimen that is dominated by plane stress, where the growth of the void is due to the shearing plastic strain (Neimitz and

Galkiewicz, 2006) and then propagates along localised shear plane at roughly 45 degree to tensile force direction. This leads to slant fractures and the formation of shear lips on both surfaces/edges of the specimen as shown in Figure 2.6(a) (Dieter, 1998; Askeland and Phule, 2006). The fracture surface of the flat portion of the cup and cone fracture when examined using a scanning electron microscope, has round or equiaxed dimples as shown in Figure 2.9(c).

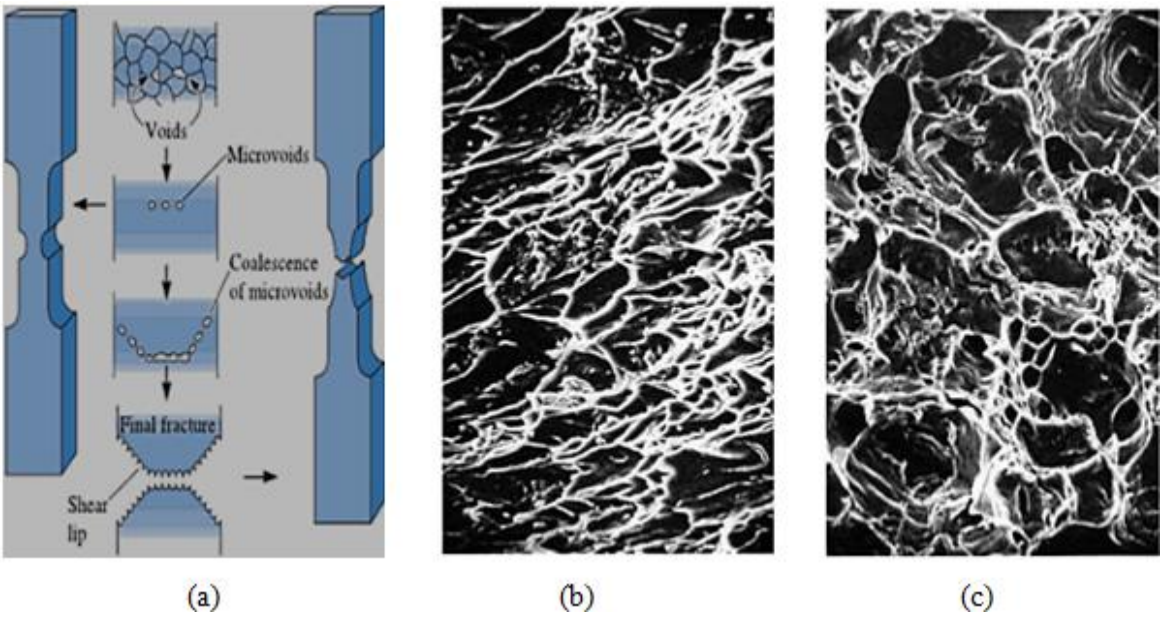

Figure 2.6: Cup and cone formation stages and micrographs of shear and ductile fractures: (a) Ductile cup and cone formation stages, (b) Elongated dimples at shear slip, (c) Equiaxed dimples at the centre of the cup and cone (Askeland and Phule, 2006).

The slant and flat fracture morphologies exhibited by moderately ductile materials are due to crack "tunnelling". Crack "tunnelling" is the term used to describe the preferential and faster crack growth at the center of the specimen which has high triaxiality and a slower crack growth on the outer regions of the specimen with low triaxiality/or a biaxial stress. The difference in the level of triaxiality and the speed of crack propagation between the centre of the specimen and its outer edges/surfaces results in a flat fracture at the centre of the specimen and a slant fracture and formation of a shear lips on the edge (outer region) of the specimen (Anderson, 2005). The combination of the flat and slant fracture morphologies results in the cup and cone fracture mode/shape associated with moderately ductile metals failures (Dieter, 1998).

2.2.3 Tensile structural deformation prediction

Predicting the deformation of a structure is done by "mapping" the history of the movement of a particle from its initial location at some position X in the initial configuration of a structure to a new position x as the structure deforms throughout the history of loading of the structure. The "mapping" is done using the deformation gradient matrix F given in equation 2.4 obtained from (Simulia, 2007).

$$F = \frac{\partial x}{\partial X} \tag{2.4}$$

The deformation gradient matrix F can also be expressed in terms of its components, the straining part of the motion and the rotating part of the deformation as given in equation 2.5 obtained from (Simulia, 2007). The straining part of the motion is represented by the stretch matrix, V , and the rotating part by the rotation matrix R . The stretch matrix V , completely defines the deformation of the material particles at x while the rotation matrix R defines the rigid body rotation of the principal directions of strain from N_I in the reference configuration to n_I in the current configuration.

$$F = V.R \tag{2.5}$$

The velocity v of a material particle during the motion is defined as the rate of change of the spatial position x , of a fixed material particle. It is calculated as the partial differentiation of the spatial position x with respect to time (t) as given in equation 2.6 obtained from (Simulia, 2007).

$$v = \frac{\partial x}{\partial t} \tag{2.6}$$

The rate of deformation or strain rate matrix $\dot{\varepsilon}$ (also known as the rate of deformation tensor) of the material or component is calculated using the strain rate matrix given in equation 2.7 obtained from Simulia, (2007) in terms of the velocity gradient $\left[\frac{\partial v}{\partial x}\right]$ and velocity gradient transpose $\left[\frac{\partial v}{\partial x}\right]^T$. The rate of rotation or spin W is calculated using the rotation rate matrix

given in equation 2.8 also obtained from (Simulia, 2007). $\left[\frac{\partial v}{\partial x}\right]$ and $\left[\frac{\partial v}{\partial x}\right]^T$ represent a "column" vector and a "row" vector respectively.

$$\dot{\varepsilon} = \frac{1}{2}\left(\left[\frac{\partial v}{\partial x}\right] + \left[\frac{\partial v}{\partial x}\right]^T\right) \tag{2.7}$$

$$W = \frac{1}{2}\left(\left[\frac{\partial v}{\partial x}\right] - \left[\frac{\partial v}{\partial x}\right]^T\right) \tag{2.8}$$

During deformation, the Effective Mises stress, q, is given in equation 2.9

$$q = \sqrt{\frac{3}{2} s : s} \tag{2.9}$$

Where s, the deviatoric part of the Cauchy stress tensor σ is given in equation 2.10.

$$s = pI + \sigma \tag{2.10}$$

p is the hydrostatic pressure given in equation 2.11

$$p = -\frac{1}{3}\sigma : I \tag{2.11}$$

2.2.3.1 Elastic-plastic structural deformation prediction

With the exception of the deformation plasticity which is used primarily for the ductile fully plastic (plastic collapse or net section yielding) fracture mechanics applications under small-displacement conditions and which defines stress in terms of the total mechanical strain with no history dependence, generally, elastic-plastic deformation are based on incremental plasticity theory (Simulia, 2007). The incremental plasticity theory in is based on the assumption that the total mechanical deformation consists of an elastic part and an inelastic (plastic) part. The incremental plasticity theory is based on three rate equations which are the strain rate decomposition equation, the flow rule equation and the hardening evolution equations. The strain rate decomposition given in equation 2.12 is based on the additive strain rate decomposition and is formulated in terms of the total (mechanical) strain rate $\dot{\varepsilon}$, the

elastic strain rate $\dot{\varepsilon}^{el}$ (rate of change of the elastic strain) and the plastic strain rate $\dot{\varepsilon}^{pl}$ (rate of change of inelastic strain)

$$\dot{\varepsilon} = \dot{\varepsilon}^{el} + \dot{\varepsilon}^{pl} \tag{2.12}$$

The flow rule equation defines the limit of the region with purely elastic response and is defined by a yield function, *f*, which may depend on the true stress, σ , temperature, θ , and hardening parameters, H_α , as shown in equation 2.13 obtained from Simulia, (2007). For isotropic yielding, the yield function given in equation 2.14 is equal to the equivalent uniaxial (Mises) stress, q .

$$f(\sigma, \theta, H_\alpha) \langle 0 \tag{2.13}$$

$$f = q = \sqrt{\frac{3}{2}} S : S \tag{2.14}$$

Where $S = 2G\varepsilon^{el}$ is the deviatoric stress and $G = \frac{E}{2(1+\nu)}$ is the shear modulus.

Isotropic hardening is exhibited by a material in which its yield surface changes size uniformly in all directions, such that the yield stress increases (or decreases) in all stress directions with plastic straining (Ken-ichiro, 2001; Simulia, 2007).The isotropic yielding modelling is based on the Mises yield surface, which is based on the assumption that yielding of the metal is independent of the equivalent pressure stress (Simulia, 2007). This assumption is not valid for voided metals.

The Gurson's porous metal plasticity theory which is based on the assumption that the yield stress of the fully dense matrix material is a function of the equivalent plastic strain in the matrix is used for the deformation prediction of voided metals. The yield condition for porous metal plasticity given by Gurson and modified by Tvergaard and Needleman is given in equation 3.6 obtained from Simulia, (2007).

$$\phi = \left(\frac{q}{\sigma_y} \right)^2 + 2q_1 f^* \cosh\left(-q_2 \frac{3p}{2\sigma_y} \right) - \left(1 + q_3 f^{*2}\right) = 0 \tag{2.15}$$

Where $p = -\frac{1}{3}\sigma : I$ is the hydrostatic pressure and I is a unit matrix. q_1 and q_2 are the coefficients of the void volume fraction introduced by Tvergaard as adjusting parameters used in bringing experimental void growth measurements in agreement with the model theory (Ragab, 2004). q_3 is the coefficient of pressure term. The function f^* models the rapid loss of stress carrying capacity that accompanies void coalescence and is defined in terms of the void volume fraction as:

$$f^* = \begin{cases} f & \text{if } f \le f_c, \\ f_c + \dfrac{\bar{f}_F - f_c}{f_F - f_c}(f - f_c) & \text{if } f_c < f < f_F \\ \bar{f}_F & \text{if } f \ge f_F, \end{cases},$$

Where:

$$\bar{f}_F = \frac{q_1 + \sqrt{q_1^2 - q_3}}{q_3}.$$

f_c Critical value of the void volume fraction at which void nucleation begins,

f_F Value of void volume fraction at which there is a complete loss of stress carrying capacity in the material (failure)

f_c and f_F model the material failure when $f_c < f < f_F$, due to mechanisms such as micro fracture and void coalescence. Total failure at the material point occurs when $f \ge f_F$. f is related to the relative density, r, of the material by equation 2.16

$$f = 1 - r \qquad (2.16)$$

For a fully dense material with a relative density $r = 1 (f = 0)$, the Gurson yield condition reduces to the Von Mises yield condition. If $f = 1 (r = 0)$, the material is completely voided and has no stress carrying capacity. The porous metal plasticity model generally gives physically reasonable results only for $f < 0.1 (r > 0.9$ (Simulia, 2007).

Kinematic hardening models are used to model the behaviour of metals that are subjected to cyclic loading and are typically applied to studies of low-cycle fatigue (Simulia, 2007). In

Kinematic hardening model, the yield surface doesn't change; but it is rather being pushed around in the stress space (Ken-ichiro, 2001) or shifts in stress space so that straining in one direction reduces the yield stress in the opposite direction (Simulia, 2007). Kinematic hardening models are the simplest theory used in modelling the Bauschinger effect in Abaqus (Simulia, 2007). In

The combined or mixed hardening model is a combination of the nonlinear kinematic and isotropic hardening models. It is used to simulate plastic hardening in cyclic loading conditions Simulia, (2007). The combined hardening model is used for modelling nonlinear isotropic combined with kinematic cyclic hardening behaviours. A typical isotropic cyclic hardening component of the combined hardening model modelled with the exponential law given in equation 2.17 obtained from Simulia, (2007) is defined by specifying the equivalent stress and the equivalent plastic strain.

$$\sigma^0 = Y_i + Q_\infty(1 - e^{-b\bar{\varepsilon}^{pl}}) \tag{2.17}$$

Where σ^0 is the size of the yield surface (size of the elastic range), Q_∞ is the maximum increase in the elastic range, b is the material parameter that defines the rate at which the maximum size is reached as plastic straining develops and Y_i is the initial yield stress. The kinematic hardening component based on the evolution of the backstress (a nonlinear evolution of the centre of the yield surface) $\dot{\alpha}$ is given in equation 2.18 obtained from Simulia, (2007).

$$\dot{\alpha} = C\frac{1}{\sigma^0}(\sigma - \phi)\varepsilon^{pl} - \gamma\phi\varepsilon^{pl} \tag{2.18}$$

2.2.3.2 Engineering and true stresses and strains

Generally the original sample/structure dimensions change uniformly and continuously as it is stressed/strained and the changes in dimension becomes more noticeable after yielding. Engineering/nominal stress σ_{nom} and strain ε_{nom} values are based on the original area and original length of the specimen/component and do not reflect the continuous changes in the specimen's dimension. Thus using engineering stress and strain values do not give a true indication of the deformation characteristics of a metal, and therefore cannot provide a proper description of the physical phenomena that are involved in the tensile test (Simulia, 2007).

Consequently, the true stress σ and true strain ε values, which are based on instantaneous area and length, estimated using the expressions in equations (2.19) and (2.20) respectively are used as material input for FEA simulation (Simulia, 2007).

$$\sigma = \sigma_{nom}(1+\varepsilon_{nom}) \tag{2.19}$$

$$\varepsilon = \ln(1+\varepsilon_{nom}) \tag{2.20}$$

For small strains (about 1% strain), there is no significant difference in the engineering and true strain values as the error is of the order of 10^{-4}. Thus, the true stress can also be related to the true strain by the expression given in equation (2.21) which is the same expression that relates engineering stress to engineering strain. This is so because the modulus of elasticity, E, is established at a small strain level when the instantaneous area A_i, and the original cross sectional area A_0; as well as the instantaneous length, L_i and original gauge length L_0 are approximately equal.

$$\sigma = E\varepsilon \tag{2.21}$$

At large strains (strains greater or equal to 5%), the most popular empirical mathematical equation that relates true stress to true stain is the Hollomon's equation (Soboyejo, 2003) or Ludwick simple power law (Chakrabarty, 2006) given in equation (2.22).

$$\sigma = K\varepsilon^n \tag{2.22}$$

Where K is the proportionality constant that represents the true stress at a true strain of 1.0 and n is the strain hardening/work hardening exponent which is a measure of the resistance to plastic deformation. The value of "n" is between 0 and 1. The higher the value of n, the more pronounced the strain-hardening characteristic of the metal (Chakrabarty, (2006). K and n are constants determined from known true stress-strain data before necking. Equation 2.21 is valid up to the onset of necking.

The true stress can also be related to the true stain using the modified power law given in equation 2.23 which represents a strict rigid/plastic behaviour of metals or by the Swift's generalised power law given in equation 2.24. When n =1, equation 2.23 gives a linear strain-hardening which is a "reasonable approximation" for heavily prestrained metals (Chakrabarty, 2006).

$$\sigma = Y_i\left(1+m\varepsilon^n\right) \tag{2.23}$$

$$\sigma = C(m+\varepsilon)^n \tag{2.24}$$

Where C, m and n are empirical constants and Y_i is the initial yield stress.

For metals without sharply defined yield stress which show smooth elastic-plastic transition and work harden, the Ramberg-Osgood elastoplastic equation given in its multiaxial stress states in equation 2.25 obtained from Simulia, (2007) defines the relationship between the strain(ε) and stress(σ) for the elastic, elastic-plastic transition and plastic regions Chakrabarty, (2006). The Ramberg-Osgood relationship is essentially a nonlinear elastic model but can also be used to model the plastic response of materials which exhibits plastic collapse (a limit state during which all of a specimen net section yields (Simulia, 2007; Broek, 1997).

$$E\varepsilon_T = (1+\nu)s - (1-2\nu)pI + \frac{3}{2}\alpha\left(\frac{q}{Y_0}\right)^{n-1} s \tag{2.25}$$

Where ε_T is the strain tensor, Y_0 is the yield stress, p is the equivalent hydrostatic stress, q is the Mises equivalent stress, s is the stress deviator, ν is the Poisson's ratio, I is the identity tensor and α is the "yield" offset.

2.2.4 Influence of testing machine on tensile properties

The characteristic of the testing machine can strongly affect the shape of the force-displacement curve and the fracture behaviour of test specimens (Dieter, 1998). "All testing machines deflect under load" (Dieter, 1998). Hence, testing machines crosshead displacement cannot be directly converted to the deformation of the specimen without applying appropriate correction. The crosshead displacement Δ_c given in equation 2.26 obtained from Dieter, (1998) and Davis, (2004) is the sum of the elastic displacement in the specimen $\Delta_E = \sigma L / E$, the plastic displacement in the specimen $\Delta_P = E_P L$ and the elastic deflection of the testing machine (elastic deflection of machine frame, load cell and grips) $\Delta_m = P / K$.

$$\Delta_c = \frac{PL}{AE} + E_P L + \frac{P}{K} \tag{2.26}$$

The machines stiffness K is calculated using the expression in equation 2.27 obtained from Davis, (2004).

$$K_1 = (\Delta_c / P - L_0 / A_0 E)^{-1} \tag{2.27}$$

Where L_0 is the specimen original gauge length, A_0 is the specimen original cross sectional area, P is the load in the specimen and E is the young modulus.

2.3 Defects in engineering materials

Most engineering materials contain defects. These defects vary in degrees and sizes; and may range from nanoscale to macroscale (i.e. can be nanoscale, microscale, mesoscale, and macroscale defects) (Shen et al, 2009). Surface defects are as a result of damage to the surface of a solid body due to its interactions with another solid body or some other medium (liquid or gas) (Lothian, 1981). These interactions could be mechanical, thermal and or chemical. Surface damage by mechanical interaction could lead to elastic deformation, plastic deformation, impression (denting) by a foreign body, adhesion, material transfer and removal (Lothian, 1981).Thermal interactions could lead to heat transfer phase changes and localized melting while chemical interactions could lead to a chemical reaction like corrosion. Interactions causing heat transfer and elastic deformation leave no permanent traces while others do.

Some mechanical surface defects such as the stress crack after rolling, groove and scratch after grinding shown in Figures 2.7 (a), (b) and (c) respectively are introduced to metal products right from the production line by certain production processes such as rolling, drawing, grinding and metal cutting operations (Lothian, 1981). Mechanical damage can also occur during transportation, construction and installation, and during the service life of the metal products.

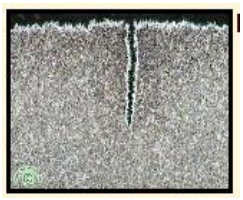

(a) Stress crack after rolling

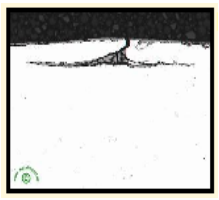

(b) Groove

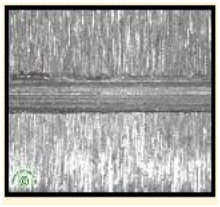

(c) Scratch after grinding

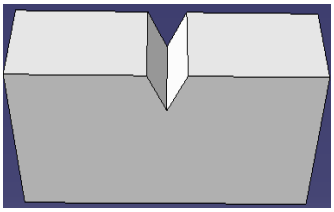

(d) V-notched specimen

Figure 2.7 Common surface defects in engineering materials (Lothian, 1981).

A typical example of an internal defect is the lamination. A lamination is an elongated line type defect or a long crack that is usually parallel to the surface of metal products produced through rolling or drawing process. Laminations result from the elongation of cylindrical cavities in the parent ingot during rolling or drawing process (Smith et al, 1957) or from slag

and or mould powder entrapment during the steel making or casting process (Moir and Preston, 2002). Lamination may also be caused by seams, non-metallic inclusions (MnS) or by alloy segregation that is made directional by working the material (Escoe, 2006). Laminations represent a material separation or discontinuity and are normally invisible at the surface (Smith et al, 1957).

2.4 Effects of surface defects on tensile properties of metals

Surface defects can generally be classified as surface cracks and notches. Notches in a broad sense are used to refer to any discontinuity in shape or non-uniformity in material (Yen and Dolan, 2007). Consequently, notches are inevitably present in a large number of structural and machine components (Tlilan et al, 2008). Traditionally, the study of notches (such as the V-notch in Figure 2.7 (d)) and the study of cracks have been carried out on parallel tracks with little overlaps (Atzori et al, 2001). However, the stress distributions around the tip of notches have been established to be quite different from the stress distributions around the tip of cracks. The effects of defects on the tensile properties of specimens/components can be determined by carrying out notch tension tests. Notch tension tests involve laboratory tensile testing of 60 degree notched specimens with root radius of 0.025mm or less (Dieter, 1998).

2.4.1 Effect of defects on yield strength

Defects such as cracks, grooves and scratches shown in Figure 2.7 act as stress concentrators and the maximum stress occurs at the root of the notch. The degree of amplification of the stress falls of rapidly while moving away from root of the notch. This creates a steep stress gradient from the peak amplified stress at notch root to the nominal stress away from the root notch. When the local amplified stress at the root of the notch reaches the yield stress, σ_0, of the material, yielding/plastic flows begins. During yielding, the material at the root of the notch attempts to stretch plastically in the direction of the applied load and contract laterally and transversely but is constrained by the rest of the material, which remains elastic, leading to the development of tensile stresses in the other two principal directions (Bayram et al, 1999). With the development of the tensile stresses in the other two principal directions, it becomes necessary to increase the axial stress (σ_y) to initiate plastic deformation as shown by the Tresca yield criterion in equation 2.28 (for a plane stress condition), leading to higher yield strength of notched specimens. This is referred to as “notch- strengthening” for ductile metals [(Dieter, 1998) and (Bayram et al, 1999)]. The plastic constraint increases with the notch depth. Consequently, the deeper the notch, the higher the axial stress required to

deform the specimen and the higher the yield strength of the notched specimen (Bayram et al, 1999).

$$\sigma_0 \approx \sigma_y - \sigma_x \tag{2.28}$$

2.4.2 Effect of defects on ductility

The steep stress gradient created by the stress concentration at the notch root is accompanied by sharp strain gradients which causes a high local plastic strain concentration around the notch root that increases the tendency for brittle fracture. The high local plastic strain concentration is accompanied by a high local strain hardening which can lead to ductile void formation that can be converted to brittle cracks. Also the high local plastic strain concentration leads to a local strain rate which is much higher than the average strain rate thereby promoting brittle fracture, since brittle fracture depends strongly on strain rate (Dieter, 1998). Furthermore, for materials prone to brittle fracture, the increase in tensile stresses due to the difficulty in spreading the yield zone in the presence of triaxial stress (plastic constraint) mentioned earlier can exceed the fracture stress/strength before the material undergoes general plastic deformation. The introduction of a triaxial stress state (which reduces plastic flow during yielding due to plastic constraint) by notches, the high local stress and strain concentrations at the root notch, the production of high local strain hardening and cracking, and the magnification of local strain rate around the notches, all increases the tendency for a brittle fracture and leads to a reduction in the ductility of a material (Dieter, 1998).

2.4.3 Effects of defects on tensile strength

Although the presence of a notch reduces the cross sectional area of specimens/components, the tensile strength of a notched specimen of ductile metals is also greater than the tensile strength of unnotched specimen due to the notch strengthening (Bayram et al, 1999) discussed in section 2.4.1. In moderately ductile metals, failure occurs by ductile damage/tearing or shear failure mechanism, both of which involve ductile crack propagation. Crack propagation in moderately ductile metal starts at a stress level far lower than the tensile strength of the material because the high local strain hardening associated with the stress concentration at the notch root promote cracking. Thus the presence of cracks leads to a reduction in the tensile strength of materials (Dieter, 1998).

2.4.4 Effects of defects on fracture strength and breaking load

Theoretically, the cohesive/bond strength estimated using the expression in equation (2.3) should be equal to the fracture strength of the material. This means that for fracture to occur, the applied stress at the atomic level must be greater than the cohesive/fracture strength of the material (Anderson, 2005). However in practice, the experimental fracture strength or breaking load of engineering materials has been found to be typically three or four orders of magnitude lower than the theoretical cohesive/fracture strength/load of the materials estimated with equation (2.3) (Anderson, 2005). The fracture strength or the breaking load depends on the cross sectional area and the ultimate tensile strength of the material (Schrems and Maclaren, 1996). Thus the lower experimental fracture strength of engineering materials is basically due to the unavoidable presence of inherent defects in these materials. The presence of defects lowers the fracture/breaking load/strength because the presence of defects reduces the cross-sectional area and the tensile strength of structures/components, the two parameters upon which fracture/breaking load depends (Schrems and Maclaren, 1996).

2.4.5 Effects of defects on fracture modes

As stated in section 2.4.2, the presence of defects, such as notches/cracks reduces the ductility of a material and increases the tendency for a brittle fracture. The presence of a notch also increases the ductile-brittle transition temperature of some metals such as steel (Anderson, 2005). Consequently, a metal such as steel that normally exhibit ductile failure at a given temperature can fail in a brittle manner at the same temperature due to the presence of defects/crack (Anderson, 2005). Thus the presence of defects can change the fracture mode of structures/components.

2.5 Defect/damage tolerance approach to design and assessment of defective structures

Generally, fracture mechanics deals with the mechanisms by which materials fracture. It specifically deals with the deformation and fracture of structures and components with cracks and/or notches (Savruk and Kazberuk, 2010). The measure of how defects, discontinuities or irregularities raise/amplify the stress around them above the nominal stress is termed the stress concentration factor, K (Shigley et al, 2004). For modern structures designed to carry high loads, stress concentration becomes the most serious issue in safe design (Tlilan et al, 2008) and maintenance of structures, and in general engineering critical assessment of structures that develop defects while in service (Li and Guo, 2001).

2.5.1 Calculation of stress concentration factors

Calculation of the stress concentration factor involves determining the nominal stress at the defect free section, σ_{nom} and the amplified stress around the defect σ_{max}. σ_{nom} and σ_{max} can be calculated from theoretical equations, by using the finite element method or by using experimental techniques such as, the photoelastic stress analysis method, the grid method, brittle coating methods and electrical strain-gauge method (Shigley et al, 2004). Discussion in this thesis is limited to calculations of stress concentration factor using the theoretical equations and the finite element method.

2.5.1.1 Calculation of stress concentration factors using theoretical equations

The theoretical stress concentration factor, K_t is defined as the ratio of the value of the maximum stress in a notched member to that in a corresponding unnotched member (Yen and Dolan, 2007). Alternatively and in many instances, the theoretical stress concentration factor, K_t, as expressed in equation 2.29 is defined as the ratio of the maximum stress around the discontinuity or irregularities, σ_{max}, to the nominal applied stress, σ_{nom} [(Garrell et al, 2003); (Yen and Dolan, 2007)]. σ_{max} and σ_{nom} can be estimated in terms of the tensile or shear stress (Garrell et al, 2003) or the equivalent stress (Harkegard and Mann, 2003). σ_{max} and σ_{nom} are estimated from the expressions given in equations (2.30) and (2.31) respectively. While either definition is acceptable, the values of K_t are slightly different and the nominal stress in many instances is calculated from the reduced net cross section/minimum section of the components at the notch (Yen and Dolan, 2007; Noda et al, 1995). The area may also be based on the original/ gross cross section; however, care must be taken to ensure that the correct nominal stress is used.

$$K_t = \frac{\sigma_{max}}{\sigma_{nom}} \tag{2.29}$$

$$\sigma_{max} = 2\sigma_{nom}\sqrt{\frac{a}{\rho}} \tag{2.30}$$

$$\sigma_{nom} = \frac{P}{A} = \frac{P}{dh} \tag{2.31}$$

Where a is the notch depth or length of a surface crack, ρ is the radius of curvature of the notch/defect tip, P is the applied force, A is the area of the specimen, h is the thickness of the specimen and d is the width of the net section of the specimen.

The subscript' t ' in K_t indicates that the stress concentration value is a theoretical calculation based only on the geometry of the component and the geometry of the defect/notch and does not depend on the material used (Shigley et al, 2004). The stress concentration factor K_t varies for different notch shapes (Kato, 1992). Notches commonly treated in published literatures such as that of Noda and Takase, (2006), and Murakami et al (1981) are 'U', 'V', circular, semi-elliptical or semicircular shaped.

When the stress remains elastic, or in small-scale yielding, where plastic deformation is limited to the notch root and nominal plastic strain is negligible, the stress concentration factor estimated using equation 2.29 is termed the elastic stress concentration factor (Harkegard and Mann, 2003). When large-scale yielding occurs, the stress concentration is redistributed leading to the reduction in the level of the maximum stress. The stress concentration factor under this condition is termed the plastic stress concentration factor and is lower than the elastic stress concentration factor (Harkegard and Mann, 2003).

From the expression for theoretical stress concentration factor, the nominal stress is raised by the factor K_t due to the presence of the notch. Although the reduction in the load-carrying capacity due to the presence of a notch has been experimentally observed to roughly tend to increase with increase in K_t ; the reduction in the load-carrying capacity is generally always smaller than the factor K_t (Yen and Dolan, 2007). Consequently, there is a discrepancy between the theoretical stress concentration factors K_t and the "effective stress concentration factors" K_e (also known the "strength reduction factor") especially for ductile materials. Discrepancy occurs because any elastic or plastic straining of the notch root tends to change/increase the root radius which might lead to lengthening of notch root by a very small length of arc at the bottom of the notch. The increase in the notch radius and the lengthening of the arc at the bottom/root of the notch evenly distributes the stress load around the flaw (especially for ductile material) leading to the reduction of the high theoretical stress concentration factor K_t to an "effective" stress concentration factor K_e (Yen and Dolan,

2007). The ratio of K_e to K_t determines the notch-sensitivity of a material. A metal that is notch-sensitive has a relatively high K_e to K_t ratio. Generally, the value of K_e is between 1 and K_t , but in exceptional cases such as for some stainless steels, K_e may be less than one, while for some quenched and tempered steels K_e may sometimes be greater than K_t (Yen and Dolan, 2007).

2.5.1.2 Calculation of stress concentration factor using finite element method.

The stress concentration factor can also be estimated using the nominal stress and the maximum stress obtained from finite element simulation/analysis. The stress concentration factor obtained from finite element analysis is designated as K_f (the subscript f indicates that the stress concentration value is estimated from finite element analysis). The maximum stress can be taken as the maximum "nodal" Von Mises stress or maximum first principal stress. Using maximum first principal stress is more suitable for the analysis of brittle materials. The nominal stress can be taken as either the average Von Mises stress or the average first principal stress on nodes in the gauge section (Garrell et al, 2003).

2.5.2 Stress concentration factor due to V-notches

Angular corners (also known as re-entrant corners), defects with angular ends and sharply notched components (such as rolling bearing seats and circlip grooves) often found in engineering structures can be represented by sharp V-notches (Strandberg, 1999). Theoretically, a sharp V-notch as shown in Figure 2.8(a) with a notch opening angle, 2β, can have an infinite stress concentration due to the approximately zero root radius ρ. They are sharp stress raisers, and under linear elastic theory, they are associated with infinite stresses at their tip. The intensity of the stress field at the tip of sharp V-notches is given in terms of the notch or generalised stress intensity factors (NSIF), K_{It}^{N} . NSIF are comparable to the fracture toughness of components made of brittle materials as a crack propagates from the notch tip when the NSIF at the tip of the notch reaches a critical value (Zappalorto et al, 2009).

However in practical cases, re-entrant corners always have a fillet radius of some size and are often modelled as blunt V-notches. A typical blunt V-notch shown in Figure 2.8(b) has straight edges with vertex rounded with a circular arc of finite root radius (Strandberg, 1999;

Savruk and Kazberuk, 2010). Sharp V-notches are V-notches with 2ρ/D values ranging in value from 0.02-0.03 (Noda et al, 1995).

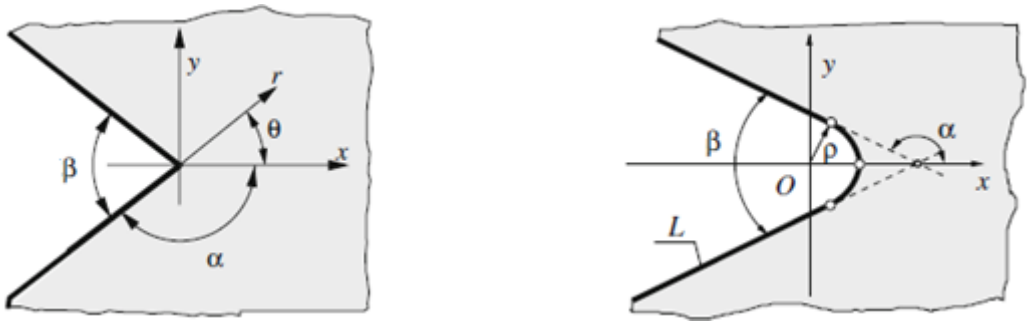

a) Sharp V-shaped notch b) Blunt/rounded V-shaped notch

Figure 2.8: Sharp and blunt V-notches in an elastic plane (Strandberg, 1999).

Also the theoretical infinite stress concentration due to sharp V-notches is not true for actual materials. This is because theoretical infinite stress concentration is based on the classical theory of elasticity which assumes that materials are perfectly homogeneous and infinitely divisible whereas actual materials are made of a finite number of particles (atoms or crystal grains) of definite dimensions. These particles are represented by many small cubic blocks of uniform size called the "structural elementary units." The size of the “structural elementary unit” depends on materials and is as a material property.

The stress concentration factor of a sharp V-notch depends upon the size of the particle or “structural elementary unit” as the values of the maximum stresses at the notch tip are averaged over the surface of an elementary structural unit. The averaging of the maximum stresses over the surface of the elementary structural unit reduces the effective maximum elastic stress due to the steep stress gradients existing over the unit. Consequently the lengthening of the notch radius and its associated lengthening of the arc at the bottom/root of the notch due to elastic or plastic straining which redistributes stresses, and the averaging of the maximum stresses over the surface of the elementary structural unit lowers the stress concentration effects of sharp V-notches. Hence the theoretical stress concentration factors due to sharp V-notches in structures are reduced to the effective stress concentration factors and are not infinite as predicted theoretically (Yen and Dolan, 2007). For sharp and blunt V-notches, loadings (even moderate loadings), cause the stresses at their vertices to significantly exceed the strength of materials. Thus, the classical criteria (traditional strength of material)

for the estimations of structures load carrying capacity are not applicable for structures/components with V-notches (Savruk and Kazberuk, 2010).

Traditionally, for over 30 years, the Neuber trigonometric rule/formula given in equation (2.32) has been used to estimate the values of approximate stress concentration factors designated as $K_{tN.}$ However, Noda et al, (1995) stated that the systematic analyses carried out using the body force method have confirmed that the stress concentration factors values estimated using Neuber trigonometric rule/formula have non-conservative errors for a wide range of notch depths. Kato, (1991) also stated that Neuber trigonometric rule gives values a little lower than numerical or experimental values and does not give accurate values.

$$K_{tN} = \frac{(K_{ts}-1)(K_{td}-1)}{\sqrt{(K_{ts}-1)^2+(K_{td}-1)^2}}+1 \qquad (2.32)$$

Where:

K_{ts} The solution of an elliptical hole in an infinite plate taken as a shallow notch

K_{td} The solution of a hyperbolic notch taken as a deep notch (Noda et al, 1995).

'In general, it is difficult to accurately calculate the stress concentration factors for sharp notches' (Noda et al, 1995). Consequently, approximate methods such as those based on the stress distribution for domains with rounded notches shown in Figure 2.8 (b) (with not necessarily small curvature radius) become very attractive alternatives (Savruk and Kazberuk, 2010). However, except for very deep notches, the stress concentration factor of a sharp notched round or flat bar K_t , shown in Figure 2.8(a), can be estimated from the stress concentration factor of a 60 degree V- notched semi-infinite plate, K_{tv}, shown in Figure 2.8(b) provided both K_t , and K_{tv} have the same shape factor, a/ρ. This is because the values of K_t , and K_{tv} are dependent on the value of $2a/D$ alone and independent of the notch shapes. K_t , becomes equal to K_{tv} as $2a/D$ tends to zero (Noda et al, 1995). D and d are the full width and the width of the net section of the specimen/component. The approximate value of K_t for single and double blunt V-notched flat bars with better than 1% accuracy obtained from using the solution of semi-infinite plates given by Noda et al, (1995) can be

obtained from Figures 2.9 and 2.10 respectively. The nominal stress, $\sigma_{nom} = {}^{p}\!/_{dh}$ for both cases.

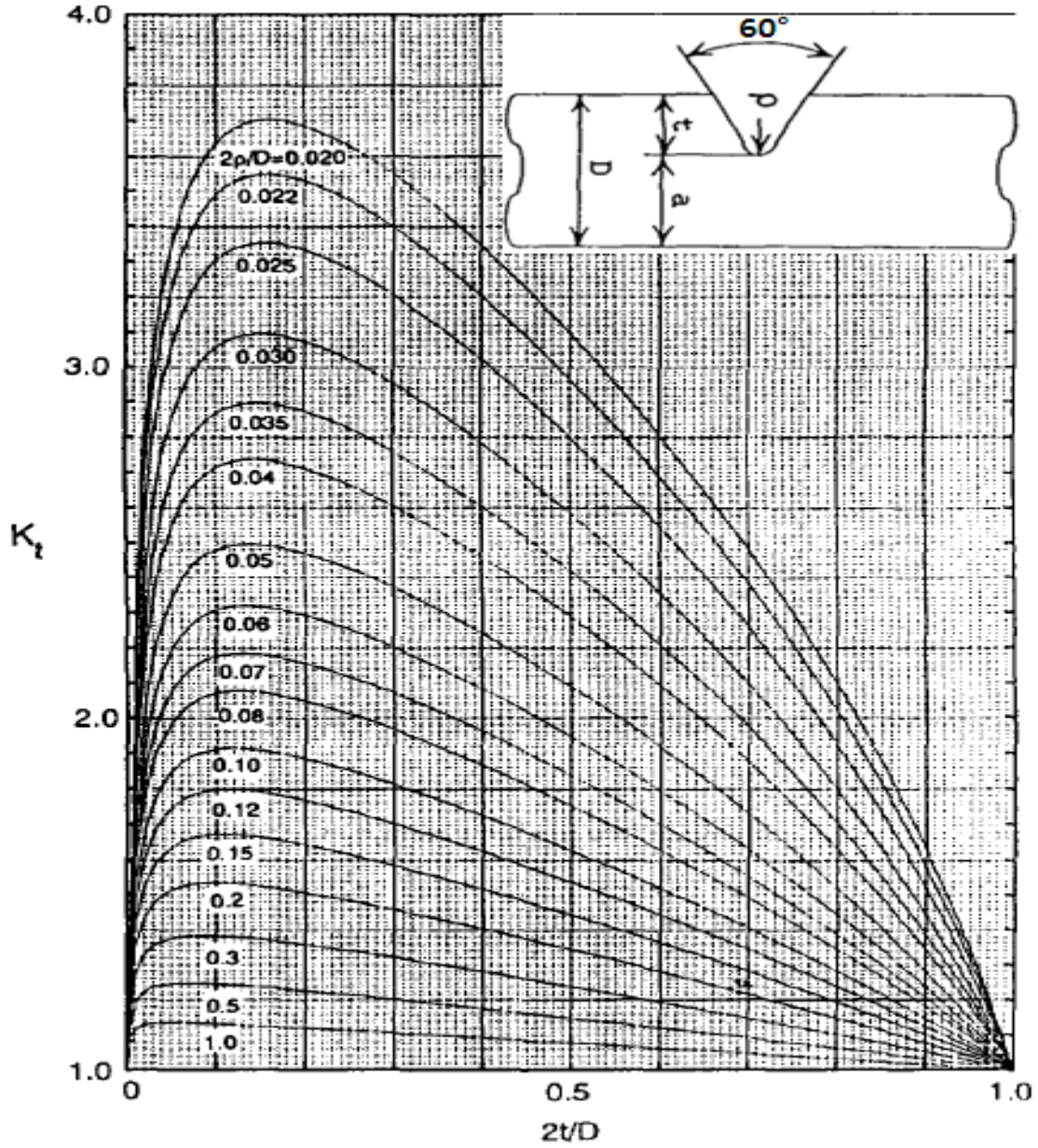

Figure 2.9: Chart for approximate K_t for a single 60° V-shaped notched flat bar under pure tension (Noda et al, 1995).

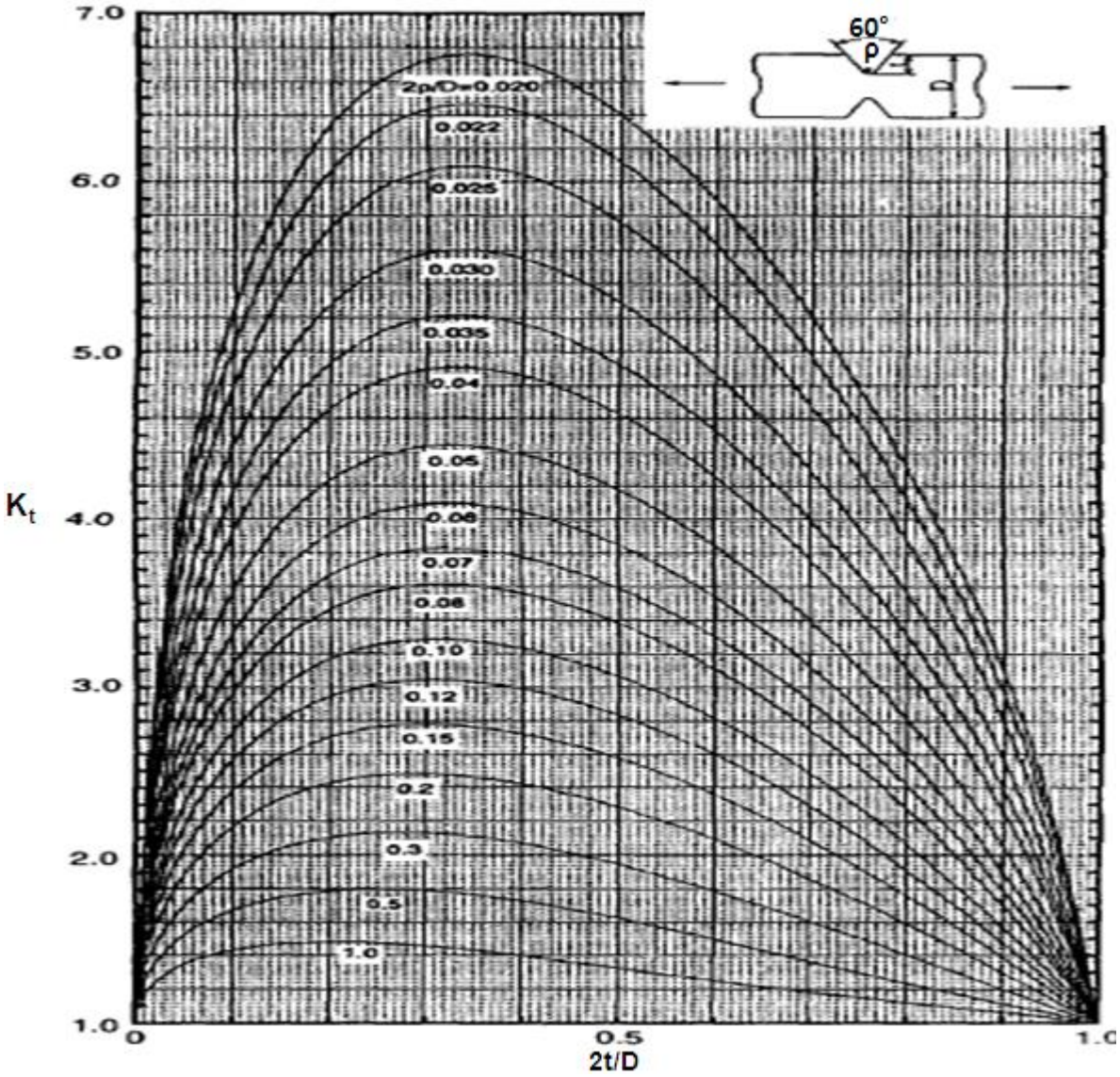

Figure 2.10: Chart for approximate K_t for a double 60° V-shaped notched flat bar under pure tension (Noda et al, 1995).

The "effective" stress concentration factor K_e for sharp notches can be estimated using the Neuber's empirical relationship/formulas given in equation 2.33 obtained from Yen and Dolan (2007). Neuber's formula comes from empirical interpolation between theoretical limiting values and is not entirely based upon rigid mathematical analysis. Also it does not include size effects and was derived for the case of static loading only for explaining the notch effect. Consequently, the extent of its application as an exact relation is likely to be limited and questions remain on how far this equation/theory can be generalized to explain the notch effect and size effect in repeated loading (Yen and Dolan, 2007).

$$K_e = 1 + \frac{K_t - 1}{1 + \frac{\pi}{\pi - \beta}\sqrt{\frac{\rho'}{\rho}}} \tag{2.33}$$

Where ρ' is half the width of the "elementary structural unit" and β is the notch opening angle.

The stress concentration factor of a sharp V-notch is related to the NSIF by the expression given in equation 2.34 obtained from Lhermet et al, (1987), Livieri, (2003); and Savruk and Kazberuk, (2010) when the notch root radios ρ tends to zero and the ratio between the V-notch depth a and notch root radios ρ tends toward infinity. Substituting $\sigma_{\max} = K_t \sigma_{nom}$ from equation 2.29 in equation 2.34 gives a complete expression relating the stress concentration factor of a sharp V-notch to the NSIF as shown in equation 2.35. Equation 2.35 can thus be used to for a rough estimation of the NSIF when the stress concentration factors is known or vice versa (Savruk and Kazberuk, 2010).

$$K_I^N = \frac{\sqrt{\pi}}{2} \lim_{\rho \to 0} (\sigma_{\max} \sqrt{\rho} \tag{2.34}$$

$$K_I^N = \frac{\sqrt{\pi}}{2} \lim_{\rho \to 0} K_t \sigma_{nom} \sqrt{\rho} \tag{2.35}$$

From the review on the calculation of the stress concentration factor for sharp V-notches, the available equations/formula can only be used for an approximate/rough estimation of the stress concentration factor for sharp V-notches and they give approximate relationships between the notch stress intensity factor and the stress concentration factor for sharp V-notches.

2.5.3 Limitation on use of stress concentration values

Generally, the stress concentration factor depends on the orientation and geometry of the defect/discontinuity/irregularity. Thus, to estimate the stress concentration factor, the part/component geometry and the defect geometry (such as the geometry of a notch or groove) must be known (Callister, 2007). When a part contains a crack, the geometry of the crack may not be known. Also for infinitely sharp cracks (with zero radius of curvature) or atomically sharp cracks (with atomic radius of curvature that is also approximately equal to zero), the stress concentration values tend to infinity. Hence for parts/components with cracks, the stress concentration factor is no longer a useful/helpful design tool and fracture

mechanics techniques should be used for the design and assessments of such components (Callister, 2007).

2.6 Fracture mechanics based design and assessment of structures with cracks

Fracture mechanics deals with the behaviour of cracked bodies subjected to stresses and strains by analyzing the flaws to determine if they are safe and will not propagate or if they will propagate and cause the failure of the flawed structures (Anderson, 2005). Fracture mechanics uses the energy criterion and the stress intensity approaches to fracture analysis. In energy criterion approach, crack propagation/failure occurs when the energy release rate G is equal to the critical energy release rate G_c as expressed in equation 2.36 obtained from Anderson, (2005) which relates the critical combinations of crack size and stress to the fracture toughness of the material at failure.

$$G_c = \frac{\pi \sigma_f^2 \, a_c}{E} \tag{2.36}$$

Where σ_f is the failure/fracture stress, a_c is the critical crack size.

In the stress intensity approach, crack propagation or failure occurs when K_I is equal to K_{Ic} as expressed in equation 2.37 obtained from Anderson, (2005) which relates the critical combinations of crack size and stress to the fracture toughness of the material at failure. The subscript I indicates that the stress intensity factor is due to mode one (I) loading which causes tensile stress at the crack tip. Y is a dimensionless geometry correction factor.

$$K_{Ic} = Y \sigma_f \sqrt{\pi a_c} \tag{2.37}$$

The stress intensity factor is related to the energy release rate by the expression in equation (2.38) obtained from Toribio et al, (2006).

$$G_c = \frac{K_{IC}^2}{E} \tag{2.38}$$

The energy release rate and the stress intensity factor are applicable to linear elastic materials. Linear elastic materials exhibit little or no crack-tip plasticity and the fracture toughness of such materials are characterised by G_{Ic} and K_{Ic}. Elastic-plastic fracture mechanics analysis is

used for fracture analysis of elastic-plastic materials which exhibit substantial time independent nonlinear behaviour which results in plastic deformation at the crack tip. The plastic deformation at the crack tip leads to blunting of the crack and the extent of the crack blunting is a measure of the fracture toughness of the material (Anderson, 2005). The crack-tip-opening displacement (CTOD) δ and the J contour integral are the two elastic-plastic fracture criteria. The CTOD is related to the stress intensity factor and the energy release rate by the expression given in equation (2.39).

$$\delta = \frac{K_I^2}{mY_0E} = \frac{G}{mY_0} \tag{2.39}$$

Where m is a dimensionless constant that depends on the stress state and material property. m is approximately equal to 1.0 for plane stress and 2.0 for plane strain (Anderson, 2005).

The J contour integral is suitable for characterising fracture in nonlinear elastic (reversible plasticity) and elastic-plastic materials (with irreversible plasticity) provided no unloading occurs. J is the nonlinear energy release rate and its critical value J_{Ic} represent the fracture toughness of the material (Anderson, 2005). J in nonlinear elastic and elastic-plastic materials is the equivalent of G, the energy release rate in linear elastic materials. J is related to K_I and CTOD by equations (2.340).

$$J = \frac{K_I}{E} = mY_0\delta \tag{2.40}$$

Failures by plastic collapse occur in materials whose plastic response involves yielding of the net cross section of the ligament of defective components/specimens. The maximum load carrying capability of the structure is attained while yielding as the yielding cross-section can no longer carry any more loads. Yielding continues at the maximum load (collapse load P_{col}, failure load, or limit load) given in equation 2.41 obtained from Broek, (1997) until it eventually results in fracture of the specimen. Fracture can even occur during yielding before the entire ligament yields (Broek, 1997). Plastic collapse occurs at the collapse strength, F_{col}, which is the yield stress for perfectly plastic materials, and at a flow stress σ_{fl} for materials that work hardens (Broek, 1997).

$$P_{col} = B(W-a)\sigma_f \tag{2.41}$$

Under the net section theory, the critical nominal stress, σ_{cr} is estimated using the expression in equations (2.42) obtained from Mahmoud, (2007) and Broek, (1997). The fracture strength

and the critical defect size of a component/specimen depend totally on the flow stress of the material and not at all on its fracture toughness (Anderson, 2005).

$$\sigma_{cr} = \frac{A_{Net}}{A} F_{Col} = \frac{A - A_{Crack}}{A} F_{Col} = \frac{W - a}{W} F_{Col} \quad (2.42)$$

Where $A = BW$ is the nominal cross-sectional area, A_{Net} is the net section area, A_{crack} is the area occupied by the crack or notch.

2.6.1 Fracture toughness test

Carrying out a fracture toughness test is the primary method to investigate the interaction between a crack and an applied stress (Gliha and Rojko, 2003). A fracture toughness test measures the resistance of a material to crack extension (Anderson, 2005). The critical stress intensity factor K_{Ic} and the critical J contour integral J_{Ic} are assumed to be material constants or material parameters (i.e. the fracture toughness of the material) only if the stress field in front of the crack is controlled by one parameter, the stress intensity factor (SIF) for brittle (linear-elastic) materials or the J-integral for ductile (nonlinear elastic or plastic) materials. For one-parameter characterization to be satisfied, a proper constraint level at the crack tip must be ensured (Neimitz and Galkiewicz, 2006). However, one-parameter characterization is not always satisfied in most practical situations because the relative crack length and/or element thickness are not appropriate to assure a proper constraint level at the crack tip (Neimitz and Galkiewicz, 2006). Consequently the fracture toughness measured according to national or international standards from highly constrained specimens is often not transferable to real structural elements containing cracks as the measured fracture toughness represents the lowest value for a variety of geometrical configurations and is thus conservative. For most real life structures without high constraint in front of the crack, the fracture toughness can be several times higher that obtained from laboratory specimens with high constraint (Neimitz and Galkiewicz, 2006).

The dependence of fracture toughness on specimen geometry, crack length and loading configuration is normally referred to as the constraint effect (Liu and Chao, 2003). In addition, fracture toughness values also depends on the crack shape and specimen size [(Chao et al, 2001) and (Liu and Chao, 2003)]. For the same thickness of the single-edge notched bend (SENB) and the compact tension (CT) specimens shown in Figures 2.11(a) and (b)

respectively, the CT specimen has a higher constraint and thus gives lower values of cleavage fracture toughness (Petti and Dodds, 2004). This is because the constraint loss in SENB is greater than that in the CT, especially during the last stage of loading (Petti and Dodds, 2004).

In terms of the effect of crack size on fracture toughness, Chao et al, (2001), Qingfen et al, (1990) and Narasaiah et al, (2010) stated that the deeper the cracks size, the higher the constraint. Chao et al, (2001) stated that for brittle materials, the deeper the cracks size, the higher the measured fracture toughness. Conversely, for spring steel and for 20MnMoNi55 pressure vessel steel, which are typical ductile materials, Qingfen et al, (1990) and Narasaiah et al, (2010) observed that the deeper the cracks size, the lower the measured fracture toughness.

The size effect relates to the effect of specimen size on the fracture toughness. Generally, smaller specimens exhibit higher loss of constraint because of their finite thickness and the deviations from plane strain conditions, and thus give higher fracture toughness values (Balart and Knott, 2006). However, the fracture toughness becomes relatively constant or insensitive beyond certain specimen thickness as shown in Figure 2.11(a) (Anderson, 2005). This observed thickness effect on fracture toughness is generally associated with materials with ductile crack propagation (that involves microvoid coalescence). It depends on the relative proportions of slant fracture and flat fracture (Anderson, 2005). In a thin specimen, the slant fracture morphology which results in shear failure dominates as shown in Figure 2.12. In a "moderately" thick specimen, a mixture of both flat and slant fractures is observed and for a very thick specimen, flat fracture mechanism dominates as shown in Figure 2.12. In a thin specimen, the apparent fracture toughness is higher. This is due to the slant fracture /shear lips associated with the fracture mode of thin specimen and is responsible for the thickness dependence of the fracture toughness of materials.

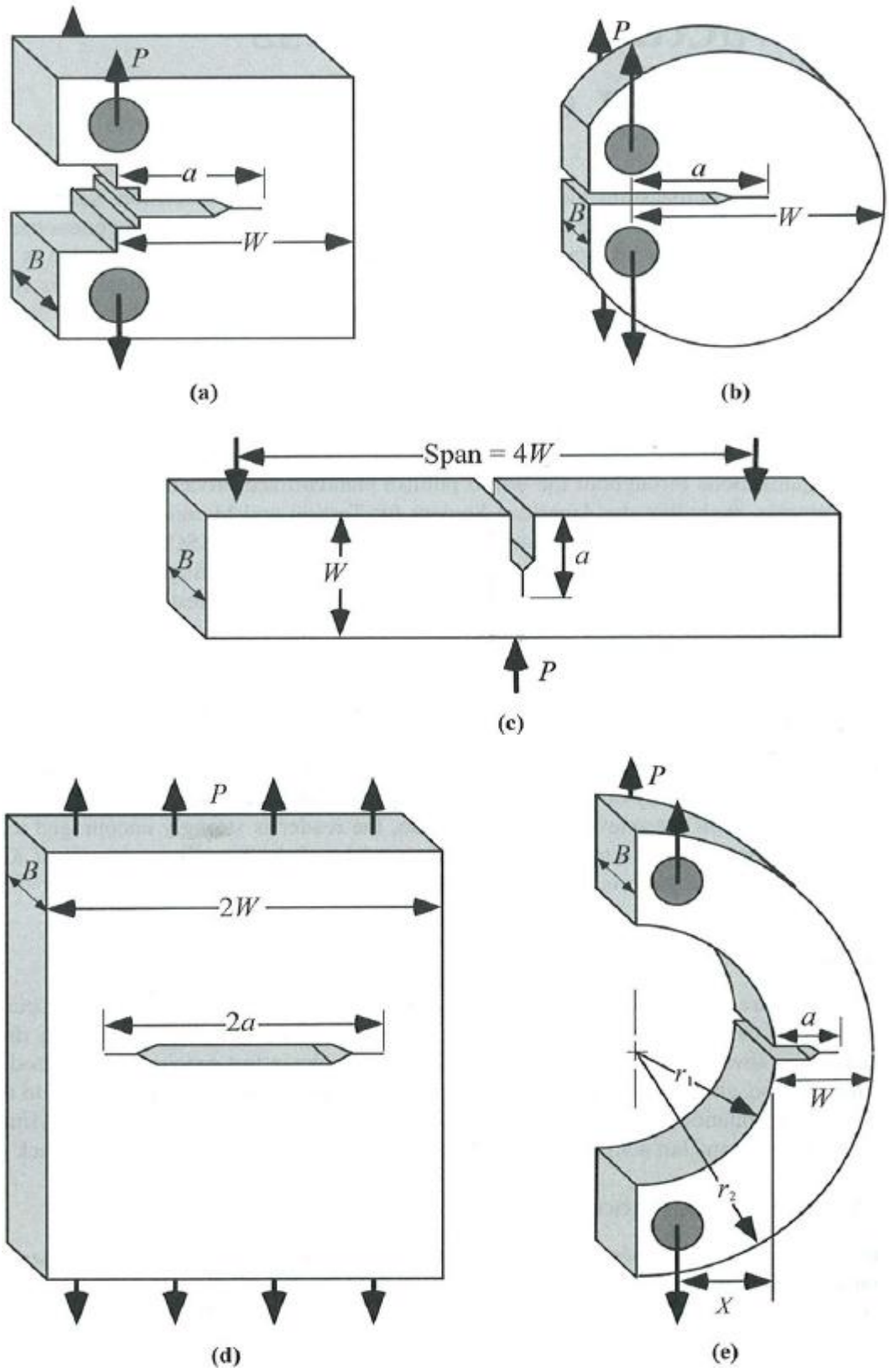

Figure 2.11: Standardised fracture mechanics test specimens: (a) compact specimen, (b) disk-shaped compact specimen, (c) single-edge notched bend (SENB) specimen, (d) middle tension (MT) specimen and (e) arc-shaped specimen (Anderson, 2005).

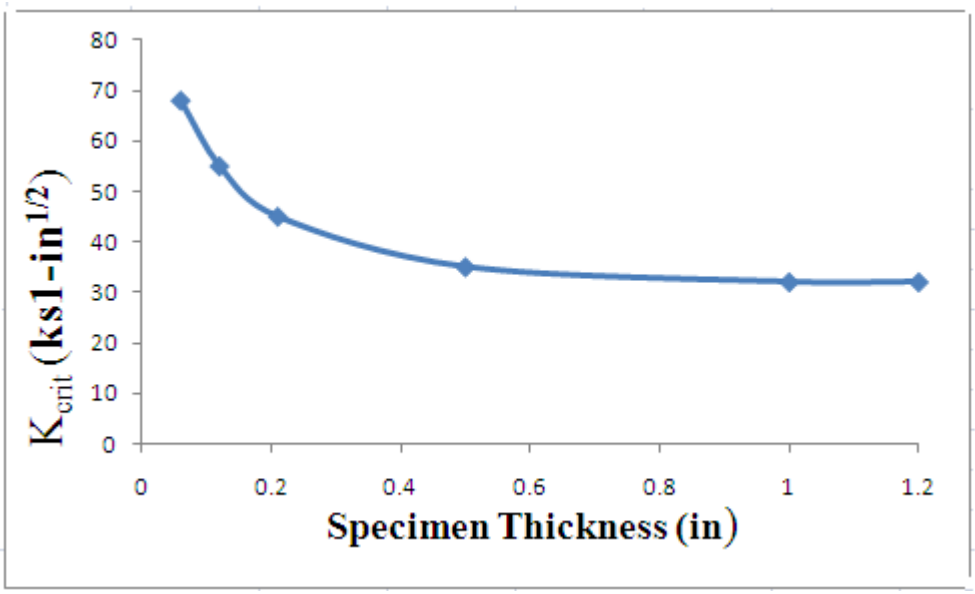

(a) Effect of thickness on fracture toughness (sketched to reproduce the Figure in Anderson, 2005).

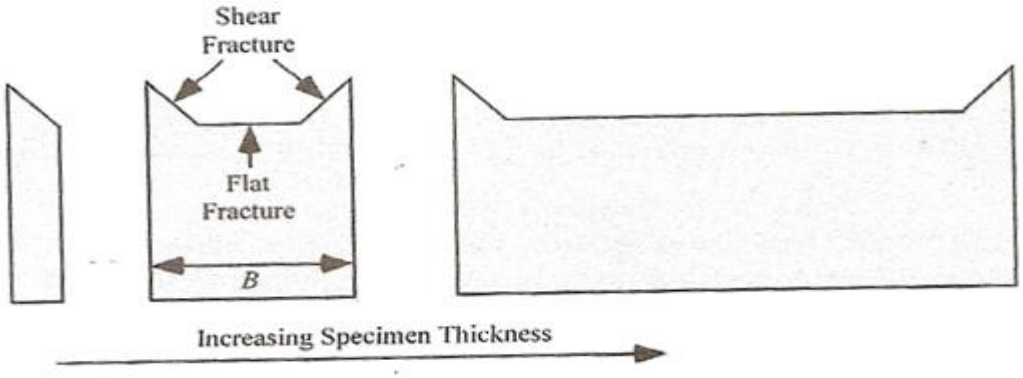

(b) Effect of thickness on fracture surface morphology

Figure 2.12 Effect of thickness on fracture toughness and fracture surface morphology of ductile materials (Anderson, 2005).

2.6.1.1 Fracture toughness test specimen dimensions

The stringent size requirements of ASTM E 399 and other standards given in equations (2.43) and (2.44) meant to ensure that the fracture toughness values obtained from tests correspond to plane strain conditions make it difficult and sometimes impossible to measure a valid K_{Ic} for low and medium strength steels used for structural applications. This is because the specimen thickness required is larger than most available material thickness and valid K_{Ic} can only be obtained for brittle materials which are probably too brittle for structural applications (Anderson, 2005).

$$B, W, a \geq 2.5\left(\frac{K_{Ic}}{\sigma_{YS}}\right) \qquad (2.43)$$

$$0.45 \leq a/W \leq 0.55 \quad (2.44)$$

The specimen size requirements for a valid, J_{Ic} measurement given in equation (2.45) obtained from (Anderson, 2005), are much more lenient than that required for valid K_{Ic} for the same material.

$$B, b_0 \geq \left(\frac{25 J_Q}{\sigma_Y}\right) \quad (2.45)$$

Where

J_Q the provisional initiation toughness becomes the J_{Ic} if the validity criterion in equation (2.45) is fulfilled.

b_0 the initial ligament length which is equal to (W-a).

The specimen size requirements for a valid, δ_{Ic} measurement given in equation (2.46) obtained from (Anderson, 2005), are much more stringent than that required for J_{Ic} measurement and are approximately two to four times the specimen size required for $\boldsymbol{J_{Ic}}$ measurement.

$$B, b_0 \geq 300\delta_Q \quad (2.46)$$

Where

δ_Q the provisional initiation toughness becomes the $\boldsymbol{\delta_{Ic}}$, if the validity criterion in equation (2.46) is fulfilled.

In conclusions, all the present fracture toughness test standards have specimens size requirements which specify the minimum thickness of the specimens to be used for fracture toughness measurement for all the fracture toughness measuring parameters (K_{Ic} , J_{Ic} or δ_{Ic}). As it would be seen in chapter four, standard fracture toughness test specimens cannot be manufactured from wires owing to their sizes.

Having presented the literature review on flexible pipes, laboratory tensile testing, defects and their effects on the tensile properties of structures, and damage tolerance approach to design and assessment of defective structures in this chapter, the literature review on finite element simulation and analysis is presented in the next chapter.

Chapter 3 Literature review: finite element modelling and simulation.

In this chapter, the use of FE as virtual testing, the verification and validation of FE results are presented. A review on virtual prototyping/testing and the verification and validation of numerical modelling and simulation are presented in sections 3.1 and 3.2 respectively. A brief introduction to Abaqus Finite Element Analysis Software is presented in section 3.3 and the elastic-plastic-simulation and damage and failure simulations in Abaqus are presented in sections 3.4 and 3.5 respectively. The limitations of existing fracture models and contact simulations in Abaqus FEA are presented in sections 3.6 and 3.7 respectively.

3.1 Virtual prototyping/testing

Virtual prototyping and virtual testing are terminologies used to describe numerical simulation for the design, evaluation and "testing" of new hardware and entire systems (Oberkampf and Trucano, 2008). Virtual prototyping or testing is also referred to as numerical or virtual experiment (Springmann and Kuna, 2005). The use of virtual testing is becoming popular and unavoidable in engineering, especially where the need to reduce the time and cost of bringing products to market is intense. This new trend of modelling and simulation based design is also driven by the high cost and time required for testing laboratory or field components

3.2 Verification and validation of numerical modelling and simulation

There is the need to have justified confidence in the credibility of the computational simulation results which are nowadays being used for engineering, safety and legal decision-making processes. In computational science and engineering (CS&E), computational simulations verification and validation (V&V) are the major processes for assessing and quantifying the required confidence in the predictions/results of computational simulations (Oberkampf et al, 2004).

Verification is defined as the assessment of the software correctness and numerical accuracy of the solution to a given computational model (Oberkampf et al, 2004). It is basically a process of assessing the accuracy of the solution of a computational model by comparing it with known solutions. It is meant to verify/determine that a model implementation accurately represents the developer's conceptual description of the model and the solution to the model.

Verification is also a way to establish that a mathematical model derived from a conceptual model is solved correctly by the computer code (Oberkampf et al, 2004).

Validation on the other hand is defined as the assessment of the physical accuracy of a computational model based on comparisons between computational simulations and experimental data. It is basically a process of determining the degree to which a model is an accurate representation of the real world from the perspective of the intended uses of the model (Oberkampf and Trucano, 2008). In validation, the relationship between computation and the real life (experimental data) is the focal point. This is because it is only through physical observations/experimentations that the adequacy of the selected conceptual and mathematical models of reality of interest can be carried out. Validation therefore serves as a way to establish how accurately the computational model simulates the real world system responses. Validation hinges on carrying out appropriate experiments correctly and on the mathematical accuracy of the computed solution (Oberkampf and Trucano, 2008).

Using V&V to achieve the required level of credibility (accuracy and reliability) in computational simulations involves issues such as: the reliability of the computer software (code verification), the estimation of numerical accuracy (solution verification), the quality of the physics models used (validation experiments), the quantification of uncertainty, and the training and expertise of users of the codes.

3.3 Abaqus Finite Element Analysis Software

Abaqus is one of the commercial software packages for finite element analysis. Abaqus consists of a group of powerful engineering simulation programs that are based on the finite element method. Abaqus can be used to solve relatively simple problems involving linear analyses as well as the most challenging nonlinear simulations. Abaqus is a general-purpose simulation tool, which can be used to simulate and study problems in the various areas of engineering such as structural (static and dynamic, stress/displacement etc), heat transfer, mass diffusion, thermal management of electrical components (coupled thermal-electrical analyses), acoustics, soil mechanics (coupled pore fluid-stress analyses), piezoelectric analysis (Simulia, 2007). For structural analysis, Abaqus has inbuilt material models which can be used for elastic, elastic-plastic, damage and fracture simulations. In Abaqus, the element and nodal output variables such as stress, strain, displacement etc are always defined

in the global Cartesian coordinate system even if a large-displacement simulation involves element rotation during the simulation (Simulia, 2007). Generally, the accuracy of the finite element simulation increases with mesh refinement and optimum mesh density obtained by performing mesh convergence should be used to obtain sufficiently accurate results

3.4 Elastic-plastic-simulation in Abaqus

Elastic-plastic simulation is required for structures subjected to high strain magnitudes (greater than 5% strain) sufficient to cause the structure to yield; and leading to a dramatic reduction in the stiffness and plastic deformation of the structure. The plastic behavior of a material is described by its yield surface, its flow rule and its post-yield hardening discussed in section 2.2.3.1. Abaqus has various inbuilt models, such as the isotropic, kinematic and combined hardening models for elastic-plastic simulations. The details of the theories and the structural deformation prediction equations used for elastic-plastic deformation in Abaqus have been presented in section 2.2.3.

3.5 Damage and failure simulation in Abaqus

Damage evolution involves the degradation of the material stiffness/elastiity in the region of strain localization (necked region) leading to the strain-softening (reduction in the load-carrying capacity of the material with straining) of the specimen. The progressive degradation of the material stiffness in the region of strain localization in accordance with specified damage evolution criterion continues until the material fails. Failure occurs in an FE simulation when there is a complete loss of load-carrying capacity due to the progressive degradation of the material stiffness. The process of progressive degradation of material stiffness is modelled using damage mechanics (Simulia, 2007). The progressive degradation of the material stiffness to failure translates to the continuous reduction in the load-carrying capacity of the specimen till failure occurs at the equivalent plastic strain at failure.

3.5.1 Models for damage and failure of ductile metals in Abaqus.

The available mechanical constitutive models with damage mechanics concepts for ductile metals in Abaqus are the classical fracture mechanics (discussed in section 2.6) and the mechanism based fracture mechanics. Mechanism based fracture mechanics consists of the micromechanical and the phenomenological failure approaches or models. Both micromechanical and phenomenological failure criteria model ductile fracture by a process of nucleation and growth of voids that ultimately link to form cracks. Micromechanics inspired fracture models such as Gurson's model, are based on the assumption that ductile fracture

occurs when the void volume fraction reaches a critical threshold value. Hence such models involve modelling void nucleation and growth. Phenomenological models are alternatives to micromechanical based models as they predict ductile fracture without modelling void nucleation and growth. Phenomenological models are based on the assumption that ductile fracture occurs when a weighted measure of the accumulated plastic strain such as the equivalent plastic strain reaches a critical value (Dunand and Mohr, 2009). The development of micromechanical models was largely driven by the fracture mechanics community to simulate crack growth in ductile materials when a safe use of the classical fracture mechanics concepts cannot be insured. (Pardoen et al, 2010). In addition, the application of the global criteria of fracture mechanics such as COD and J-integral to characterise ductile fracture initiation does not provide satisfactory results for all cases of external loading, and there are significant problems with the application of their results to describe the behavior of various structures of different geometry (Rakin et al, 2004).

The available mechanism based damage initiation criteria for ductile metals in Abaqus fall into two categories which are: the damage initiation criteria for the necking instability of sheet metal and the damage initiation criteria for the fracture of metals. The damage initiation criteria for the necking instability of sheet metal cover the forming limit diagrams used to model the formability of sheet metal and the Marciniak-Kuczynski (M-K) criterion suitable for numerical prediction of necking instability in sheet metal taking into account the deformation history (Simulia, 2007). The onset of necking is immediately followed by fracture and the model therefore represents a conservative failure criterion in structures discretised with shell elements (Werner et al, 2005).

The damage initiation criteria for the fracture of metals cover, the ductile and shear failure criteria models which are the two main phenomenological fracture mechanisms for ductile metals. Another damage and fracture model available in Abaqus is the micromechanical ductile damage and failure model known as the porous metal plasticity model. This is suitable for modelling damage and fracture of voided metals. The coupling of the damage variables and constitutive relation of materials make calibration of material parameters or constants and damage laws difficult to carry out as the damage variables required to use these models are generally are not a direct output of tensile tests (Yingbin and Tomasz, 2004).

3.5.2 Micromechanical failure model in Abaqus

The Gurson-Tvergaard-Needleman damage and fracture model for porous ductile material is a widely used micromechanical model [(Yingbin and Tomasz, 2004) and (Springmann and Kuna, 2005)] and is based on the porous metal plasticity damage and failure criterion. The porous metal plasticity damage and failure criterion is used in modelling damage and failure of voided metals (with a dilute concentration of inherent voids) with relative density (ratio of the volume of solid material to the total volume of the material) that is greater than 0.9. The model is based on the Gurson's porous metal plasticity discussed in section 2.2.3.1. Using the Gurson-Tvergaard-Needleman damage and fracture model for fracture simulations requires over ten material parameters. These are the elastic-plastic parameters, the porous metal plasticity parameters, the void nucleation parameters and the porous failure parameters. The elastic-plastic parameters are the initial yield, σ_0, and the two hardening parameters, the plastic yield strain, ε_0, and the work hardening exponent, n (Springmann and Kuna 2004). The porous metal plasticity data are the relative density *r* with a value between 0.9 and 1, the coefficients of the void volume fraction q_1 (with a value between 1.0 and 1.5), and q_2 (with a value of 1.0); and the coefficient of pressure term $q_3 = q_1^2$ (with a value between 1.0 and 2.25) (Springmann and Kuna 2004). q_1, q_2 and q_3 are used to model the yield behaviour of the material (Bernauer and Brocks, 2002).

The void nucleation data are the average nucleation strain ε_N (with values ranging from 0.1 to 0.3.), the standard deviation of the normal distribution of the nucleation strain S_N (with values ranging from 0.05 to 0.1) and the void volume fraction of the nucleated voids f_N (Simulia, 2007). These three parameters are used in modelling void nucleation (Bernauer and Brocks, 2002). The porous failure data are the critical void volume fraction, f_c, which characterises the beginning of void nucleation; and f_F, the value of void volume fraction at which fracture occurs (Springman et al, 2004). These two parameters are used to model the evolution of void growth up to coalescence and final failure (Bernauer and Brocks, 2002).

Determining these parameters requires extensive and expensive material testing (Bernauer and Brocks, 2002). Yingbin and Tomasz, (2004), and Bernauer and Brocks, (2002) stated that these shortcomings are also associated with other micromechanical fracture models such as the Rousselier models, Rice and Tracy model; and Hancock-Mackenzie- Gunawardena

models, and make these model unattractive in the industrial environment. Consequently, the determination of the damage and failure data/parameters remains predominantly a phenomenological fitting procedure which requires a combination of testing and numerical simulations. The phenomenological fitting procedure involves keeping some parameters constant and varying others during numerical simulations until the simulation results fit the experimental data. The onset of macroscopic fracture which represents the point/instance at which void coalescence is "supposed" to start is marked by a sudden drop of load. Hence the values of the set of damage and fracture parameters used for the simulation at which the numerical data fits with experimental data at this point of sudden drop of load has become a common technique to determine critical fracture parameters like the critical void volume fraction in the Gurson-Tvergaard-Needlemam model (Bernauer and Brocks, 2002). However, there is still a problem with regards to the uniqueness and transferability of parameters sets (Bernauer and Brocks, 2002).

3.5.3 Phenomenological failure models in Abaqus

The ductile damage criterion is a phenomenological model for predicting the onset of damage by micro-void nucleation, void growth and void coalescence. Micro-void nucleation could be as a result of micro-cracking of particles and/or fracture or decohesion of second phase inclusions. Plastic straining causes the nucleated voids to grow or enlarge, leading to localisation of plastic flow between the enlarged voids and eventual ductile tearing of the ligaments between the enlarged voids which leads to ductile cup and cone fracture (Kim et al (2007). The ductile failure model assumes that the equivalent plastic strain at the onset of damage ε_D^{pl}, is a function of stress triaxiality η and the equivalent plastic strain rate ε^{pl}. The criterion for damage initiation is met when the condition in equation 3.1 is satisfied:

$$\omega_D = \int \frac{d\varepsilon^{pl}}{\varepsilon_D^{pl}(\eta, \varepsilon^{pl})} = 1 \tag{3.1}$$

ω_D is a state variable that increases monotonically with plastic deformation. At each increment during the analysis, the incremental increase in ω_D is computed using the expression in Equation 3.2 obtained from Simulia, (2007).

$$\Delta\omega_D = \frac{\Delta\varepsilon^{pl}}{\varepsilon_D^{pl}(\eta, \varepsilon^{pl})} \geq 0 \tag{3.2}$$

The shear criterion is a phenomenological model for predicting the onset of damage due to shear band localisation. Applied stress causes shear band formation and localisation, leading to the formation of cracks within the shear bands and an eventual failure due to fracture within the shear bands (Simulia, 2007). The model assumes that the equivalent plastic strain at the onset of damage ε_s^{pl} is a function of the shear stress ratio θ_s and strain rate ε^{pl}. The shear stress ratio is calculated using the expression in equation 3.3 obtained from Simulia, (2007).

$$\theta_S = (q + k_s p)/\tau_{\max} \tag{3.3}$$

Where $\tau_{\max}$, is the maximum shear stress and k_S is the material parameter.

The criterion for damage initiation is met when the condition in equation 3.4 is satisfied:

$$\omega_S = \int \frac{d\varepsilon^{pl}}{\varepsilon_S^{pl}(\theta_S, \varepsilon^{pl})} = 1 \tag{3.4}$$

ω_S is a state variable that increases monotonically with plastic deformation proportional to the incremental change in equivalent plastic strain. At each increment during the analysis the incremental increase in ω_S is calculated using the expression in equation 3.5 obtained from (Simulia, 2007).

$$\Delta\omega_S = \frac{\Delta\varepsilon^{pl}}{\varepsilon_S^{pl}(\theta_S, \varepsilon^{pl})} \geq 0 \tag{3.5}$$

3.5.3.1 Material parameters for ductile and shear damage and fracture simulations.

The material parameters required for ductile damage and failure simulations in Abaqus are the equivalent plastic strain at the onset of ductile damage (simply referred to as the fracture strain) ε_D^{pl}, the stress triaxiality and the strain rate. Similarly, the material parameters required for shear damage and failure simulations are the equivalent plastic strain at the onset of shear damage (fracture strain) ε_s^{pl}, shear stress ratio, strain rate, and a material parameter k_S. For both ductile and shear damage simulations, the displacement at failure, $\bar{u}_f^{pl}$, a parameter required for damage evolution is also required. The displacement at failure is the effective total displacement (for elastic materials in cohesive elements) or the plastic displacement at failure (for bulk elastic-plastic materials), measured from the time of damage initiation. The value of plastic displacement at failure ranges from 0 to 1. Instantaneous failure occurs when the plastic displacement at failure value is 0 (Simulia, 2007).

These parameters needed for shear and ductile failure simulations could be obtained experimentally. However, obtaining these parameters through direct experimentation may be difficult because it would require experiments over a range of stress triaxiality for the ductile failure, and requires experiments over a range of shear stress ratio for shear failure simulation (Simulia, 2007). An alternative approach is to estimate these parameters needed for shear and ductile failure simulations using Hooputra et al. (2004)'s simplified analytical expressions giving in equations 3.6 and 3.7 respectively. Even using Hooputra et al. (2004)'s simplified analytical expressions to estimate the equivalent plastic strain at the onset of both ductile and shears damage initiations also requires a number of specially designed experiments (Simulia, 2007).

$$\varepsilon_D^{pl}(\eta, \dot{\bar{\varepsilon}}^{pl}) = \frac{\varepsilon_T^+ \sinh\left[k_0(\eta^- - \eta)\right] + \varepsilon_T^- \sinh\left[k_0(\eta - \eta^+)\right]}{\sinh\left[k_0(\eta^- - \eta^+)\right]} \tag{3.6}$$

$$\varepsilon_S^{pl}(\theta, \dot{\bar{\varepsilon}}^{pl}) = \frac{\varepsilon_S^+ \sinh\left[f(\theta_s - \theta_s^- \eta)\right] + \varepsilon_S^- \sinh\left[f(\theta_s^+ - \theta_s)\right]}{\sinh\left[f(\theta_s^+ - \theta_s^-)\right]} \tag{3.7}$$

Where:

ε_T^+ and ε_T^- are the equivalent plastic strain at ductile damage initiation for equibiaxial tensile and equibiaxial compressive deformation, respectively,

η^+ and η^- are the stress triaxiality in equibiaxial tensile deformation state and equibiaxial compressive deformation state with a value of 2/3 and -2/3 respectively for isotropic materials,

ε_S^+ and ε_S^- correspond to the equivalent plastic strain at shear damage initiation for equibiaxial tensile and equibiaxial compressive deformation respectively,

θ_S^+ and θ_S^- correspond to the values of θ_S at $\eta = \eta^+$ and $\eta = \eta^-$ respectively and

$\theta_S = (1 - k_s\eta)/\phi$ with $\phi = \tau_{\max} / \sigma_{eq}$

3.5.3.2 Determination of parameters for ductile damage and failure simulation

To use Hooputra et al, (2004)'s simplified analytical expression given in equation 3.37 to estimate the equivalent plastic strain at the onset of ductile damage ε_D^{pl}, three material parameters: ε_T^+, ε_T^-, and k_0 must be determined experimentally. These three parameters depend on the strain rate. Thus, for each strain rate of interest; three different experiments are needed at different values of stress triaxiality to obtain the three material parameters (Hooputra et al, 2004).

The first experiment involves determining ε_T^+ from Erichsen test ($\eta = \eta^+$). The second experiment involves three-point bending of sheet coupons (with width/thickness > 4) under plane strain tension ($\eta = \frac{1}{\sqrt{3}}$) and the third experiment involves fracture at the notch root of waisted tensile coupons in uniaxial tension ($\eta = \frac{1}{3}$). The last two experiments are to determine ε_T^- $\bar{\varepsilon}_T$ and k_0 (Hooputra et al, 2004).

3.5.3.3 Determination of parameters for shear damage and failure simulation

Similarly, to estimate the equivalent plastic strain at the onset of shear damage ε_s^{pl}, using the Hooputra et al. (2004)'s simplified analytical expression given in equation 3.38, four parameters: k_s, ε_S^+, ε_S^- and f must be determined experimentally: These parameters depend on the material and strain rate. The first experiment involves using tensile specimens with a groove (rectangular cross-section with groove depth of half the sheet thickness) at 45^0 to the loading direction $(\theta_S = 1.469)$. The second experiment involves using specially designed tensile specimens with a groove parallel to the loading direction (pure shear, $(\theta_S = 1.732)$. The third experiment involves carrying out Erichsen tests $(\theta_S = 1.6)$. The three experiments are used to determine ε_S^+, ε_S^- and f (Simulia, 2007).

3.5.3.4 Limitations of Hooputra et al. (2004)'s simplified analytical expressions

From the scope and scale of the experiments required to be carried out in other to use Hooputra et al. (2004)'s simplified analytical expressions to obtain the parameters required to carry out shear and ductile failure simulations, this alternative approach, does not present either an easy or a fast way to obtain these parameters. In addition, Hooputra et al. (2004)'s simplified analytical expressions may give very high values of the equivalent plastic strain at

damage initiation when the stress triaxiality or the shear stress ratio is very small (Simulia, 2007). 'A cut-off value of the equivalent plastic strain can be provided in such cases' (Simulia, 2007).

3.6 Limitations of existing fracture models

The available ductile damage and fracture criteria are only able to predict accurately the elastic and plastic responses of materials up to the beginning of fracture phase which involves micro-crack nucleation and growth (Kut, 2010). Modelling of the actual material fracture phase which involves macro-crack initiation (occurring by microvoids coalesce) and the fracture development (ductile tearing/ductile crack growth) is modelled by these damage and fracture models by element deletion or node separation. The accuracy of such fracture phase modelling is affected by the ductile fracture criterion on which the model is based, the modelling parameters, the method of modelling parameters determination and the accuracy of the material parameters themselves (Kut, 2010). Hence these damage and fracture models cannot describe in an adequate form the macrocrack formation that takes place at the last instants of the fracture process (Celentano and Chaboche, 2007). They are also yet to be able to exactly predict materials fracture trajectory (Kut, 2010).

3.7 Contact simulations in Abaqus FEA

When two surfaces are in contact, a force normal to their contacting surfaces acts on the two bodies (causing normal stresses) and if friction exists between their surfaces, shear forces (causing frictional shear stresses) may be created that prevent sliding or tangential motion of the bodies (Simulia, 2007). Contact analysis basically involves detecting when two surfaces are in contact or separated, identifying the areas on the surfaces that are in contact, applying/removing contact constraints accordingly and calculating the contact pressures generated (Simulia, 2007).

The contact formulation in Abaqus consists of the constraint enforcement method, the contact surface weighting, the tracking approach, and the sliding formulation (Simulia, 2007). The penalty contact method is used to enforce both normal contact constraint and tangential contact constraint. Its penalty friction formulation incorporates allowable "elastic slip". The "elastic slip" refers to the small amount of relative motion between the surfaces that occurs when the surfaces should be sticking (Simulia, 2007). The penalty friction formulation works well for most problems, including most metal forming applications (Simulia, 2007). The general contact algorithm in Abaqus uses the balanced master-slave weighting which

minimises the penetration of the contacting bodies and, thus, gives accurate results (Simulia, 2007)..

Sliding formulation deals with the relative sliding of the two surfaces during the analysis. Small sliding formulation is used for analyses where the magnitude of sliding or relative motion of the two surfaces is less than a small proportion of the characteristic length of an element face. Finite sliding formulation is used where the magnitude of sliding may be finite. General contact interactions use only the finite-sliding formulation option.

In this chapter, the review of literature on the use of FE as virtual testing, the verification and validation of FE results, and the FE models updating are presented. The background information on Abaqus finite element analysis code, the details of the mechanics of elastic-plastic and damage and failure models in Abaqus, and the contact simulations in Abaqus are presented. In the next chapter, the review of the past work done on mechanical testing is presented.

Chapter 4 Literature review: mechanical testing and finite element simulations involving wires and other steel products

The review of the past work done on defects and failures investigations in wires and the past work done on tensile testing simulations, indentation and its effects on the mechanical properties of steel products, and bending and reverse bending and their effects on the mechanical properties of wires and other steel products are presented in this chapter. Where the work done in any of these aforementioned areas is not on wires, the review of literatures on the work done in these areas on other steel products are presented to show the approaches used and the conclusions drawn by the researchers. The review of the past work done on defects and failure investigations in wires is presented in section 4.1 and the past work done on tensile testing simulations, and indentation and its effects on the mechanical properties of steel products are presented in sections 4.2 and 4.3 respectively. Section 4.4 presents the review on bending and reverse bending and their effects on the mechanical properties of wires and plates.

4.1 Review of research on defects and failures in wires

Recent research involving the determination of the fracture mechanism and the fracture strength of defective wires, such as the research conducted by Mahmoud, (2007) on bridge cable wires, and by Toribio and Valiente, (2004) and Toribio and Valiente, (2006) on concrete pre-stressing wires used the classical fracture mechanics approach for toughness analysis. These researchers used non-standardised fracture mechanics specimens as standard test specimens could not be manufactured from the wires owing to their sizes. Mahmoud, (2007) stated that the current state of practice used by engineers to estimate the safe load carrying capacity of cracked wire by multiplying the ultimate strength obtained from a tension test by the original nominal area of the wire may overestimate the strength of the wire due to crack tip plasticity. He pointed out that the fracture parameters of the wire material are not considered in the current state of practice used by engineers. Mahmoud, (2007) and Toribio and Valiente, (2004) argued for fracture mechanics based analysis of cracked wires.

Mahmoud, (2007) evaluated the fracture strength of the bridge cable wires using both LEFM and net section theory/plastic collapse fracture mechanics theorems using non-standardised fracture mechanics specimens because the cable wires are too small to meet the standard specimen dimensional requirements for a valid K_{IC} measurement. The fracture strength

estimated using the net section theory was even higher than the designed/ in-situ dead load stress imposed on the broken wires of the suspension bridge. Consequently, Mahmoud, (2007) concluded that "the bridge cable wires fracture strength is not governed by the net section theory" and recommended that for the purpose of safety evaluation of main bridge cables, the toughness criterion provides a better understanding and evaluation tool than the net section theory.

Toribio and Valiente, (2004) used un-notched 30 cm long cylindrical specimens shown in Figure 4.1 that were fatigue pre-cracked by axial fatigue loading to determine the directional toughness (toughness in both the longitudinal/wire axis and the transverse/perpendicular directions) of the wires. In Figure 4.1, the part-through crack was assumed to be semi-elliptical in shape with a crack depth a (minor axis of the ellipse), b is the other dimension of the crack (major axis of the ellipse) and D is the diameter of the bar. The pre-cracked specimens were subjected to monotonic tensile loading at a crosshead speed of 3 mm/min up to fracture to represent the fracture behaviour of the steels.

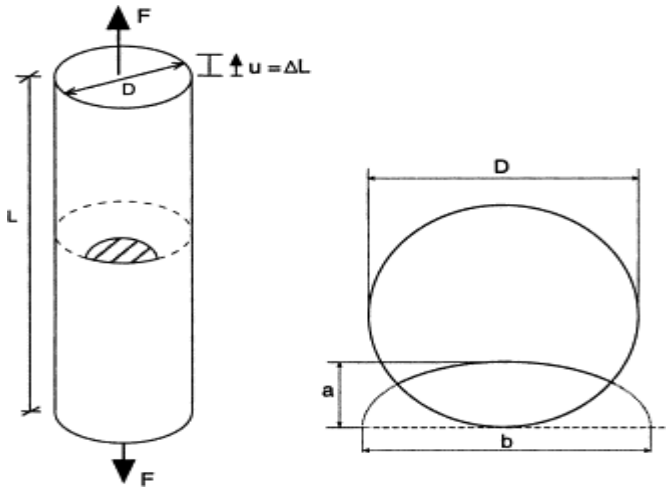

Figure 4.1: Cracked bars used in Toribio and Valiente, (2004) experimental programme.

Toribio and Valiente, (2004) and Toribio and Valiente, (2006) evaluated the fracture toughness for 7mm, 7.5mm and 8.15 mm diameters wires designated as Steel4, Steel5 and Steel6; and steel0, steel1, steel2 and steel3 respectively from the load-extension plot obtained from the tensile testing of the cracked bars. The numbers 0-6 represent the number of cold-drawing passes the wire underwent. Toribio and Valiente, (2004) observed that the heavily cold drawn pre-stressing wires exhibited fracture behaviour with crack deflections

whereas the slightly drawn wires did not. The crack deflections caused an approximately 90° change in crack propagation direction from the original single mode (mode I) propagation in the radial direction observed in slightly drawn wires shown in Figure 4.2(a); to a crack propagation in the wire axis/cold drawing/axial direction shown in Figure 4.3(b). Consequently, the directional fracture toughness in the radial and axial crack propagation directions were obtained for the heavily cold drawn pre-stressing wires.

The crack deflection occurs at a load level F_Y (associated with the *pop-in* and the 90°-step) as shown in Figure 4.2(c) while the final fracture in the radial direction occurs at a load level F_{max} as shown in Figure 4.2(d). F_Y is associated with a detectable pop-in at the initiation of non-linear behaviour; while F_{max} is the maximum load level at the point of final fracture. For the slightly drawn steels, $F_Y = F_{max}$ as the load–displacement point is linear up to the fracture point). The 90°- propagation step shown in Figures 4.2 (b) and (c) is quasi-parallel to the cold drawing/wire axis direction and the 90° change in crack propagation direction occurred due to the presence of local interlamellar spacing created by the cold drawing process. The interlamellar spacing has minimum local toughness which makes it the more preferred fracture path compared to the radial direction.

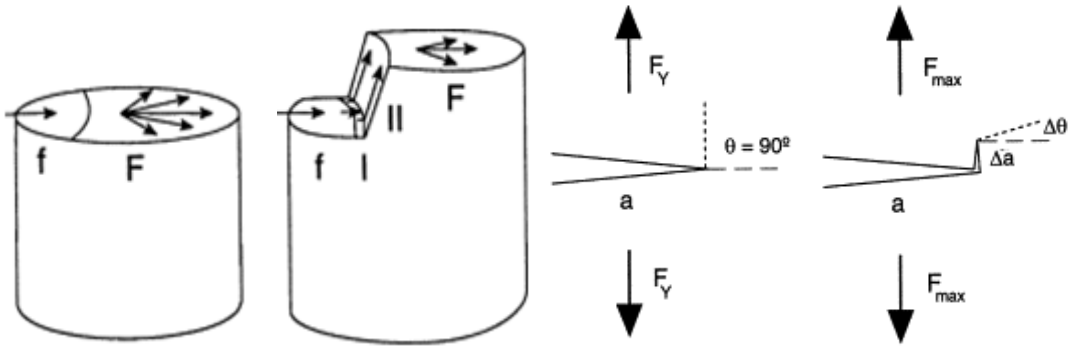

(a) (b) (c) (d)

f, fatigue pre-crack; I, mode I propagation; II, crack deflection; F, final fracture

Figure 4.2: Fracture modes of heavily and slightly drawn steels (Toribio and Valiente, 2006)

For the heavily cold drawn steel, Toribio and Valiente, (2004) found that the radial directional toughness was higher than the axial directional toughness which shows strength anisotropy in the heavily cold drawn steels. The slightly drawn pre-stressing steel wires with 0–3 cold-drawing passes exhibited isotropic or quasi-isotropic fracture behaviour. Steel0 which did not undergo any cold drawing pass/step (a typical hot rolled bar), exhibiting a fully isotropic fracture behaviour.

Toribio and Valiente, (2006) used the Linear Elastic Fracture criterion to estimate the toughness of the pre-stressing wires. They estimated the fracture toughness of the slightly drawn wires which failed in a brittle manner using a local fracture criterion that is based on stress intensity factor; and estimated the radial and axial fracture toughness of the heavily drawn pre-stressing wires which failed in a more ductile manner using a global fracture criterion that is based on the energy release rate. The expressions used by Toribio and Valiente, 2006 to estimate the fracture toughness in terms of the stress intensity factors (calculated from the energy release rate which was obtained from the specimen compliance) under the global fracture criterion and the local fracture criterion are given in equations 4.1 and 4.2 respectively.

$$K_1^* = Y^*(a/D_i)\sigma_{app}\sqrt{\pi a} \tag{4.1}$$

$$K_1^{**} = Y^{**}(a/D_i, a/b)\sigma_{app}\sqrt{\pi a} \tag{4.2}$$

σ_{app} is expressed as the tensile load applied on the cylinder divided by the cross section area of the cylinder ($\sigma_{app} = 4P\frac{4P}{\pi D^2}$). Y*(a/D) is a dimensionless function given in equation 4.3

$$Y^*(a/D) = [0.473\text{-}3.286(a/D)+14.797(a/D)^2]^{1/2}[(a/D)\text{-}(a/D)^2]^{1/4} \tag{4.3}$$

The double asterisk used in equation (4.2) indicates that two parameters, the relative crack depth a/D and the crack aspect ratio a/b are needed to obtain local fracture criterion K_I compared with the relative crack depth a/D alone required for global fracture criterion.

Krishnadev et al, (2008) conducted a research to identify the failure modes and failure mechanisms of a guy rope assembly by studying the microstructures, mechanical properties and fracture morphologies of carefully sectioned specimens. The research revealed that the guy assembly failed as a result of the failure of the tube housing the wire rope. The failure occurred due to local microstructural weakness attributed to decarburisation and the unusually large ferrite grain size of the tubing. The local microstructural weakness reduced the strength of the tubing locally because the yield strength is inversely proportional to the grain size. Also the reduction in carbon content due to the decarburisation further reduced the

strength. On the basis of the result of scanning electron microscope which indicated the presence of dimples, Krishnadev et al, (2008) concluded that failure occurred by micro void coalescence (MVC) due to tensile overload.

Mapelli and Barella, (2009) carried out research to identify the failure mechanism and the origin of failure of a cable-way rope made up of many wires. The metallographic examination carried out revealed a sound and very fine pearlite microstructure and the micro-hardness tests carried out revealed reliable homogeneous strength properties along the wire section. The visual examination of the rope showed that the wires fractured without traces of visible necking or significant plastic deformation of the wires. Mapelli and Barella, (2009) concluded that the cable-way rope failed by fatigue based on the fractographic analysis carried out with the Scanning Electron Microscope coupled with an Energy Dispersion X-ray Spectrometer (SEM–EDS) which clearly indicated that failure occurred by crack initiation and fatigue cracks propagation.

Smith and Easterline, (1993) carried out an investigation to explain the premature failure of the 1.3mm diameter single strand, drawn, high tensile, pearlitic high carbon wires used as cables for towing target behind aircraft. They conducted tensile tests on: wire specimens with scratches made with a sharp blade, wire specimens subjected to cyclic loading and shock/stress wave propagation, wire specimens straightened after being bent through 180 degrees about decreasing radii of a curvature, and wire specimens that have been subjected to a compressive loading. The metallographic examination of the failed wires, the wires that have been flown several times without failure and the wires tensile tested revealed a ductile cup-and-cone failure. A Few failed wires exhibited a shear failure mode. The cup-and-cone failure mostly occurred at the locations of transverse scratches that were observed to be approximately 0.1 to 0.15mm deep and at the locations of localised heating effects (e.g. wires being struck by lightning). The shear failure mode was said to have occurred due to a combination of a tensile overload with a loss of ductility in the wire. Shear failure also occurred where kinking of the wire due to severe bending occurred. The metallographic examination of wires that have been flown several times without failure revealed local necking.

Based on the breaking loads of the used and unused wires, Smith and Easterline, (1993) concluded that that was no evidence of faults in the manufacturing process of the wires and also there was no evidence of overall degradation of the strength of the wires. However,

while the breaking load of wires that have been flown several times without failure increased due to working hardening occurring during the winding and unwinding processes, and during cyclic loading of the wires, a lost of ductility was observed in the used wires

4.1.1 Concluding remarks

From the review of the past research carried out on wires, it is obvious that there is the need to use fracture mechanics based analysis and design for the design and assessment of defective wires. However, the test procedures in the present fracture toughness standards are not suitable for the determination of the fracture toughness of wires due to their small sizes. While the net section theory overestimates the fracture strength/capacity of the low ductility wires considered, the alternative option considered, the LEFM is only suitable for wires with low ductility. Neither the net section theory nor the LEFM has been proven to be suitable for high ductility wires such as the tensile armour wires.

4.2 Previous works on tensile test simulations

A tensile test is simulated by applying an axial displacement (a quasi-static displacement controlled loading) to one end of the model of the tensile test specimen with the other end fixed (Bernauer and Brocks, 2002; and Dunand and Mohr, 2009). The tensile test specimen can be modelled with a uniform cross section or with tapered profile as specified in ASTM Standards (1988) to trigger necking formation in the middle of the specimen (Bernauer and Brocks, 2002; Celentano and Chaboche, 2007). The value of the axial displacement to be imposed on the specimen model can be taken as the value corresponding to the average fracture elongation observed in tensile test experiments (Celentano and Chaboche, 2007). The force-displacement response predicted by the tensile test (numerical results) needs to correlate well with the experimental results as getting a correct force-displacement response is a necessary condition for a perfect tensile test simulation (Yingbin and Tomasz , 2004). The mechanical properties of the material such as the yield strength, the ultimate strength, the fracture load and the displacement at which fracture occurs can be estimated from the predicted force-displacement curve. Other parameters such as the stress triaxiality, the equivalent plastic strain and the fracture strain can also be obtained from the tensile test simulation results (Dunand and Mohr, 2009).

Cabezas and Celentano, (2004) carried out large strain isotropic elastic-plasticity simulations of the tensile testing of cylindrical and sheet tensile test specimens of SAE 1045 steel using the properties obtained from the laboratory tensile testing of cylindrical specimens. The

experimental and finite element simulation predicted engineering stress-strain curves obtained by Cabezas and Celentano, (2004) for cylindrical and sheet specimens are presented in Figures 4.3 (a) and (b) respectively. Cabezas and Celentano, (2004) attributed the discrepancies in the experimental and finite element simulations engineering stress-strain curve to the inaccuracy of the potential correlation at the beginning of the plastic region where no hardening is produced.

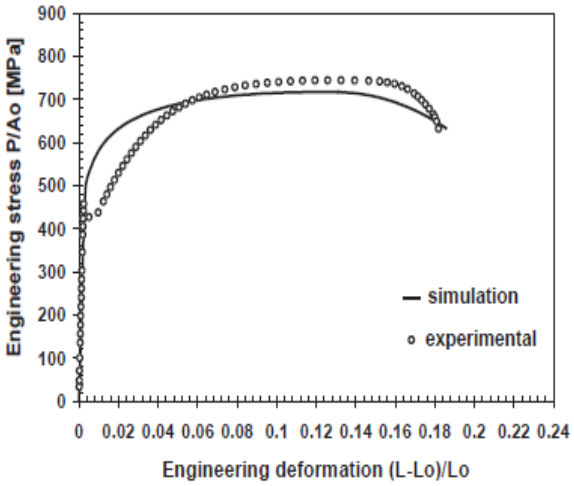

(a) Cylindrical specimen

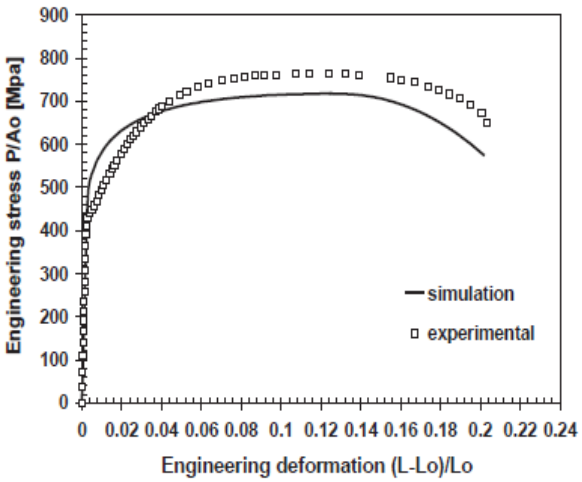

(b) Sheet specimen

Figure 4.3: Experimental and FE tensile test results from SAE 1045 steel cylindrical and sheet specimens (Cabezas and Celentano, 2004).

From the results of the full 3D and a simplified 2D simulation in Figure 4.4, Cabezas and Celentano, (2004) concluded that the 3D and plane stress/2D simulations practically predicted the same response up to the onset of necking. Beyond necking, the 2D simulation provides an unrealistic response. Cabezas and Celentano, (2004) attributed this unrealistic response to the fact that the outward unit normal to the specimen in the thickness (z- axis) rotates at high levels of elongation as the thickness reduces during necking and concluded that the typical plane stress relation $e_{xx} = e_{zz} = -1/2e_{yy}$ is only valid before the onset of necking.

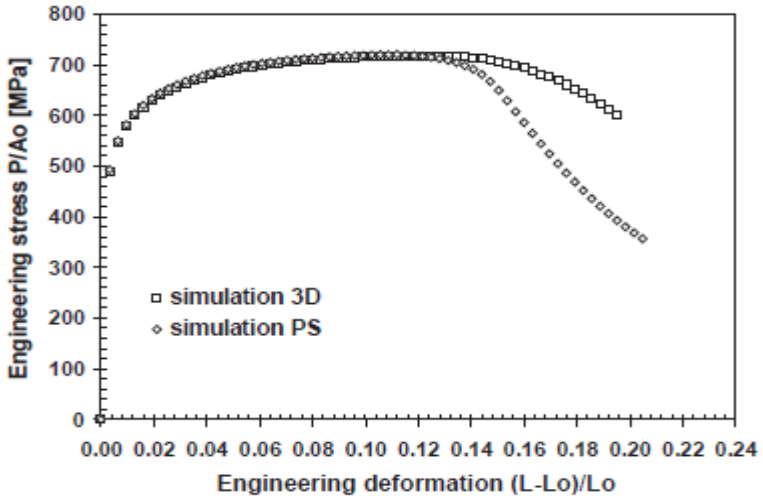

Figure 4.4: Engineering stress-strain curves predicted by 3D and 2D simulations (Cabezas and Celentano, 2004).

Figure 4.5 shows the force-displacement curves obtained from the simulations of the tensile testing of smooth round tensile specimens carried out by 15 participants of the "European numerical round robin on the application of constitutive equations for ductile damage to simulate tearing of ferritic steel" presented by Bernauer and Brocks, (2002). The participants used various FE codes and various micromechanical fracture models including the Gurson-Tvergaard-Needlemen (GTN), Rousselier, Rice and Tracy, and Hancock-Mackenzie-Gunawardena models (Bernauer and Brocks, 2002). All the participants varied only the critical void volume fracture till the sudden load drop and fracture in the numerical curves correspond to the sudden load drop and fracture in the experimental curve.

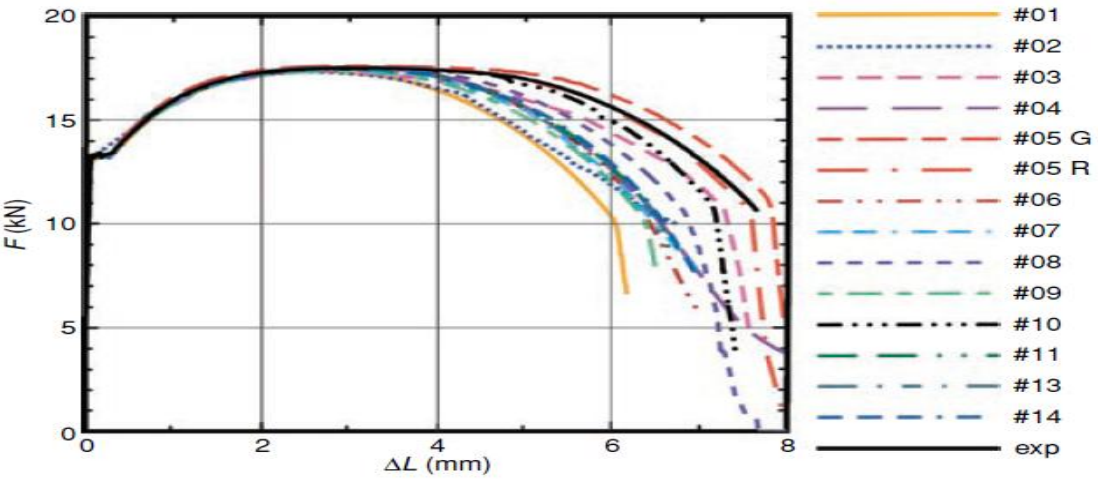

Figure 4.5: Experimental and FE force displacement curves predicted by simulations with various damage and fracture models (Bernauer and Brocks, 2002).

The differences in the force-displacement curves beyond the ultimate load is attributed to the differences at which necking progressed in the various FE models for the same imposed displacement (Bernauer and Brocks, 2002). They also attributed the difference to the beginning of necking that is subject to arbitrary imperfections in the simulation as well as in the experiment. They substantiated this with the fact that even the experimental curves obtained from the five specimens they tested did not lie on a unique curve. Bernauer and Brocks, (2002) also observed that the FE simulations carried out without imperfection introduced in the specimen to induce necking necked early and even necked earlier than in the experiment. From Figure 4.5, the force-displacement curve predicted by the simulation carried out using the Rousselier model by participant 05 (i.e. curve #05 R) is the closest to the experimental curve. This may be because the FE code (which is not explicitly stated in the literature) used by participant 05 models necking better than the codes used by the other participants, as this is the only reason that can be established from the literature.

The experimental and finite element tensile test stress-strain curves and force-displacement curves obtained by Celentano and Chaboche, (2007) and Kut, (2010) are presented in Figure 4.6 and 4.7 respectively. Celentano and Chaboche, (2007) used a ductile damage evolution method that is based on the reduction of the Young's modulus, E, of a material due to the appearance of microcracks and cavities inside the material. They used load-unload tensile cyclic tests to track the deterioration or degradation of the young modulus and expressed the damage variable d^p in terms of the Young's modulus of the undamaged material, E_0, and the effective elasticity Young's modulus of the degraded or damaged material, E, as shown in equation 4.4. They adopted the Young's modulus of the undamaged material as the young modulus of the first load path in the tensile test and the values of the effective elasticity Young's modulus, E were taken as the degraded young modulus obtained from the subsequent load-unload tensile cyclic tests. Celentano and Chaboche, (2007) concluded that there is an overall good agreement between the numerical predictions by the simulation conducted with the damage characterisation and constitutive model they proposed and the average experimental values as shown in Figure 4.6

$$d^p = 1 - \frac{E}{E_0} \tag{4.4}$$

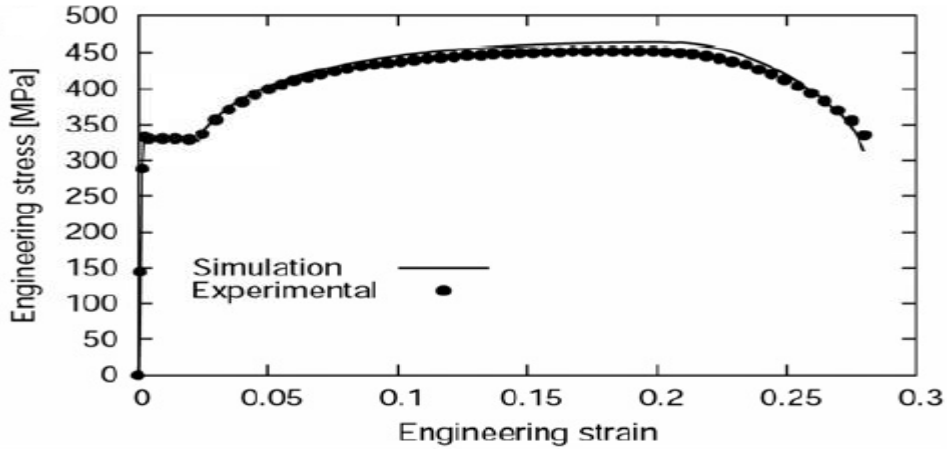

Figure 4.6: Experimental and FE simulation engineering stress-strain curves for SAE 1020 steel (Celentano and Chaboche, 2007).

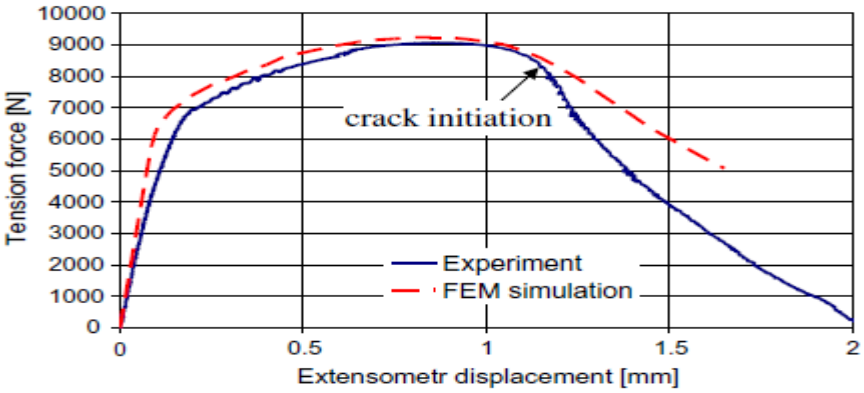

Figure 4.7: Experimental and finite element tensile force-displacement curves for S355JR sheet steel (Kut, 2010).

4.2.1 Concluding remarks

Nearly all the force-displacement curves from the laboratory and numerical tensile testing presented in the papers reviewed stopped at the fracture initiation point without the portions of the curves describing the fracture trajectories of the specimens/materials. This could be because the fracture initiation point is the last point from which the displacement after fracture (and invariably, the ductility), which is the last mechanical property of interest for design and quality assurance, is determined from the curves. It could also be because there is no good agreement between the experimental and FE predicted fracture trajectories as shown in the few ones with the fracture trajectories such as the curves shown in Figures 4.5 and 4.7, which could be because most of the FE codes are not yet able to describe in an adequate form the macrocrack formation that takes place at the last instants of the fracture process and

predict the fracture trajectory accurately as earlier stated by Celentano and Chaboche, (2007) and Kut, (2010).

4.3 Past research on effects of indentation on steel products.

Most research reported in open literature such as those conducted by Duan et al, (1993); Duan et al, (1994); Ueda Y, (1991), and Abdel-Nasser et al, (2006) is on denting of steel structures in service by mechanical damage, such as denting by: impact from dropping heavy objects, an excavator prong, supply workboat collisions, and minor mishaps during offshore structure construction, loadout or installation. Past research reported in the open literature such as those conducted by Paik et al, (2003) and Paik, (2005) have investigated the effects of dents on the ultimate compressive strength and the ultimate shear strength of dented steel plates. Other research such as those conducted by Duan et al, (1994); Abdel-Nasser et al, (2006); Ueda Y,(1991); Chun and Nho, (2005); etc, have focused on the effect of dents on the ultimate (mostly compressive) strength of dented tubular members subjected to various loads and load combinations such as axial compressive loads, end bending moments, laterally distributed and concentrated loads. A research on the influence of denting on stiffness and ductile strength of ships and offshore steel structures was also carried out by Smith and Dow, (1981). In all this research, denting was found to have a detrimental effect on the strength of the offshore structural members.

4.3.3 Localised indentation of elastic-plastic solids

The knowledge of the contact between two non-conforming bodies is fundamental in mechanics of materials as it has a wide range of applications such as in instrumented spherical indentation tests (Mesarovic and Fleck, 1999). Most research reported in the open literature on miniature localised dents is on instrumented spherical indentation test. The research has focused on carrying out experimental and finite element simulations of instrumented spherical indentation tests which involves a local indentation with a sphere indenter to obtain the mechanical properties of materials from their hardness/indentation response. The instrumented spherical indentation tests have been used to obtain/predict mechanical properties such as the yield stress, Young Modulus, plastic hardening parameters, tensile strength, other flow properties and even residual stresses of materials (Cao and Lu, 2004; Kim et al, 2006; Kim et al, 2009; Kim et al, 2010 etc). It has even been used to evaluate the entire stress-strain curve of metallic materials (Beghini et al, 2006).

Local indentation involves complex deformation processes and the indentation region exhibits multiaxial stress conditions with high stress gradients, and may exhibit large elastic-plastic strains if plastic deformation is involved (Beghini et al, 2006). Figure 4.8 shows a sphere indenter of radius, R, under a load, L, making a typical local spherical (Brinell) indentation of contact radius, r, with a slope of , β, at its edge producing a pile-up of height, ℓ, at indent depth h. The spherical (Brinell) indentation shown in Figure 4.8 begins with an elastic indentation regime with elastic response at small indent depths, h.

The elastic response is given by the Hertz elastic solution for frictionless indentation. At small indentation depths, the region beneath the indenter is under a high hydrostatic pressure that is roughly semicircular or hemispherical in shape, which forces the surrounding material to have a radial elastic expansion to accommodate the material displaced by the penetrating indenter (Johnson, 1987).

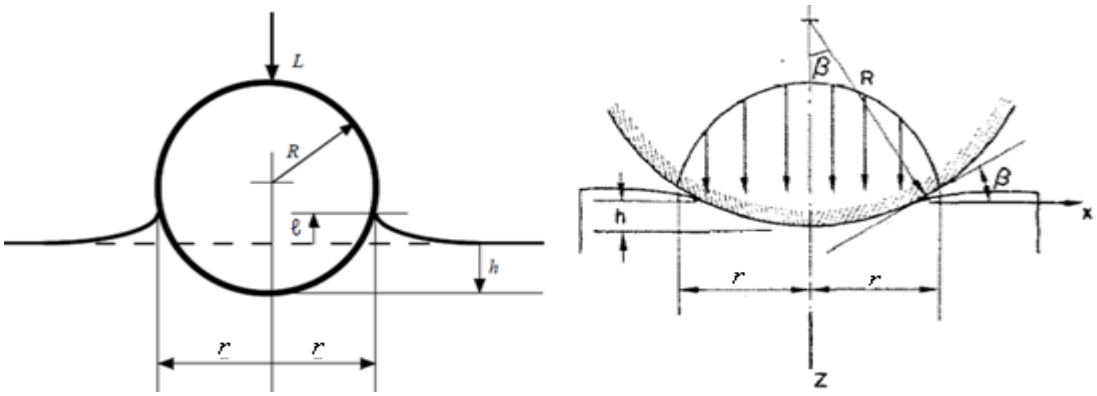

Figure 4.8: Geometry of a spherical indentation (Mesarovic and Fleck, 1999; Johnson, 1970).

As the indent depth increases, a small portion of the material under the centre of the indenter yields but the strain remains small because the surrounding elastic material acts as a constraint. This marks the beginning of elastic-plastic indentation during which the deformation and the indentation pressure are influenced by both elastic and plastic strains (Johnson, 1987). Plastic deformations begin with a small plastic deformation/flow which is confined to a small region beneath the indenter (core). As the indentation depth further increases, a greater region of the material becomes plastic and the plasticity spreads. The material displaced by the penetrating indenter is now accommodated by the elastic-plastic expansion of the surrounding material. Further increase in indentation depth increases the pressure. At a sufficient pressure, the elastic-plastic indentation regime changes to a fully

plastic indentation regime resulting into a fully-plastic flow and leading to the region of plasticity breaking to the surface and pilling up at the sides as in Figure 4.12 [(Johnson, 1987) and (Mesarovic and Fleck, 1999)].

For fully plastic regime, a similarity solution for rigid-plastic indentation exists. A typical loading and unloading (indenter load-penetration depth) curves for a spherical indentation is shown in Figure 4.9. The loading curve generally follows the power relation given in equation 4.5.

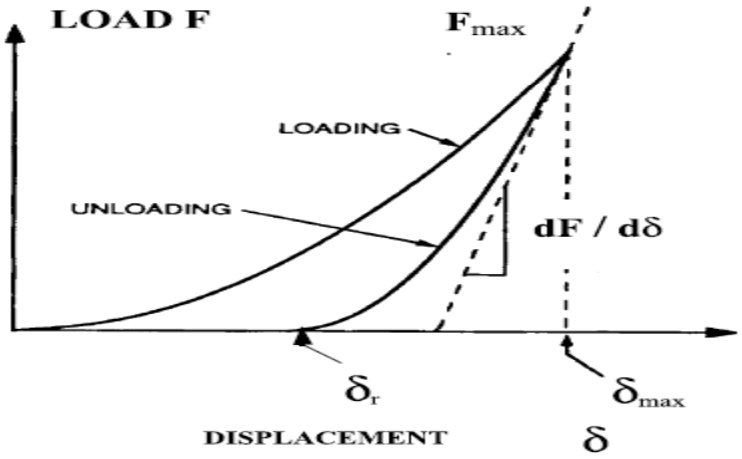

Figure 4.9: Typical loading and unloading curves during spherical-indentation (Nayebi et al, 2001)

$$F = K\delta^n \tag{4.5}$$

Where F is the indenter force and δ is the indenter displacement. K and n depend on the mechanical material parameters and on the indenter geometry.

For a spherical indenter, n is 1.5 and K is given by the expression in equation 4.6 (Johnson, 1987).

$$K = \left(\frac{4E^* R^{0.5}}{3} \right) \tag{4.6}$$

Where R is the radius of the spherical indenter and E* is the effective modulus which is obtained from Hertz equation given in equation (4.7) obtained from Nayebi et al, (2002).

$$\frac{1}{E^*} = \frac{1-\upsilon^2}{E} + \frac{1-\upsilon_{Ind}^2}{E_{Ind}} \tag{4.7}$$

Where E and ν are the Young's modulus and Poisson ratio, respectively of the dented material and E_{Ind} and ν_{Ind} are the Young's modulus and Poisson ratio, respectively of the indenter.

4.4 Past research on effects of reverse bending on metal products

Metal products such as sheets and wires/wire rods are subjected to bending and reverse bending during their service life or while being processed to manufacture other engineering structures, such as during sheet metal forming processes, descaling of wire rods, winding wires round mandrel for transportation or installation purposes and during routine testing to detect defects, especially laminations in wires. There are a few literature on bending and reverse bending of wires as most literature deals with bending and reverse bending of sheet metal. Consequently, a review of literature on bending and reverse bending of sheet metals and wires are presented.

4.4.1 Effects of bending and reverse bending on sheets metals

During sheet metal forming processes, sheet metals are subjected to bending followed by unbending deformations (Brunet et al, 2001) and reverse bending (to reduce springback) (Chen and Ko, 2006). Figure 4.10 shows a bent plate of thickness, h, with a bend radius, R, (radius of curvature on the concave surface of the bend). For elastic bending (bending stress/strain below the elastic limit), the strain passes through zero half way through the thickness of the sheet as the location of the neutral axis is at the centre of the sheet thickness (Dieter, 1998). In plastic bending (stress/strain beyond the elastic limit), the neutral axis moves closer to the inside surface of the bend as the bending proceeds and the plastic strain is proportional to the distance from the neutral axis. Consequently, the fibers on the outer surface are strained more than the fibers on the inner surface are contracted and the fiber at the mid-thickness (which is the average fiber) is stretched, leading to a decrease in thickness in the radial direction at the bend to preserve the constancy of volume (Dieter, 1998).

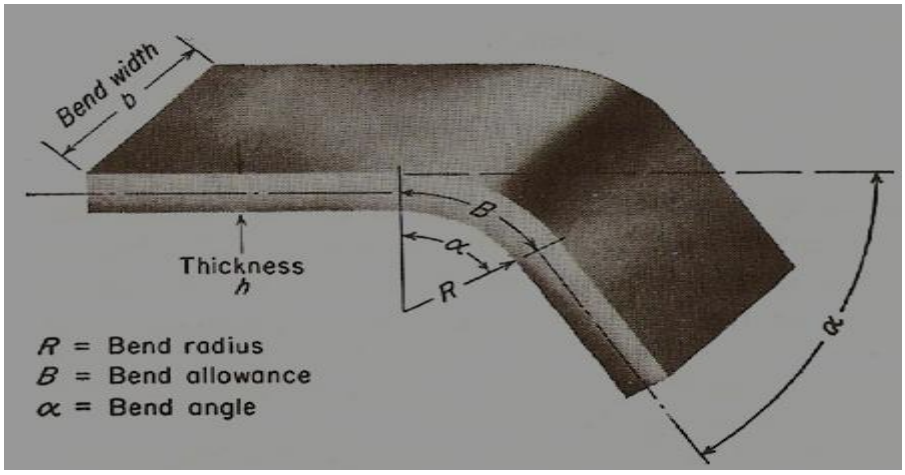

Figure 4.10: Bent plate (Dieter, 1998).

The smaller the radius of curvature, the higher the straining and the greater the reduction in the thickness of the sheet on bending. If the bend radius is smaller than a certain value called the minimum bend radius, the metal will crack on the outer tensile surface. The minimum bend radius is usually expressed in multiples of the sheets thickness (T) and it represents a forming limit. For high-strength sheets, the bend radius may be 5T or higher.

Most literature on bending and reverse bending of steel sheets deals with experimental and finite element simulations of sheet metal forming. In the published literature, emphasis has been particularly placed on the importance of the material constitutive models in FE sheet metal forming. This is because the reliability of both the formability and springback predictions depends on the selected computational modelling approach (Firat, 2007; Gau and Kinzel 2001). Material constitutive models that have been used in FE forming predictions and springback analyses include; isotropic, kinematic, anisotropic or combinations of two or more of these hardening plasticity models called the combined/mixed hardening model. The Mroz multiple yield surfaces method, which is based on the concept that the yield surfaces are concentric at the origin of the stress space before the material undergoes plastic deformation and become nonconcentric after plastic deformation, has also been used by Gau and Kinzel, (2001) for FE forming and springback predictions.

Elastic–plastic models with isotropic hardening are able to give a rather good prediction of the material behaviour (Carbonnie et al, 2008). However, the isotropic hardening plasticity model does not predict the through-thickness stress distribution properly because it does not take into consideration the Bauschinger effect and also overestimates the hardening

component (Firat, (2007); Zhao and Lee, (1999)). Isotropic hardening plasticity model has no mechanism to capture Bauchinger effect (Ken-ichiro, 2001).

Experimental sheet metal deformation analysis has shown that the Bauschinger effect is important (Firat, 2007) and has a significant influence on the internal stress calculation when sheet metal undergoes complicated cyclic deformation (Gau and Kinzel, 2001). Using the kinematic hardening model is the most popular method to handle the reverse yielding problem and is the most popular way used to model the Bauschinger effect. The Mroz multiple yield surfaces method can be used to monitor the Bauschinger effect even when experimental reverse loading data are not available (Gau and Kinzel, 2001).

While Brunet et al, (2001) reported that using a kinematic hardening law, even linear, that takes the Bauschinger effect into account instead of isotropic hardening has been shown to improve the performance of the model in predicting cyclic and other transient material behaviours, Zhao and Lee, (1999) reported that "the Kinematic hardening rule underestimates the hardening component and exaggerates the Bauschinger effect". An emerging new standard of models with mixed or combined hardening has proven to increase the numerical prediction reliability; particularly in the case of springback. Such new models describe the mechanical behaviour under monotonic, as well as reversed strain paths (Carbonnie et al, 2008).

The internal stress distributions within a sheet specimen obtained from FEA simulations of multiple-bending processes which involves bending (B); bending and reverse-bending (BR); bending, reverse-bending and bending (BRB); and bending, reverse-bending, bending and reverse-bending (BRBR) processes carried out with isotropic, kinematic and combined (isotropic and kinematic) hardenings as well as Mroz multiple yield surfaces are shown Figure 4.11 (a), (b), (c) and (d) respectively. From Figure 4.11, Gau and Kinzel, (2001) also concluded that isotropic hardening overestimates while kinematic hardening underestimates the material hardening result, during the multiple-bending processes. They also stated that, while the Mroz multiple yield surfaces gave a better prediction than the isotropic and kinematic hardening models, the best springback prediction results were obtained with the combined hardening model, which also gave the most accurate internal stress distribution. Zhao and Lee, (1999) also reported that combined isotropic and nonlinear kinematic hardening accurately predict the Bauschinger effect. From the results of the reverse bending

simulations carried out by the various authors and their conclusions, it can be inferred that the combined hardening model gives the best prediction of the response of metals subjected to strain reversal.

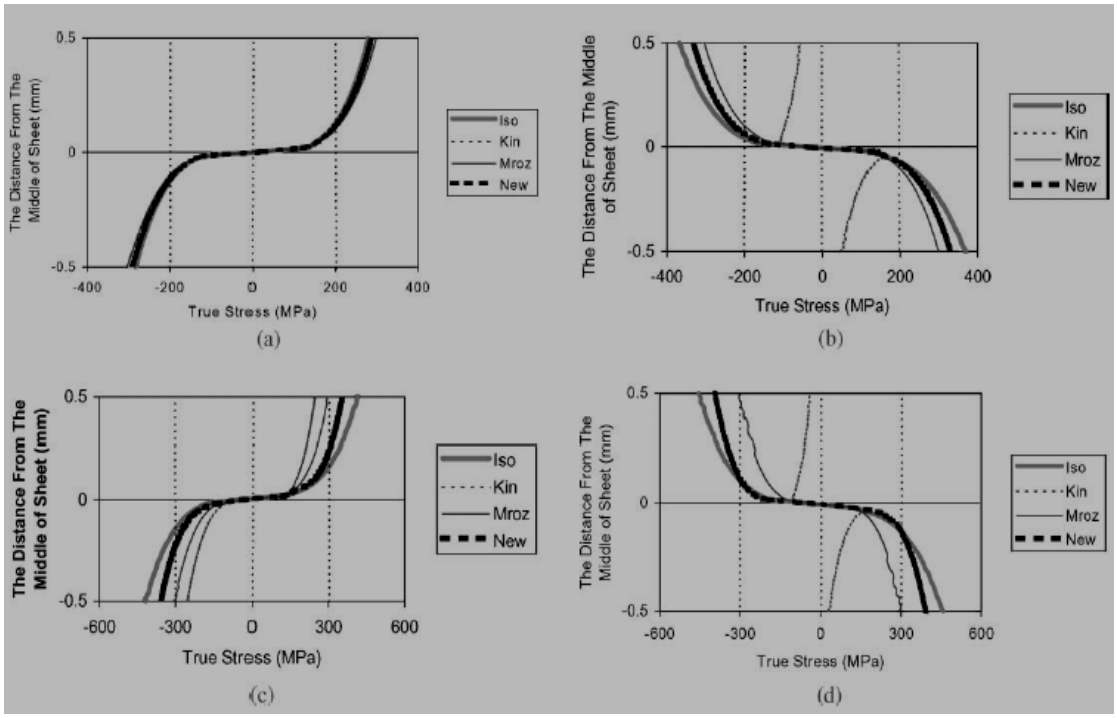

Figure 4.11: Internal stress distributions in sheet specimen predicted by various hardening models (Gau and Kinzel, 2001).

4.4.2 Effects of bending on hybrid composite core of ACCC wires

Burks et al, (2009) numerically investigated the effect of mandrel size on the compressive stress state in the composite core of the ACCC conductor. They carried out the modelling by pinning the nodes on the end of the composite rod that are in contact with the mandrel at the beginning of the simulation as shown in Figure 4.12(a) and applying a concentrated load to the free end of the wire to bend and wrap the rod round the mandrel as shown in Figure 4.12 (b). The non-linear finite element predicted stress distribution in the deformed composite core is presented in Figure 4.12(c). Burks et al, (2009) stated that the axial compressive stress state in the ACCC rods is controlled by the radius of the mandrel. They concluded that due to lower compressive strength of ACCC conductor composite core, ACCC rods will be mechanically damaged by excessive bending over small diameter mandrels used for their transportation and installation purposes. (Burks et al, 2009).

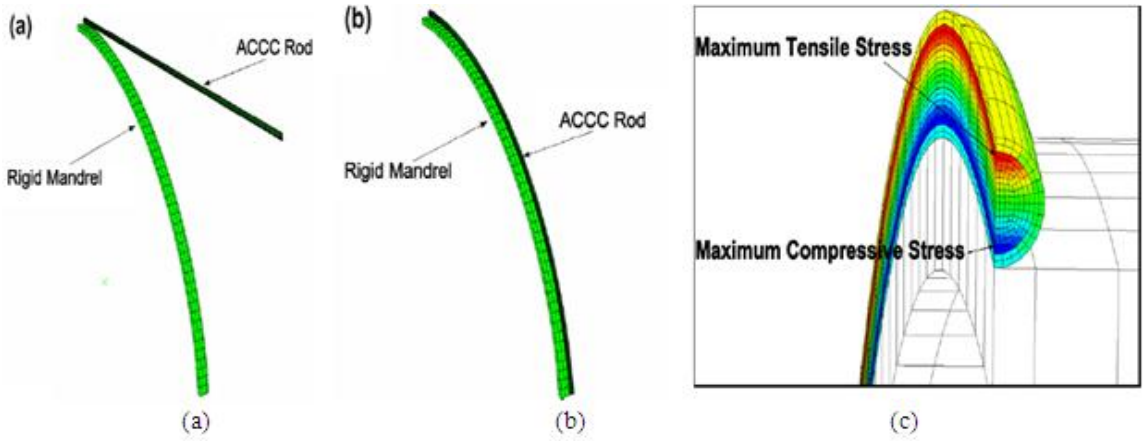

Figure 4.12: Undeformed shape, deformed shapes and stress distribution in ACCC rod wound round mandrel (Burks et al, 2009).

Burks et al, (2010) also investigated the effect of excessive bending induced in ACCC hybrid composite rods when wound round mandrels on their residual tensile strength and concluded that excessive bending of the ACCC core up to 90% of the average flexural strength had no effect on the residual tensile strength of the material as SEM work revealed that the majority of the micro-structural damage that occurred during the excessive bending of the cores are in the form of matrix damage without any significant fibre kinking.

4.4.3 Effects of bending and reverse bending on steel wires and wire rods

During mechanical descaling by reverse bending and during one of the routine tests to detect defects, especially laminations in wires, wires are subjected to a reverse bending test using the roller arrangement shown in Figure 4.13 [(Gillstrom and Jarl, 2006); (Bruehl, 1984)]. Repeated bending/reverse bending leads to permanent elongation in wire rod and heavy deformation during bending/reverse bending could lead to an undesirable work hardening of the steel and cause increased back tension on the rod line leading to stretching and necking-down of the rod (Gillstrom and Jarl, 2006).

Figure 4.13: Reverse bending equipment with three steel rollers (Gillström and Jarl, 2006).

Figure 4.14 shows that elongation occurs at the top surface of a wire of diameter φ bent over a roller with diameter, D_r, while compression occurs at the interface between the rod and the roller leading to stretching of the outer fibre and the compression of the inner fiber (Gillstrom and Jarl, 2006). The maximum elongation occurs at the surface and provided there are no frictional forces between the scale breaker rollers and the rod, it can be calculated by the expression in equation 4.8 obtained from Gillstrom and Jarl, (2006). The location of the neutral line is at the centre of the cross-section when there is no back-pull or frictional forces between the scale breaker rollers and the rod. If the compression of the rod at the interface between the rod and the roller is smaller than the maximum elongation at the top of the rod, which can occur when there is back-pull or friction between the roller and the wire, the location moves to a plane under the centre of the cross-section and produces elongation of the rod (Gillstrom and Jarl, 2006).

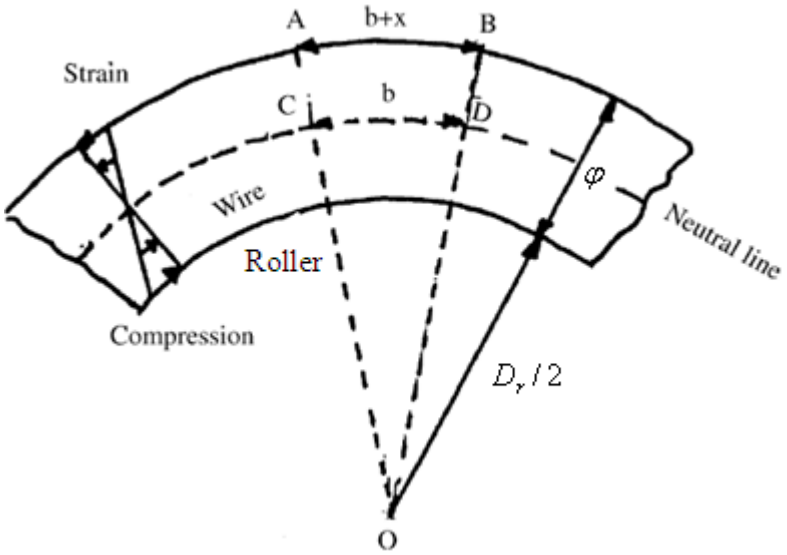

Figure 4.14: Elongation and compression of a rod bent over a roller (Gillström and Jarl, 2006)

$$e = \frac{\varphi}{\varphi + D} \tag{4.8}$$

In this chapter, the review of the past work done on defects and failures in wire and plate, bending and reverse bending of wire and plate, tensile testing and indentation simulations are presented. The experimental methodology and techniques used in this research is presented in the next chapter.

Chapter 5: Experimental methodology and techniques

In this chapter, the experimental methodology and techniques used for the laboratory and the numerical or virtual experiments as well as the description of the materials (tensile armour wires) used for this research are presented. This chapter also describes the experimental techniques used for the tensile testing, hardness testing, metallography, microscopy and finite element analyses.

5.1 Experimental methodology

As stated in section 2.1.1.2, tensile armour wires are subjected to tensile stresses/loading while providing the resistance to axial tension and hoop stress which flexible pipes are subjected. Their structural performance thus depends on their tensile properties. Although classical fracture mechanics tests can also be used to investigate the effects of defects particularly cracks in structures, the tensile armour wires have a maximum dimension of 12mmx7mm and are not large enough to make standard fracture mechanics specimens. Consequently, to understand the effects of defects types and sizes on the structural performance of tensile armour wires, a series of tensile tests were carried out on the as-received wires and on wires with engineered defects in the form of notches.

Laboratory tensile strength testing of the as-received wires was conducted to characterise the wires, to obtain material data input for the finite element analysis and to serve as references against which the finite element analysis results could be validated. Tensile testing finite element simulations were carried out on the specimens of the as-received wires, following which the FE results were updated and validated with experimental results and the appropriate fracture mechanism for the tensile armour wires was identified.

Scanning electron microscope images were taken to identify the defect types on the surface of the as-received wires. The scanning electron microscope images revealed depressions/dents, groove shaped scratches and scratches with pointed end defects. Larger dimensions of these defects were introduced onto the surface of the as-received wires in the forms of dents, channel shaped notch and V-notches. Laboratory tensile tests were carried out on the wire specimens with these engineered defects. Tensile testing finite element simulations were carried out on wire specimens with engineered V-notch, channel shaped notch and dent

defects. The FE results were validated with the experimental results obtained from tensile tests carried out on V-notched, channel shaped notched and dented wires respectively and good agreements were obtained between the experimental and FE predicted force-displacement curves.

Finite element tensile testing simulations were subsequently used as virtual experiments to determine the effects of these defects with miniature sizes below and above the 0.2mm minimum detection capability of the inline eddy current defects detector used in the flexible pipe manufacturing industry. Finite element simulations were also used to investigate the effects of defects shallower and deeper than the standard calibration defects used to calibrate the eddy current detector. The variation of the tensile properties of the wires with various defect types and sizes were plotted to obtain design curves which could serve as handy tools to be used by the flexible pipe manufacturers and engineers to estimate the tensile properties of defective tensile armour wires with dents, channel shaped scratches and V-shaped scratches.

In the manufacturing process of flexible pipes, the as-received tensile armour wire is subjected to a reverse bending process using two offset rollers and straightened over a third roller as a lamination check and to ensure quality. To investigate the effects of reverse bending over 100mm diameter rollers on laminations and other surface defects, as well as the effects of reverse bending on the tensile properties of tensile armour wires generally, laboratory tensile testing of as-received wire specimens that have been subjected to bending, reverse bending and straightening were carried out. Finite element simulations of the as-received tensile armour wires subjected to reverse bending, straightening and tensile testing were also carried out and the results validated with the experimental results. Also finite elements simulations of wire specimens with laminations, channel shaped notch and V notch defects subjected to bending, reverse bending, straightening and tensile testing were carried out to investigate the effects of reverse bending and straightening processes on laminations and other surface defects.

5.2 Experimental techniques

The experimental techniques used in carrying out the tensile testing, hardness testing, metallography, microscopy and finite elements analyses are presented in this section.

5.2.1 Tensile testing techniques

The tensile tests were carried out with the Instron universal testing machine series IX 4505 which is a precision electromechanical device with a load frame which applies tension, compression or reverse stresses to a test specimen and with Instron series IX software for data acquisition, control and analysis. The load frame uses a moving crosshead on which a strain gauge based Instron load cell is mounted to apply a load to the test specimen. The specimens were gripped with the wedge grip, because it is suitable for holding flat specimen as stated by ASTM E 8M: 2000.

An Instron 2518 series load cell with a maximum static capacity of ±100 kN and an accuracy of at least 0.025% of the rated output or 0.25% of the indicated load was used for the load measurement as it has the sufficient capacity to test the tensile armour wires with an ultimate load of approximately 77kN. An Instron 2630 -112 clip on strain gauge extensometer with a 50 mm gauge length and a +50% -5% maximum strain (+25/-2.5mm axial travel) was used for the displacement measurement as it is able to measure the displacement over the entire 50mm gauge length of the wire specimens. The Instron 2630-112 belongs to the Instron 2630-100 series which complies with the BS EN ISO 9513:2002 standard (Instron, 2004). BS EN ISO 9513:2002 is a British standard that covers the specifications for extensometers with relative error on the gauge length and bias error ranging from 0.2 to 2 and with resolution ranging from 0.1 to 1.

5.2.2 Hardness testing techniques

The through thickness hardness profile of the tensile armour wires was measured using a Buehler MMT-7 digital micro-hardness tester fitted with a Vickers diamond indenter. The measurements were performed using a test load of 200gf (1.96N). A JVC colour video camera was used to photograph the indents at 400x magnification and the corresponding hardness values were calculated using the Buehler OmniMet HMS software, which is a calibrated image analysis package.

5.2.3 Metallography techniques

The metallography was carried out on polished and etched tensile armour wire specimens, mounted in resin, using the optical metallography method. The etching was done with Nital and the optical metallography was carried out using a µEye digital camera attached to a

Nikon Eclipse LV150 reflected light microscope and the images were captured using Buehler OmniMet.

5.2.4 Microscopy techniques.

The image of the surface of the as-received tensile armour wires was taken with an FEI XL 30 environmental scanning electron microscope (ESEM) –FEG (field emission gun) operated at high voltage (HV 10kV), high vacuum, using a secondary electron detector (Det SE) because of the high vacuum, with a working distance (WD) of 22.6 and 1mm micro-marker.

5.2.5 Finite element techniques

The finite element simulations carried out in this research were conducted with Abaqus version 6.9.1 research edition which has Abaqus/Standard, which is ideal for static and low-speed dynamic events; Abaqus/Explicit, which is well-suited to simulate brief transient dynamic events; and Abaqus/CAE which is used for modelling, visualisation and process automation. These Abaqus products are discussed in details in Chapter 3.

5.3 Materials

The tensile armour wire used for this research was provided by Wellstream International limited, a manufacturer and supplier of flexible pipe systems. The wires provided are 12mmx5mm and 12mmx7mm in dimension which are used for the manufacturing of unbonded flexible pipes.

Details of the experimental methodology and techniques used for the tensile testing, hardness testing, metallography, microscopy and finite elements analyses, as well as the description of the materials used in this research have been presented in this chapter. The next Chapter introduces the development of the test method used in this research.

Chapter 6 Laboratory and virtual/numerical experiments test methods development

This section describes the development of the laboratory and virtual or numerical experiments test methods used for the tensile testing of the as-received wire and wires with engineered defects. It also contains the test methods used for the identification of the types and geometries of defects on the tensile armour wire surface. The development of the laboratory and numerical tensile test methods for the as-received wires are presented in sections 6.1 and 6.2 respectively. The global and local mesh convergence conducted to determine the appropriate finite element sizes are presented in sections 6.2.1 and 6.2.2 respectively. The determination of the appropriate fracture model and modelling parameters calibration are presented in section 6.2.3, and the correction of the experimental crosshead displacement after the extensometer removal is presented in section 6.2.4.

6.1 Laboratory tensile testing of as-received wires

Due to the various shortcomings that are associated with using machined specimens stated in Section 2.2 that could lead to unsatisfactory and incorrect test results, and the requirements of BS EN 10218-1:1994 and EN10002-1:2001E that full size specimens be used for specimen thickness less than 4mm, full size specimens were used for the tensile testing conducted in this research. The INSTRON 4505 testing machine with a ±100 kN load cell discussed in sections 5.2.1 was used for the tensile testing. The Instron 2630 -112 clip on strain gauge extensometer also discussed in sections 5.2.1 was used for the displacement measurement since the testing machine cross head displacement does not represent the actual deformation of the specimen as stated in section 2.2.4. A gauge length of 50mm specified by ASTM E 8M :2000 was used and the tensile tests were conducted at cross head speed of 5mm/minute which translates to a straining rate of $0.0017s^{-1}$ which is within the 0.00025 to 0.0025 s^{-1} limit specified in BS EN 10002-1:2001E and ASTM E 8M :2000.

The results of the laboratory tensile tests carried out on three full size tensile armour wires specimens labeled as specimen1, 2 and 3 with cross sectional dimensions of 12mmx5mm are presented in the form of force-displacement curves as shown in Figure 6.1. The engineering stress-strain curves obtained from these curves are shown in Figure 6.2.

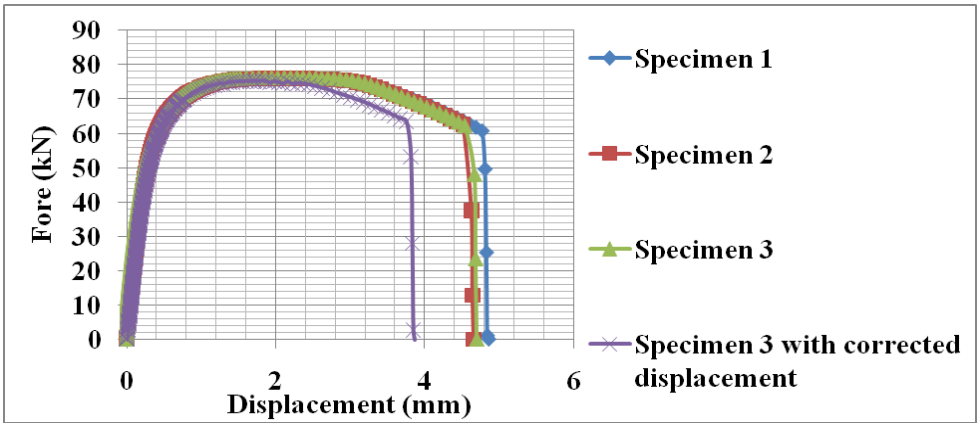

Figure 6.1: Tensile force-displacement curves for tensile armour wire specimens with 12mmx5mm cross-sectional dimensions and 50mm gauge length.

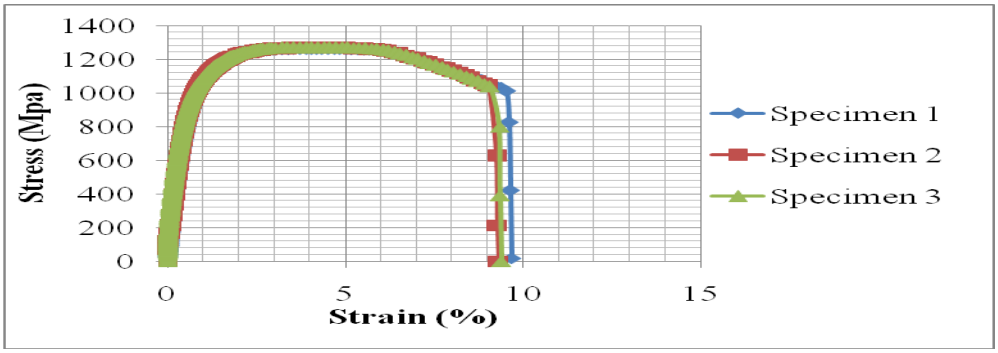

Figure 6.2: Engineering stress-strain curves for tensile armour wire specimens with 12mmx5mm cross-sectional dimensions and 50mm gauge length.

Since the extensometer was removed immediately after the maximum load point, the experimental displacement values beyond the ultimate load point are crosshead displacement values. Consequently, the experimental displacement values beyond the ultimate load point were corrected by subtracting the testing machine elastic deflection (Δ_E). Using the expression in equation 2.27, with a crosshead displacement of 0.083mm, specimen extensometer gauge length L_0 of 50mm, specimen cross sectional area A_0 of 60mm^2, E of 2x10^{5}MPa and the force P in the specimen of 26.87kN, the testing machines stiffness was calculated as follows:

$$K = (\Delta_c / P - L_0 / A_0 E)^{-1} = (0.083/26.87052 - (50/60 \times 200000))^{-1} = 322 \cdot 9 \, {}^{kN}\!/_{mm}$$

The machine deflection at the ultimate load point is calculated as follows:

$$\Delta_E = {}^{P}\!/_{K} = {}^{76.01}\!/_{322.88} = 0.24mm$$

The machine stiffness and deflection values calculated for the remaining force-displacement values using Excel spreadsheet is presented in columns 1 and 2 of Table A1 of appendix A. The corrected experimental curve for specimen 3 (with tensile properties closest to the average values) obtained by subtracting the machine deflection uncorrected experimental curve is shown in Figure 6.1.

The average offset yield strengths for the three wire specimens were estimated to be 960MPa when rounded up to the nearest 5MPa as recommended by ASTM E 8M: 2000. The average tensile strength for the three wires specimens estimated at the ultimate load sustained by specimens 1, 2 and 3, which are 75.68kN, 76.01 kN and 76.30kN respectively is 1270MPa when rounded up to the nearest 10MPa as recommended by ASTM E 8M: 2000. The percentage elongation after fracture based on an average extension after fracture of 4.45mm as shown in Table 6.1 is of 9.0% when rounded up to the nearest 0.5%. The summary of the mechanical properties of the tensile armour wires with their averages and standard deviations are presented in Table 6.1.

Table 6.1 Summary of the mechanical properties of the tensile armour wires

	Specimen number			Reported value
Parameters	1	2	3	
0.2% Offset yield stress (MPa)	960.0	960.0	960.0	960 0± 0.00
Ultimate load (kN)	75.68	76.30	76.01	75.97 ± 0.31
Ultimate strength (MPa)	1261	1270	1270	1267 ± 5.51
Fracture load (kN)	28.35	30.13	30.09	29.52 ±1.02
Nominal fracture strength (MPa)	502	502	473	492.1 ± 16.95
Extension after fracture (mm)	4.40	4.48	4.46	4.45 ± 0.03

6.2 Development of virtual experiment test methods for tensile testing of as-received tensile armour wires

There dimensional (3D) finite element tensile testing simulation was used as the virtual experiment. Figure 6.3(a) and (b) show the full size model of 50mm long, 12mmx5mm wire with the actual and simplified (rectangular) shapes meshed with 1mmx1mmx1mm C3D8R elements. One end of the specimen was fixed and the other end which was free to move in the longitudinal (x-axis or length) direction was subjected to a displacement longitudinal displacement.

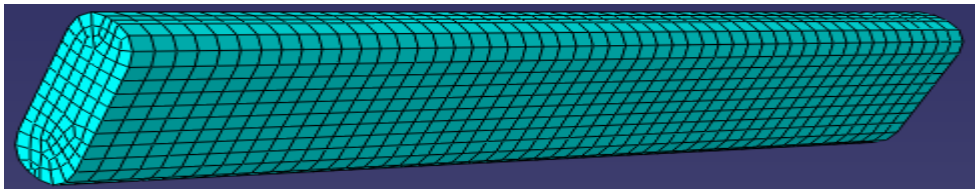

(a) Actual wire shape

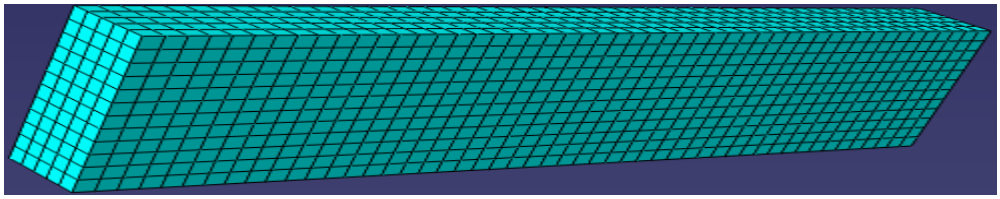

(b) Simplified rectangular shape

Figure 6.3: Meshed models of actual and simplified rectangular wire shapes.

An elastic-plastic-damage simulation with the isotropic hardening model and the shear damage and fracture criterion was conducted. The true stress-true plastic strain data used as the material input for the elastic-plastic simulation is presented in Appendix A. The preliminary damage and fracture criterion modelling parameters used are fracture strain of 0.2761, shear stress ratio of 10, strain rate of 0.0001 and a material parameter Ks of 0.3. These values are the parameters for a typical ductile material obtained from Simulia, 2007.

The deformed shapes showing the Mises stress distribution in the wire model with rectangular shape during necking at an applied displacement of 1.86mm, during fracture initiation at an applied displacement of 3.75mm and after fracture at an applied displacement of 4.6mm are shown in Figures 6.4 (a) to (c) respectively. The fracture shape of the model with actual wire shape is shown in Figure 6.4(d). The Mises stress distribution in the wire specimens is indicated by colour coding with the maximum stress represented by red and the least stress represented by blue. The numerical values of the various colour coding are show in the contour plot. From Figure 6.4, fracture started at the middle of the necked region, which agrees with what is reported by Tvergaard and Needleman, (1984) and Kim and Chao, (2008) due to the rapid void growth at the center leading to the fracturing of the centre of the specimen.

The force-displacement curves predicted by the simulations conducted with the actual and simplified wire shapes are shown in Figure 6.5(a). On the basis of the negligible difference in

the force-displacement behaviour predicted by the simulations carried out with the actual and simplified wire shapes; and for ease of modelling, especially when defects are introduced, subsequent simulations were carried out with the simplified (rectangular) shape.

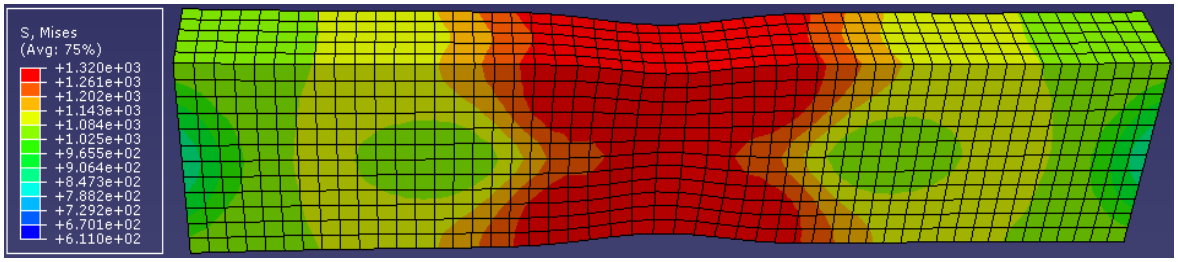

(a) During necking at an applied displacement of 1.86mm

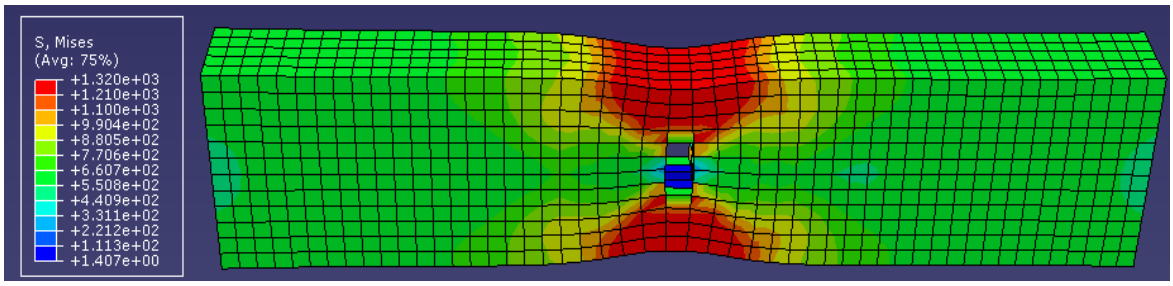

(b) During fracture initiation at an applied displacement of 3.75mm

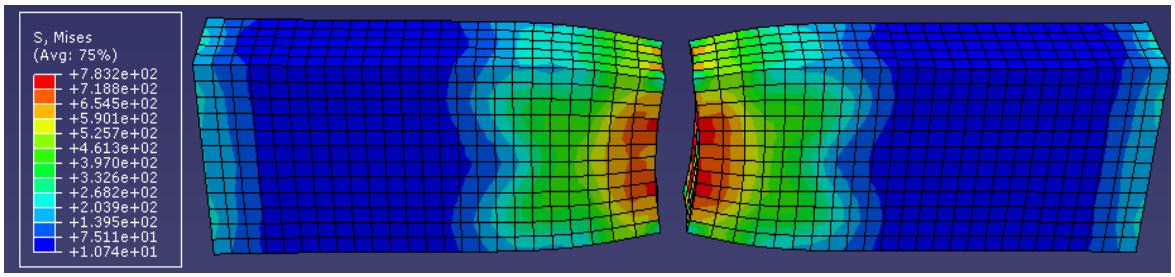

(c) Fracture shape of model with rectangular shape at an applied displacement of 4.6mm

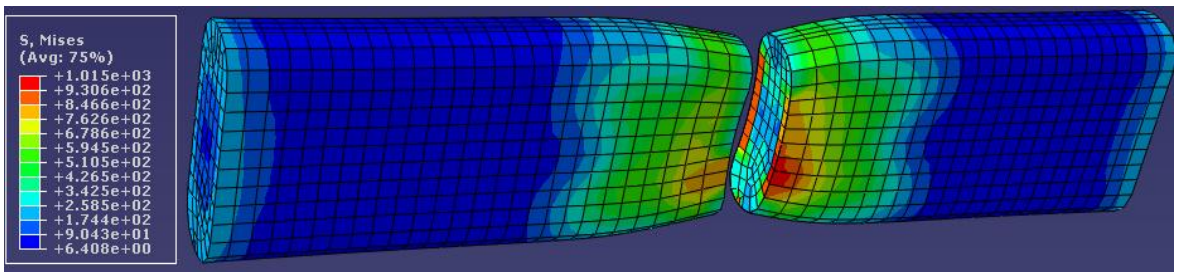

(d) Fracture shape of model with actual wire shape at an applied displacement of 4.6mm

Figure 6.4: Deformed shapes of wire model meshed with 1mmx1mmx1mm elements showing Mises stress (MPa) distribution at various stages of tensile testing simulation.

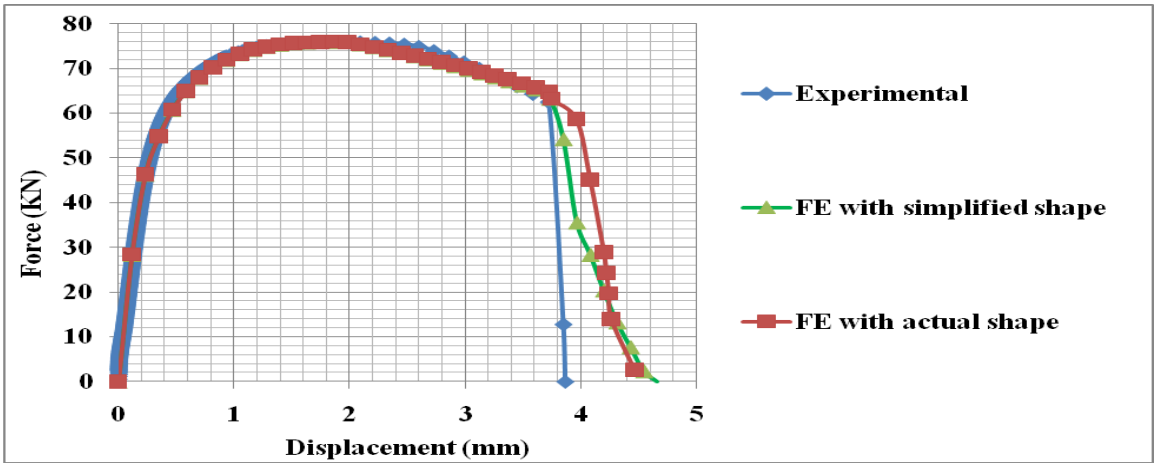

(a) Force-displacement curves from simulations with actual and simplified wire shapes

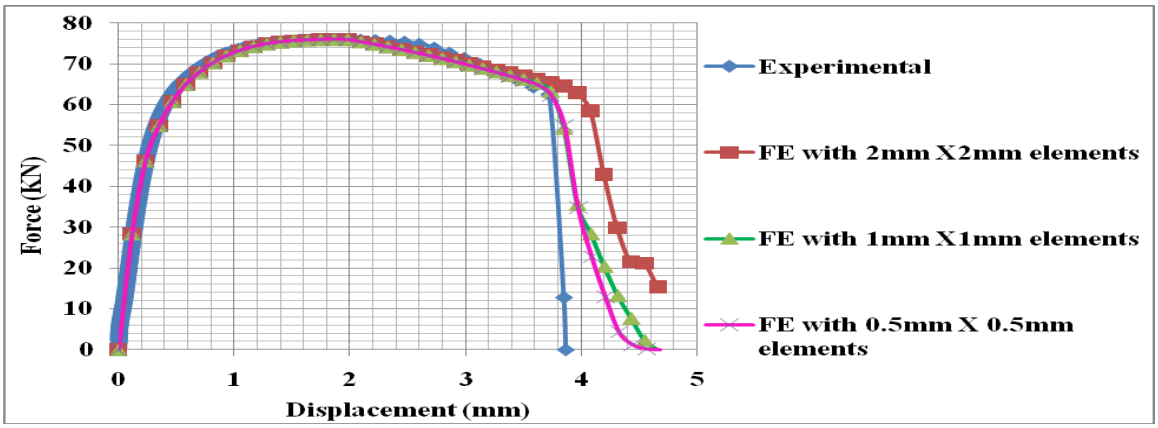

(b) Force-displacement curves from simulations with successive global mesh refinement

Figure 6.5: Experimental and FE force-displacement curves from tensile testing of 50mm gauge length, 12mmx5mm wire specimens.

6.2.1 Global mesh convergence

Figure 6.5(b) shows the force-displacement curves predicted by the simulations with elements having 2mmx2mmx1mm ($4mm^3$), 1mmx1mmx1mm ($1mm^3$) and 0.5mmx0.5mmx1mm ($0.25mm^3$) dimensions and Figure 6.6 shows the fractured shapes obtained from the simulations with the three elements sizes. The 1mm element dimension is in the thickness (Z) direction. From Figure 6.5(b) and the negligible percentage difference (<1.5%) between the values of yield loads, ultimate loads, fracture loads, yield point displacements and ultimate load point displacements predicted by the simulations with the three mesh sizes as shown in Table 6.2, it shows that the mesh has converged except for the

larger fracture point displacement predicted by the simulation with 2mmx2mmx1mm elements.

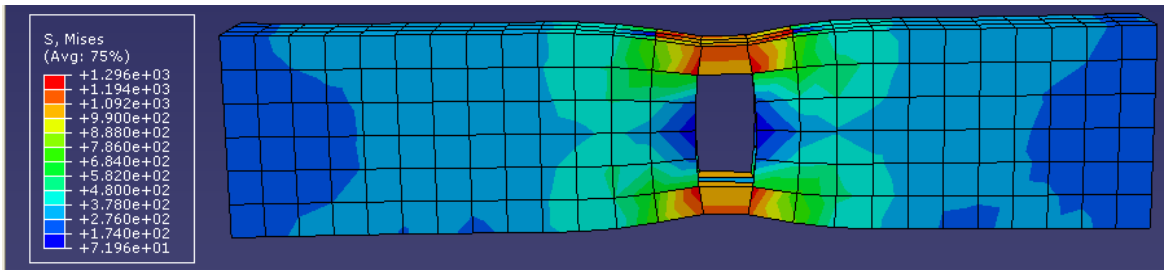

(a) Fractured shape predicted by simulation with 2mm square elements at 4.66mm displacement.

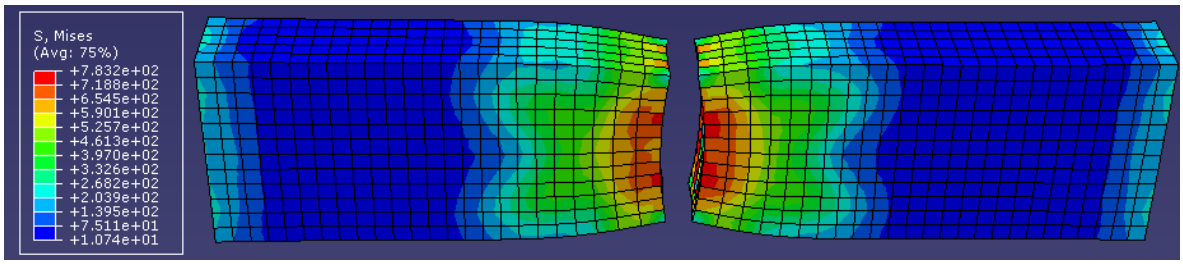

(b) Deformed shape predicted by simulation with 1mm square elements at 4.66mm displacement.

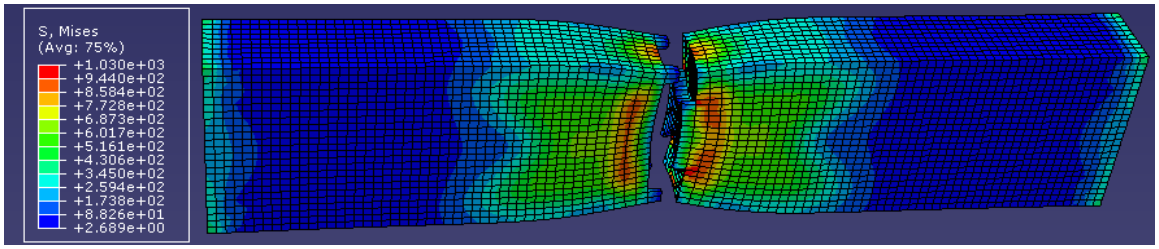

(c) Deformed shape predicted by simulation with 0.5mm square elements at 4.00mm displacement.

Figure 6.6: Mises stress (MPa) distribution and deformed shapes predicted by simulations with successive mesh refinement.

The simulation with 2mmx2mmx1mm elements also predicted that at the prescribed experimental fracture point displacement, the specimen still had some load carrying capacity (15.3kN) which does not agree with the experimental observations/values. This result agrees with what is reported by Besson et al, (2003). The larger fracture point displacement and the remaining load carrying capacity predicted by the simulation conducted with 2mmx2mmx1mm elements is due to the fact that the bigger the mesh size, the higher the

fracture energy. Thus, the model meshed with 2mmx2mmx1mm elements requires a higher level of stress/strain for it to fracture than that required by the models meshed with the finer mesh. Consequently, carrying out the simulations with 2mmx2mmx1mm elements would predict a larger fracture point displacement, thereby overestimating the ductility of the tensile armour wires. Also carrying out the simulations with 0.5mmx0.5mmx1mm elements was not necessary as the simulations with 1mm square elements predicted exactly the same force-displacement curve as the simulation with 0.5mmx0.5mmx1mm elements. This shows that 1mmx1mmx1mm elements are refined enough to produce sufficiently accurate results.

Table 6.2: Variation in mechanical properties of tensile armour wires with mesh sizes

Element size (mm)	Yield load (kN)	% difference	Ultimate load (kN)	% difference	Fracture load (kN)	% difference
2x2x1	46.27	-	75.95	-	62.98	-
1x1x1	46.27	0.011	75.97	0.024	63.25	0.428
0.5x0.5x1	46.28	0.023	75.98	0.003	62.37	1.419
Element size (mm)	Yield point displacement (mm)		Ultimate load point displacement (mm)		Displacement at Fracture (mm)	% difference
2x2x1	0.23	-	1.87	-	3.97	-
1x1x1	0.23	0.00	1.86	0.049	3.74	6.16
0.5x0.5x1	0.23	0.00	1.86	0.00	3.73	0.13

6.2.2 Local mesh refinement

To capture the high stress concentration at the centre of the specimen during necking and capture the high stress triaxiality at the centre of the specimen during fracturing, the mesh at the middle of the specimen was refined with 0.25mm elements as shown in Figure 6.8. The force-displacement curves predicted by the simulations with and without local mesh refinements at the middle of the wire models are shown in Figure 6.7. The deformed shapes at an applied displacement of 0.12mm during necking at an applied displacement of 1.9mm during fracture initiation at an applied displacement of 3.73mm and after fracture at an applied displacement of 3.96mm are shown in Figures 6.8(a), (b), (c) and (d) respectively.

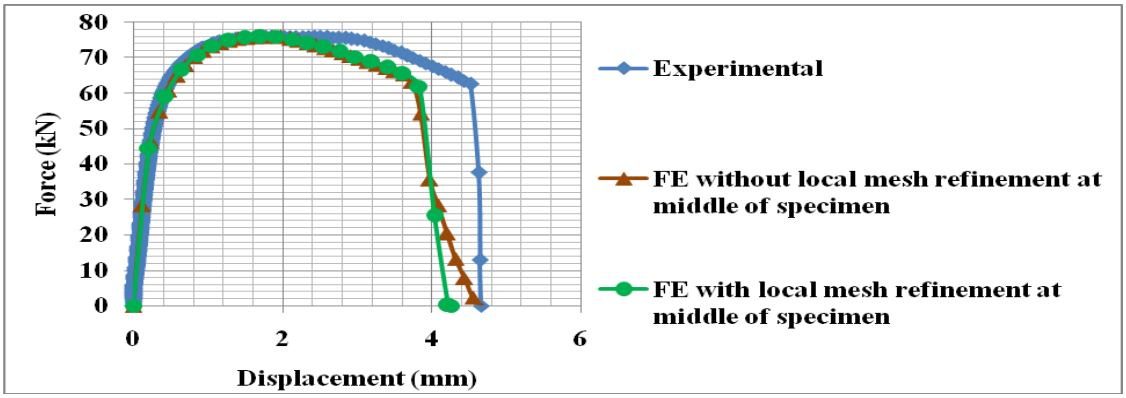

Figure 6.7: Force-displacement curves from simulations of tensile testing of 50mm gauge length, 12mmx5mm wire specimens with and without local mesh refinements at specimens' middle.

From Figures 6.7, there are no significant differences in the values of the yield loads, the ultimate loads and the displacements at fracture predicted by the simulation with and without mesh refinement at the middle of the wire specimen models. However, the fracture trajectories (the portion of the curves after the fracture initiation points) predicted by the simulations with mesh refinement at the middle of the specimens agree better with the fracture trajectory of the experimental curve, as they have lower extensions than the fracture trajectories predicted by the simulations without mesh refinement at the middle of the specimens. Also the simulation with mesh refinement at the middle of the wire specimen predicted a cup and cone failure compared to the flat failure predicted by the simulation without mesh refinement at the middle of the specimen shown in Figure 6.4 and 6.6. Thus, refining the mesh at the centre of the model improves the FE predictions of the fracture shape and the fracture trajectory of the specimen but has negligible effects on the force-displacement response of the model up to the fracture point. This result agrees with what is reported by Besson et al, (2003) and Tvergaard and Needleman, (1984) as sufficient mesh refinement at the middle of tensile specimen is required to capture the gradients of stress and strain fields adequately in order to predict a cup-cone fracture.

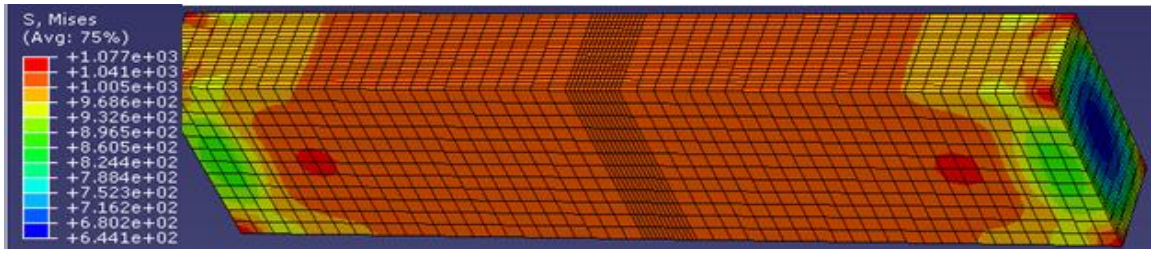

(a) Deformed shape at an applied displacement of 0.12mm.

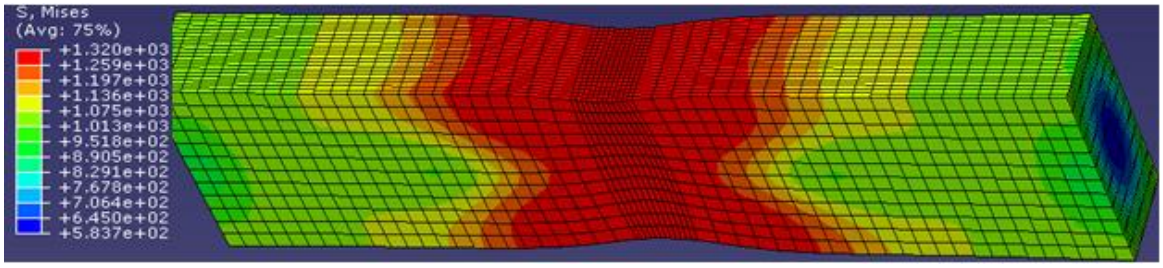

(b) During necking at an applied displacement of 1.9mm.

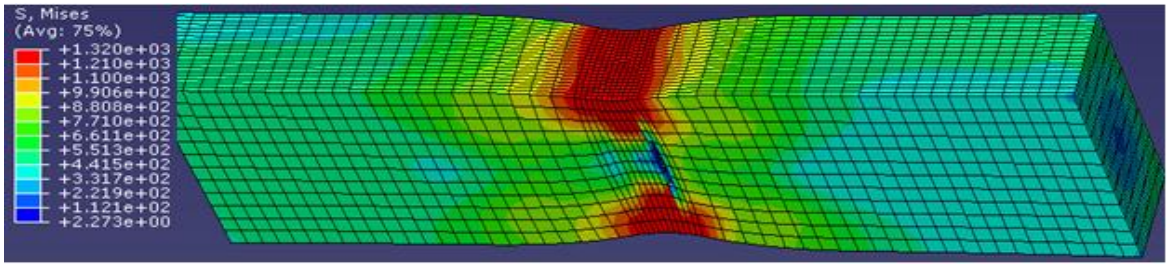

(c) During fracture initiation at an applied displacement of 3.73mm.

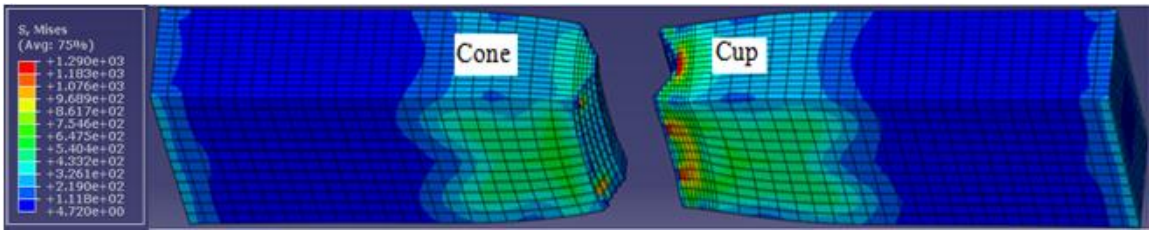

(d) Fractured specimen an applied displacement of 4.08mm.

Figure 6.8: Mises stress (MPa) distribution and deformed shapes at various stages of tensile testing predicted by simulation with local mesh refinement at the middle of wire.

6.2.3 Determination of appropriate fracture model and modelling parameters.

To determine which of the failure models best predicts the failure of the wire specimen, FE simulations were conducted with both phenomenological (shear and ductile) failure models and a micro mechanical (porous metal plasticity) failure model. To obtain the appropriate failure modelling parameters, modelling parameters calibrations were conducted using the

phenomenological curve fitting method explained in section 3.3.2. The FE simulations were conducted with varying parameter combinations, a few of which are designated as parameter combinations A to D, E to H and I to L presented in Tables 6.3, 6.4 and 6.5 for the shear, ductile and porous metal plasticity models respectively. Parameter combinations A, E and I which were the starting parameter values for the shear, ductile and porous metal plasticity models are typical parameters for ductile materials.

Table 6.3: Fracture loads predicted by varying shear fracture parameter combinations

	Fracture strain	Shear stress ratio	Strain rate	Parameter Ks	Fracture load (kN)
Parameters combination A	0.2761	10	0.0001	0.3	66.05
Parameters combination B	0.345125	12.5	0.000125	0.3	63.25
Parameters combination C	0.41415	15	0.00015	0.3	61.94
Parameters combination D	0.5522	20	0.0002	0.3	58.08

Table 6.4: Fracture loads predicted by varying ductile fracture parameter combinations

	Fracture strain	Stress triaxaility	Strain rate	Fracture load (kN)
Parameters combination E	33.238	3.3333	0.0001	64.56
Parameters combination F	36.5618	3.66663	0.00011	62.62
Parameters combination G	49.857	4.99995	0.00015	57.07
Parameters combination H	66.476	6.6666	0.0002	55.97

Table 6.5: Fracture loads with varying porous metal plasticity parameter combinations

	Void volume fraction f_N	Critical void volume fraction at failure f_c	Total void volume fraction at failure f_F	Fracture load (kN)
Parameters combination I	0.01	0.01	0.15	59.23
Parameters combination J	0.001	0.001	0.015	65.30
Parameters combination K	0.002	0.002	0.03	64.18
Parameters combination L	0.004	0.004	0.06	62.85

The parameters were numerically optimised until the FE simulations predicted force-displacement curves with approximately the same fracture load/point as the experimental curve. For the porous metal plasticity model, the coefficients of the void volume fraction q_1 and q_2 were fixed at 1.5 and 1.0 respectively, while the coefficient of pressure term q_3, the average nucleation strain ε_N and the standard deviation S_N were fixed at 2.25, 0.3 and 0.1 respectively for all the simulations. The force-displacement curves predicted by the simulations with varying shear, ductile and porous metal plasticity models parameter combinations presented in Tables 6.3, 6.4 and 6.5 are shown in Figures 6.9, 6.10 and 6.11 respectively.

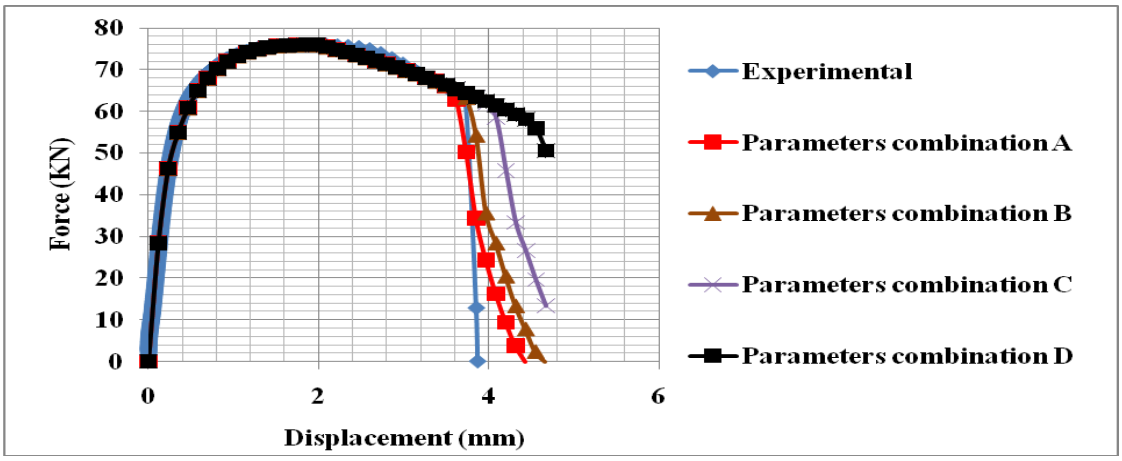

Figure 6.9: Force-displacement curves for 50mm gauge length, 12mmx5mm wire specimens predicted by the simulations with varying shear model parameter combinations.

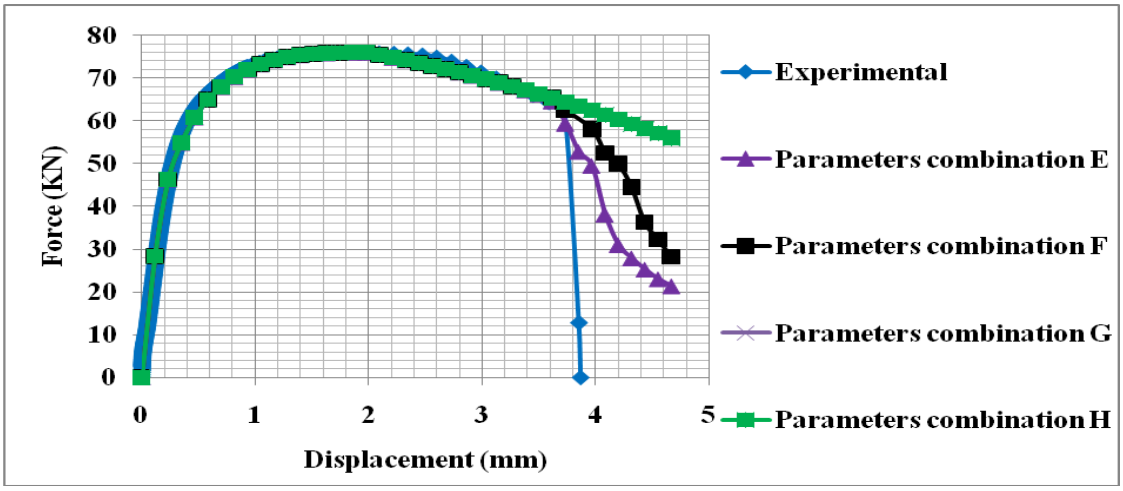

Figure 6.10: Force-displacement curves for 50mm gauge length, 12mmx5mm wire specimens predicted by the simulations with varying ductile model parameter combinations.

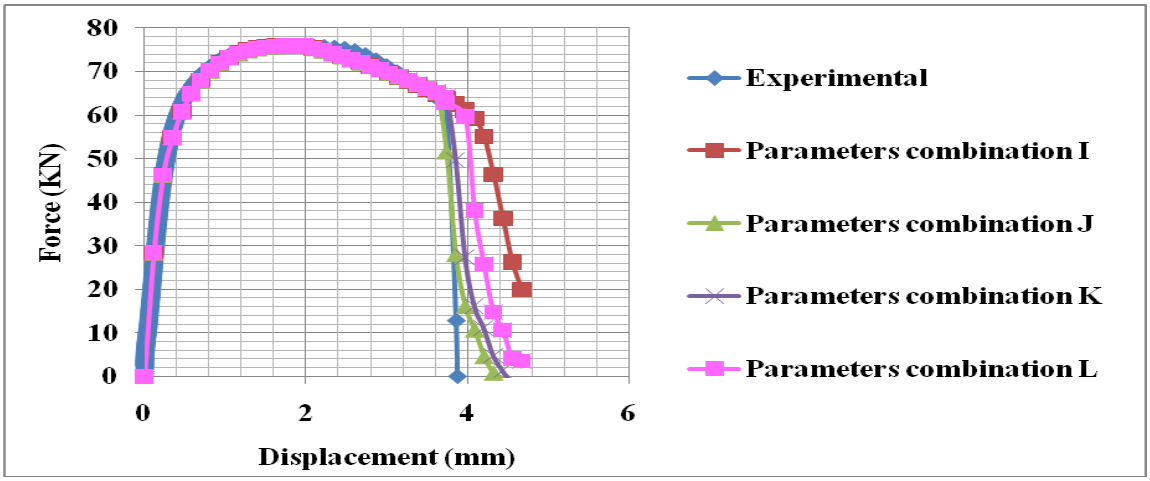

Figure 6.11: Force-displacement curves for 50mm gauge length, 12mmx5mm wire specimens from the simulations with varying porous metal plasticity model parameter combinations.

The fracture loads in Tables 6.5 were estimated as the load values at the point on the force-displacement curves beyond which pop-in (sudden increase in displacement and sudden drop in force) occurs as typically shown in Figures 6.12 for the curves predicted by the simulations with shear damage parameter combinations A. The fracture points and the fracture shapes predicted by the simulations with the shear parameters combination B, ductile parameter combination F and porous metal plasticity parameters combination L which are the closest to the experimental fracture point are shown in Figures 6.13 and 6.14 respectively.

The small percentage difference between the experimental fracture load and the fracture loads predicted by the simulations with shear failure parameters combination B, ductile failure parameters combination F and porous metal plasticity failure parameters combination L as shown in Table 6.6 indicates that the three fracture models can be used to predict the tensile properties/behaviors of the tensile armour wires accurately up to the fracture point. However, a comparison of the fracture shapes in Figure 6.14 predicted by the three damage and fracture criteria with the experimental fracture shape shows that only the shear failure criterion predicted a cup and cone fracture, which is the fracture shape displayed by the fractured laboratory specimen as shown in Figure 6.14(e).

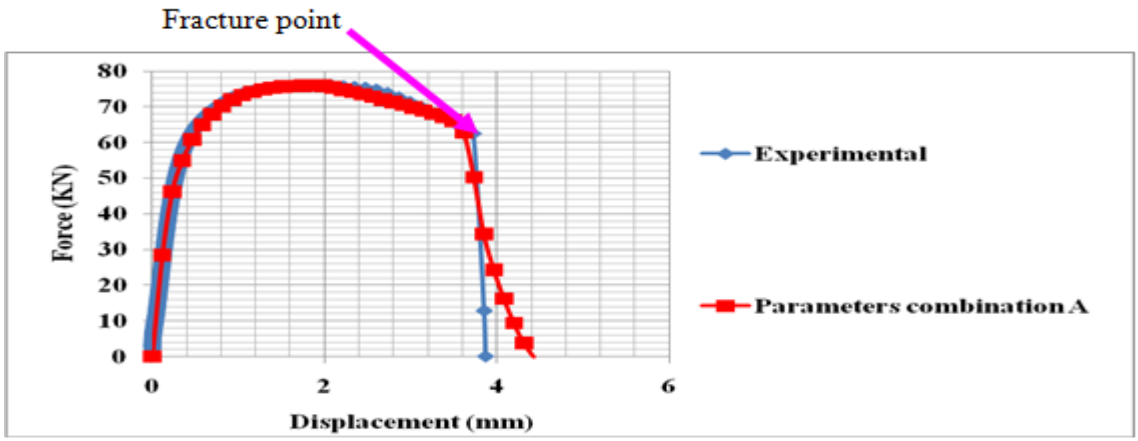

Figure 6.12: Fracture point for 50mm gauge length, 12mmx5mm wire specimen predicted by the simulation with shear damage parameters combination A.

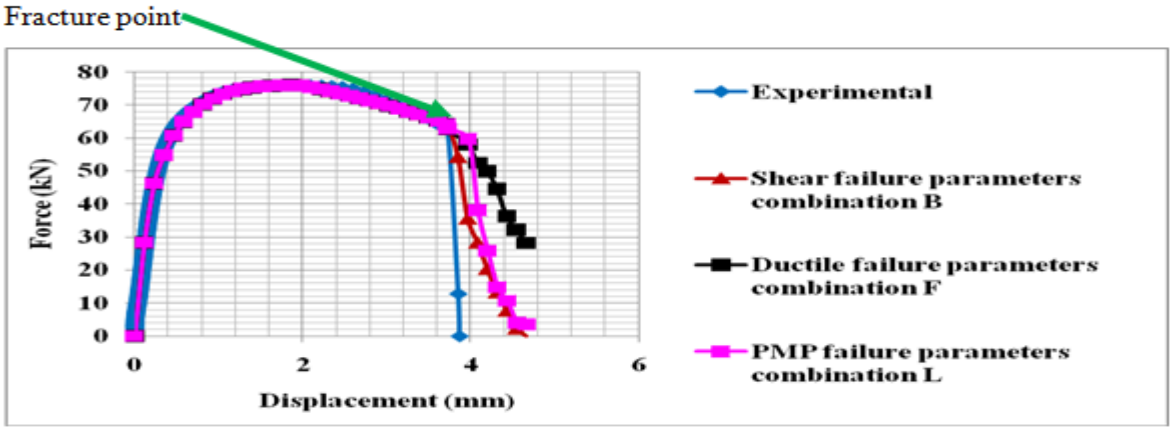

Figure 6.13: Force-displacement curves predicted by simulation with shear, ductile and porous metal plasticity failure models for 50mm gauge length, 12mmx5mm wire specimen.

Table 6.6: Experimental and FE with damage for ductile metals parameters combination and fracture points

	Fracture load (kN)	Percentage difference
Experimental	62.55	N/A
Shear failure parameters combination B	62.95	0.64
Ductile failure parameters combination F	62.62	0.12
Porous metal plasticity failure parameters combination L	62.85	0.48

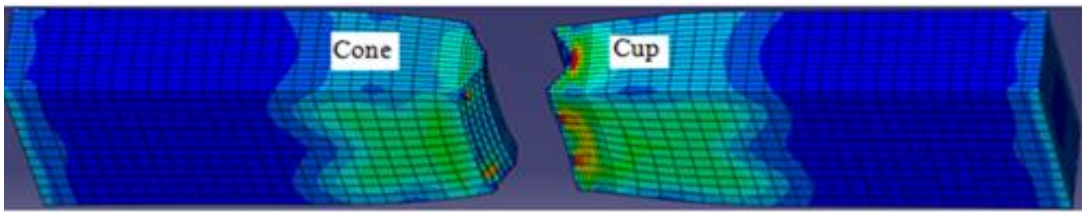

(a) Fracture shape predicted by simulation with shear failure model

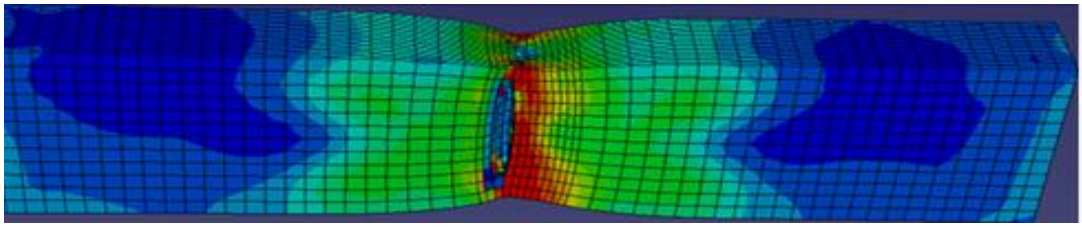

(b) Fracture shape predicted by simulation with ductile failure model

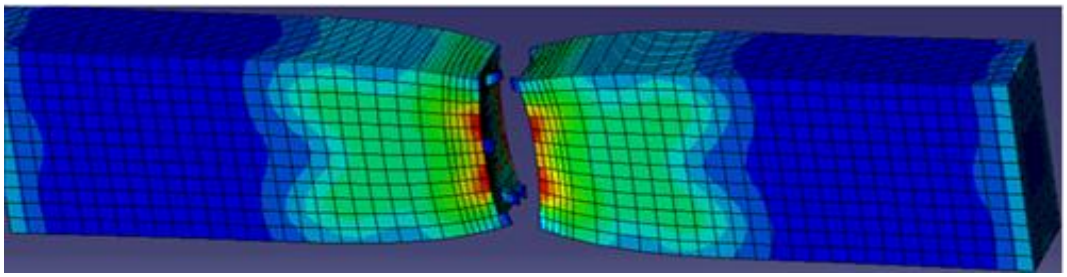

(c) Fracture shape predicted by simulation with ductile failure model with a larger displacement value.

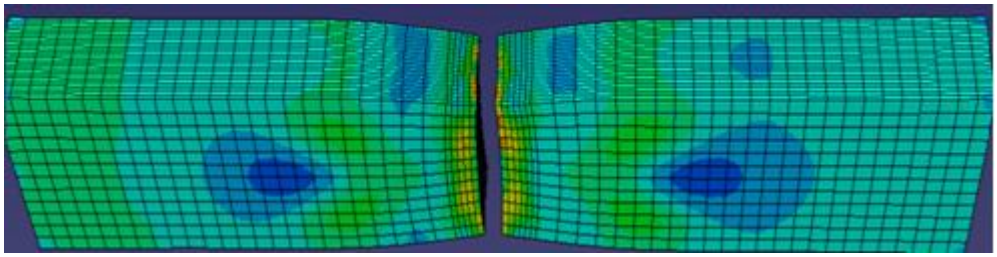

(d) Fracture shape predicted by simulation with porous metal plasticity failure model

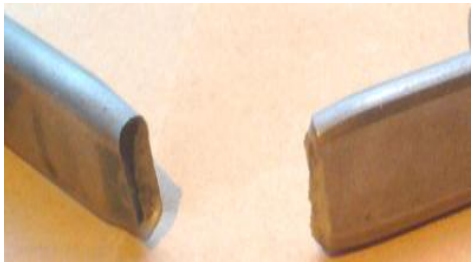

(e) Fractured specimen from experiment

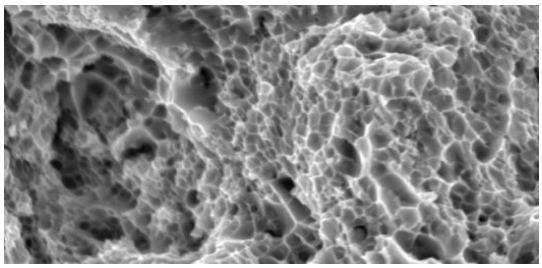

(f) Micrograph of fractured surface of wire

Figure 6.14: Fractured specimen from FE simulations with shear, ductile and porous metal plasticity failure models.

Since the shape of the fractured specimen predicted by the simulation with the shear damage and fracture model agrees best with the fractured mode displayed by the fractured specimen obtained from the laboratory experiment, it can be concluded that the shear failure mechanism is the appropriate failure mechanism for the tensile armour wires and the shear failure parameter combination B represents an appropriate parameter combination to predict the shear failure of the tensile armour wires. Consequently, subsequent simulations were carried out with the shear failure parameters combination B.

6.2.4 Percentage reduction in area from laboratory and numerical tensile testing

The reduction in area of the tensile armour wire predicted by the simulation of the tensile testing of the as-received wire was calculated from the reductions in the thickness and width of the middle of the specimen after fracture. The reduction in thickness was calculated from the vertical displacements of the upper and the lower nodes, and the reduction in width was calculated from the lateral displacements of the face and the back nodes shown in figures 6.15. The reductions in the thickness and the width of the fractured experimental specimen are shown in Figure 6.15(c).

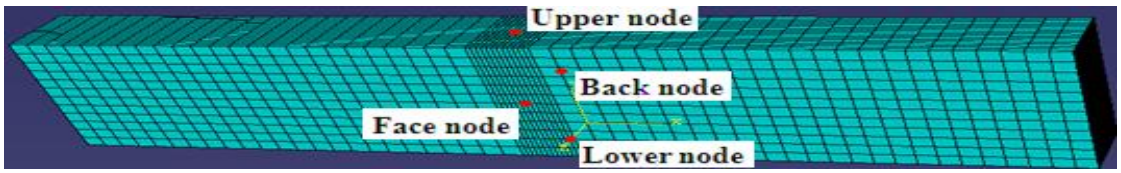

(a) Locations of nodes before tensile testing simulation

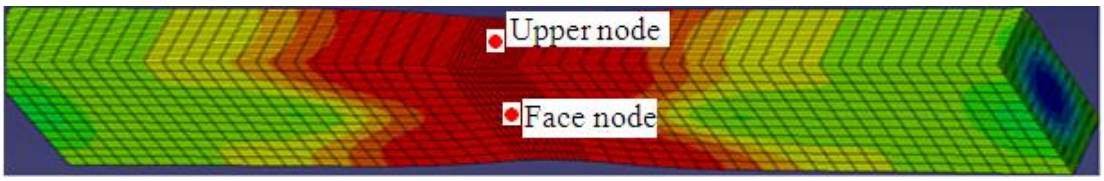

(b) Locations of nodes before during necking

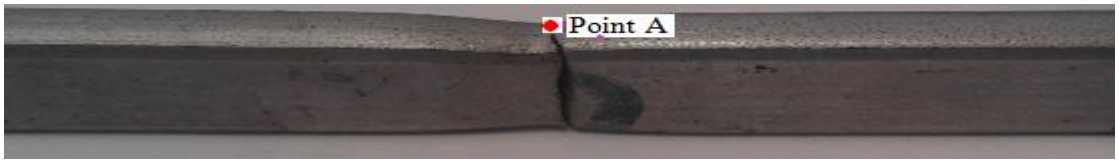

(c) Reduction in thickness and width of fractured experimental specimen

Figure 6.15: Locations of nodes used to calculate reduction in area at various stages of tensile testing simulation.

The vertical displacement profiles of the upper and the lower nodes, and the lateral displacement profiles of the face and the back nodes throughout the tensile testing simulation are shown in Figure 6.16 (a) and (b) respectively. As shown in Figure 6.16 (a), the downward vertical displacement of the upper node and the upward vertical displacement of the lower node increased up to the fracture initiation point at an applied displacement of 2.68mm, and remained relatively constant throughout the fracturing stage of the simulation. Similarly, as shown in Figure 6.16 (b), the lateral displacements of the face node and the back node increased up to the fracture initiation point at an applied displacement of 2.68mm and remained relatively constant throughout the fracturing stage of the simulation.

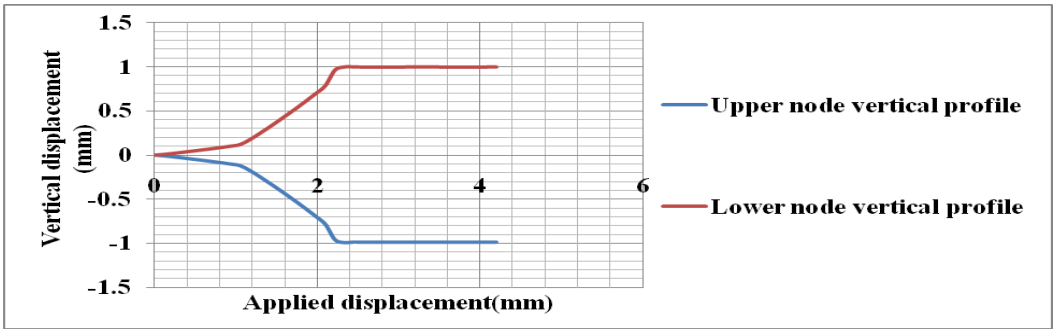

(a) Vertical displacement profiles of the upper and the lower nodes

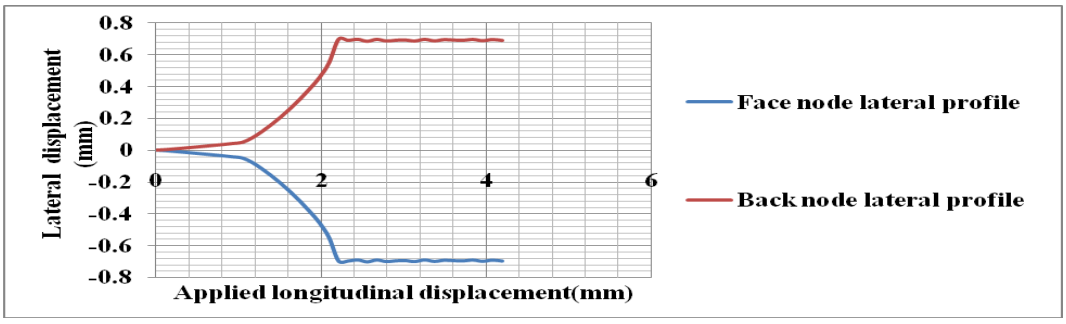

(b) Lateral displacement profiles of the face and the back nodes

Figure 6.16: Vertical and lateral displacement profiles of nodes used for reduction in area calculation

The addition of the vertical displacements of the upper and the lower nodes, and the addition of the lateral displacements of the face and the back nodes represent the reduction in the thickness and the reduction in the width of the wire specimen respectively. The reduced thickness of the wire after fracture is calculated in equation 6.1 as the difference between the

original thickness (5mm) and the reduction in thickness at step time 0.475s. Similarly, the reduced width of the wire after fracture is calculated in equation 6.2 as the difference between the original width (12mm) and the reduction in width at step time 0.475s. The reduced area after fracture and the percentage reduction in area are calculated in equations 6.3 and 6.4 respectively.

The reduced thickness after fracture = $5-(0.70+0.70)=3.60mm$ 6.1

The reduced width after fracture = $12-(0.96+0.96)=10.08mm$ 6.2

The reduced area after fracture = $10.08x3.60=36.33mm^2$ 6.3

The percentage reduction in area = $((60-36.33)/60)x100=39.45\%$ 6.4

The reduced width and reduced thickness of the fractured experimental specimen measured at point A are 9.96mm and 3.80mm respectively, leaving the fractured experimental specimen with a reduced area of 37.84mm^2 at its middle, which gives a percentage reduction in area of 36.92%. This percentage reduction in area compares well with the percentage reduced in area of 39.45% obtained from the FE with 2.53% difference between the percentage reduced in area obtained from the experiment and FE. This difference could be due to experimental errors which arise from the measurement of the reduced thickness and width of the experimental specimen.

At this stage, a suitable virtual testing/numerical experiment test method for testing the as-received wires has been developed. This involves the 3D modelling of the tensile armour wire with the simplified rectangular shape meshed with a 1mmx1mmx1mm global element size and refined at the centre with 0.25mmx0.25mmx1mm elements, and carrying out the simulation with an absolute yield stress and shear failure criterion. The investigations of the effects of channel shaped scratches, V-shaped scratches and dents are presented in Chapters 7, 8 and 9 respectively.

Chapter 7 Effects of miniature channel shaped scratches on tensile properties of tensile armour wires

Scratches are one of the surface defect types that BS EN ISO13628-2, (2006) recommends should be looked out for and which was identified from the SEM image of the surface of the as-received tensile armour wires. The scratches considered in this chapter have a flat bottom as shown in the SEM image in Figure 7.1(a) and are hereinafter referred to as grooves, channel shaped scratches or simply as channels. Grooves with dimensions around the 0.2mm detection capability of the online eddy current detection systems used by the flexible pipe manufacturing industry as well as grooves with depth up to 1mm were considered. The effects of these miniature channel shaped scratches on the tensile properties of tensile armour wires were investigated using both laboratory and numerical tensile testing experiments.

The details of the laboratory tensile testing of the as-received wire specimens and the wire specimens with a large engineered groove/channel shaped cut are presented in section 7.1. The FEA simulations of the tensile testing of the as-received wire specimens and the wire specimens with an engineered channel shaped cut are presented in sections 7.2 and 7.3 respectively. The mesh convergence to determine the appropriate finite element sizes is presented in section 7.4. The effects of the across-the-thickness and the across-the-width miniature groove on the tensile properties of the tensile armour wires are presented in section 7.5, and the effects of the mid-thickness g, mid-width and an edge grooves are presented in section 7.6. The effects of the channel dimensions on the tensile properties of the tensile armour wire and the summary of the effects of the channel shaped scratches on the tensile properties of the tensile armour wire are presented in sections 7.7 and 7.8 respectively.

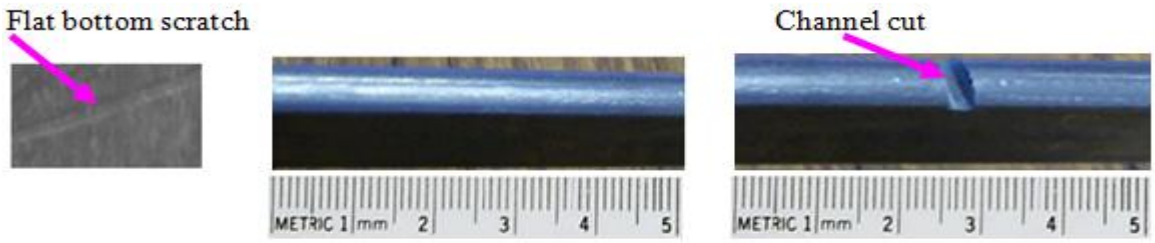

(a) SEM image (b) As-received wire specimen (c) Wire specimen with a channel cut

Figure 7.1: As-received wire specimen and wire specimen with groove/channel cut

7.1: Laboratory tensile testing of as-received wire specimens and wire specimens with groove/channel shaped scratches

Laboratory tensile tests were carried out on 50mm long as-received tensile armour wire specimens with 12mm X 7mm cross sectional dimensions shown in Figures 7.1 (b) and on tensile armour wire specimens from the same wire length as the as-received wire with 2mm wide by 2mm deep groove/channel cut shown in Figures 7.1(c). The 2mm wide by 2mm deep groove/channel cut was made on the wire specimens to ensure that the engineered defects is substantially larger than any inherent defects in the wire for its effect to be dominant on the tensile behaviour, as it was observed that failure occurred not at the locations of the engineered defects in some test specimens with engineered defects that were relatively larger than the inherent defects in the wire. The substantially larger engineered channel cut is also practically easier to make. Most importantly, the channel could have been of any other dimension, as the aim of cutting the channel out of the specimen was basically to have the laboratory data to validate the simulation of the tensile testing of wire with an engineered channel shaped defect.

The force-displacement curves and the engineering stress-strain curves obtained from the laboratory tensile testing of the as-received wire specimens and the wire specimens with engineered 2mm wide by 2mm deep groove/channel are shown in Figure 7.2 (a) and (b) respectively. The engineering stress for the wire with 2mm wide by 2mm deep channel was obtained by dividing the load in the wire by the cross-section area at the notch ($70mm^2$).

From Figure 7.2(a), the ultimate load and the fracture displacement of the as-received wire are 68.25kN and 8.81mm respectively while the ultimate load and the displacement at fracture of the wire with a 2mm x 2mm are 57.99kN and 2.51mm respectively. The 2mm wide by 2mm deep groove/channel has reduced the ultimate load and the fracture displacement of the wire by 15.03% and 71.54% respectively. This result agrees with what is reported by Kossakowski, (2010). Conversely, the introduction of the 2mm wide by 2mm deep channel into the specimen has increased the offset yield and ultimate strengths of the wire from 520MPa to 600Mpa and 810MPa to 830MPa respectively. The introduction of the 2mm wide by 2mm deep channel into the specimen also reduced the fracture strain of the wire from 17.60% to 4%. This result agrees with what is reported by Bayram et al, (1999) and the increase in the yield and ultimate strengths of the notched wire is due to notch

strengthening, which occurs due to the effect of constraint in the notched specimen as stated by Dieter, (1998) and Bayram et al, (1999).

The reduction in the ultimate load of the wire can be attributed to the reduction in the gross cross sectional area of the specimen leading to a reduction in the load crying capacity of the wire. Similarly, the reduction in the displacement at fracture or the fracture strain, and invariably, the ductility of the wire, can be attributed to the entire phenomenon associated with the presence of notch in a structure which promotes brittle fracture as discussed in section 2.4.2.

In practical terms, the reduction in the yield load of the tensile armour wire would cause a reduction in the amount of axial load flexible flowlines and risers can carry before being plastically or permanently deformed (yielding). Also, the reduction in the maximum load of the tensile armour wire would lead to the reduction in the maximum load flexible pipe (flowlines and risers) can carry. These reductions could have a significant effect on the integrity of flexible flowlines and flexible risers, particularly flexible risers, where the weight of the riser and its content is carried by the tensile armour wires. Furthermore, for both flowlines and risers without pressure armour, where the tensile armour wire is meant to resist the internal pressure load, the reduction in the yield and ultimate loads of the wire would reduce the amount of the internal pressure flowlines and risers can carry. The reduction in the fracture strain or the displacement at fracture of the tensile armour wire would reduce the ductility of the wire and consequently reduce the extent to which flexible flowlines and risers can be stretched. The reduction in the ductility of the tensile armour wire can cause flexible riser and flowlines to fail during installation, when they experience the highest straining as stated by Bai and Bai, (2005).

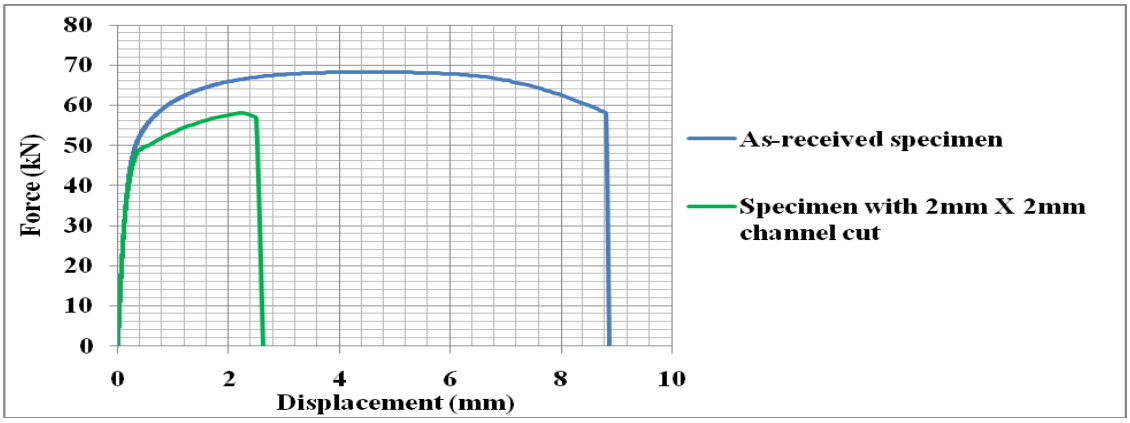

(a) Force-displacement curves

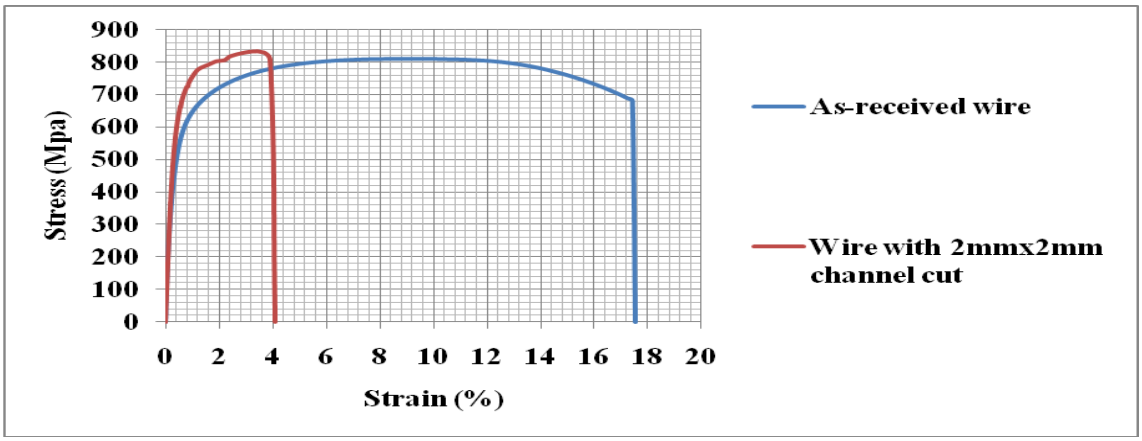

(b) Engineering stress-strain curves

Figure 7.2: Force-displacement and engineering stress-strain curves from laboratory tensile testing of 50mm gauge length, 12mmx7mm as-received wire and wire specimen with groove.

7.2 FEA tensile testing simulation of as-received wire specimen

The FE tensile testing simulation was carried out by modelling a 50mm long, 12mm X 7mm cross-sectional area full size wire specimen meshed with 1mm C3D8R (8-node hexahedral linear brick reduced integration elements with hourglass control) elements as shown in Figure 7.3. The mesh at the middle of the specimen was refined with 0.25mm elements. The left hand end of the specimen was fixed while the right hand end, which is free to move only in the direction of the tensile load, was subjected to a longitudinal displacement as shown in Figure 7.3.

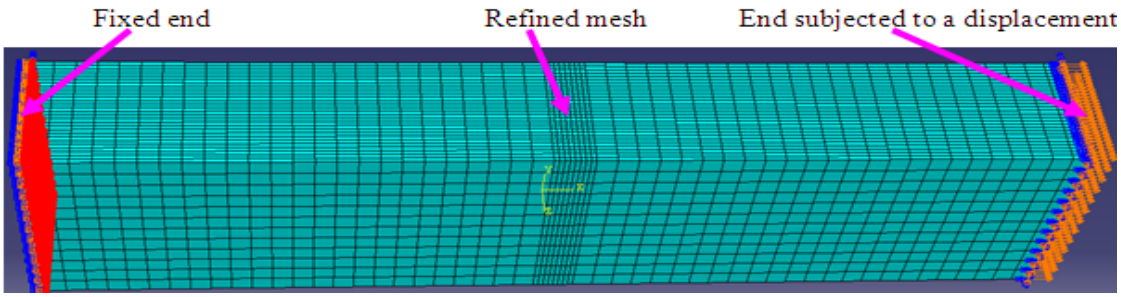

Figure 7.3: Meshed full size model of as-received wire with ends boundary conditions.

The material input data used for the simulation consists of true yield stress and true plastic strain calculated for all the experimental data points from the nominal absolute yield stress of 358.4MPa at 30.11kN force to the nominal ultimate tensile strength of 809.7MPa at 68.02kN. This was combined with fracture strain, shear stress ratio and strain rate of 0.3589, 13 and 0.00013 respectively being the appropriate shear damage and failure parameters obtained by numerical optimisation. The FEA predicted stress distributions and deformed shapes during necking at an applied displacement of 3.68mm, fracture initiation at an applied displacement of 5.93mm and the completely fractured specimen at an applied displacement of 6.75mm are shown in Figures 7.4 (a), (b) and (c) respectively.The FEA predicted a cup and cone failure which is the same as the failure mode exhibited by the wire tested in the laboratory as shown in Figure 7.4(d).

The force-displacement curves obtained from experimental and FEA tensile testing of the as-recieved wire specimens are shown in Figure 7.5. Both curves agree well up to the ultimate load with 0.053% difference between experimental and FE predicted ultimate loads as shown in Table 7.1. Beyound the ultimate load point, which is the point at which the extensometer was removed, the force values also agrees well with 2.552% difference between experimental and FE predicted fracture loads as shown in Table 7.1. The large percentage difference (31.846%) between the experimental and FE predicted fracture displacement was because the experimental displacement values after the ultimate load point are crosshead displacement values. The experimental curve with corrected displacement gives a better agreements with the FE curve as shown in Figure 7.5. Technically, the FE curve displacement values are the actual displacements within the 50mm gauge length wire specimen alone and the FE curve therefore represents the actual tensile armour wire tensile behaviour.

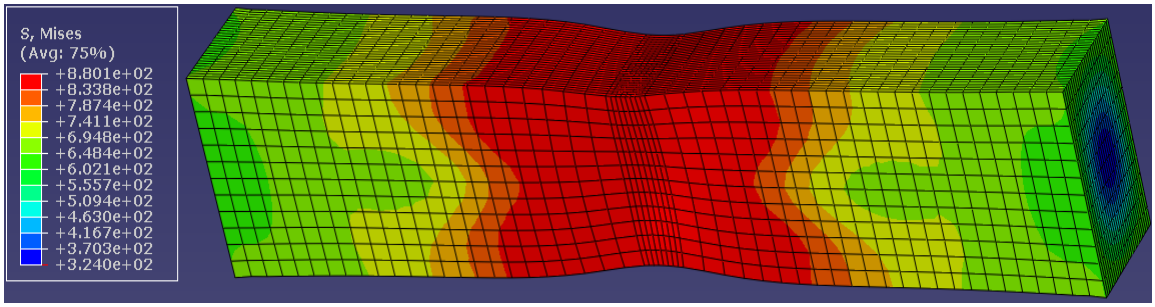

(a) During necking at an applied displacement of 3.68mm (67.97kN load).

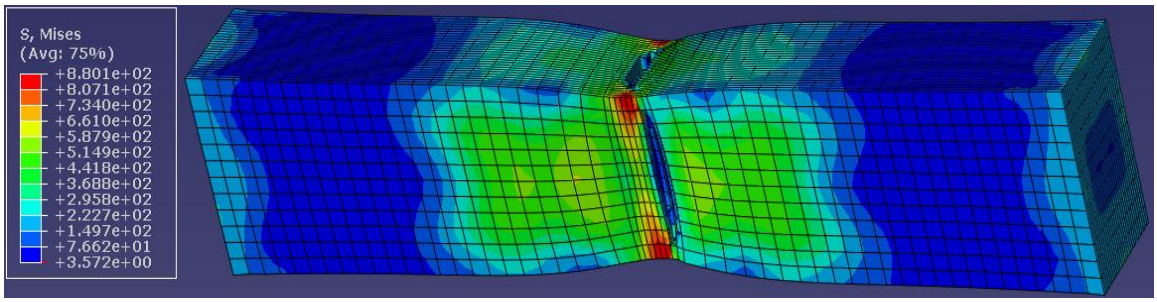

(b) During fracture initition at an applied displacement of 5.93mm (58.56kN load).

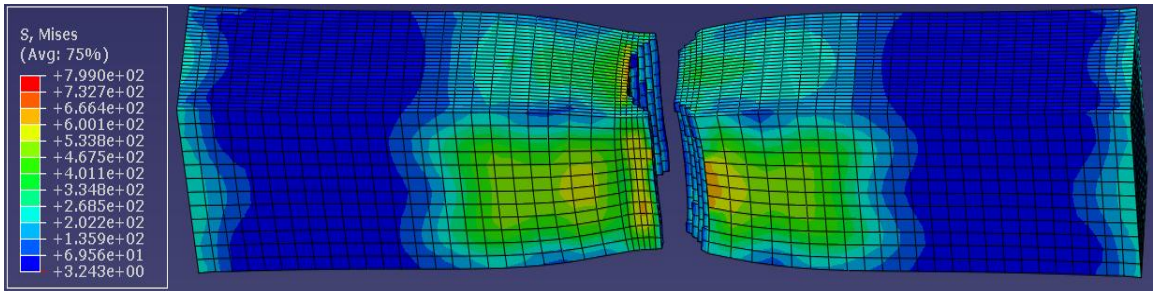

(c) Completely farctured wire specimen at an applied displacement of 6.75mm (0kN load)

(d) Fractured wire specimen from laboratory tensile testing

Figure 7.4: Mises stress (MPa) distribution and deformed shapes of wire specimen at various stages of tensile testing simulation.

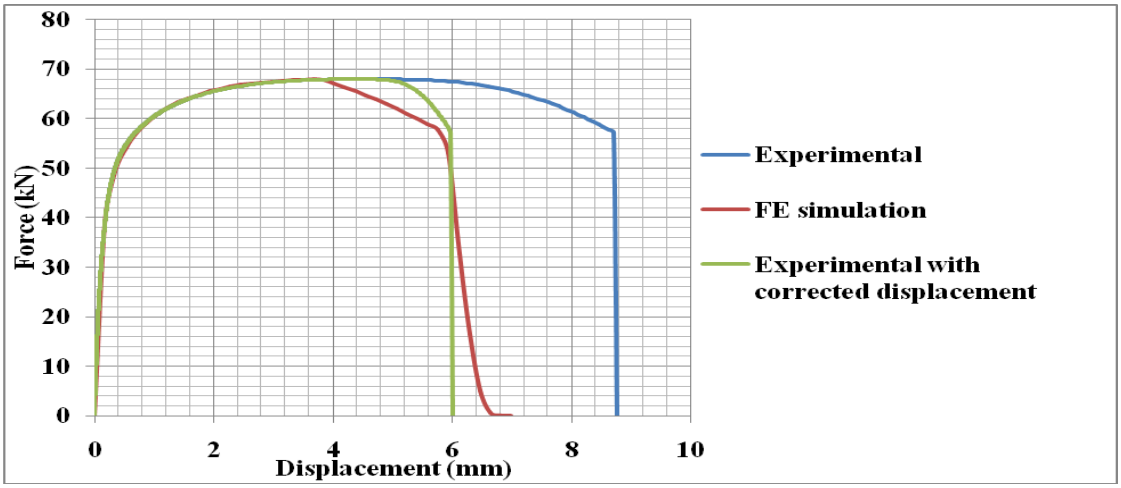

Figure 7.5: Force-displacement curves from laboratory and FEA tensile testing of 12mmx7mm as-received wire specimens with 50mm gauge length.

Table 7.1: Experimental and FE predicted mechanical parameters for as-received wire specimen

	Experiment	FE simulation	Percentage difference
Ultimate load (kN)	68.01	67.97	0.053
Fracture load (kN)	57.11	58.56	2.552
Displacement at fracture point (mm)	8.71	5.933	31.85
Percentage reduction in area	40.85	41.25	0.9%

7.3 FEA tensile testing simulation of wire specimen with a channel shaped scratch

The full size model of a tensile armour wire tensile test specimen with a groove shown in Figure 7.6 was obtained by cutting a 2mm wide and 2mm deep channel out of the as-received wires model shown in Figure 7.3. The model with the same end boundary conditions as the model of the as-received wire in Figure 7.3 was also meshed with 1mm C3D8R elements as shown in Figure 7.6.

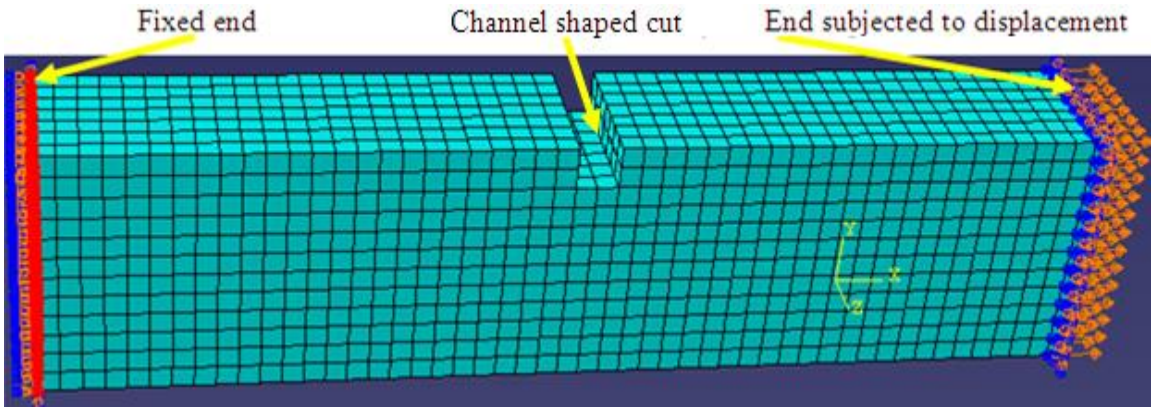

Figure 7.6: Meshed full size model of wire with channel cut showing ends boundary conditions.

The deformed shapes and the stress distributions at an applied displacement of 0.15mm and the predicted fracture shape of the wire specimen with 2mm wide by 2mm deep groove at an applied displacement of 3.25mm are shown in Figures 7.7 (a) and (b) respectively. From Figure 7.7 (a), the stress around the channel is higher than the stresses at all other sections of the specimen. This is due to the stress concentration effect of the groove.

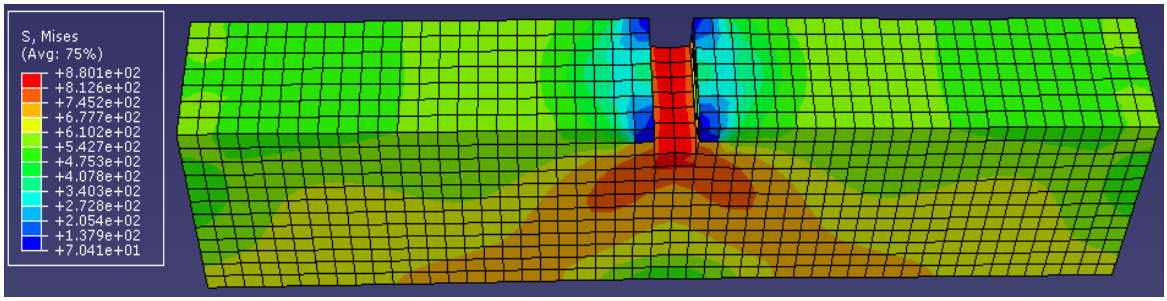

(a) Deformed shape at an applied displacement of 0.15mm

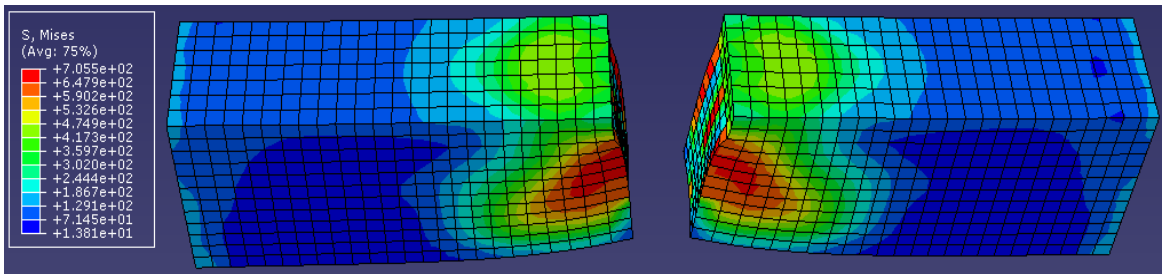

(b) Completely fractured specimen at an applied displacement of 3.25mm

Figure 7.7: Mises stress (MPa) distribution and deformed shape predicted by tensile testing simulations of wire specimen with groove.

The accuracy of the FE simulation was validated by comparing the force-displacement curve predicted by the FE simulation with the force-displacement curve obtained from the laboratory tensile testing of wire specimens with a 2mm x 2mm groove/channel cut as shown in Figure 7.8. The FEA predicted curve agrees well with the experimental curve up to the point at which the extensometer was removed. The FEA predicted maximum load and fracture load are very close to the experimental value with negligible percentage difference as shown in Table 7.2. The large percentage difference between the values of the FEA predicted and the laboratory experimental displacements at fracture in Table 7.2 is due to the fact that the experimental displacement values beyond the ultimate load point are crosshead displacement values. Figure 7.8 shows the difference between the experimental curve with the crosshead displacement and the experimental curve with the corrected displacement. The experimental curve with the corrected displacement agress more with the Fe curve as shown in Figure 7.8. Consequently, the experimental curve with the corrected displacement was used for the validation of the results of the subsequent simulations.

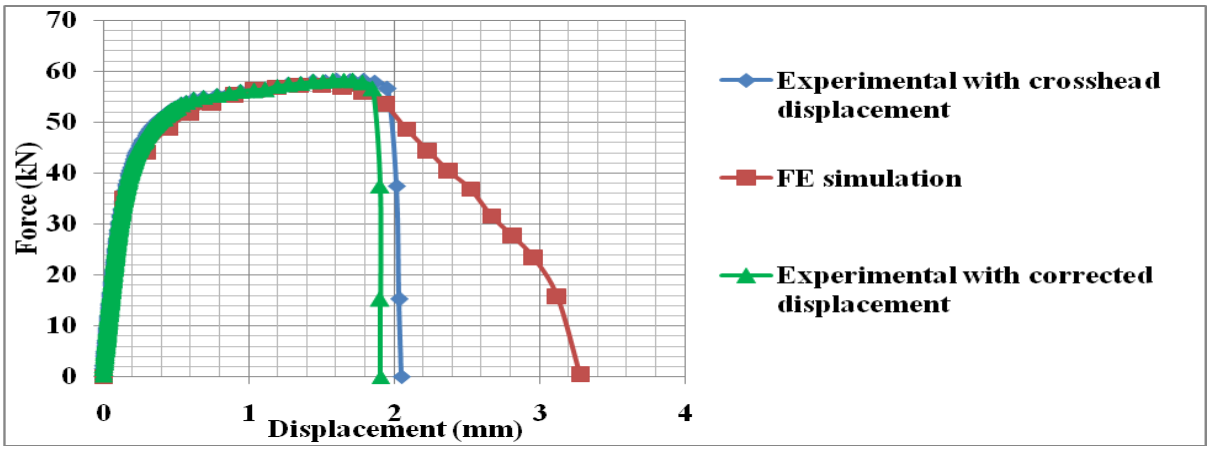

Figure 7.8: Experimental and FE predicted curves for 12mmx7mm wire specimens with a channel shaped cut and 50mm gauge length.

Table 7.2: Experimental and FE predicted mechanical parameters for wire specimen with a groove

	Experiment	FE simulation	Percentage difference
Ultimate load (kN)	57.99	57.75	0.416
Fracture load (kN)	56.65	55.71	1.659
Displacement at fracture point (mm)	2.51	1.80	28.23

7.4 Mesh convergence

To capture the rapid stress gradient in the area around the channel with amplified stress identified in Figure 7.7 (a) accurately and to obtain the optimum mesh density for the FE simulation, the mesh around the channel was successively refined. The deformed shapes showing the elastic Mises stress and the zero equivalent plastic strain distributions at an applied displacement of 0.02mm for the simulations conducted with 1mm, 0.5mm and 0.25mm elements around the channel are shown in Figures 7.9(a) to (c) and 7.10(a) to (c) respectively. The deformed shapes at the beginning of the plastic deformation showing the Mises stress and the equivalent plastic strain distributions at an applied displacement of 0.05mm for the simulations conducted with 1mm, 0.5mm and 0.25mm elements around the channel are shown in Figures 7.11(a) to (c) and 7.12(a) to (c). The equivalent plastic strain in the wire specimens in Figure 7.10 is zero because the maximum Mises stress in the specimens at an applied displacement of 0.02mm as shown in Figure 7.9 is less than the 359.2MPa absolute yield strength of the wire. This implies that the stress in the wire specimen at an applied displacement of 0.02mm merely stretched the atomic and molecular bonds of the wire and was not sufficient to break the metallic bond in order for slip to occur as explained by Askeland and Phule, (2006) and Dieter, (1998). Consequently, when the stress/applied load is removed at this stage of the tensile testing simulation, the wire will return to its original shape as no plastic deformation has occurred.

As shown in Figure 7.12, the plastic deformation of the wire specimen begins at an applied displacement of 0.05mm because the Mises stress in the wire specimens as shown in Figure7.11 is greater than the 359.2MPa absolute yield stress of the wire. This implies that the stress in the wire specimen at an applied displacement of 0.05mm has sufficiently broken the atomic/molecular bonds between the atoms/molecules of the wire and slip on the active slip plane has occurred leading to the plastic deformation of the wire as explained by Askeland and Phule, (2006) and Dieter, (1998).

The fracture shapes of the wire showing the Mises stress and the equivalent plastic strain distributions at the applied displacements shown in the Figures for the simulations conducted with 1mm, 0.5mm and 0.25mm elements around the channel are shown in Figures 7.13 and 7.14 respectively. This implies that at the applied displacements shown in Figures 7.4, the strain in the wire specimen is greater than the 4% fracture strain obtained for the notched wire

experimentally, leading to void nucleation, growth and ductile crack propagation as explained by Askeland and Phule, (2006) and Dieter, (1998). Further refinement of the elements around the channel with 0.1mm elements was carried out with the full size model. However, the result could not be opened due to the limited computer resources (i.e. limited computer processor capacity).

To reduce the output file capacity for the simulation with 0.1mm elements around the channel, the simulation was carried out on a model with a half of the wire thickness (3.5mm) using the symmetry boundary condition in ABAQUS. The symmetry boundary condition allows half the specimen size to be modelled with the force values obtained multiplied by two to obtain the force values for the full specimen. The deformed shapes of the half wire models showing the Mises stress and the equivalent plastic strain distributions are shown in Figures 7.9(d) to 7.12(d) for the simulations carried out with 0.1mm elements around the channel.

Further refinement of the elements around the channel with 0.05mm elements was carried out with the half size model but the result could not also be opened due to the limited computer resources. Consequently, the simulations with the limiting 0.1mm elements around the channel were used to predict the tensile response of the tensile armour wire specimens with channel shaped cut. The force-displacement curves obtained from the FE 3D simulations with successive mesh refinement around the groove are shown in Figure 7.15. The variation in the mechanical properties and the variation in the amplified elastic Misers stress at the bottom corner of the channel predicted by the FE simulations with successive mesh refinement around the channel are presented in Table 7.3 and 7.4 respectively.

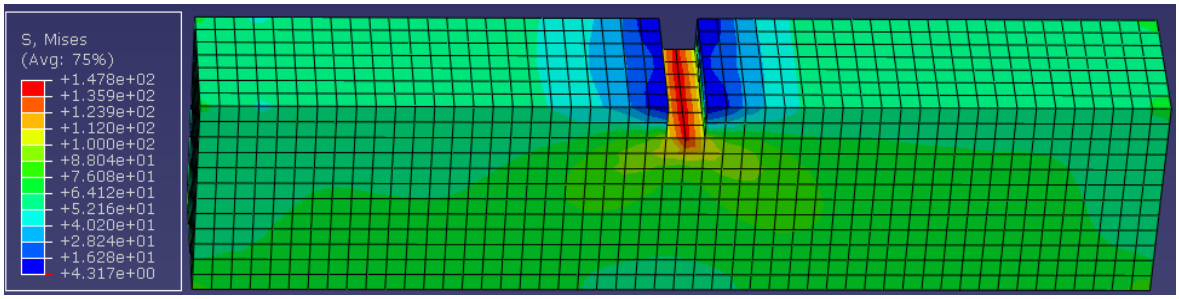

(a) Full wire size model having 1mm elements around the channel tip

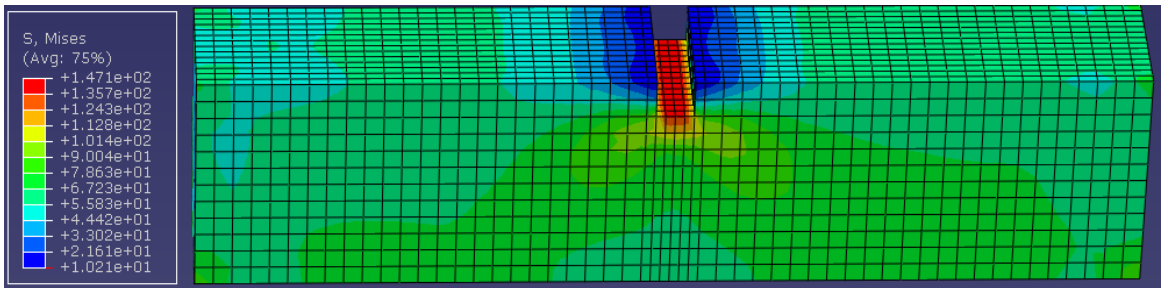

(b) Full wire size model having 0.5mm elements around the channel tip

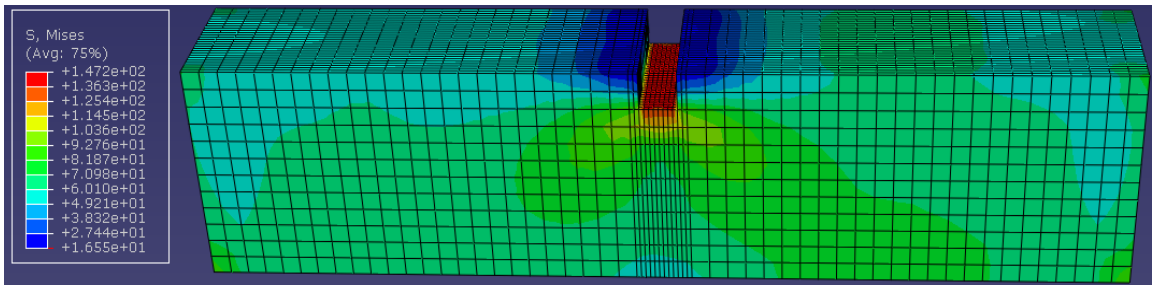

(c) Full wire size model having 0.25mm elements around the channel tip

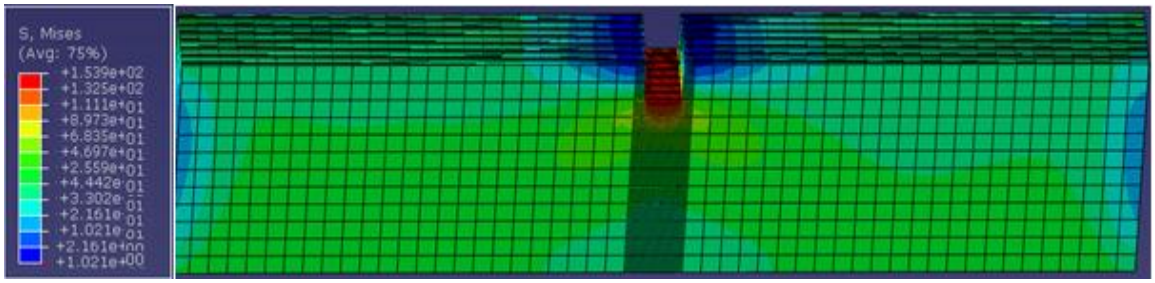

(d) Half wire size model having 1mm elements around the channel tip

Figure 7.9: Deformed shapes showing the Mises stress (MPa) at an applied displacement of 0.02mm predicted by simulations with successive mesh refinement around channel.

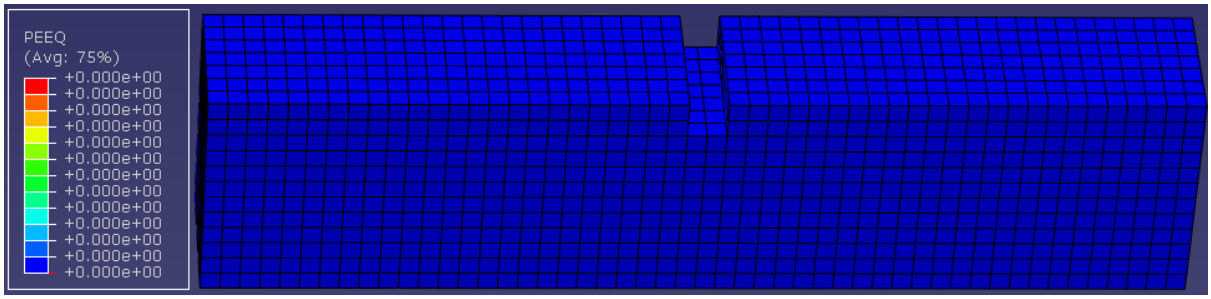

(a) Full wire size model having 1mm elements around the channel tip

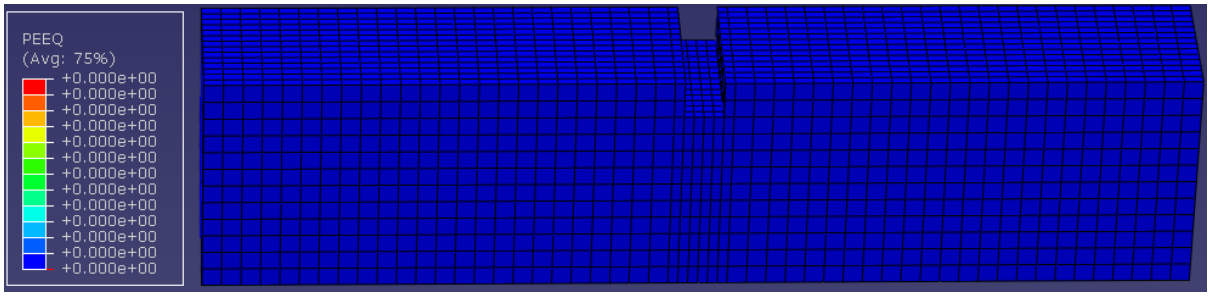

(b) Full wire size model having 0.5mm elements around the channel tip

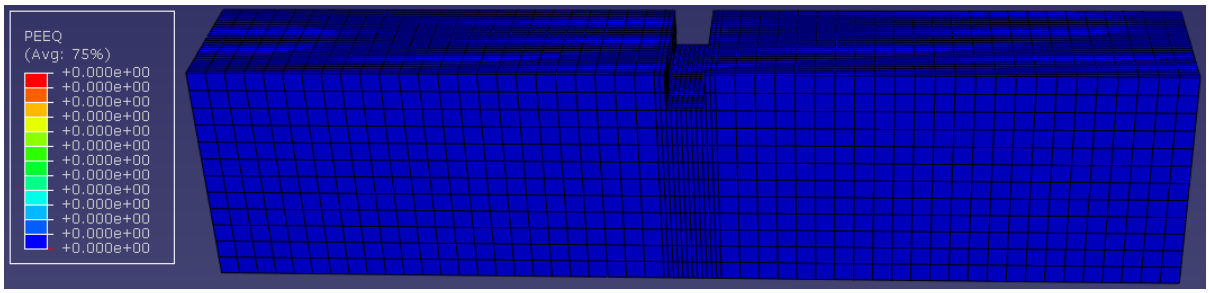

(c) Full wire size model having 0.25mm elements around the channel tip

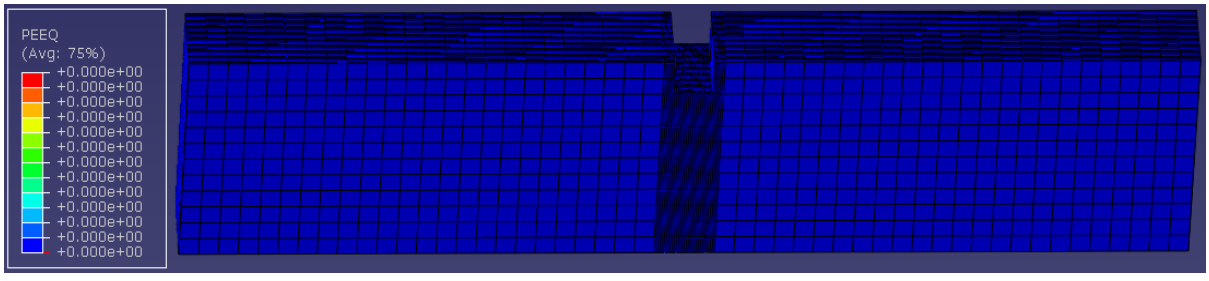

(d) Half wire size model having 1mm elements around the channel tip

Figure 7.10: Deformed shapes showing zero equivalent plastic strain (%) at an applied displacement of 0.02mm predicted by simulations with successive mesh refinement around the channel.

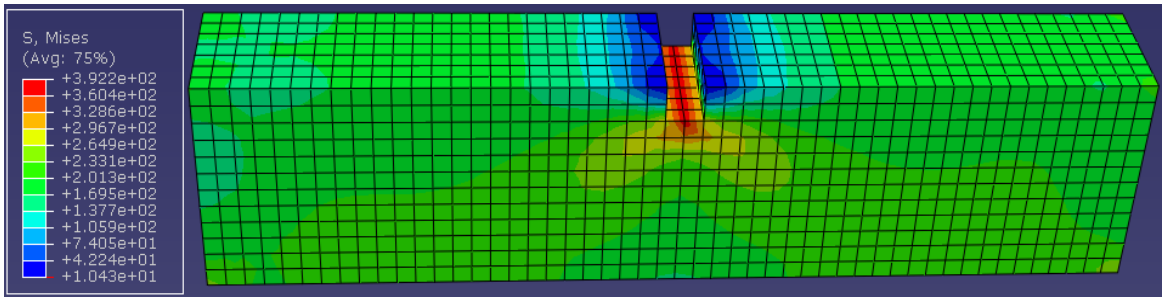

(a) Full wire size model having 1mm elements around the channel tip

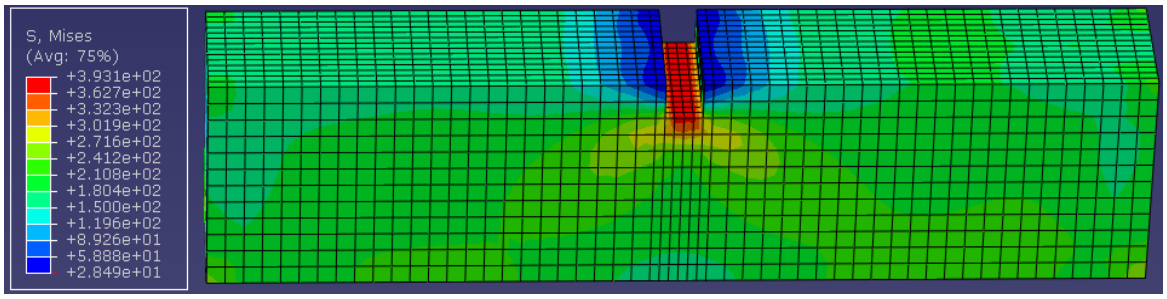

(b) Full wire size model having 0.5mm elements around the channel tip

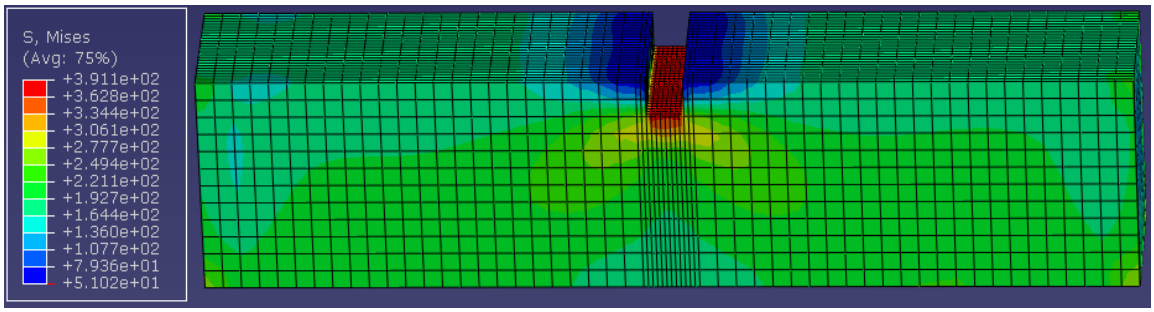

(c) Full wire size model having 0.25mm elements around the channel tip

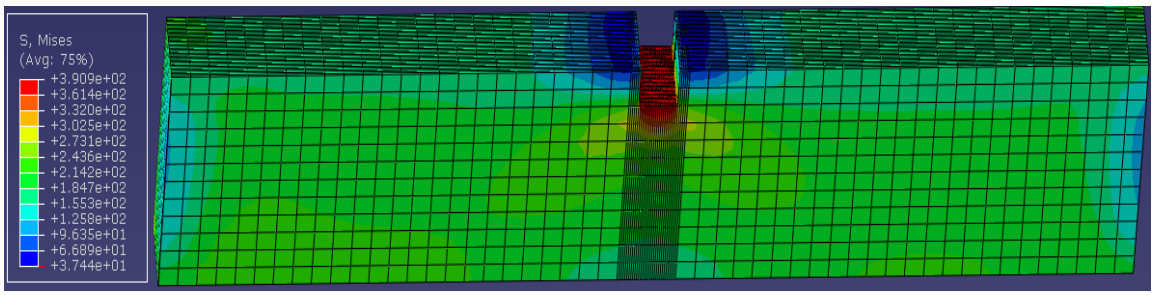

(d) Half wire size model having 1mm elements around the channel tip

Figure 7.11: Deformed shapes showing the Mises stress (MPa) at an applied displacement of 0.05mm predicted by simulations with successive mesh refinement around channel.

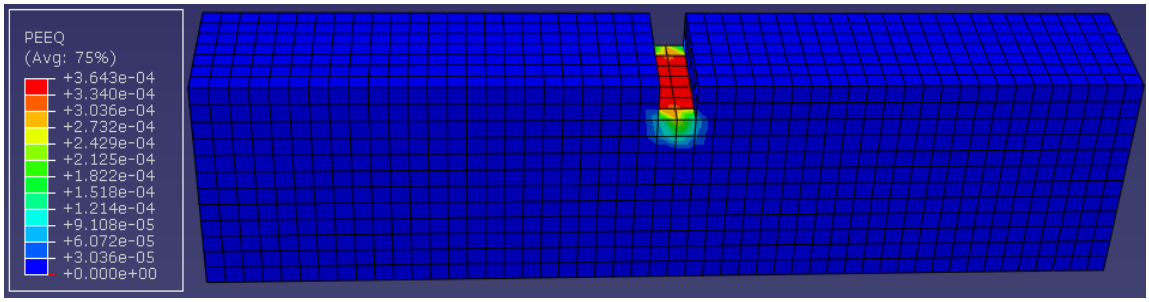

(a) Full wire size model having 1mm elements around the channel tip

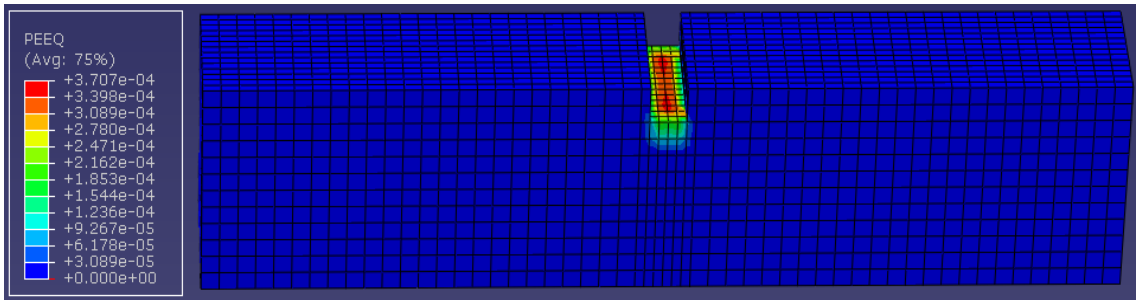

(b) Full wire size model having 0.5mm elements around the channel tip

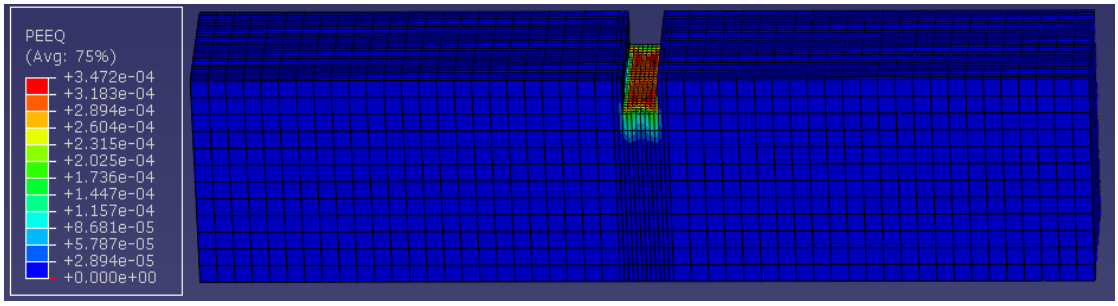

(c) Full wire size model having 0.25mm elements around the channel tip

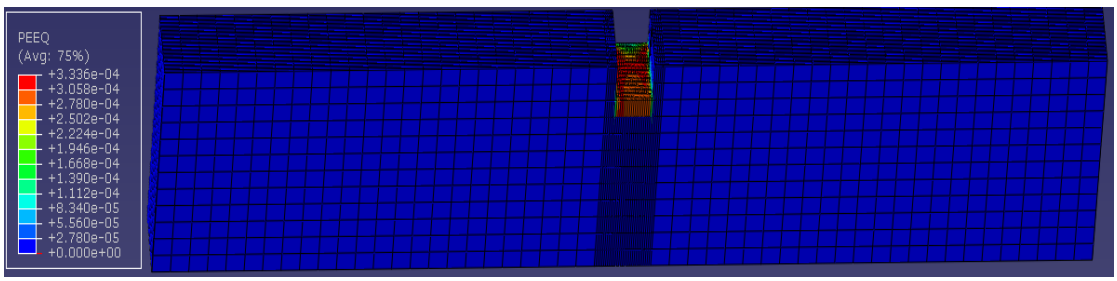

(d) Half wire size model having 1mm elements around the channel tip

Figure 7.12: Deformed shapes showing equivalent plastic strain (%) at an applied displacement of 0.05mm predicted by simulations with successive mesh refinement around the channel.

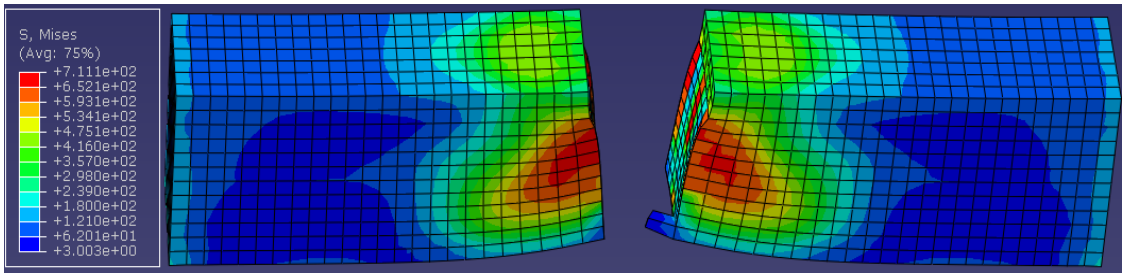

(a) Full wire size model with 1mm elements around the channel tip at an applied displacement of 1.80mm

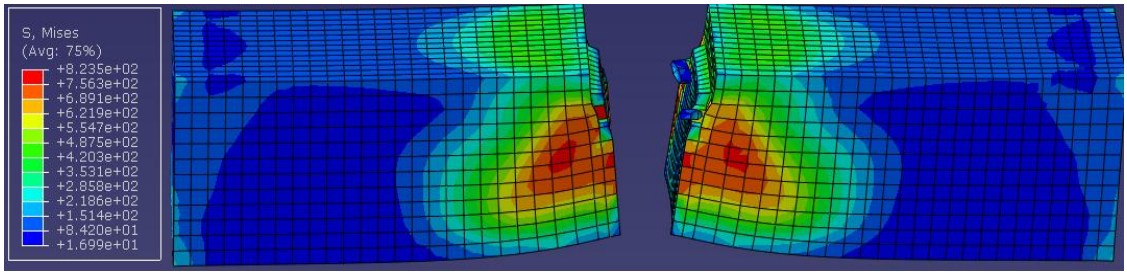

(b) Full wire size model with 0.5mm elements around the channel tip at an applied displacement of 1.65mm

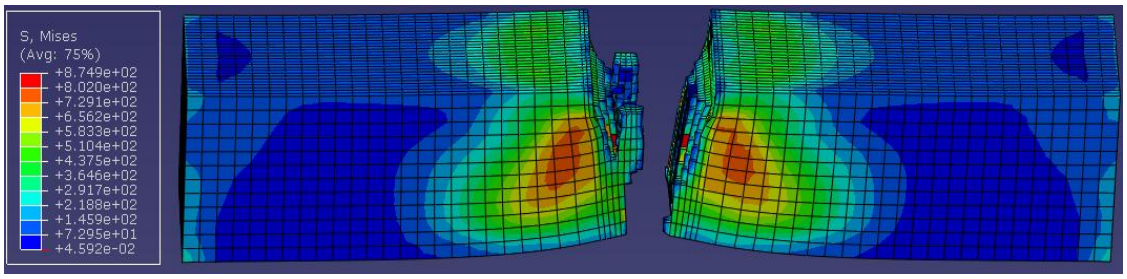

(c) Full wire size model with 0.25mm elements around the channel tip at an applied displacement of 1.64mm

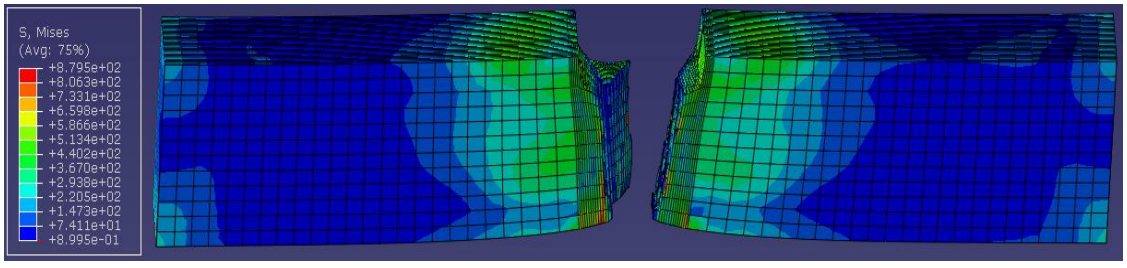

(d) Half wire size model with 0.1mm elements around the channel tip at an applied displacement of 1.64mm

Figure 7.13: Fracture shapes showing Mises stress (MPa) distributions and the fracture shapes from simulations with successive mesh refinement around the channel.

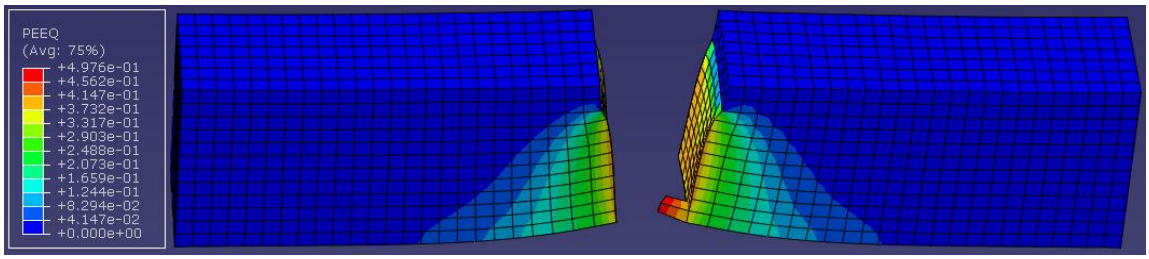

(a) Simulation with full wire size model having 1mm elements around the channel tip

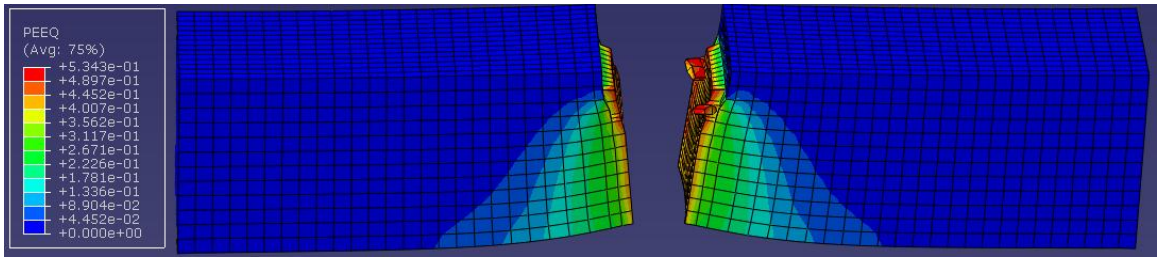

(b) Simulation with full wire size model having 0.5mm elements around the channel tip

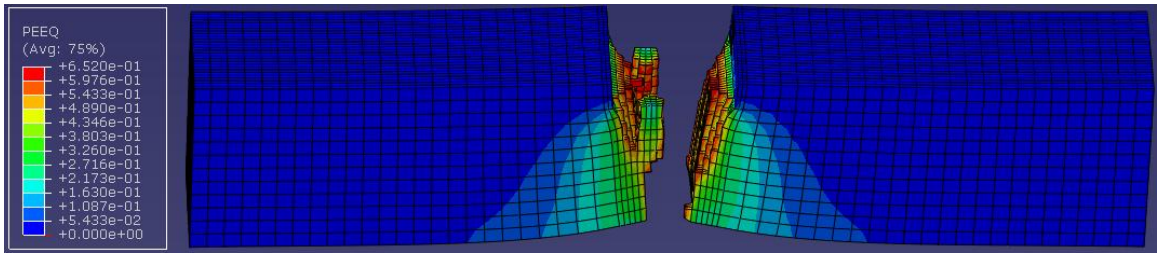

(c) Simulation with full wire size model having 0.25mm elements around the channel tip

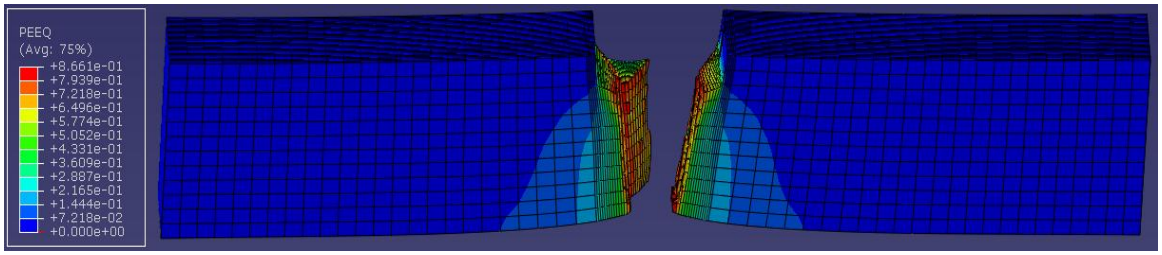

(d) Simulation with half wire size model having 0.1mm elements around the channel tip

(e) Fractured specimen with 2mmx2mm channel cut from laboratory tensile testing

Figure 7.14: Fracture shapes showing the equivalent plastic strain distributions and the fracture shapes from simulations with successive mesh refinement around the channel.

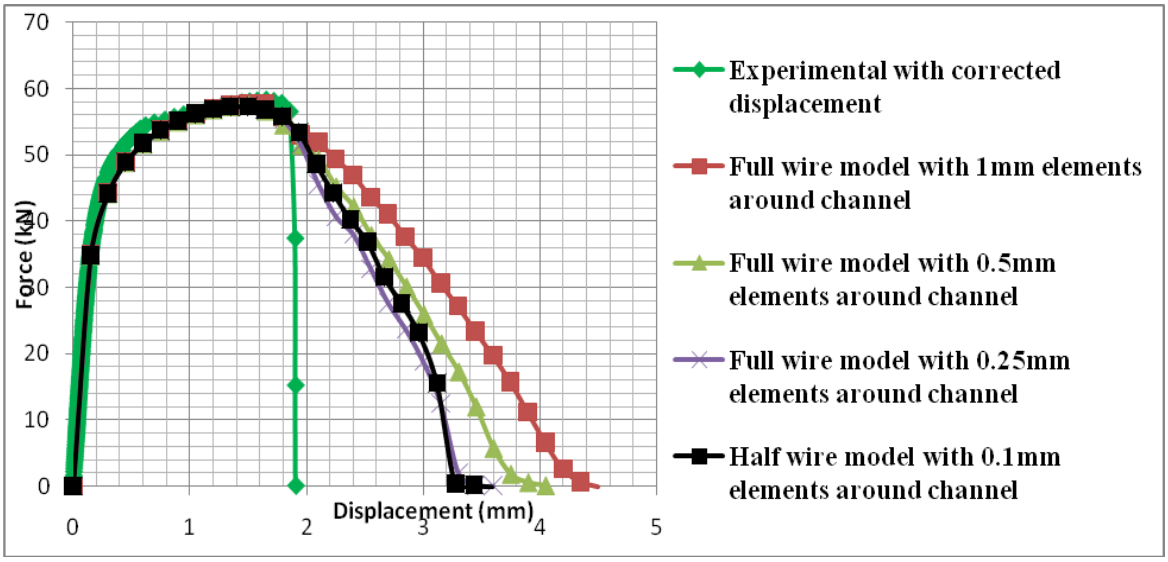

Figure 7.15: Force-displacement curves variation with successive mesh refinement around 2mmx2mm channel cut in 12mmx7mm wire with 50mm gauge length.

Table 7.3: Variation of mechanical properties predicted by FE simulations with successive mesh refinement

Ultimate load point parameters					
Size of elements around the groove (mm)	Ultimate load (kN)	Percentage difference		Ultimate load point displacement (mm)	% difference
Experimental	57.99	-		2.25	-
1mm	57.75	-		1.50	-
0.5mm	57.56	0.32		1.50	0
0.25mm	57.20	0.63		1.49	0.06
0.1mm	57.29	0.15		1.49	0
Fracture point parameters					
	Fracture load (kN)	Percentage difference		Displacement at fracture (mm)	Percentage difference
Experimental	56.64	-		2.51	-
1mm	55.71	-		1.80	-
0.5mm	56.68	1.74		1.65	8.25
0.25mm	56.67	0.02		1.64	0.61
0.1mm	56.80	0.23		1.64	0.00

Table 7.4: Variation of elastic Mises stress predicted by FE simulations with successive mesh refinement

Element size (mm)	Amplified elastic Mises stress (N/mm^2)	Nominal elastic Mises stress (N/mm^2)	Elastic stress concentration factor	% difference in stress concentration
1	103.9	59.23	1.75	-
0.5	104.2	59.69	1.75	0
0.25	105.2	59.91	1.76	0.6
0.1	105.8	59.97	1.76	0

From the negligible percentage difference (maximum of 0.25%) between the values of force, displacement, amplified and nominal elastic Mises, and elastic stress concentration factors predicted by the simulations with 0.25mm and 0.1mm elements around the channel shown in Table 7.3, it can be concluded that the mesh has converged and carrying out the simulation with 0.1mm elements around the channel produces accurate results. However, there is a disparity between the fracture trajectories (the portion of the curves from the fracture initiation point to the end of the curves) predicted by the curves predicted by the FE and that obtained from the laboratory experiments.

The experiment curve shows a rapid loss of the force carrying ability of the specimen with a little extension, while the FE predicted a gradual loss of the force carrying ability with large extensions. As shown in Figure 7.15, the disparity between the fracture trajectories reduces with the increase in the mesh density around the groove, with the fracture trajectory predicted by the simulation with 0.1mm element around the groove agreeing most with the experimental fracture trajectory. This result agrees with what is reported by Besson et al, (2003) and is due to the fact that the smaller the mesh size, the smaller the fracture energy required and the lower the displacement to fracture after fracture initiation. From this trend, carrying out simulations with finer element sizes would make the fracture trajectory predicted by the FE agree more with the experimental fracture trajectory. However as earlier stated, carrying out simulations with finer element sizes would have no significant effects on the mechanical properties of the wire that are required for designs and quality assurance. Also the ability of the simulation carried out with 0.1mm elements to predict the same fracture shape

displayed by the fracture specimen from laboratory tensile test shown in Figure 7.14(e) shows that the simulation with 0.1mm elements gives sufficiently accurate results.

7.5 Effects of across-the-thickness and across-the-width miniature groove on tensile properties of tensile armour wires

The effects of across-the-thickness and across-the-width miniature grooves on tensile properties of tensile armour wires were investigated by carrying out tensile testing simulations on models of wire specimens with 0.2mm wide and 0.2mm deep groove/channel across their entire thickness and across their entire width as shown in Figures 7.16 (a) and (b) respectively.

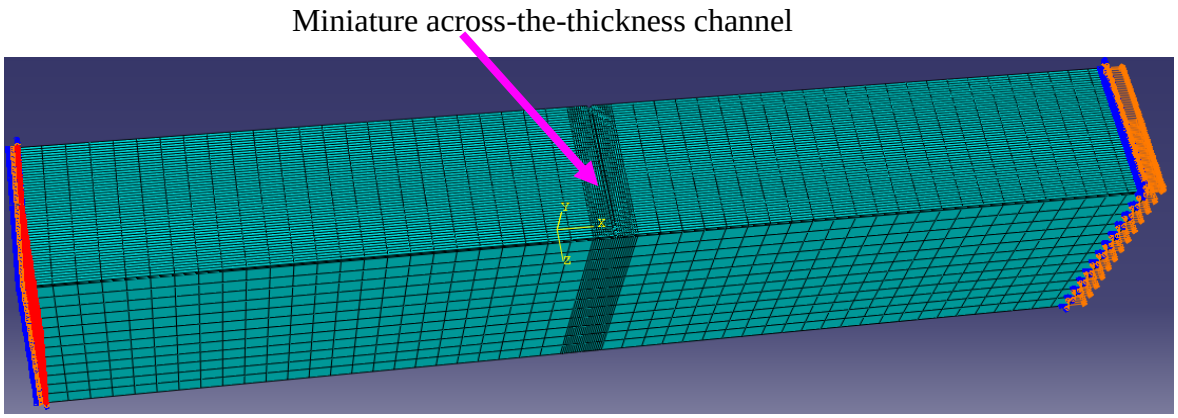

(a) Miniature across-the-thickness groove.

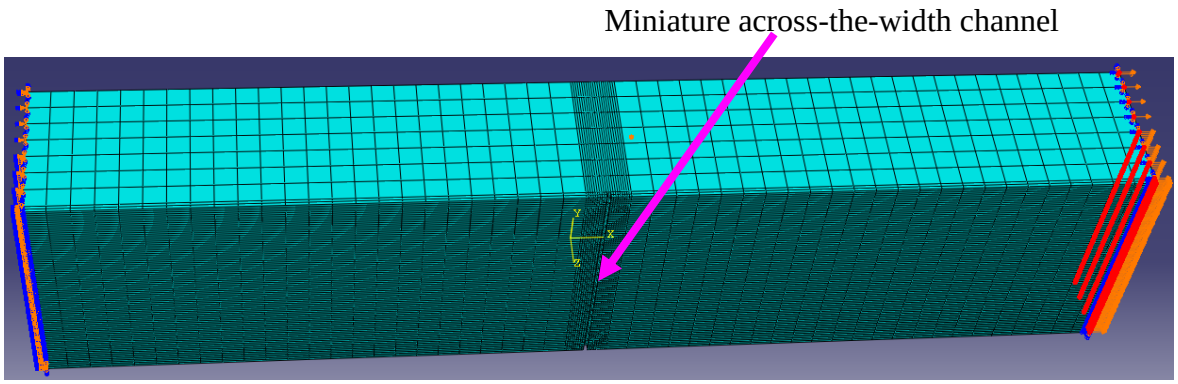

(b) Miniature across-the-width groove

Figure 7.16: Miniature channel across full wire thickness and full wire width

To minimise the computation time and reduce the output file capacity, the simulation was carried out using a model with half the thickness of the wire (3.5mm). The deformed shapes and Mises stress distributions of the whole specimen and of the regions around the channel across the thickness at the beginning of the tensile testing simulation at an applied displacement of 0.38mm, during necking at an applied displacement of 3.59mm, during

fracture initiation at an applied displacement of 5.78mm and after fracturing at an applied displacement of 6.95mm are shown in Figures 7.17 (a), to (d) and Figures 7.18 (a), to (d) respectively.

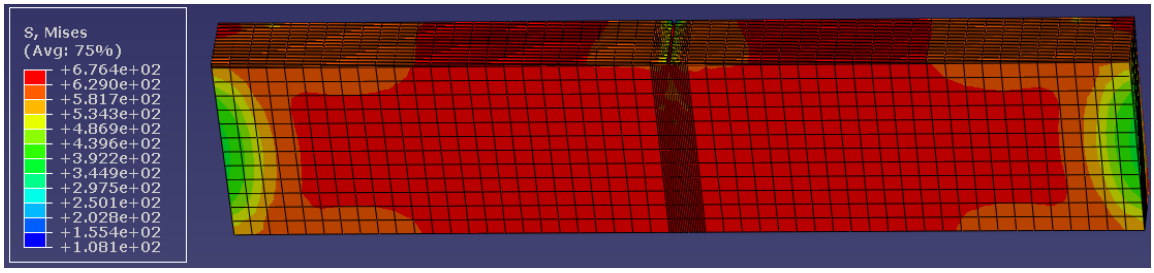

(a) Beginning of simulation at an applied displacement of 0.38mm

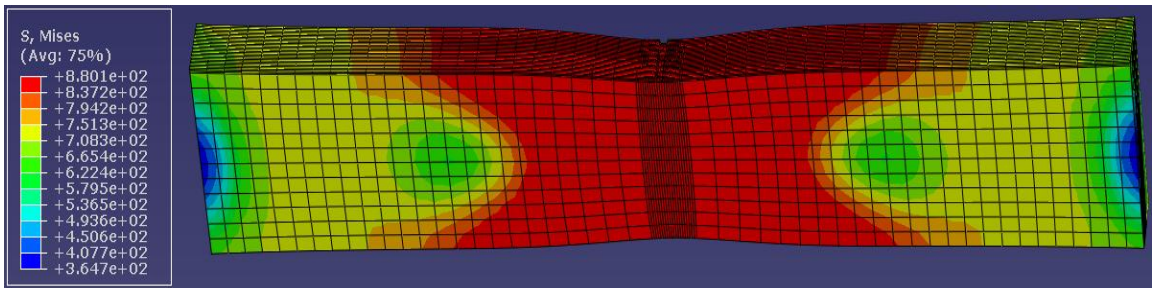

(b) During necking at an applied displacement of 3.59mm

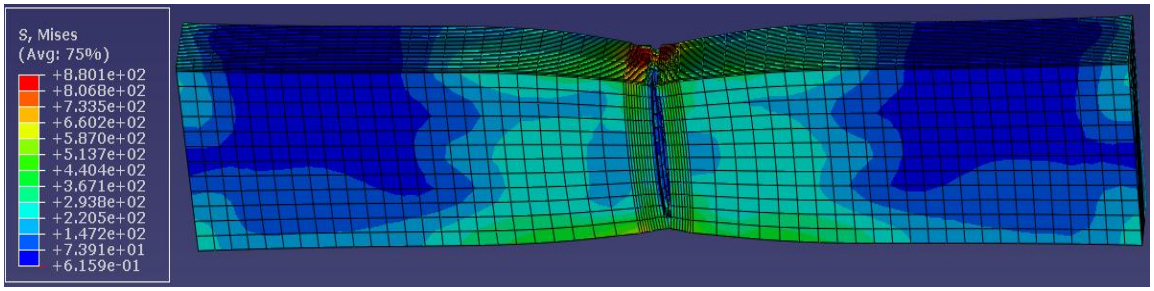

(c) During fracture initiation at an applied displacement of 5.78mm

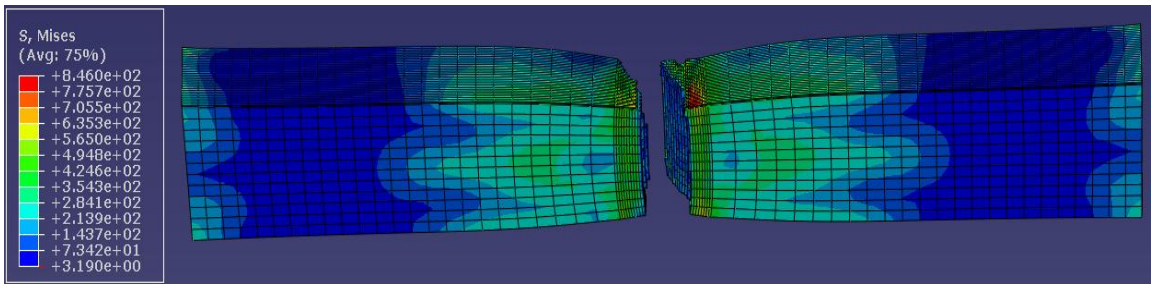

(d) Fractured specimen after simulation at an applied displacement of 6.95mm

Figure 7.17: Deformed shapes of whole model of wire specimen with across-the-thickness groove showing Mises stress (MPa) at various stages of the tensile testing simulation.

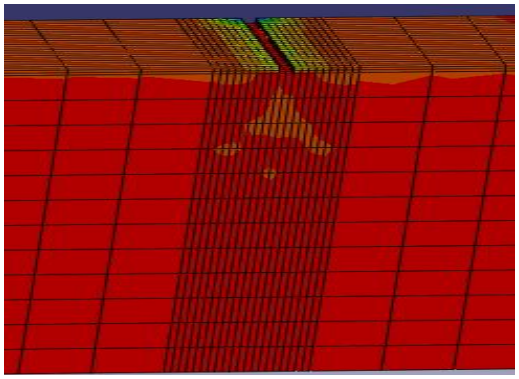

(a) At an applied displacement of 0.38mm

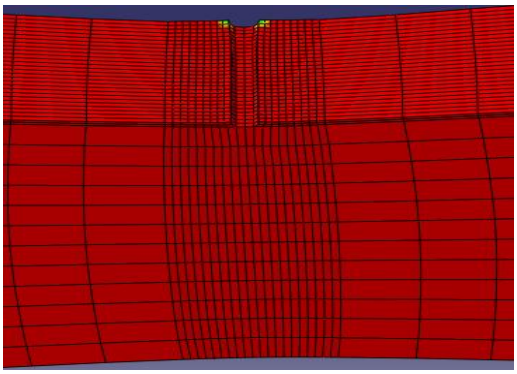

(b) At an applied displacement 3.59mm

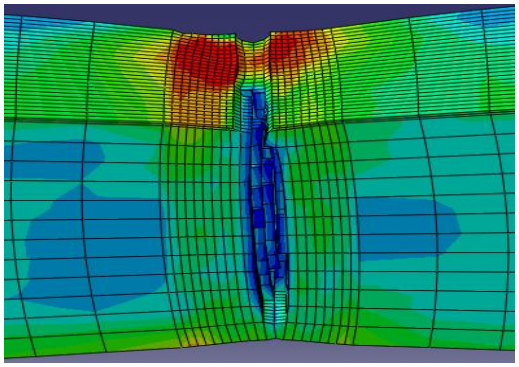

(c) At an applied displacement of 5.78mm

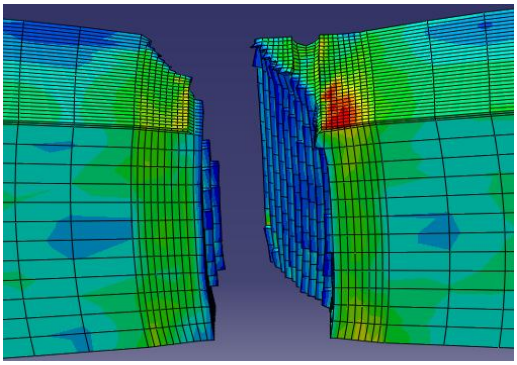

(d) At an applied displacement of 6.95mm

Figure 7.18: Deformed shapes around across-the-thickness channel during tensile testing simulation.

Similarly, the deformed shapes and Mises stress distributions of the whole specimen and of the regions around the across-the-width channel at the beginning of the tensile testing simulation at an applied displacement of 0.38mm, during necking at an applied displacement of 3.40mm, during fracture initiation an applied displacement of 5.28mm and after fracturing at an applied displacement of 5.83mm are shown in Figures 7.19 (a), to (d) and Figures 7.20 (a), to (d) respectively.

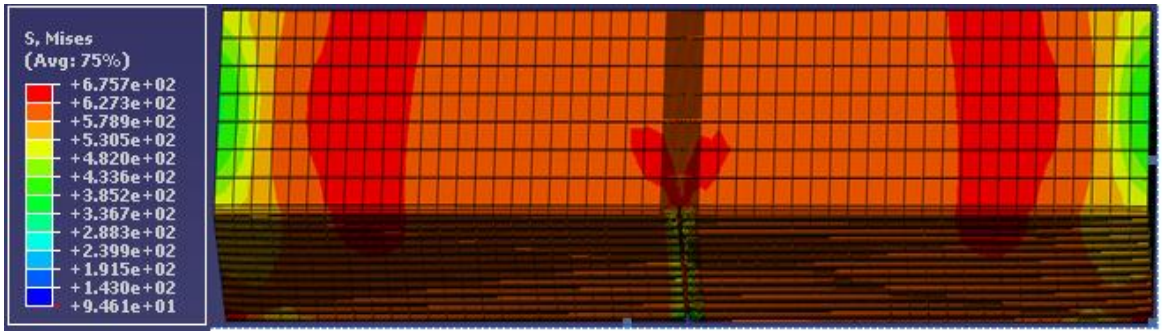

(a) Beginning of simulation at an applied displacement of 0.38mm

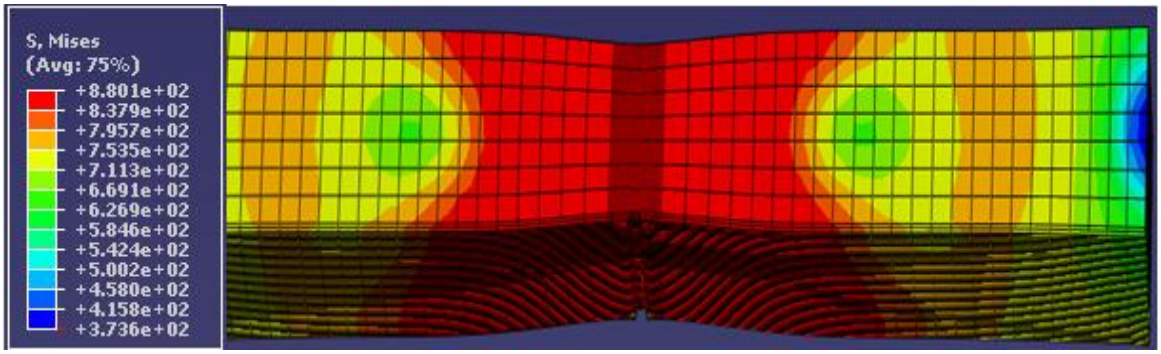

(b) During necking at an applied displacement of 3.40mm

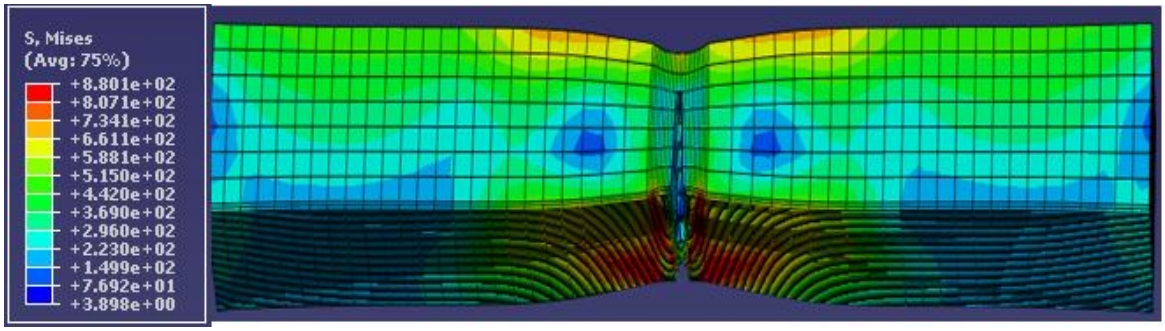

(c) During fracture initiation at an applied displacement of 5.28mm

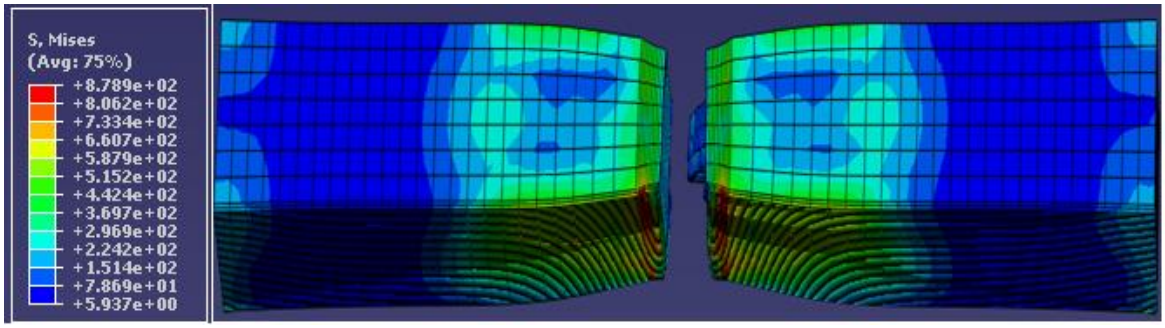

(d) Fractured specimen after simulation at an applied displacement of 5.83mm

Figure 7.19: Deformed shapes of whole model of wire specimen with across-the-width groove showing Mises stress (MPa) at various stages of the tensile testing simulation.

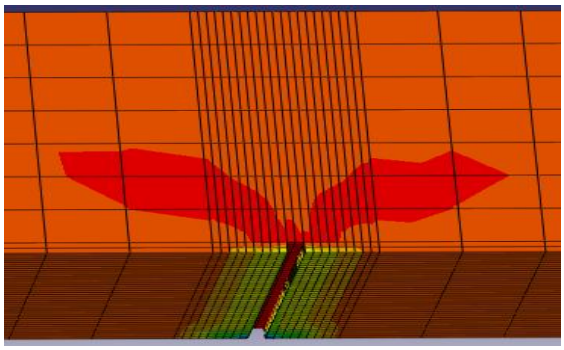

(a) At an applied displacement of 0.38mm

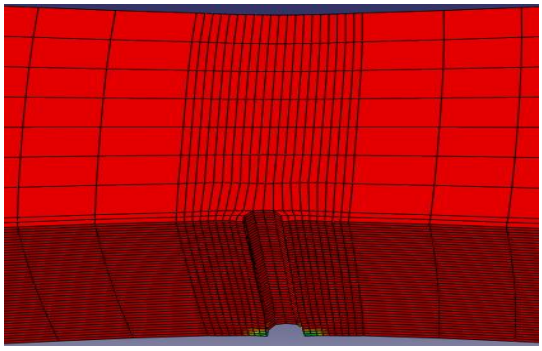

(b) At an applied displacement of 3.40mm

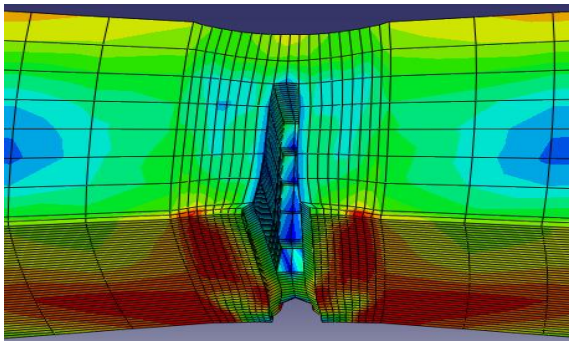

(c) At an applied displacement of 5.28mm

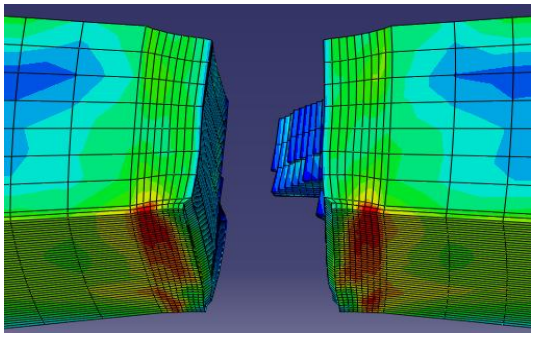

(d) At an applied displacement of 5.83mm

Figure 7.20: Deformed shapes around across-the-width groove during tensile testing simulation.

Figures 7.21 and 7.22 show the variations in the tensile responses obtained from the tensile testing simulations of the wire specimen with across-the-thickness groove and the wire specimen with across-the-width groove with varying relative depths of the across-the-thickness and across-the-width grooves.

7.5.1 Analysis of results

As shown in Figures 7.21(a) and 7.22 (a), the ultimate loads and the fracture displacements reduce with increase in relative groove depth for both the specimen with the across-the-thickness groove and the specimen with the across-the-width groove. From Figures 7.21(b) and 7.22 (b), the yield and the tensile strengths of both the wire specimens with the across-the-thickness groove and the wire specimens with the across-the-width groove increase with an increase in the relative notch depth, while the fracture strain reduces with increase in the relative notch depth. This result agrees with what is reported by Bayram et al, (1999) and is due to the notch strengthening effect of the groove as described in section 7.1. While the

yield and the tensile strengths of the wire with grooves increase with increase in groove depth, in practical terms, the load carrying capacity of the wire reduces with increase in groove depth. Consequently, the force displacement response of the wire with grooves is used to assess the detrimental effect of the grooves on the tensile properties of the tensile armour wire.

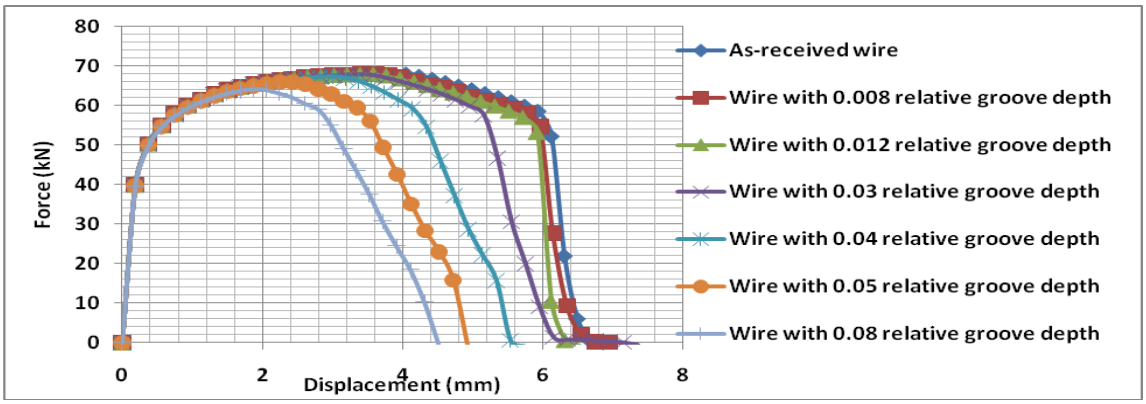

(a) Force-displacement curves

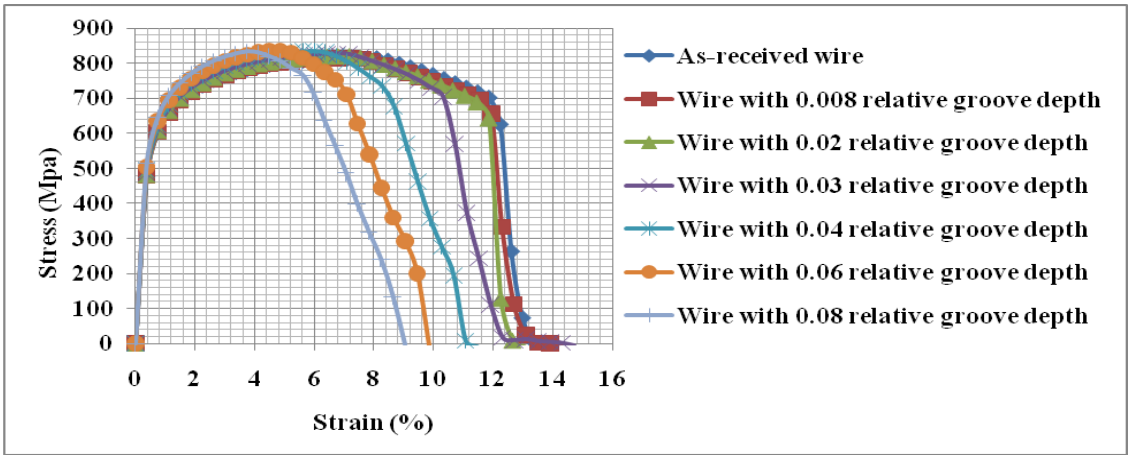

(b) Stress-strain curves

Figure 7.21: Force-displacement and stress-strain variations with across-the-thickness relative groove depth for 12mmx7mm wire specimen with 50mm gauge length.

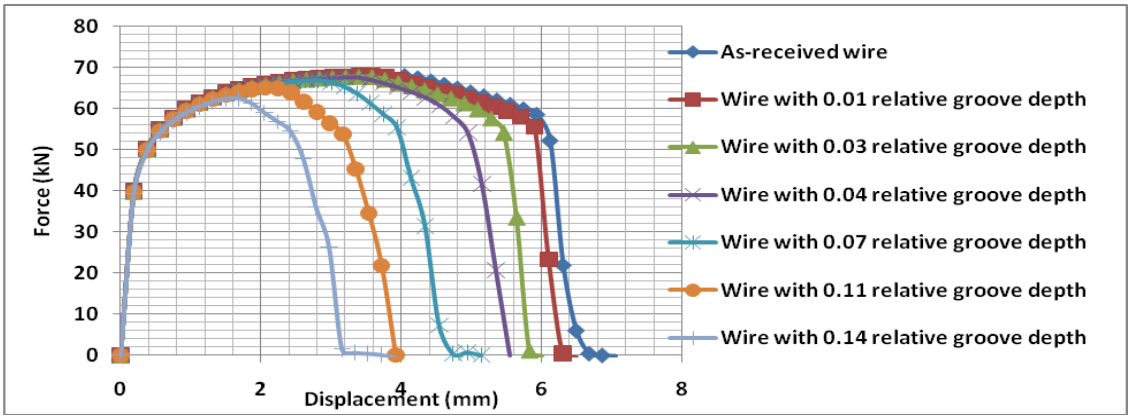

(a) Force-displacement variation

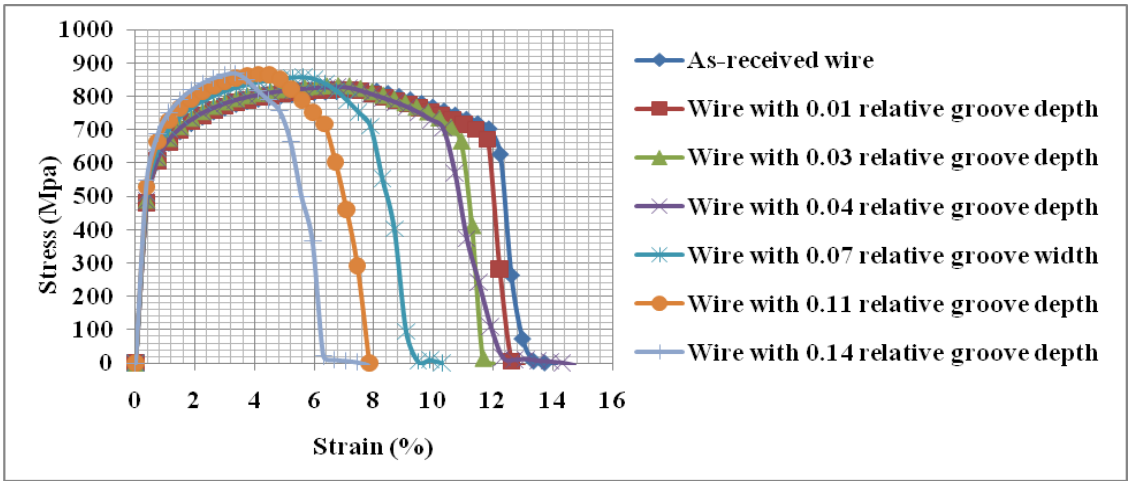

(b) Stress-strain variation

Figure 7.22: Force-displacement and stress-strain variations with across-the-width groove depth for 12mmx7mm wire specimen with 50mm gauge length.

From Table C1 of appendix C, the yield loads, the ultimate loads and the fracture displacements reduced by 0.025 to 1.030%, 0.057 to 5.612% and 2.626 to 51.12% respectively due to the presence of the across-the-thickness groove with relative depths ranging from 0.008 to 0.08. Similarly, from Table C2 of appendix C, the yield loads, the ultimate loads and the fracture displacements reduced by 0.044 to1.591%, 0.065 to 8.199% and 3.837 to 59.20% respectively due to the presence of the across-the-width groove with depths ranging from 0.01mm to 0.14mm. Generally, as shown in Figure 7.23, the reductions in these mechanical properties are higher for the specimen with the across the width groove**.** For both specimens, the percentage reduction in the fracture displacement is the highest, followed by the percentage reduction in the ultimate loads with the yield loads having the

least percentage reduction. This shows that the presence of the groove/channel shaped scratches have the worst effect on the fracture displacement/strain leading to 3.837% and 59.202% reduction in the ductility of the tensile armour wires for 0.01mm and 14mm relative groove depths respectively. The effect of the reductions in these mechanical properties on the flexible flowlines and risers are as discussed in section 7.1

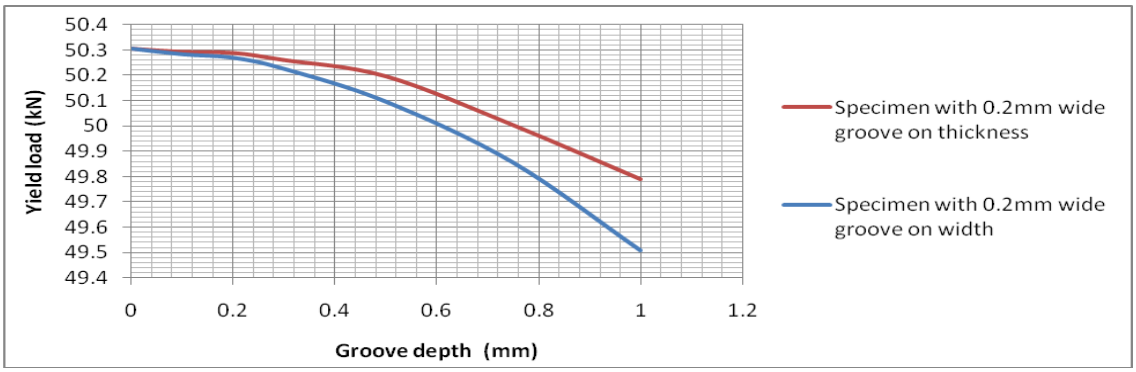

(a) Yield load variation with channel depths

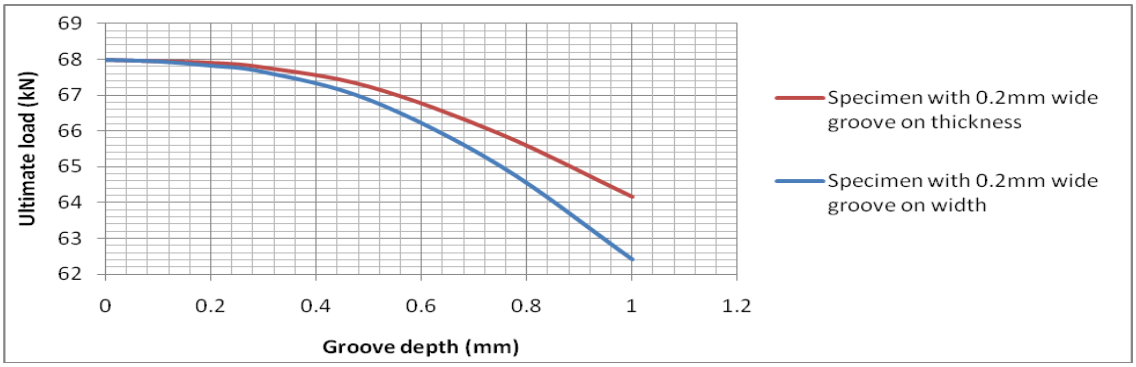

(b) Ultimate load variation with channel depth

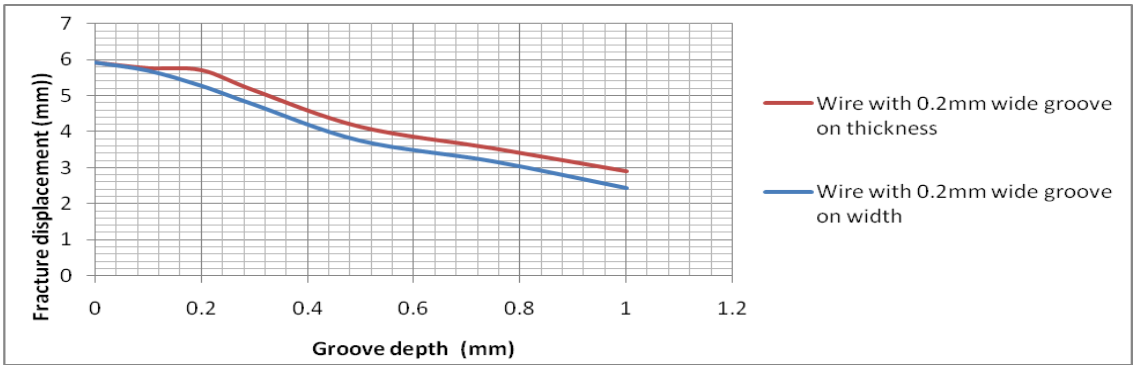

(c) Fracture displacement variation with channel depth

Figure 7.23: Variation in mechanical properties with across the thickness and across the width groove depths for 12mmx7mm wire specimen with 50mm gauge length.

7.6 Effects of mid-thickness groove, mid-width and an edge groove.

Figure 7.24 shows the locations of the 0.2mm wide, 0.2mm long and 0.2mm deep edge groove, mid-thickness groove and mid-width groove on the model of the tensile armour wire specimen. The force-displacement curves and the fracture shapes predicted by the simulations conducted with specimens having edge, mid-thickness and mid-width grooves are shown in Figures 7.25 and 7.26 respectively. As shown in Figure 7.25, there is no noticeable or significant difference in the global force-displacement responses of the three specimens. Consequently, the location of the miniature grooves/scratches does not make any significant difference to the tensile responses of the tensile armour wire

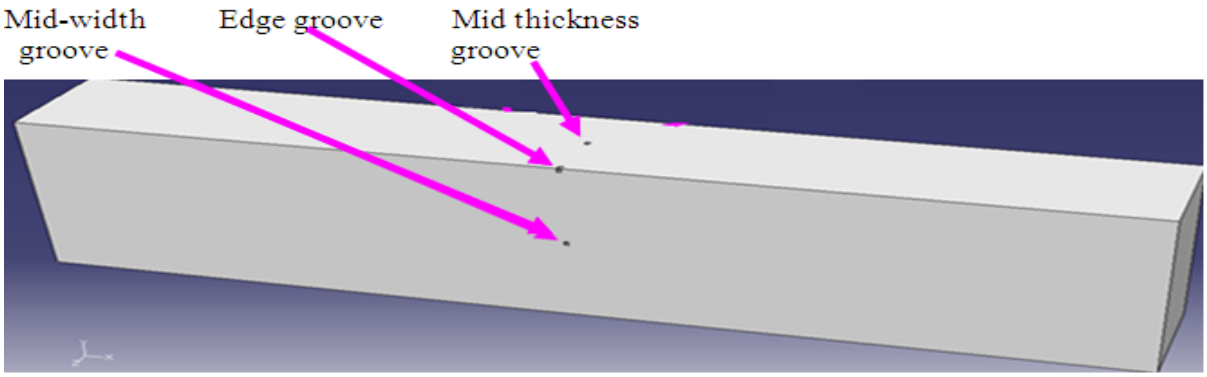

Figure 7.24: Edge channel, mid-thickness channel and mid-width channel locations

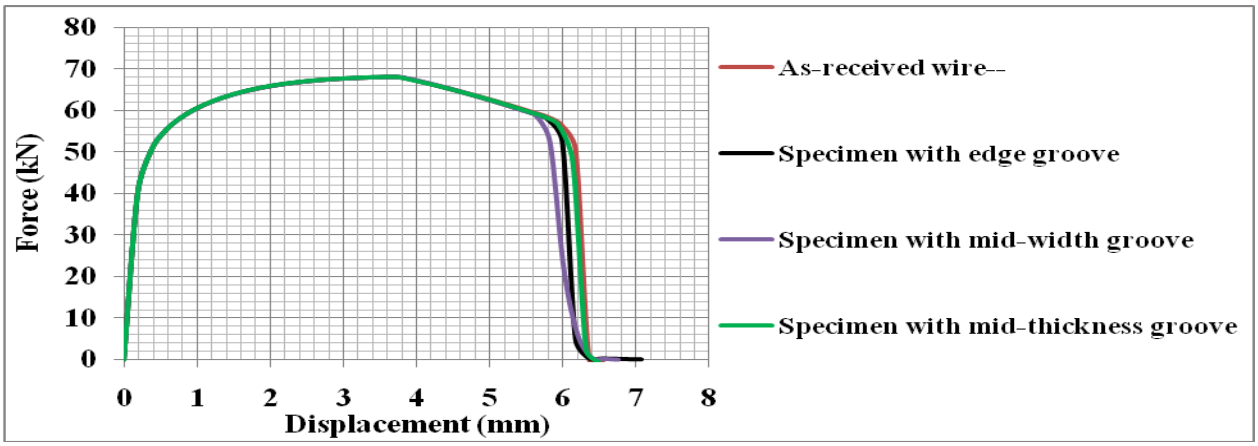

Figure 7.25: Force-displacement curves for 12mmx7mm, 50mm gauge length specimens with mid-thickness, mid-width and edge groove.

With this observation, it can be inferred that the higher reduction in the mechanical properties of tensile armour wire predicted by the simulation with the specimen having across-the-width groove when compared with the specimen with the across-the-thickness groove observed in

section 7.5.1 is due to the longer length of the across-the-width groove (12mm) and consequently, larger reduction in the gross area of the specimen with the across-the-width groove compared with the 7mm long across-the-thickness groove.

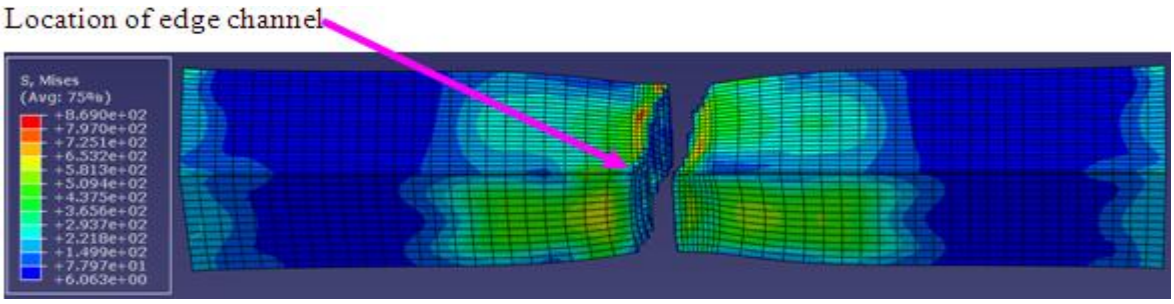

(a) Specimen with edge channel.

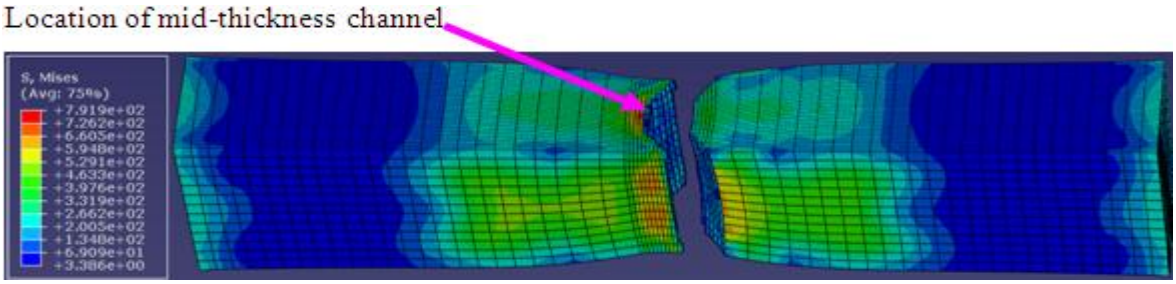

(b) Specimen with mid-thickness channel.

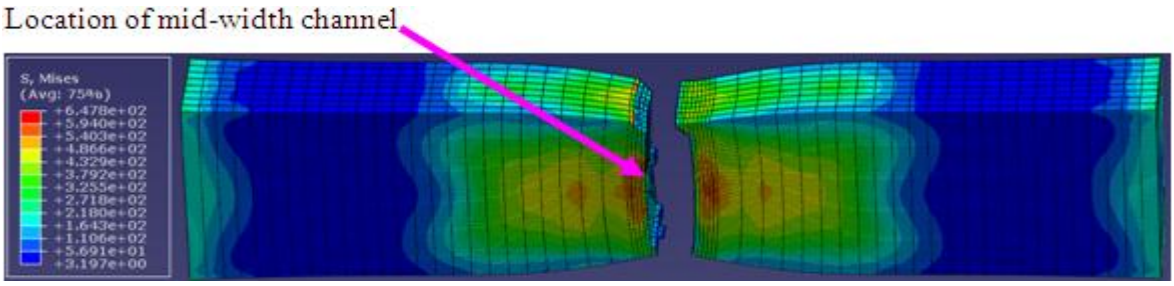

(c) Specimen with mid-width channel

Figures 7.26: Fractured specimens of wire models with edge, mid-thickness and mid-width grooves at an applied displacement of 5.96mm showing Mises stress (MPa) distribution.

7.7 Effects of channel dimension on tensile properties of tensile armour wires.

The effects of the channel dimensions on the tensile response/properties of tensile armour wires were investigated by carrying out tensile testing simulations on models of wire specimens with varying groove widths, depths and lengths. The channel sizes considered are 0.1mm, 0.2mm and 0.3mm wide with relative depths varying from 0.008 to 0.08. Figures

7.27 (a), (b) and (c) show the variations of the yield loads, the ultimate loads and the displacement at fracture with groove depths for three specimens with 7mm long across the thickness groove but with 0.1mm, 0.2 and 0.3mm widths.

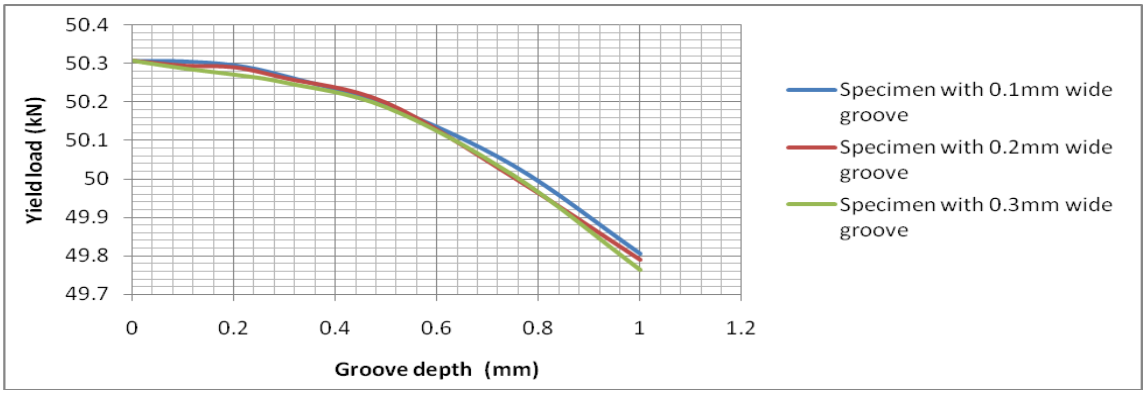

(a) Variation of yield load with groove width and depth

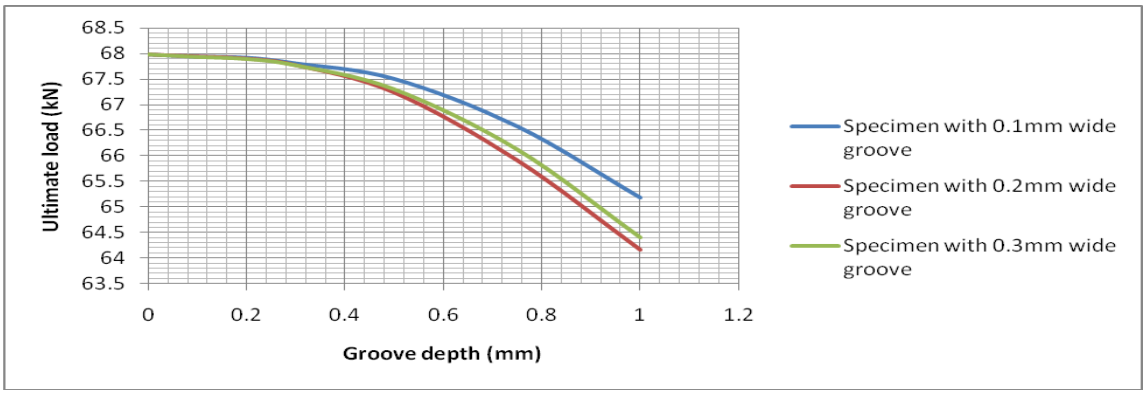

(b) Variation of ultimate load with groove width and depth

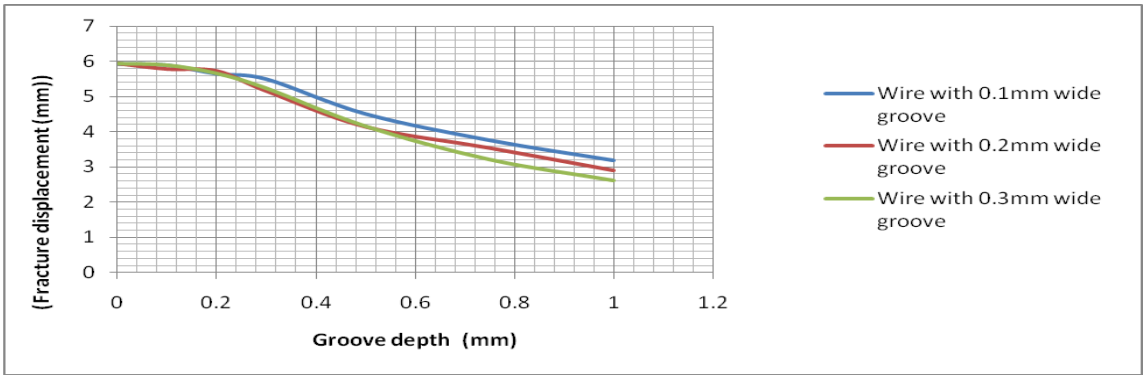

(c) Variation of displacement at fracture with groove widths and depths

Figure 7.27: Variation in mechanical properties of 12mmx7mm, 50mm gauge length wire specimens with groove depth and width.

From Figures 7.27(a), (b) and (c) and Tables C3, C4 and C5, at any given relative groove depth, the yield loads, the ultimate loads and the fracture displacements generally reduces with increase in groove widths. For example, at a groove depth of 0.012, there are 0.022%, 0.034%, and 0.072% reductions in the yield loads of the specimens with 0.1, 0.2 and 0.3mm wide across-the thickness grooves respectively. Similarly, at a groove depth of 0.012mm, there are 0.092%, 0.119% and 0.131% reductions in the ultimate load; and 4.735%, 5.576% and 6.622% reductions in the fracture displacements of the specimens with 0.1, 0.2 and 0.3mm wide across-the-thickness grooves respectively. Thus it can be concluded that in the worst scenario, the presence of a flat bottom scratch which is 0.2mm wide, 0.2mm deep and which cuts across the entire 12mm width of the wire (i.e. 12mm long) reduces the yield load, the ultimate load and the fracture displacement of the wire by at most 0.072%, 0.238% and 10.95% respectively. Hence, flat bottom scratches with dimensions less than 0.2mm which cannot be detected by the eddy current detector will not reduce the yield load, the ultimate load and the fracture displacement of the wire by more than 0.072%, 0.238% and 10.95% respectively.

7.8 Summary

From the numerical experiments carried out to investigate the effects of miniature flat bottom scratches on the tensile properties of tensile armour wires, it can be concluded that:

1) Flat bottom scratches with dimensions less than 0.2mm which cannot be detected by the eddy current detector will not reduce the yield load, the ultimate load and the fracture displacement of the wire by more than 0.072%, 0.238% and 10.95% respectively.
2) The presence of the groove/channel shaped scratches have the worst effects on the ductility (in terms of fracture displacements), followed by the ultimate loads (and invariably the tensile strength) with the least effect on the yield load (and invariably the yield strength) of tensile armour wires.
3) The extent of the reduction in the mechanical properties of the tensile armour wires depends on the size rather than the location of the flat bottom scratches.

Having completed the investigation of the effect of flat bottom scratches on the tensile properties of tensile armour wires, the investigation of the effect of the pointed end scratches on the tensile properties of tensile armour wires is presented in the next chapter.

Chapter 8: Effect of miniature V shaped scratches on tensile properties of tensile armour wires

The scratches considered in this chapter have a pointed end as shown in the SEM image in Figure 8.1(a) and were modelled as 60 degree V-shaped notches as shown in Figure 8.1 and are hereinafter referred to as V-notches or V-shaped scratches. The effects of these V-shaped scratches on the tensile properties of the tensile armour wires were investigated using both laboratory and virtual/numerical tensile testing experiments. The investigation covers the effects of the groove dimensions and the effect of the location of the groove on the tensile properties of the tensile armour wires.

The details of the laboratory tensile testing of the as-received wire specimens and the wire specimens with a large engineered V-shaped cut are presented in section 8.1. The FEA simulations of the tensile testing of the as-received wire specimens and the wire specimens with an engineered 1mm deep, 60 degree V- notch are presented in sections 8.2 and 8.3 respectively. The effects of miniature V-notch locations on the tensile properties of the tensile armour wires investigated by considering the effect of the across-the-thickness and the across-the-width miniature V-shaped scratches, as well as the effects of mid-thickness, mid-width and an edge grooves on the tensile properties of the tensile armour wires are presented in section 8.4. The summary of the findings of the effects of V-shaped scratches on the tensile properties of the tensile armour wire is presented in sections 8.5

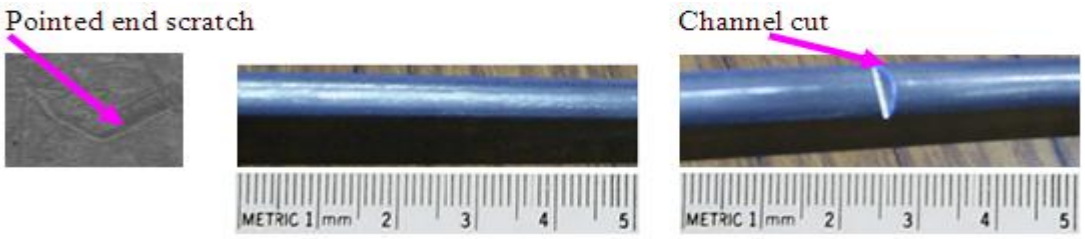

(a) SEM image (b) As-received wire specimen (c) Wire specimen with a V-shaped cut

Figure 8.1: As-received wire specimen and wire specimen with a V-shaped cut

8.1: Laboratory tensile testing of as-received wire specimens and wire specimens with V-shaped scratches

Laboratory tensile tests were carried out on 50mm long as-received tensile armour wire specimens with 12mmx7mm cross sectional dimensions shown in Figures 8.1(b) and on

tensile armour wire specimens from the same wire length as the as-received wire with a 60 degree V-shaped cut shown in Figures 8.1(c). The depth of the V-notch was made 1mm because it is practically easier to make 1mm deep V-shaped cut than making a V-shaped cut with 0.2mm depth. The force-displacement curves and the engineering stress-strain curves obtained from the laboratory tensile testing of the as-received wire specimen and the wire specimens with engineered/simulated 2mm wide by 2mm deep groove/channel are shown in Figure 8.2 (a) and (b) respectively.

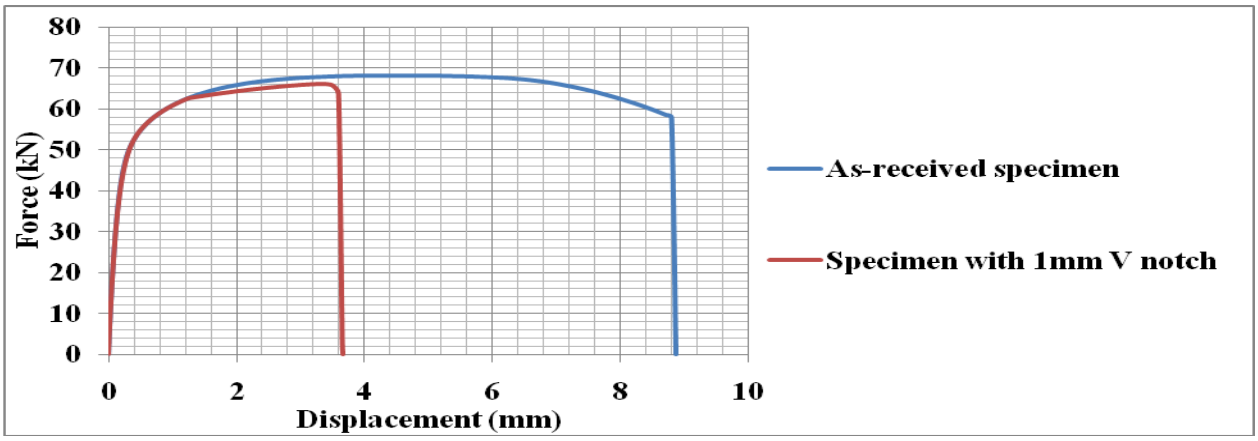

(a) Force-displacement curves

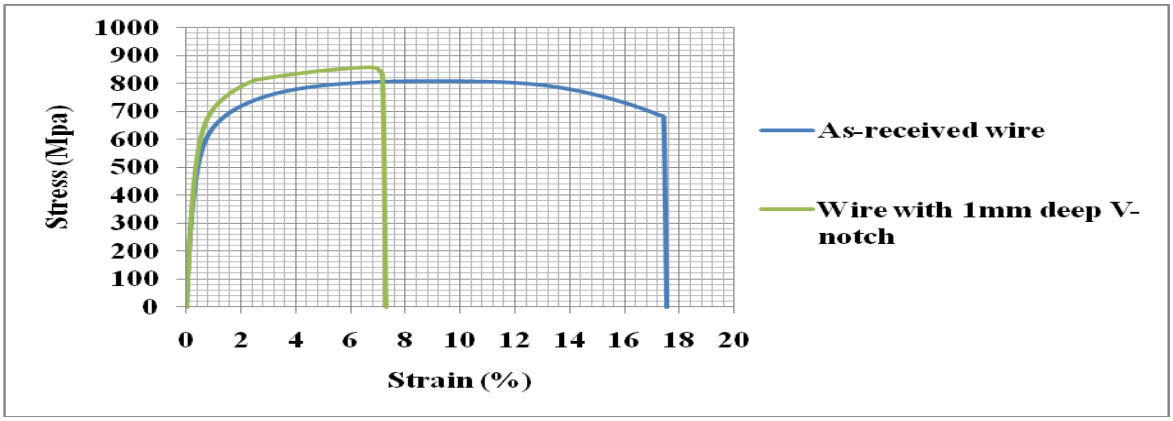

(b) Engineering stress-strain curves

Figure 8.2: Force-displacement and engineering stress-strain curves from laboratory tensile testing of 12mmx7mm, 50mm gauge length as-received wire and wire specimen with V-shaped cut.

From Figure 8.2 (a), the ultimate load and the displacement at fracture of the as-received wire are 68.25kN and 8.81mm respectively while the ultimate load and the fracture displacement

of the wire with 1mm deep 60 degree V-shaped cut are 66.09kN and 3.51mm respectively. The 1mm deep 60 degree V-notch has reduced the ultimate load and the fracture displacement of the wire by 3.16% and 60.22% respectively. This result agrees with what is reported by Kossakowski, (2010). The introduction of the 1mm deep 60 degree V-notch into the specimen has increased the offset yield and ultimate strengths of the wire from 520MPa to 700Mpa and 810MPa to 858MPa respectively, and reduced the fracture strain of the wire from 17.60% to 7.01%. This result agrees with what is reported by Bayram et al, (1999). The reasons for the increase in the yield and ultimate strengths of the V- notched tensile armour wire, and the reductions in the yield load, the ultimate load and the fracture displacement and strain, as well as the practical implications of these reductions on the integrity of flexible flowlines and risers are the same as that presented in section 7.1 for the reduction in the ultimate load and the fracture displacement of the wire by the channel shaped notch.

8.2 FEA tensile testing simulation of as-received wire specimen

The FEA tensile testing simulation of the as-received wire specimen has been dealt with in section 7.2 and the modelling techniques used have been shown to be appropriate as the result of the FE has been validated in the same section. Consequently, the FEA tensile testing simulation of the as-received wire, its results and validation are not repeated here to conserve space.

8 .3 FEA tensile testing simulation of wire specimen with a V-shaped cut

Having established in section 7.4 that meshing the region around the notch with 0.1mm elements gives accurate results, the simulation of the tensile testing of the tensile armour wire with a V-shaped cut was conducted by meshing the region around the V-notch with 0.1mm C3D8R elements as shown in Figure 8.3. The deformed shapes showing the Mises stress and equivalent plastic strain distributions during elastic deformation at an applied displacement of 0.03mm, at the beginning of plastic deformation at an applied displacement of 0.05mm, during necking at an applied displacement of 2.93mm, during fracture initiation at an applied displacement of 3.01mm and the fracture shape of the wire specimen with 1mm deep 60 degree V-shaped cut at an applied displacement of 4.5mm are shown in Figures 8.4(a) to (e) and 8.5 (a) to (e) respectively. The explanation of the mechanics and physics of deformation of the V-notch at the various stages of the tensile testing deformation is the same that given for the deformation of tensile armour wire with the channel shaped cut given in section 7.4.

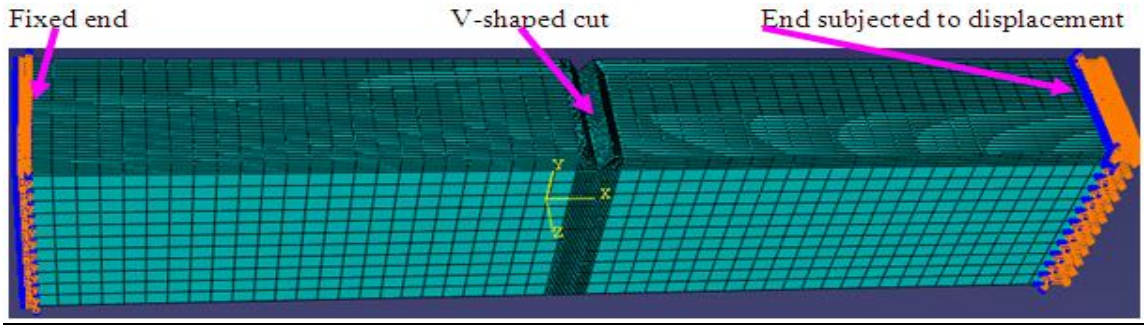

Figure 8.3: Model of a wire specimen with a 1mm deep 60 degree V-shaped cut with 0.1mm elements around V-notch.

The good agreement between the experimental and FE curves shown in Figure 8.7 and the small percentage difference between the experimental ultimate and fracture loads presented in Table 8.1 shows that the simulation is accurate. Also, since the fracture shape predicted by the simulation with 0.1mm elements around the V-shaped cut shown in Figure 8.5(e) is similar to the fracture shape obtained from the laboratory tensile testing shown in Figure 8.6, it can be concluded that carrying out the simulation with 0.1mm elements produces sufficiently accurate results. However, the percentage difference (9.45%) between the experimental and FE displacement at fracture is large and a finer mesh would be required to narrow the difference. Also, carrying out simulations with finer element sizes would make the fracture trajectory predicted by the FE agree more with the experimental fracture trajectory. However, further mesh refinement was not possible due to the limitation in the computer resources used for this project and as earlier stated, carrying out simulations with finer element sizes would have no significant effects on the mechanical properties of the wire that are required for designs and quality assurance.

Table 8.1: Mechanical properties from experiment and FE simulation for wire with 1mm deep 60 degree V-shaped cut

Parameters	Experiment	FE simulation	Percentage difference
Ultimate load (kN)	66.09	67.57	2.23
Fracture load (kN)	63.67	63.26	0.64
Displacement at fracture point (mm)	2.75	3.01	9.45

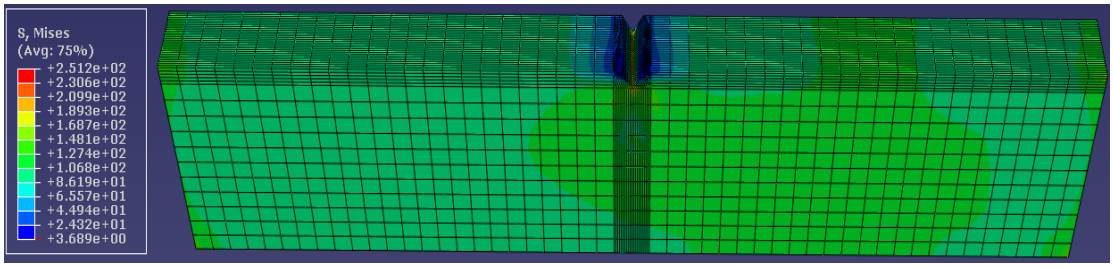

(a) During elastic deformation at an applied displacement of 0.03mm.

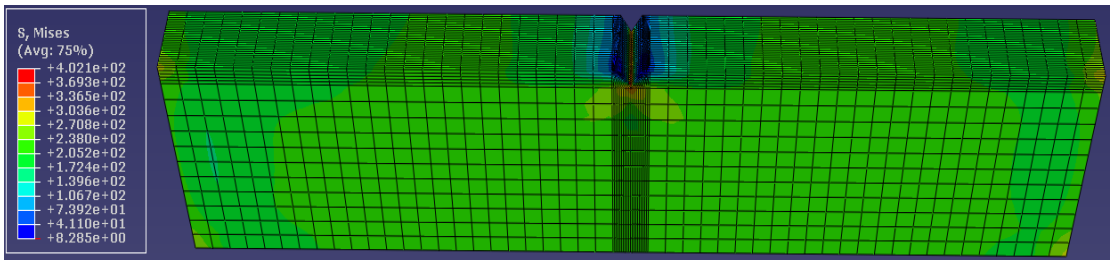

(b) At the beginning of plastic deformation at an applied displacement of 0.05mm.

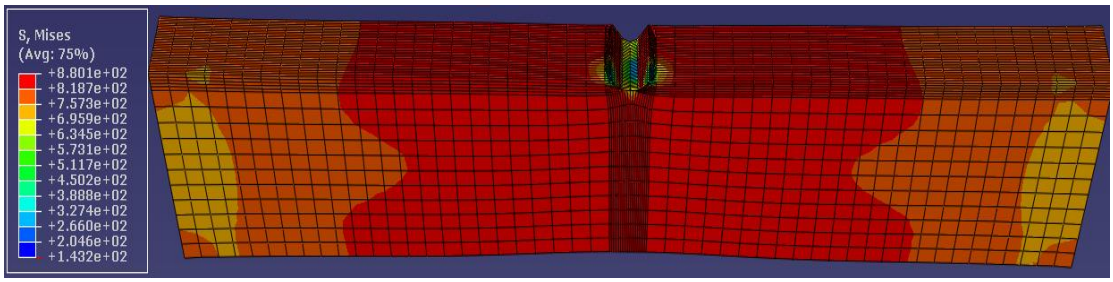

(c) During necking at an applied displacement of 2.93mm.

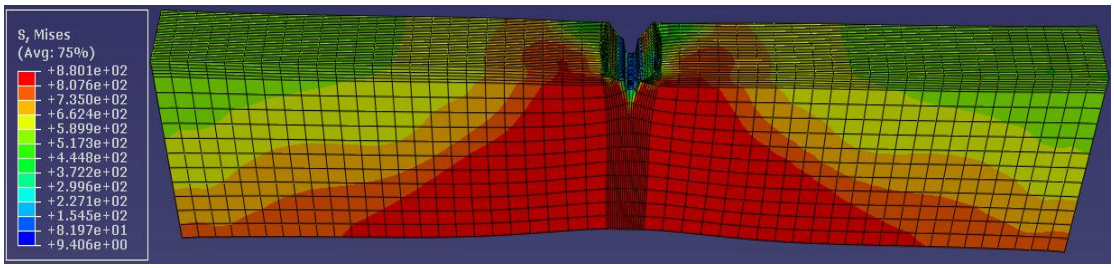

(d) During fracture initiation at an applied displacement of 3.01mm.

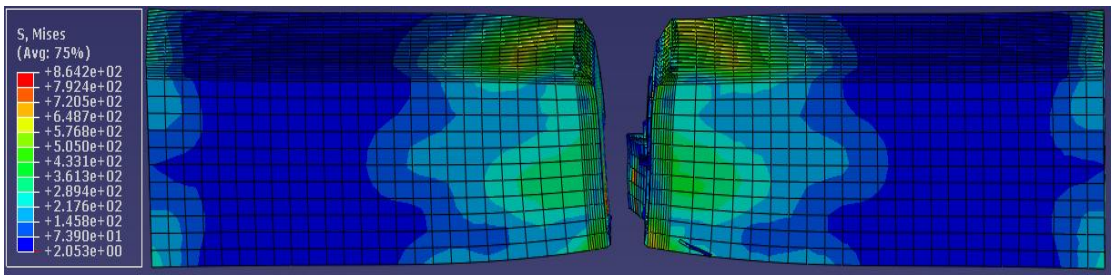

(e) Completely fractured specimen at an applied displacement of 4.5mm.

Figure 8.4 Deformed shapes showing the Mises stress (MPa) distribution at various stages of the simulation of tensile testing of wire with 1mm deep V-shaped cut.

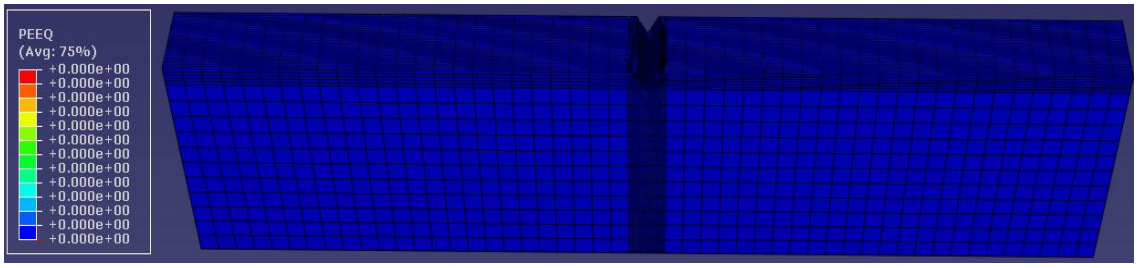

(a) During elastic deformation at an applied displacement of 0.03mm.

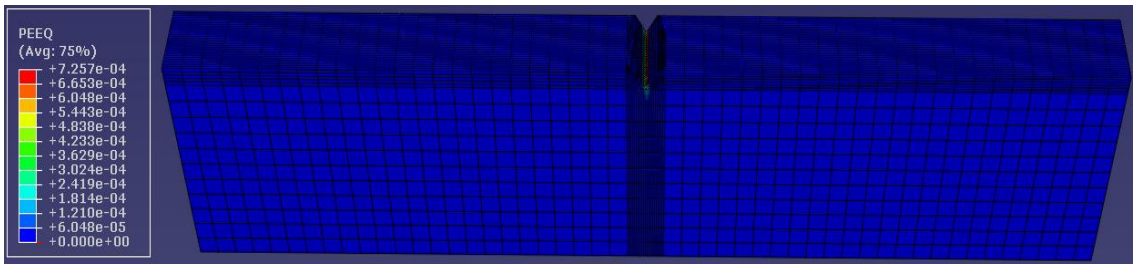

(b) At the beginning of plastic deformation at an applied displacement of 0.05mm.

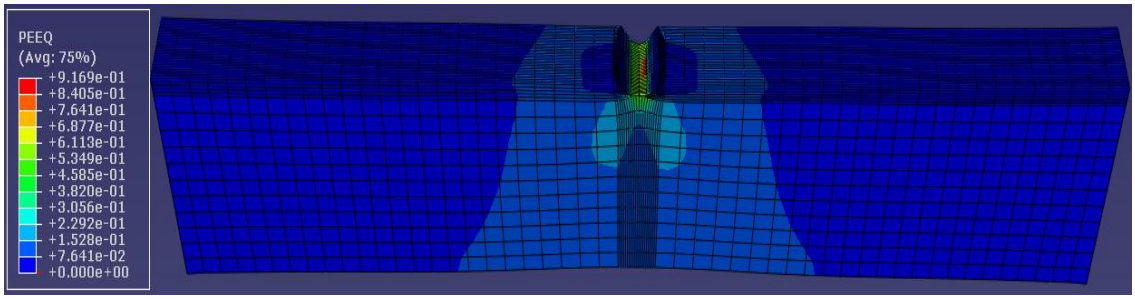

(c) During necking at an applied displacement of 2.93mm.

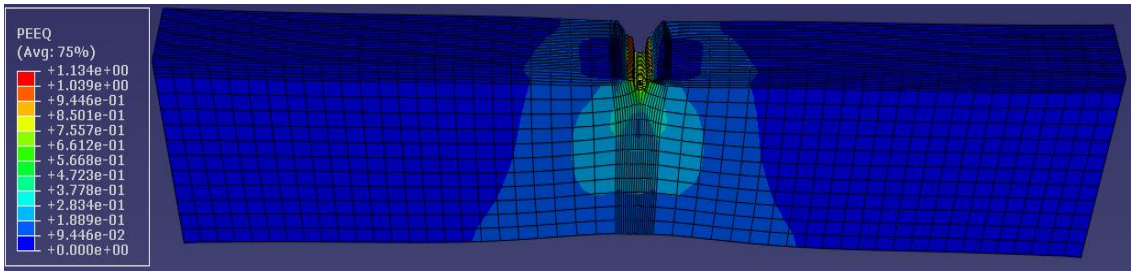

(d) During fracture initiation at an applied displacement of 3.01mm.

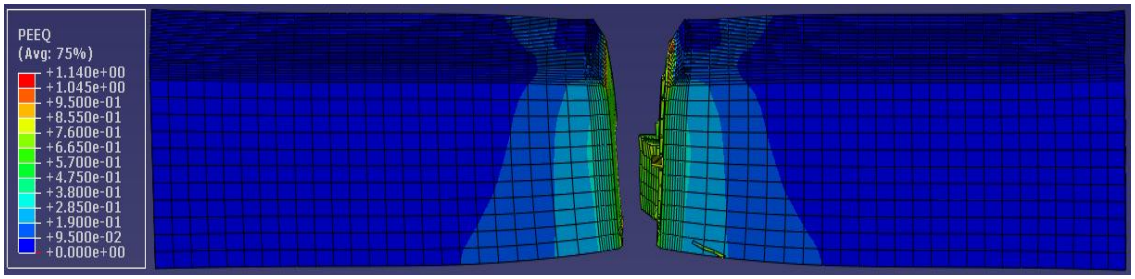

(e) Completely fractured specimen at an applied displacement of 4.5mm.

Figure 8.5 Deformed shapes showing the equivalent plastic strain distribution at various stages of the simulation of tensile testing of wire with 1mm deep V-shaped cut.

Figure 8.6: Fractured specimen from laboratory tensile testing of specimen with 1mm deep V-shaped cut.

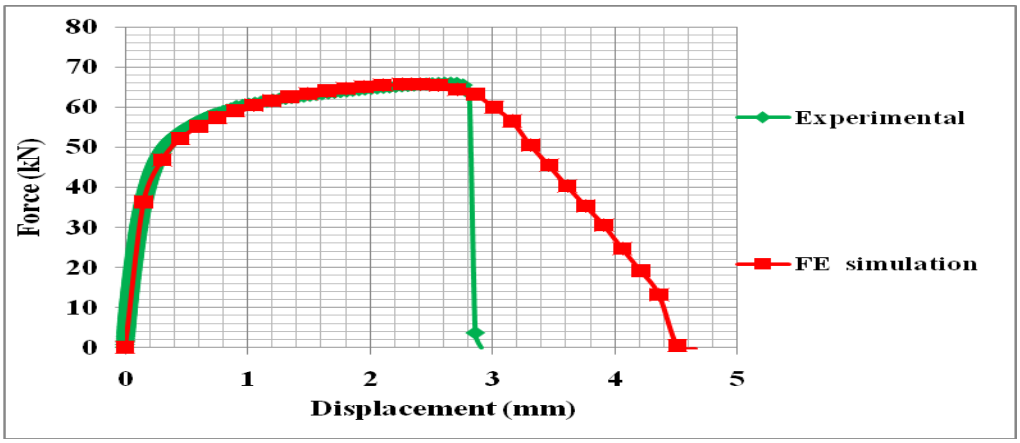

Figure 8.7: Experimental and FE force-displacement curves for 12mmx7mm, 50mm gauge length wire with a 1mm deep 60 degrees V-notch.

8.4 Effects of miniature V-notch locations on tensile properties of tensile armour wires

The effect of the locations of the V-shaped scratches was investigated by carrying out tensile testing simulations on models of wire specimens with a V-shaped scratch that cut across their entire thickness hereinafter referred to as an "across-the-thickness" V-shaped scratch/notch and on models of wire specimens with a V-shaped scratch that cut across their entire width hereafter referred to as the "across-the-width" V-shaped scratch. Furthermore, tensile testing simulations were carried out on wire models with miniature V-shaped scratches on their edge, along their width hereinafter referred to mid-width V-shaped scratch and along their thickness hereinafter referred to as a "mid-thickness" V-shaped scratch.

8.4.1 Effects of across-the-thickness and across-the-width miniature groove on tensile properties of tensile armour wires

The effects of across-the-thickness and across-the-width miniature V-shaped scratches on the tensile properties of then tensile armour wires were investigated by carrying out tensile testing simulations on the models of wire specimens with V-shaped cut across their entire

thickness and across their entire width as shown in Figures 8.8(a) and (b) respectively. In both cases, the left ends of the specimens were fixed and the right ends that are free to move only in the longitudinal direction were subjected to longitudinal displacements. The base and the depth of the triangularly shaped V cut are both 0.2mm. The regions around the V-shaped scratches were meshed with 0.1mm elements, which have been established to be the element size at which mesh convergence occurred.

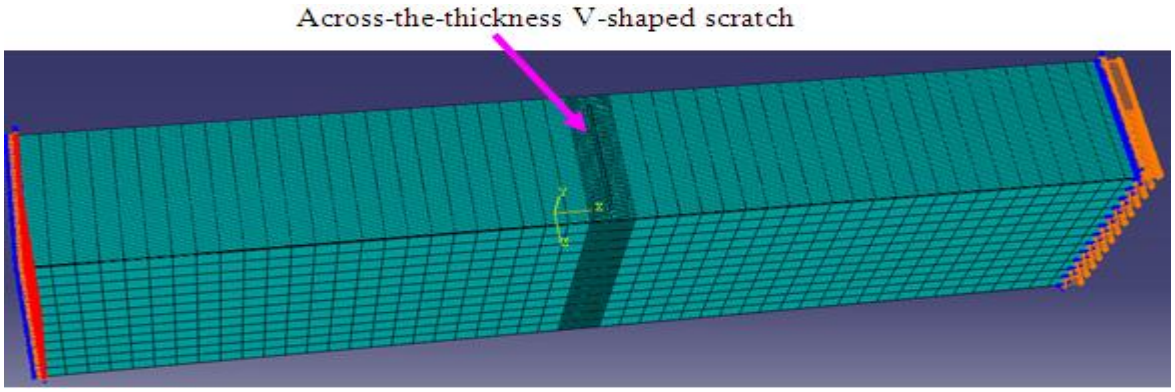

(a) Miniature across-the-thickness V-shaped scratch

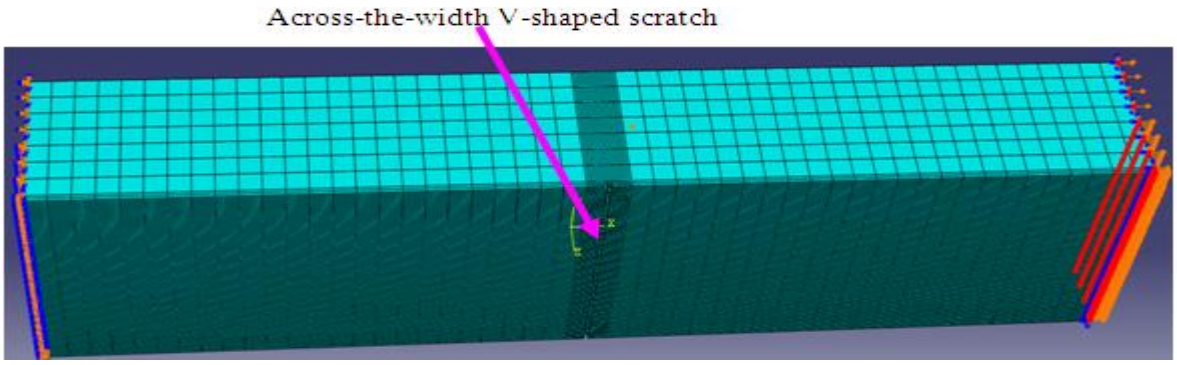

(b) Miniature across-the-width V-shaped scratch

Figure 8.8: Miniature V-shaped scratch across full wire thickness and full wire width.

To minimise the computation time and reduce the output file capacity, the simulation was carried out using a model with half the thickness of the wire (3.5mm). The deformed shapes and Mises stress distributions of the whole specimen and of the regions around the V-shaped scratch across the thickness at an applied displacement of 0.37mm, during necking at an applied displacement of 3.54mm, during fracture initiation at an applied displacement of 5.76mm and after fracturing at an applied displacement of 6.73mm are shown in Figures 8.9(a), to (d) and Figures 8.10(a), to (d) respectively.

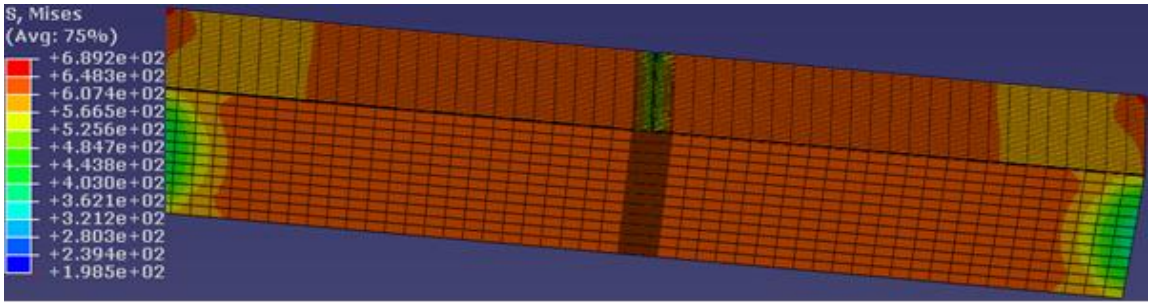

(a) At an applied displacement of 0.37mm.

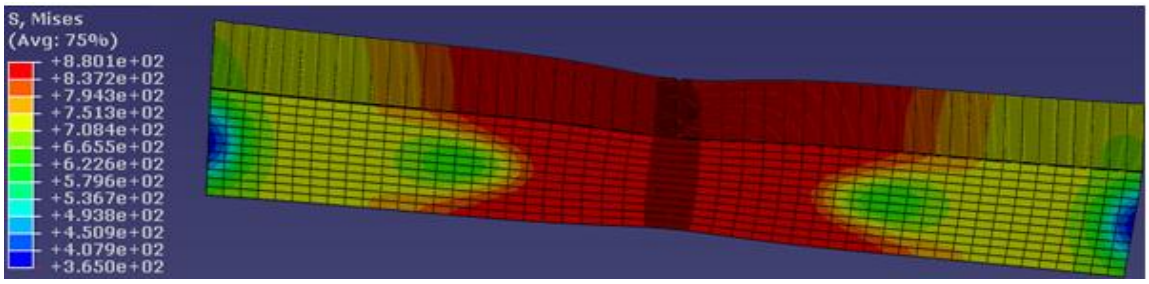

(b) During necking at an applied displacement of 3.54mm

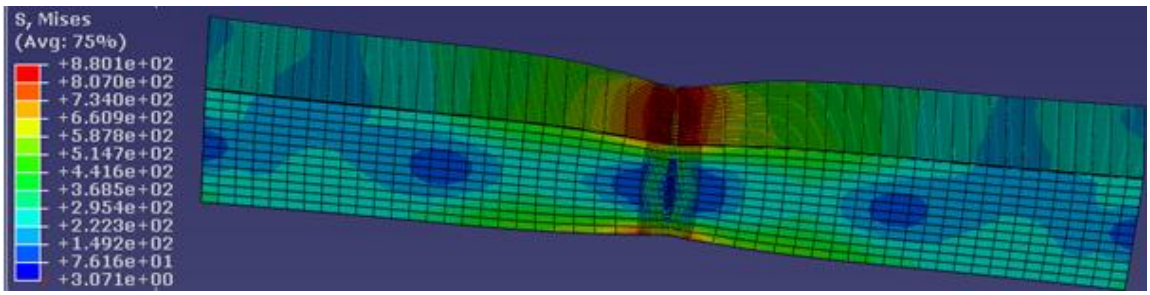

(c) During fracture initiation at an applied displacement of 5.76mm

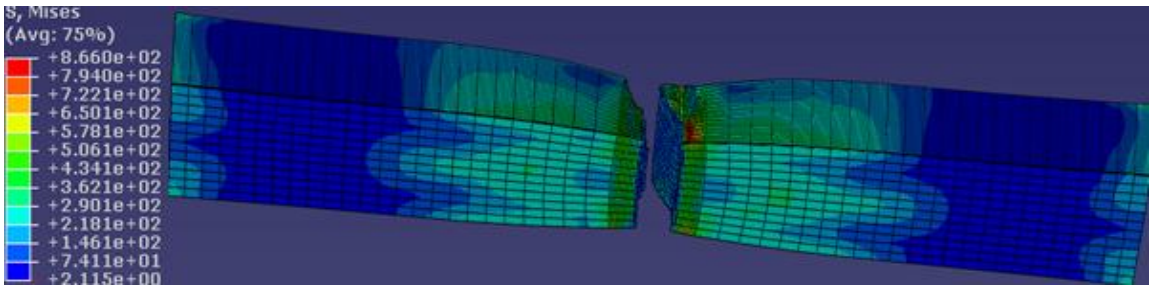

(d) Fractured specimen after the simulation at an applied displacement of 6.73mm

Figure 8.9: Deformed shapes and Mises stress (MPa) distribution for whole model of specimen with across-the-thickness V-shaped scratch during tensile testing simulation.

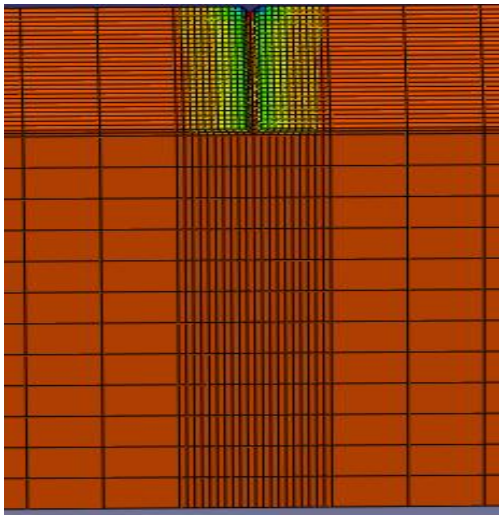

(a) At an applied displacement of 0.37mm.

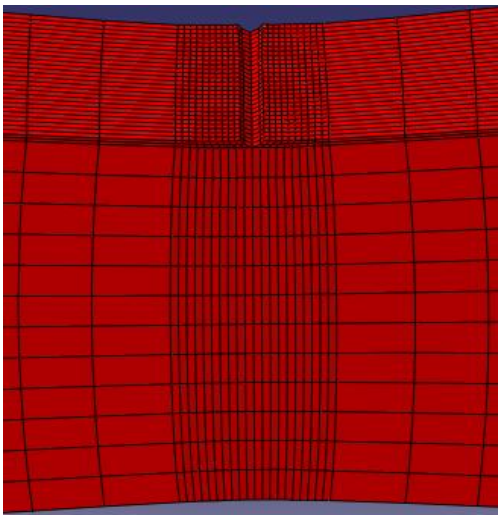

(b) At an applied displacement of 3.54mm

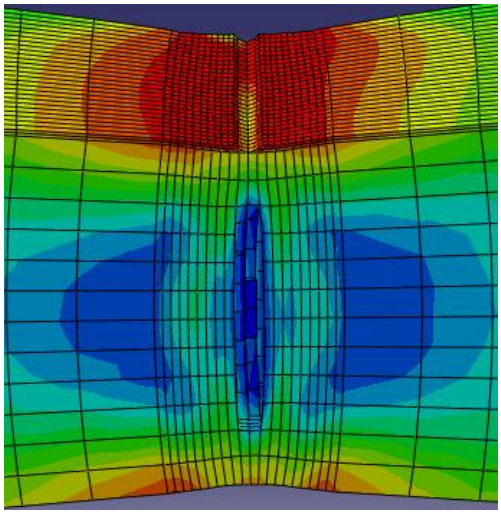

(c) At an applied displacement of 5.76mm

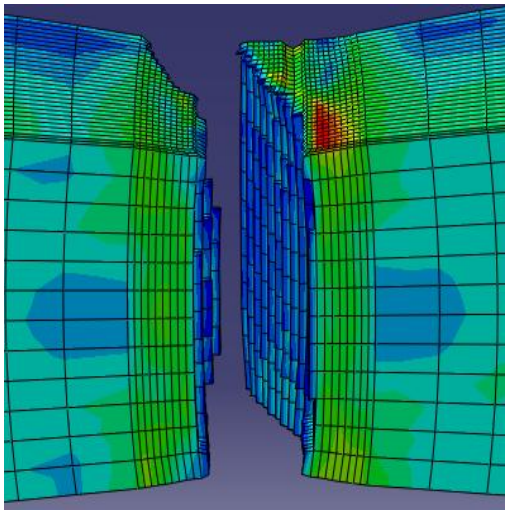

(d) At an applied displacement of 6.73mm

Figure 8.10: Deformed shapes around the across-the-thickness V-shaped scratch at various stages of the tensile testing simulation.

Similarly, the deformed shapes and Mises stress distributions of the whole specimen and of the regions around the V-shaped scratch across the width at an applied displacement of 0.37mm, during necking at an applied displacement of 3.54mm, during fracture initiation at an applied displacement of 5.76mm and after fracturing at an applied displacement of 6.13mm are shown in Figures 8.11 (a), to (d) and Figures 8.12(a), to (d) respectively.

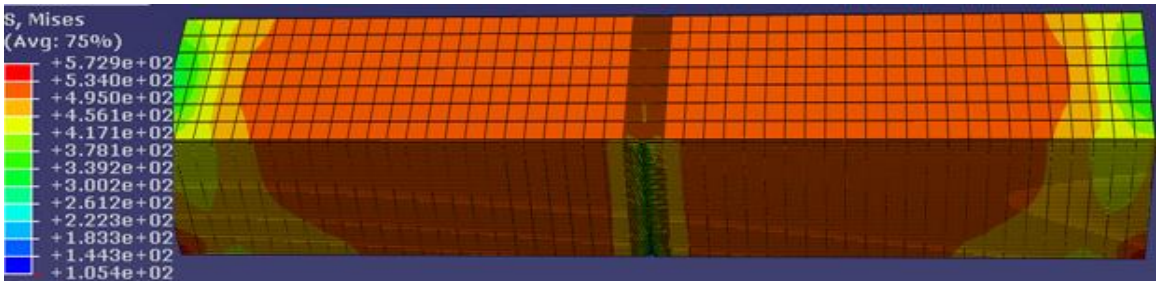

(a) At an applied displacement of 0.37mm.

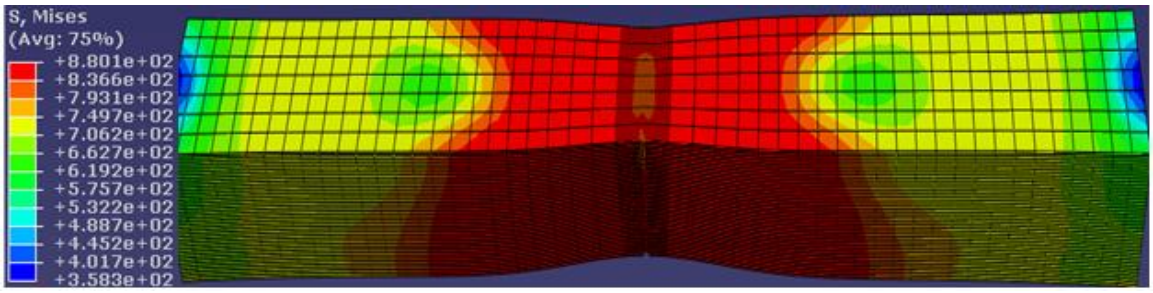

(b) During necking at an applied displacement of 3.54mm

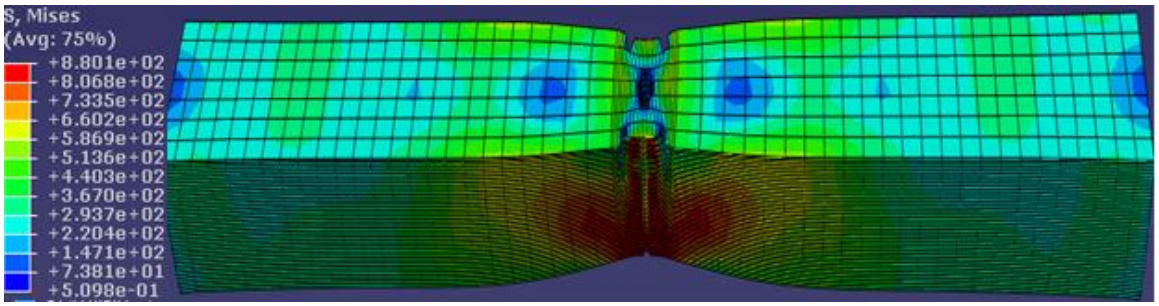

(c) During fracture initiation at an applied displacement of 5.76mm

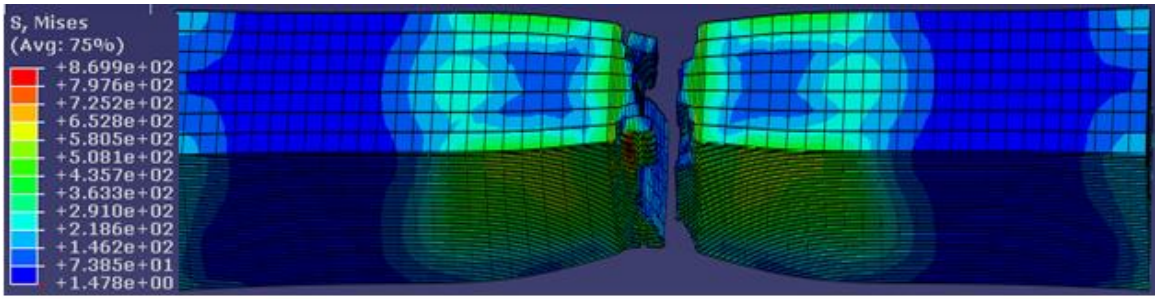

(d) Fractured specimen after the simulation at an applied displacement of 6.73mm

Figure 8.11: Deformed shapes and Mises stress (MPa) distribution for whole model of specimen with across-the-width V-shaped scratch during tensile testing simulation.

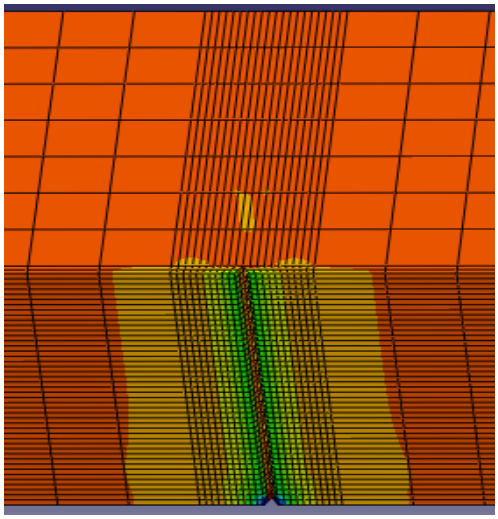

(a) At an applied displacement of 0.37mm.

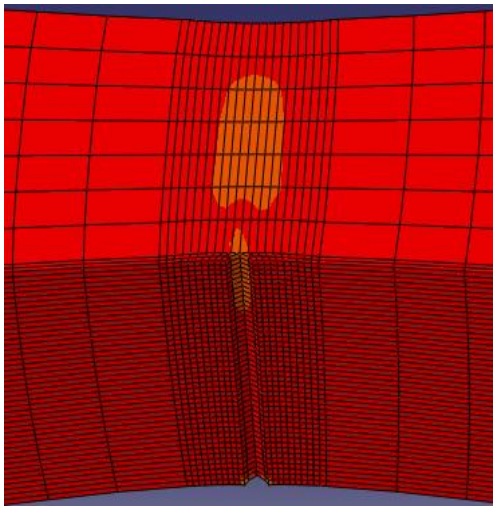

(b) At an applied displacement of 3.54mm

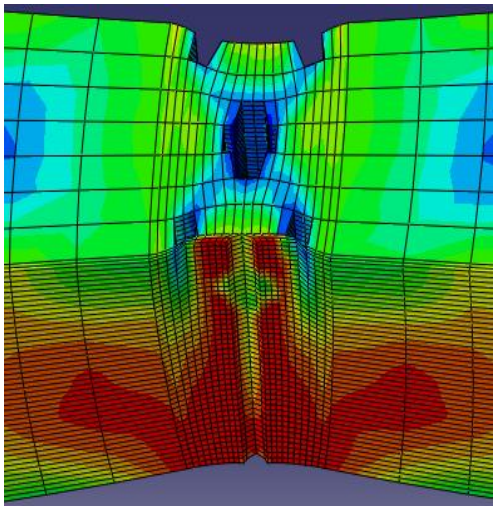

(c) At an applied displacement of 5.76mm

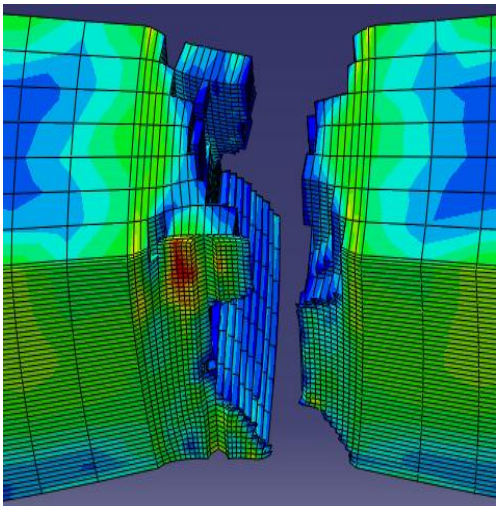

(d) At an applied displacement of 6.13mm

Figure 8.12: Deformed shapes around across-the-width V-shaped scratch during tensile testing simulation.

Figures 8.13 and 8.14 show the variations in the tensile responses obtained from the tensile testing simulations of the wire specimen with across-the-thickness V-shaped scratch and the wire specimen with across-the-width V-shaped scratch with varying V-shaped scratch relative depths.

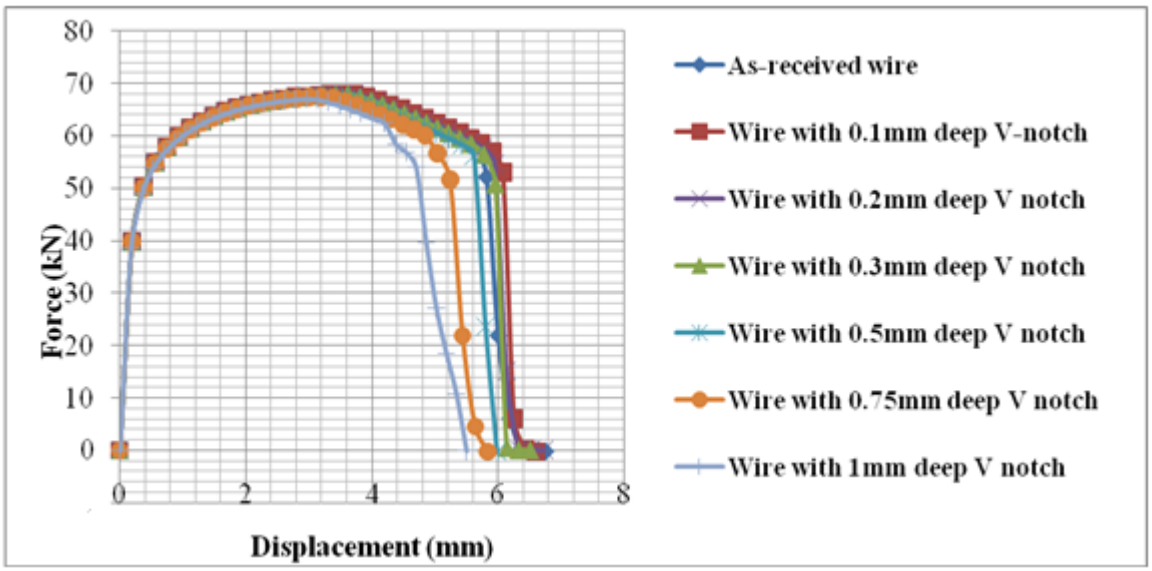

Figure 8.13: Force-displacement variation with across-the-thickness V-shaped scratch depth

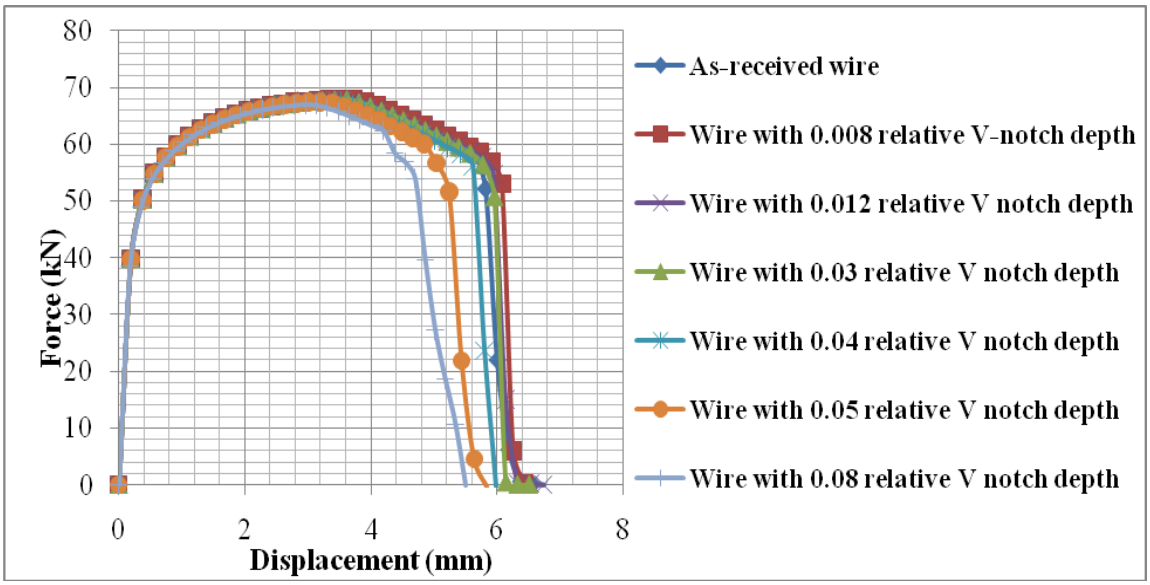

Figure 8.14: Force-displacement variation with across-the-width V-shaped scratch depth.

The variation of the yield loads, the ultimate loads and the fracture displacements with V-shaped scratch relative depth for the wire specimen with across-the-thickness V-shaped scratch and the wire specimen with across-the-width V-shaped scratch are shown in Figures 8.15(a), (b) and (c) respectively.

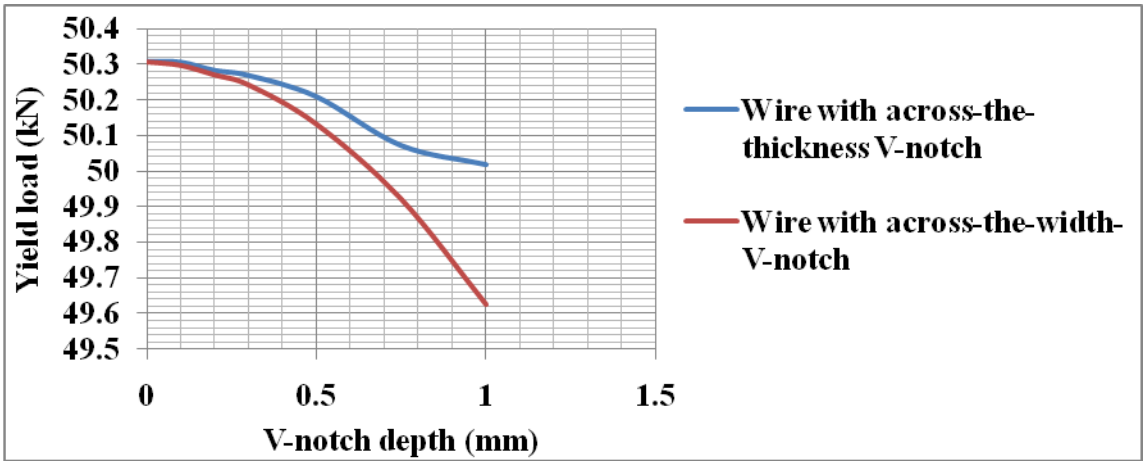

(a) Yield load variation with V-shaped scratch depths

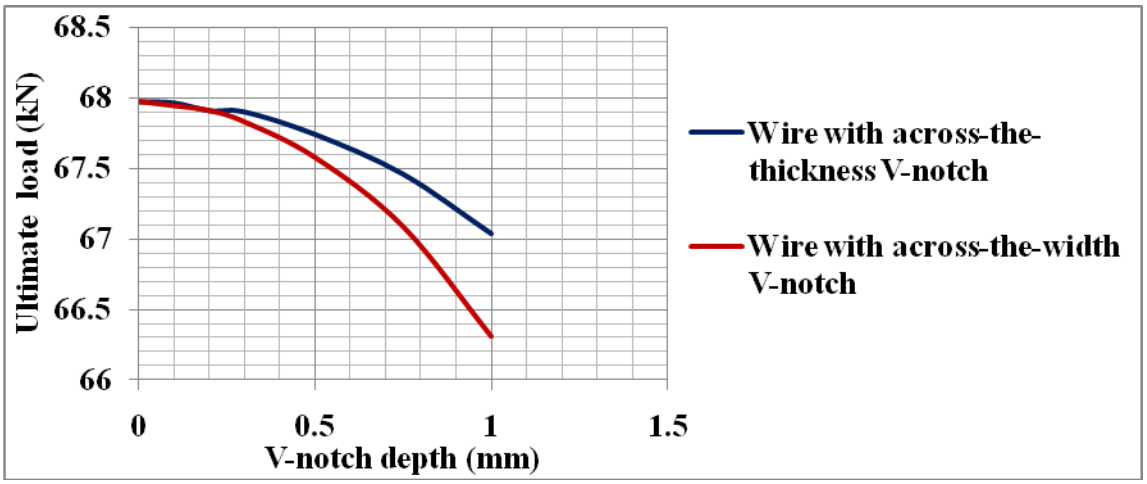

(b) Ultimate load variation with V-shaped scratch depth

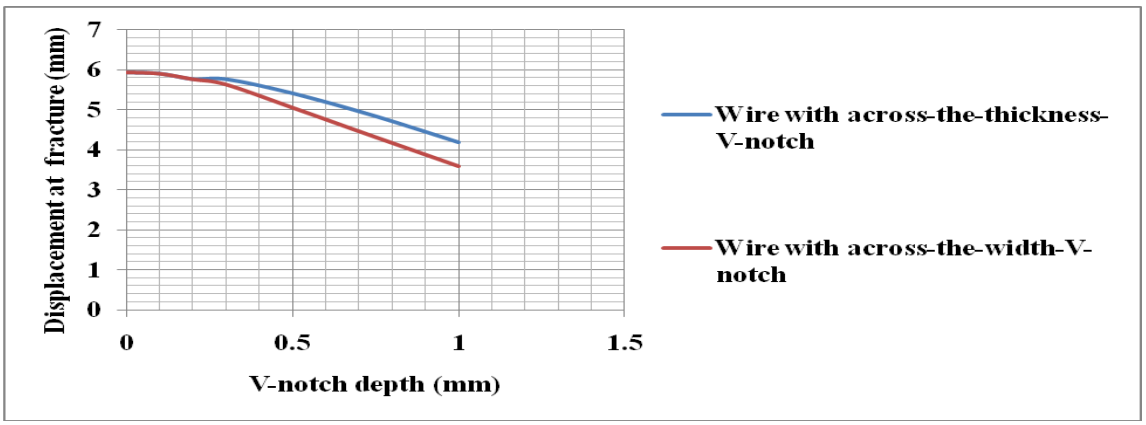

(c) Displacement at fracture variation with V-shaped scratch depth

Figure 8.15: Variation in mechanical properties with across the thickness and across the width V-shaped scratch depths.

8.4.1.1 Analysis of results

As shown in Figures 8.13 and 8.14, the yield load, the ultimate loads and the fracture displacements reduce with increase in relative groove depth for both the specimen with the across-the-thickness groove and the specimen with the across-the-width groove. From Table 8.2, the yield loads, the ultimate loads and the fracture displacements reduced by 0.05 to 0.57%, 0.01to 1.37% and 0.43 to 29.22% respectively due to the presence of the across-the-thickness V-shaped scratch with depths ranging from 0.1mm to 1mm. Similarly, from Table 8.3, the yield loads, the ultimate loads and the fracture displacements reduced by 0.02 to1.36%, 0.04 to 2.44% and 0.56 to 39.66% respectively due to the presence of the across-the-width V-shaped scratch with depths ranging from 0.1mm to 1mm.

Generally, the reduction in these mechanical properties are higher for the specimen with the across the width V-shaped scratch**.** For both specimens, the percentage reduction in the fracture displacement is the highest, followed by the percentage reduction in the ultimate loads with the yield loads having the least percentage reduction. This shows that the presence of the V-shaped scratches have the worst effect on the fracture displacement/strain leading to 0.567% and 39.66% reduction in the ductility of the tensile armour wires for 0.1mm and 1mm V-shaped scratch depths respectively.

Table 8.2: Mechanical properties variation with groove depths for wire specimens with across-the- thickness V-shaped scratch

V-notch depth (mm)	Yield load (kN)	% reduction in yield load (kN)		Ultimate load (kN)	% reduction in ultimate load (kN)		Displacement at fracture (mm)	% reduction in displacement at fracture (mm)
0	50.31			67.97			5.93	
0.1	50.31	0.00		67.97	0.01		5.91	0.43
0.2	50.28	0.05		67.91	0.09		5.77	2.79
0.3	50.27	0.08		67.90	0.11		5.76	2.82
0.5	50.21	0.19		67.74	0.34		5.42	8.69
0.75	50.07	0.47		67.46	0.75		4.85	18.28
1	50.02	0.57		67.04	1.37		4.20	29.22

Table 8.3: Mechanical properties variation with groove depths for wire specimens across-the-width V-shaped scratch

V-notch depth (mm)	Yield load (kN)	% reduction in yield load (kN)		Ultimate load (kN)	% reduction in ultimate load (kN)		Displacement at fracture (mm)	% reduction in displacement at fracture (mm)
0	50.31			67.97			5.93	
0.1	50.30	0.02		67.94	0.04		5.90	0.56
0.2	50.27	0.07		67.91	0.09		5.76	2.92
0.3	50.24	0.13		67.83	0.21		5.63	5.11
0.5	50.13	0.35		67.58	0.58		5.05	14.88
0.75	49.92	0.77		67.09	1.30		4.31	27.35
1	49.62	1.36		66.31	2.44		3.58	39.66

8.4.2 Effects of mid-thickness, mid-width and edge V-shaped scratch on tensile properties of tensile armour wires.

Figure 8.16 shows the locations at which the 0.2mmx0.2mm base/plan and 0.2mm deep edge V-shaped scratch, mid-thickness V-shaped scratch and mid-width V-shaped scratch were cut out of the model of the as-received tensile armour wire specimen.

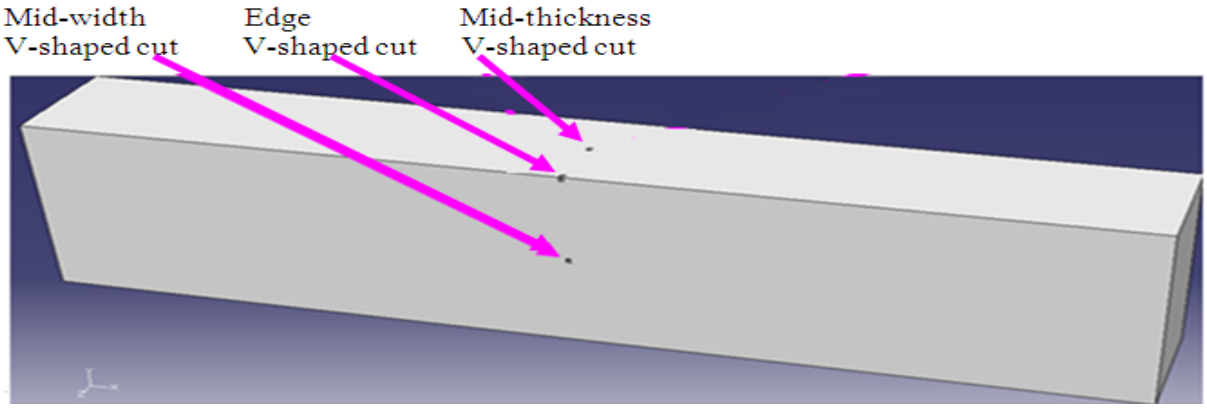

Figure 8.16: Locations of the edge groove, mid-thickness groove and mid-width groove.

Cutting out a scratch in the 3 dimensional model of the tensile armour wire can only be done by sketching the two dimensions (plan) of the scratch and extruding the sketched plan in the

third direction that is perpendicularly to the sketched plan. With this provision, it was possible to readily cut out the full edge V-shaped scratch from the full wire model by extruding the triangular/V-shaped plan sketched along the length and the width in the thickness direction as shown in Figure 8.22(a).

The full mid-thickness V-shaped scratch and the full mid-width V-shaped scratch could not be cut out from the full wire model because it was not possible to extrude the 0.2mmx0.2mm square base/plan of the scratches at an angle less than 90 degrees required to form the triangular/V-shaped cut. In order to model the mid-thickness V-shaped scratch, half the size of the mid-width V-shaped scratch and half the size of the mid-thickness V-shaped scratch were cut out of the models with half the thickness and half the width of the wire. Figure 8.17 (a), (b) and (c) shows the refined mesh around the full edge V-shaped scratch, and the refined mesh and the symmetry boundary condition around the half mid-width V-shaped scratch and the half mid-thickness V-shaped scratch respectively.

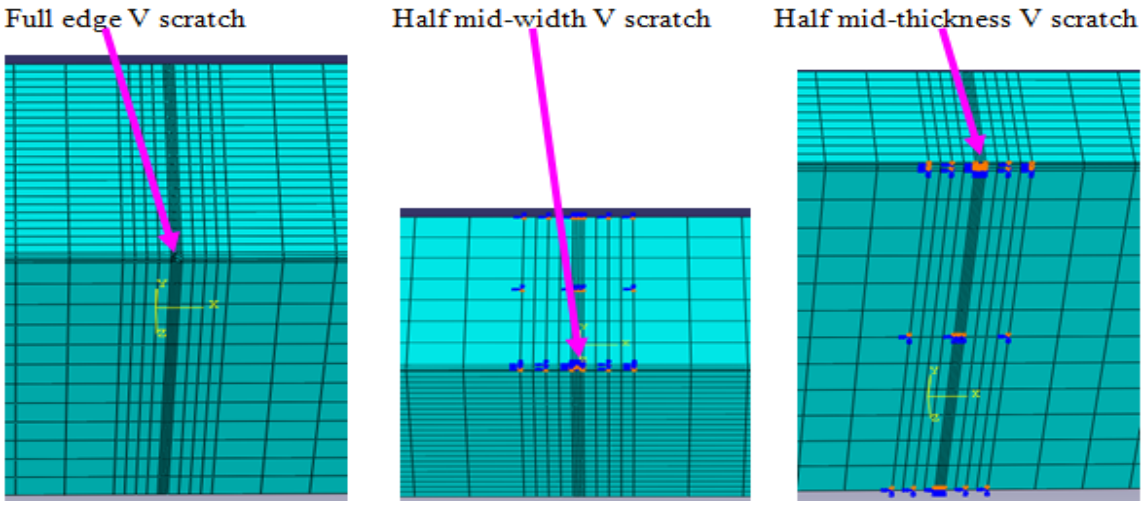

(a) Full edge V scratch. (b) Half mid width V scratch. (c) Half mid thickness V

Figure 8.17: Refined mesh and symmetry boundary condition around full edge, half mid-width and half mid-thickness V-shaped scratches.

The deformed shapes showing the Mises stress distributions in the whole during necking at an applied displacement of 3.74mm, during fracture initiation at an applied displacement of 5.92mm and after fracturing of the specimens at an applied displacement of 6.38mm are shown in Figures 8.18, 8.19 and 8.20 respectively for the specimens with the edge, mid-thickness and mid-width V-shaped scratch.

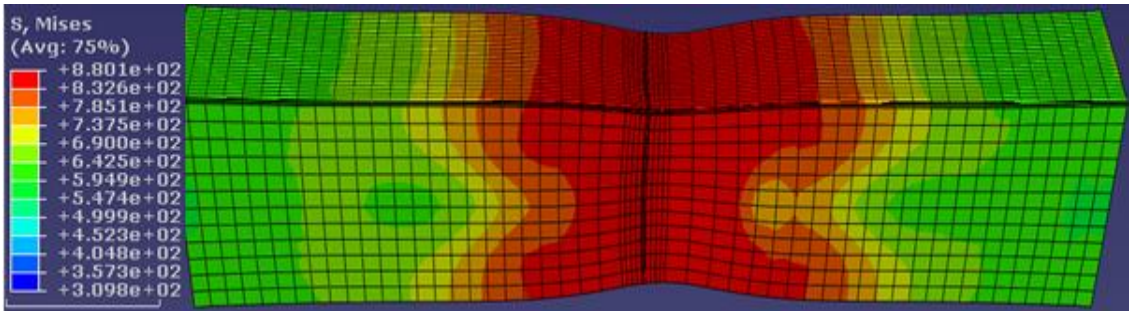

(a) Full wire model with full edge V-shaped scratch

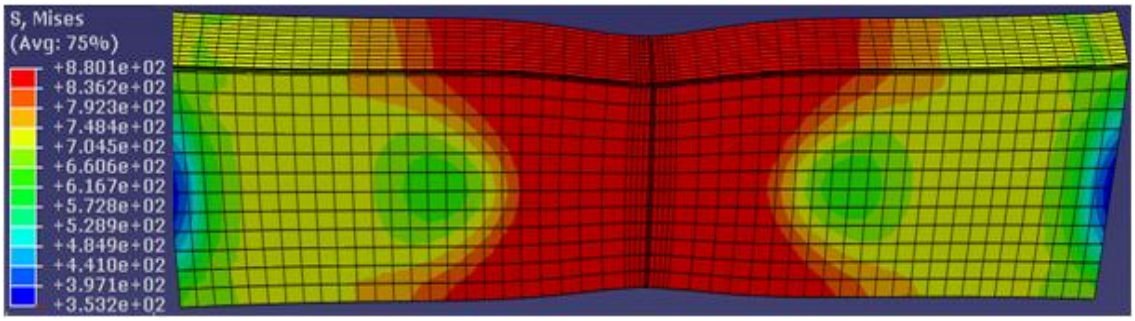

(b) Half wire model with half mid-thickness V-shaped scratch

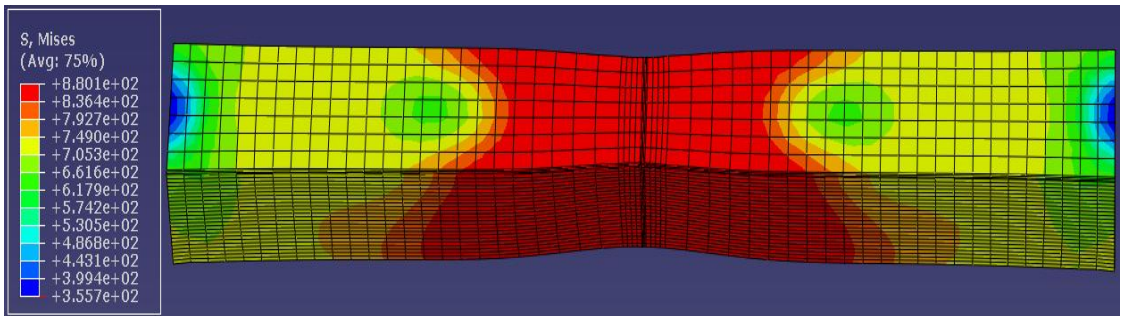

(c) Half wire model with half mid-width V-shaped scratch

Figures 8.18: Deformed shapes and Mises stress (MPa) distribution for wire models with edge, mid-thickness and mid-width V-shaped scratch during necking at an applied displacement of 3.74mm

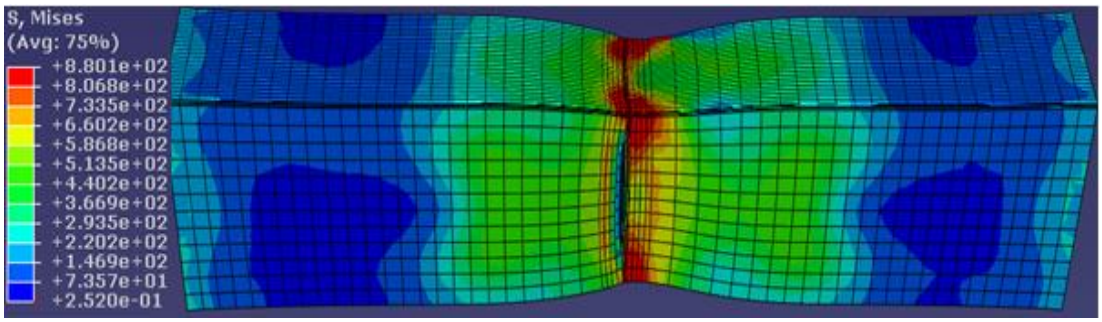

(a) Full wire model with full edge V-shaped scratch

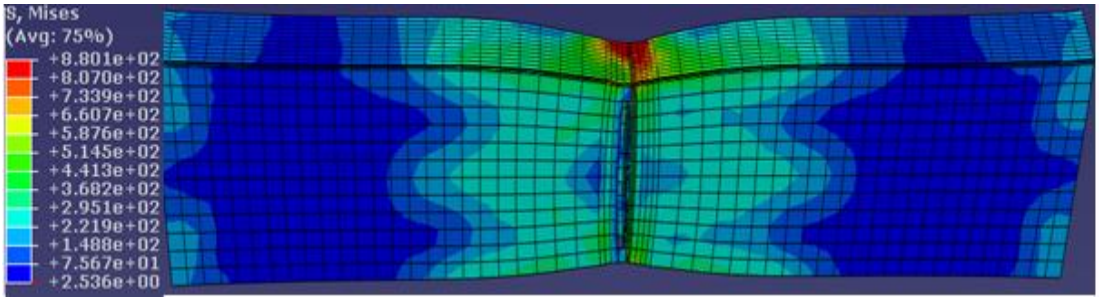

(b) Half wire model with half mid-thickness V-shaped scratch

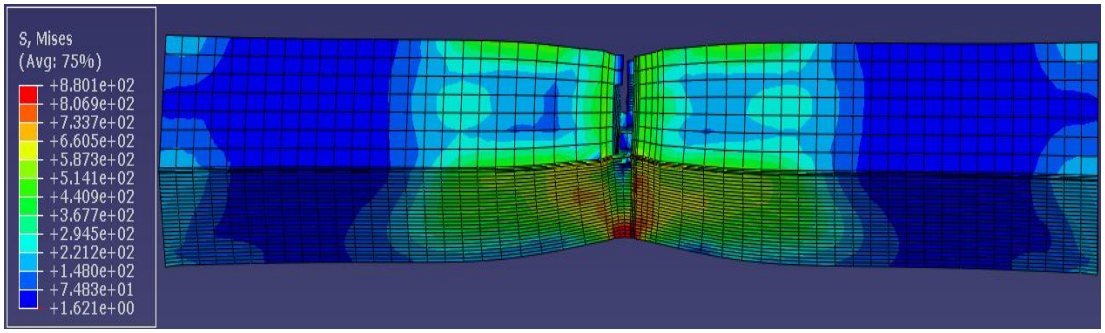

(c) Half wire model with half mid-width V-shaped scratch

Figures 8.19: Deformed shapes and Mises stress (MPa) distribution for wire models with edge, mid-thickness and mid-width V-shaped scratch during fracture initiation at an applied displacement of 5.92mm

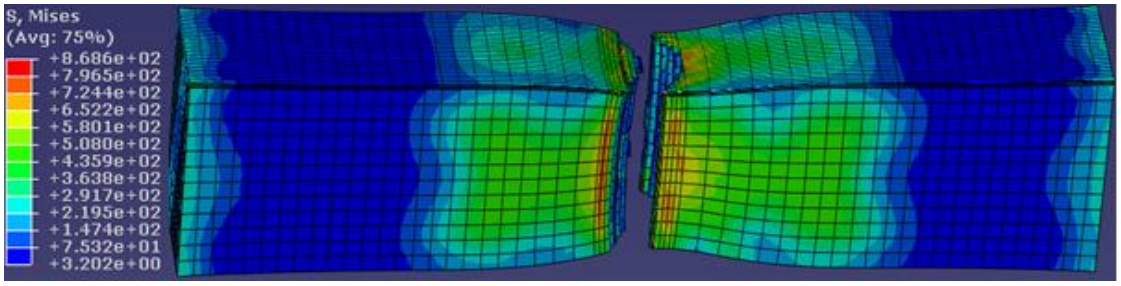

(a) Full wire model with full edge V-shaped scratch

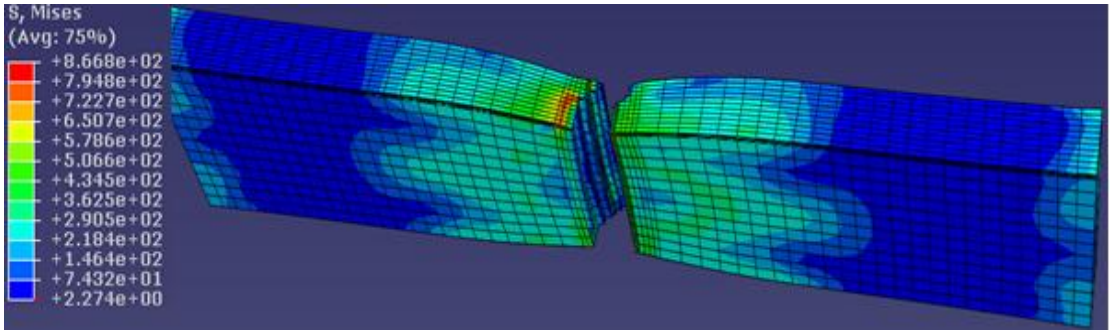

(b) Half wire model with half mid-thickness V-shaped scratch

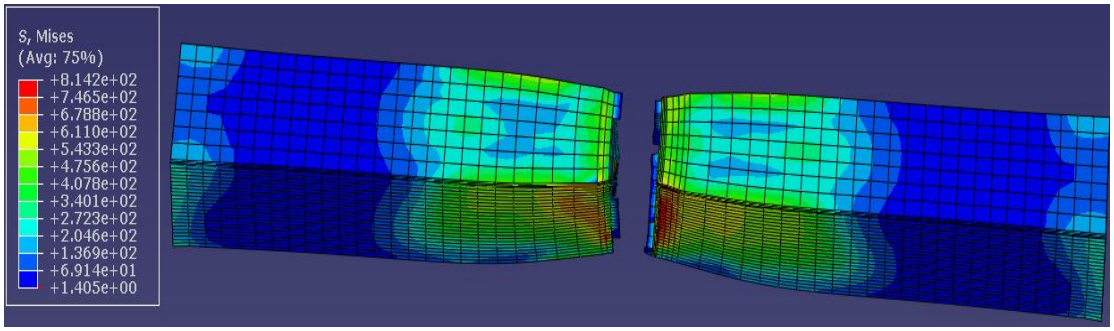

(c) Half wire model with half mid-width V-shaped scratch

Figures 8.20: Deformed shapes and Mises stress (MPa) distribution for wire models with edge, mid-thickness and mid-width V-shaped scratch after fracture at an applied displacement of 6.38mm.

As shown in Figure 8.21, there is no noticeable difference in the force-displacement responses of the specimens with the edge, mid-thickness and mid-width V-shaped scratches. Thus, the location of the miniature V-shaped scratches does not make any significant difference to the tensile responses of the tensile armour wire. With this observation, it can be inferred that the higher reduction in the mechanical properties of tensile armour wire with the across-the-width V-shaped scratches when compared with the specimen with the across-the-

thickness V-shaped scratches observed in section 8.4.1.1 is due to the longer length of the across-the-width V-shaped scratches groove (12mm) compared with the 7mm long across-the-thickness groove.

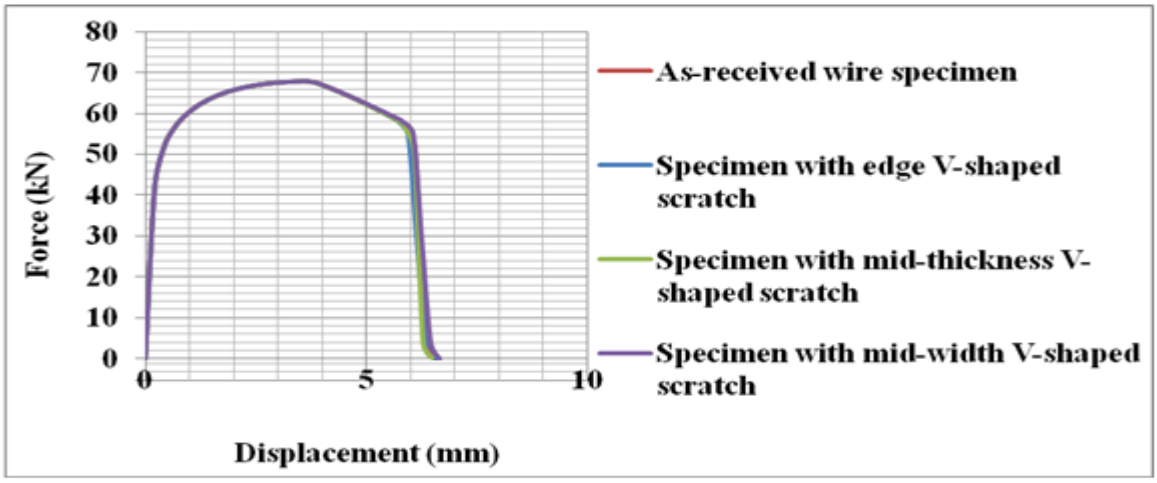

Figure 8.21: Force-displacement curves for 12mmx7mm, 50mm gauge length specimens with mid-thickness, mid-width and edge V-shaped scratches.

8.5 Summary

This chapter presents the results of the investigation of the effects of the V-shaped scratches on the tensile properties of the tensile armour wires. The investigation revealed that the presence of the V-shaped scratches reduces the yield load, the ultimate load and the displacement at frcture of the wires. The presence of the V-shaped scratches with dimensions less than 0.2mm which cannot be detected by the eddy current detector used in the flexible pipes manufacturing industry will not reduce the yield load, the ultimate load and the fracture displacement of the wire by more than 0.07%, 0.09% and 2.92% respectively. The presence of the V-shaped scratches have the worst effects on the ductility (in terms of displacements at fracture), followed by the ultimate loads (and invariably the tensile strength) with the least effect on the yield load (and invariably the yield strength) of tensile armour wires. The extent of the reductions in the wire tensile properties depends largely on the size rather than the location of the V-shaped scratches.

Having dealt with the effects of the V-shaped scratches on the tensile properties of the tensile armour wires, the investigation of the effects of denting on the tensile properties of the tensile armour wires is presented in the next chapter.

Chapter 9 Effect of miniature dents on tensile properties of tensile armour wires

Dents are one of the surface defect types that BS EN ISO13628-2, (2006) recommends should be looked out for and which were identified in the SEM image of the surface of the as-received tensile armour wires shown in Figure 9.1(a). The investigation of the effects of miniature dents on the tensile behaviour and the tensile properties of tensile armour wires with 12mm x 7mm cross sectional dimensions was carried out using both laboratory and numerical tensile testing methods. The numerical tensile testing of dented wire specimens was carried out using the finite element method to simulate the indentation of the wire specimens, the removal of the indenter after indentation and the tensile testing of the dented wire specimens in three FE simulation steps. The indentation simulation was verified with an analytical expression while the simulations of the tensile testing of the as-received (dent free) and dented tensile armour wires specimens were validated with experimental results. The effects of the sizes and locations of the miniature dents with dimensions close to the 0.2mm detection capability of the in-line eddy current detector used in the flexible pipe manufacturing industry were considered.

The laboratory tensile testing of the as-received wire specimens and the wire specimens dented with a ball bearing indenter is presented in section 9.1. The FE simulations of the tensile testing of the as-received wire specimens, and the contact simulation and its verification are presented in sections 9.2 and 9.3 respectively. Section 9.4 presents the simulation of the tensile testing of dented tensile armour wires and its validation. The effect of the dent sizes and locations on the tensile properties of the tensile armour wires is presented in section 9.5. The analysis of results and conclusions are presented in sections 9.6 and 9.7respectively.

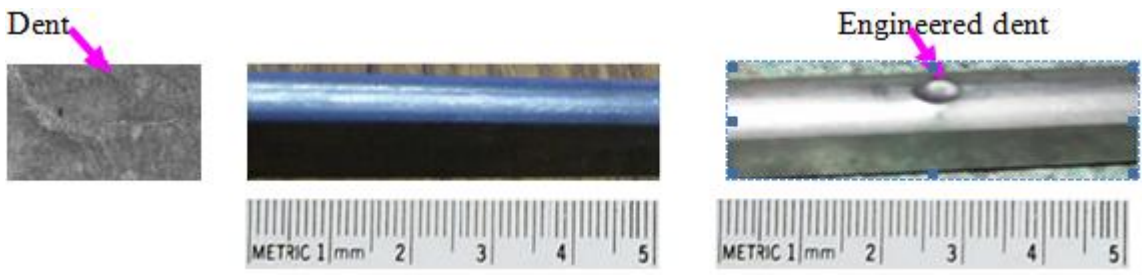

(a) SEM image (b) As-received wire specimen (c) Dented wire specimen

Figure 9.1: As-received and dented wire specimens

9.1: Laboratory tensile testing of as-received and dented wire specimens

Laboratory tensile tests were carried out on the as-received tensile armour wire specimens and on the wire specimens dented to a depth of 0.3mm with a 6.35mm diameter ball bearing indenter shown in Figures 9.1(b) and (c) respectively. The force-displacement curves and the mechanical properties obtained from the laboratory tensile testing of the as-received wire specimen and the wire specimen with 0.6mm diameter, 0.3mm deep dent are shown in Figure 9.2. The dent was made with a 6.35mm diameter ball bearing to ensure that the engineered dent is substantially larger than any inherent dent in the wire for its effect to be dominant on the tensile behaviour of the wire, as it was observed that failure did not occur at the locations of the dents made with the standard Rockwell hardness scale B (1.588mm diameter ball indenter under 100kgf/980.6N) indenter. This could be because the dent made by the standard Rockwell hardness scale B indenter was not larger than the inherent dents in the wire.

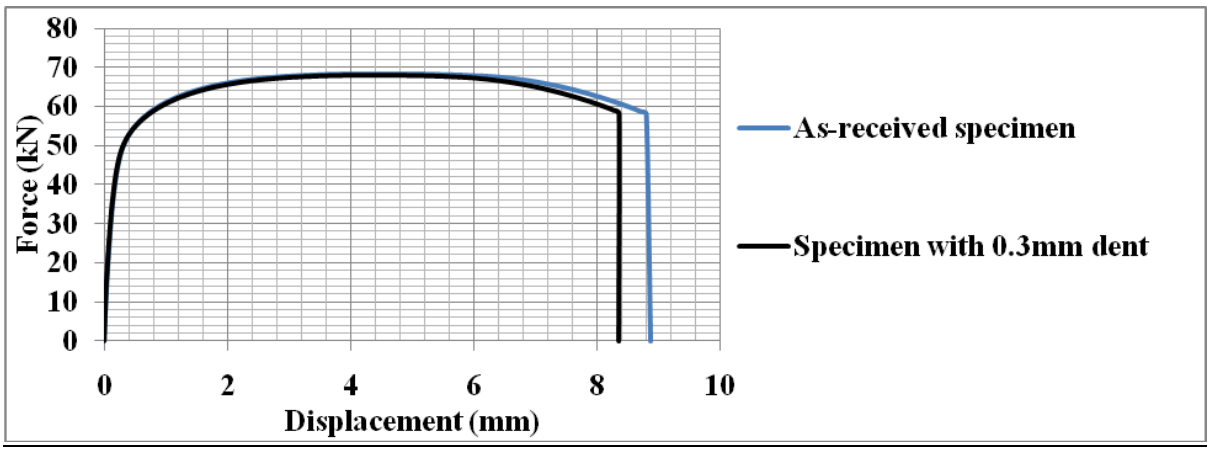

Figure 9.2: Force-displacement curves from laboratory tensile testing of 12mmx7mm 50mm gauge length as-received and dented wire specimens.

Table 9.1: Mechanical properties of as-received and dented wire specimens

Parameters	As received specimen	Dented specimen	Percentage difference
Ultimate load (kN)	68.25	67.82	0.63
Fracture load (kN)	57.95	58.13	0.30
Fracture point displacement (mm)	8.81	8.37	5.06

The denting caused 0.3% and 5.06% reduction in the ultimate load and the fracture displacement (ductility) of the wire as shown in Table 9.1. The reduction in the ductility of the dented wire can be attributed to the work hardening of the dented region, while the slight reduction in the ultimate load of the dented wire can be attributed to the residual stress due to the indentation and/or the stress concentration effects of the dent.

9.2 FE simulation of tensile testing of as-received wire specimen

The FEA tensile testing simulation of the as-received wire specimen has been dealt with in section 7.2 and the modelling techniques used have been shown to be appropriate as the result of the FE has been validated in the same section. Consequently, the FEA tensile testing simulation of the as-received wire, its results and validation are not repeated.

9.3 FE indentation simulation.

The simulation of the indentation of the top surface of the tensile armour wire was carried out using the assembly shown in Figure 9.3. The bottom, left and right ends of the wire specimen were fixed and the 10mm diameter rigid spherical indenter placed 1mm above the top surface of the wire specimen was subjected to downward vertical displacement until it contacted and dented the wire surface as shown in Figure 9.6(b). The contact interaction between the indenter and the wire surface was carried out using a penalty contact interaction to enable both shear and normal forces to be transmitted across the interface of the two surfaces**.** The coefficient of friction of 0.0 was used for the simulation of the frictionless contact between the indenter and the square plate in section 9.3.1, which was conducted to verify the contact simulation output. The coefficient of friction of 0.3 was used for the simulation of the indentation of the tensile armour wires which is within the 0.0 to 0.3 generally used in literature, (such as the publications by Montmitonnet et al, (1993), Verleene et al, (2002) and Nayebi et al, (2002)) for the simulation of indentation of steel.

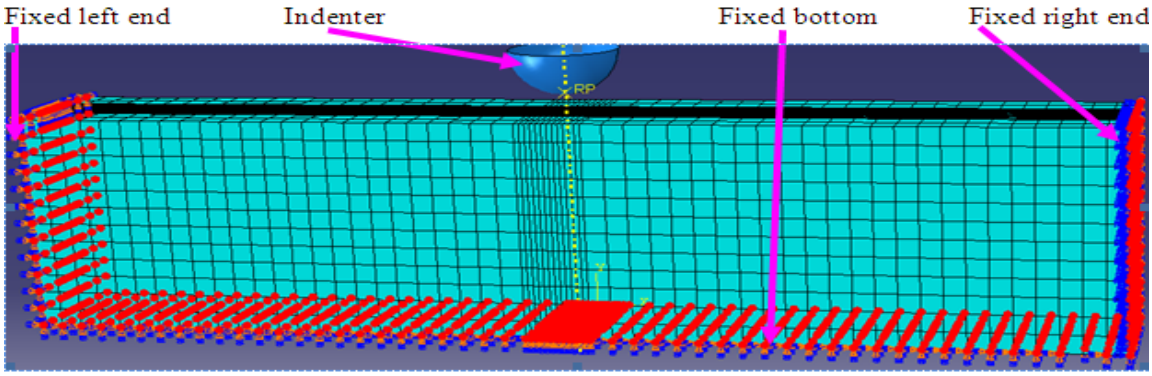

(a) Wire specimen-indenter assembly before indentation with end boundary conditions.

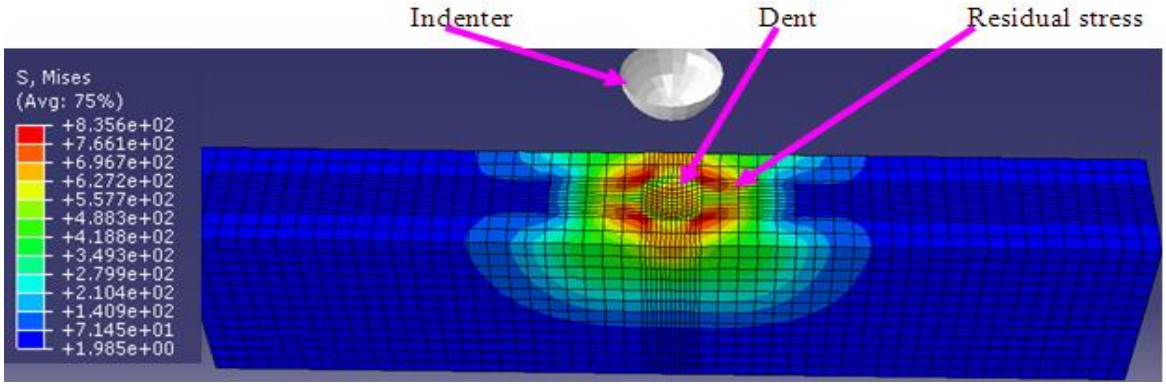

(b) Dented wire with residual Mises stress (MPa)

Figure 9.3: Wire specimen-indenter assembly before and after indentation.

9.3.1 Verification of indentation simulation output

The accuracy of the indentation and contact interaction simulations was verified by comparing the power law relating the FE predicted indenter force to indenter displacement with the analytical power law expression given in equation 9.1 that relates indenter force to indenter displacement. As stated in section 2.21.1, this analytical expression relates the spherical indenter force, F, to the indenter displacement, δ , in an elastic indentation (elastic response at small indent depth) of infinite plates. Infinite plates have widths and thicknesses that are very large compared with the dent or the defect dimension, which ensures that there are no stress relaxations in the plate and also ensures that the outer boundaries of the plate exert no influence on the stresses in the dented or defective area.

$$F = K\delta^n \tag{9.1}$$

Where K and n are constants. n is taken as 1.5 for spherical indentation.

However, as shown in Figure 9.3(b), due to the size of the tensile armour wires, the residual stress around the dent extends to the outer edges of the wire leading to stress relaxations in the wires and the interference of the outer boundaries or edge of the wire with the stress state in the dented area. Thus, the sizes of the tensile armour wires make it impossible to achieve the conditions required for using equation 9.1 to validate the indentation simulation output. Consequently, a simulation of the elastic indentation of a 50mm square plate with the same 12mm thickness as the tensile armour wires with a 10mm indenter shown in Figure 9.4 was carried out in order to be able to validate the indentation simulation with the analytical expression. With dent depths of up to 1mm, the plate has a dimension that is at least ten times the dent dimension, which is sufficient to fulfil the required conditions obtainable in infinite plates. The mesh around the location of the indentation of the plate was successively refined and seeded with 0.5mm and 0.25mm elements as shown in Figures 9.4

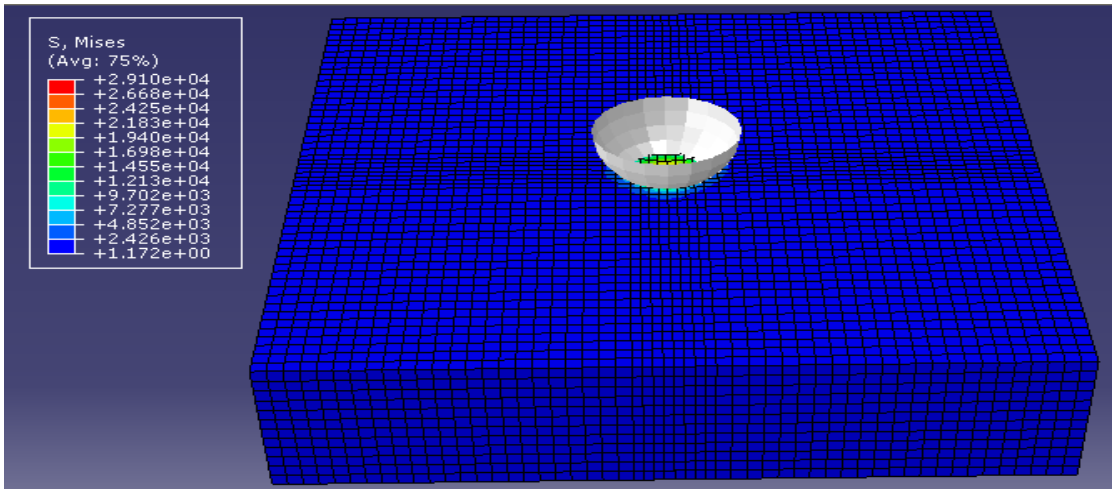

Figure 9.4: Deformed shape showing Mises stress (MPa) distribution for a dented infinite plate at the end of indentation simulation.

As stated in section 2.21.1, the K in equation 9.1 and n depend on the mechanical material parameters and on the indenter geometry. For a spherical indenter, n is 1.5 while K is given in equation 9.2

$$K = \left(\frac{4E^{*}R^{0.5}}{3} \right) \tag{9.2}$$

Where R is the radius of the spherical indenter and E^{*} is the effective modulus obtained from the Hertz equation given in equation (9.3).

$$\frac{1}{E^*} = \frac{1-\upsilon^2}{E} + \frac{1-\upsilon_{Ind}^2}{E_{Ind}} \tag{9.3}$$

Where E and ν are the Young's modulus and Poisson's ratio, respectively of the dented material and E_{Ind} and ν_{Ind} are the Young's modulus and Poisson's ratio, respectively of the indenter. For a non deformable indenter, E_{Ind} is approximately infinity (∞). Hence equation 9.3 becomes

$$\frac{1}{E^*} = \frac{1-\upsilon^2}{E} + \frac{1-\upsilon_{Ind}^2}{\infty} \rightarrow \frac{1-\upsilon^2}{E} \tag{9.4}$$

Substituting ν of 0.3 and E of 200GPa for steel in equation 9.4, E* is calculated in equation 9.5 as follows:

$$E^* = \frac{E}{1-\upsilon^2} = \frac{200000}{1-0.3^2} = 2.19x10^5 \, N/mm^2 \tag{9.5}$$

Substituting the calculated value of E and the indenter radius R of 5mm, K is calculated in equation 9.6 as follows:

$$K = \left(\frac{4X219789X5^{0.5}}{3} \right) = 6.55x10^5 \, N/mm^{-3/2} \tag{9.6}$$

Fitting a power law curve to the indenter force-displacement curve predicted by the simulation carried out with 0.25mm elements in the refined area at the location of the indentation as shown in Figure 9.5 gives a K value of 6.58 $X10^5 Nmm^{-3/2}$, which compares well with the K value of $6.56X10^5 Nmm^{-3/2}$ obtained from the analytical equation. This shows that the refinement at the location of the indentation with 0.25mm elements is sufficient, and the indentation and contact interaction simulations carried out with the 0.25mm refined elements at the location of the indentation is accurate.

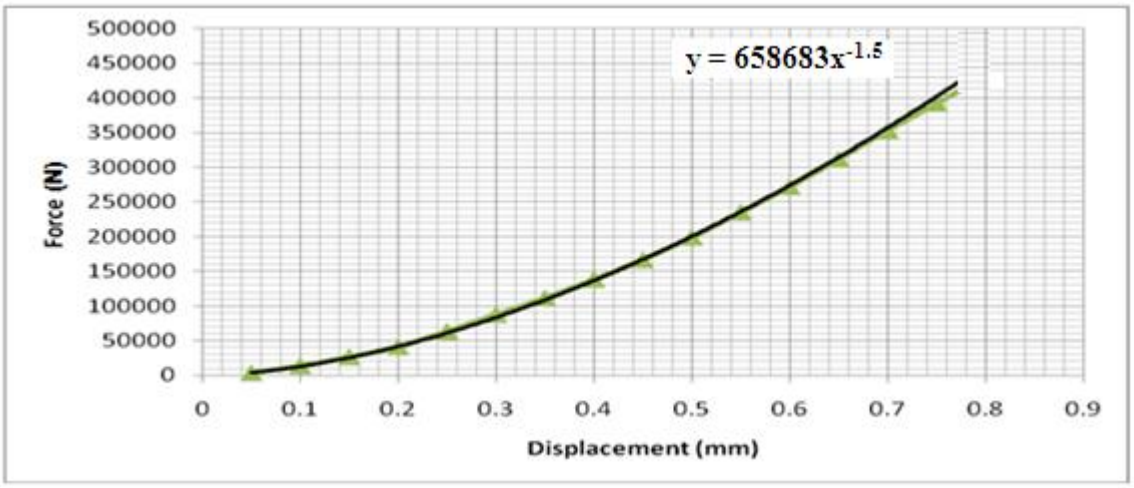

Figure 9.5: Power curve on indenter force-displacement curve predicted by simulation with refined mesh at location of indentation.

9.4 Simulation of tensile testing of dented tensile armour wires

The simulation of the tensile testing of the dented tensile armour wires was carried out with indentation, indenter removal and tensile testing simulation steps. During the indentation and the indenter removal simulations, the bottom of the specimen and the left and right ends were fixed. During the tensile testing simulation, only the left end of the specimen was fixed and the right end, which is free to move in the longitudinal direction (x-axis) was subjected to a longitudinal displacement. An indenter with the same 6.35mm diameter as the ball bearing indenter used for denting the laboratory tensile test specimen was positioned 1mm above the top surface of the wire and was subjected to a downward vertical displacement (in the Y-axis direction) of 1.315mm which dented the wire to a depth of 0.3mm as the dented experimental specimen.

The deformed shape of the wire showing the longitudinal axial stress (S_{11}) and the equivalent plastic strain distributions in the wire after the denting or indentation simulation is shown in Figures 9.6(a) and (b) respectively. In the longitudinal axial stress S_{11} contour plot, the positive stresses represent tensile stresses while the negative stresses represent compressive stresses. The highest tensile stress is indicated at the top of the contour plot with the deepest red colour while the highest compressive stress is indicated at the bottom of the contour plot with the deepest blue colour.

As shown in Figures 9.6, the stresses at the location of the indentation (directly under the indenter) and at some distance around it are compressive because the elements in this regions

were directly and indirectly compressed by the indenter during the indentation. The highest equivalent plastic strain and compressive longitudinal axial stress of 1550MPa is directly under the indenter as the elements that are directly under the indenter experience the most compression. The stresses in the remaining part of the specimen outside the area with compressive stresses are tensile. This is because the elements in this part were not directly compressed by the indenter but were stretched as the elements in the region under compression deflected during indentation. The highest tensile longitudinal axial stress occurred at the edge of the wire closest to the location of the indentation as they are stretched most during the deflection associated with the indentation.

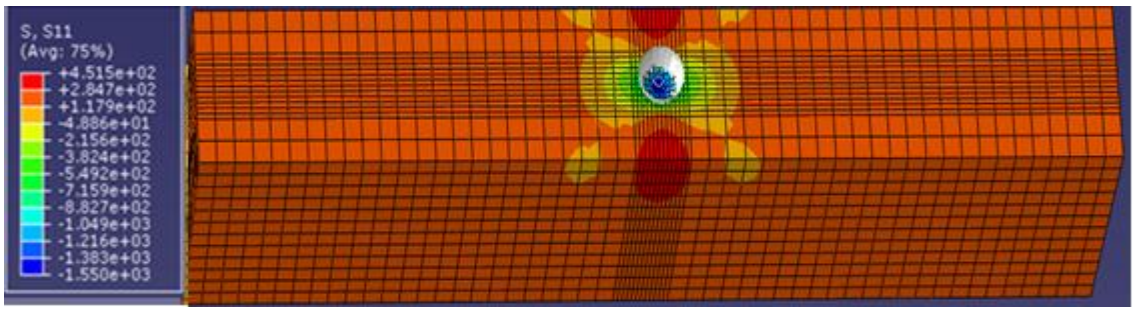

(a) Longitudinal axial stress (MPa) distribution

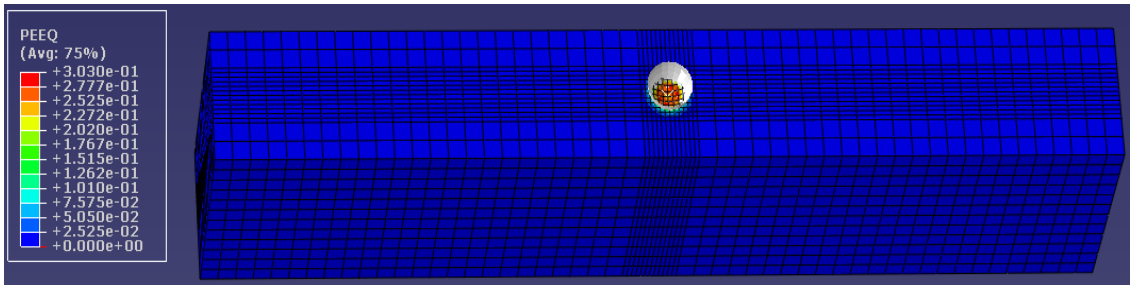

(b) Equivalent plastic strain distribution

Figure 9.6: Deformed shape showing longitudinal axial stress (MPa) and equivalent plastic strain distributions after indentation.

During the indenter removal simulation, the indenter was given an upward vertical displacement which pulled up the indenter and separated it from the surface of the wire as shown in Figure 9.7. The deformed shape of the wire showing the longitudinal axial stress (S_{11}) and the equivalent plastic strain distributions in the wire after the indenter removal simulation is shown in Figures 9.7(a) and (b) respectively. The maximum longitudinal axial compressive stress which reduced to 795.2MPa after the indenter removal simulation still

occurred around the bottom of the dent. The reduction in the axial stress is due to the stress relaxation in the wire and the rebounding of the dent due to the elastic recovery after the removal of the indenter.

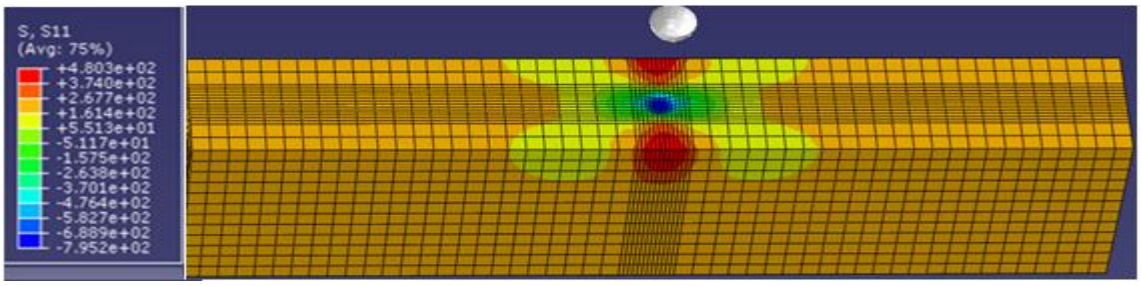

(a) Longitudinal axial stress (MPa) distribution

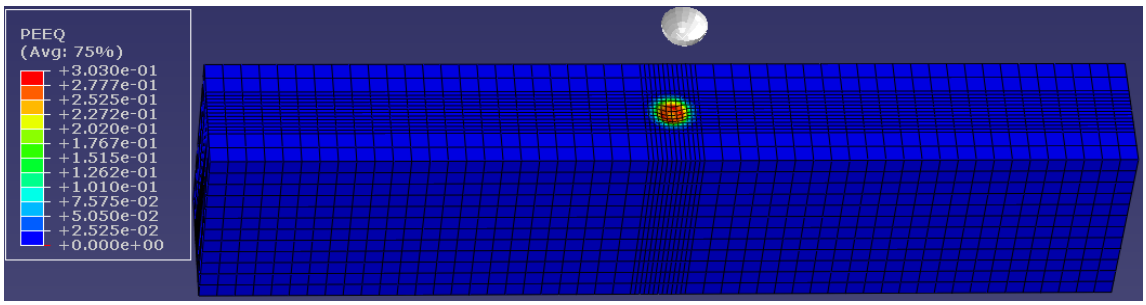

(b) Equivalent plastic strain distribution

Figure 9.7: Deformed shape showing longitudinal axial stress (MPa) and equivalent plastic strain distributions after indenter removal.

The stress state in the wire specimen at the end of indenter removal simulation represents the residual stress in the wire at the beginning of the tensile testing simulation. From Figure 9.8(a), the 795.2MPa residual compressive stress at the location of indentation reduced rapidly to 173.8MPa at the beginning of the tensile testing simulation due to the applied tensile stress in the specimen which neutralised part of the compressive stresses. As the applied tensile load increased, the compressive stress at the location of the indentation progressively decreased until it became tensile as shown Figure 9.9 (a). Figure 9.9(a) also shows that the maximum tensile longitudinal axial stress of 1016MPa occurred at the location of the indentation/dent. This is due to the stress concentration effect of the dent. The deformed shapes of the specimen showing the longitudinal axial stress and the equivalent plastic strain distributions after necking and during fracturing are shown in Figures 9.10 (a) and (b), and 9.11 (a) and (b) respectively.

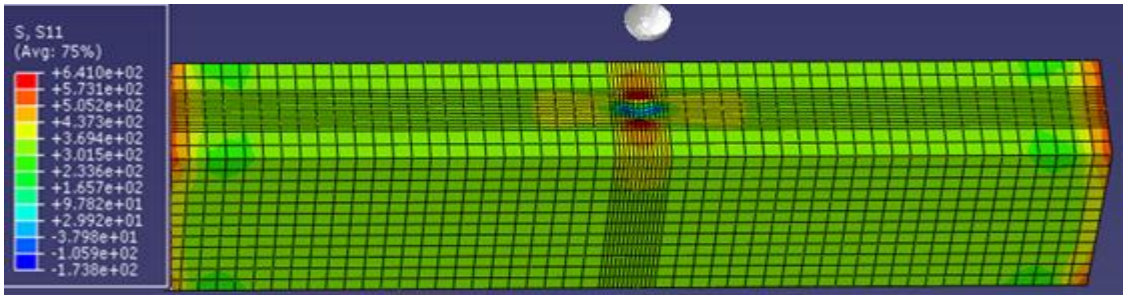

(a) Longitudinal axial stress (MPa) distribution

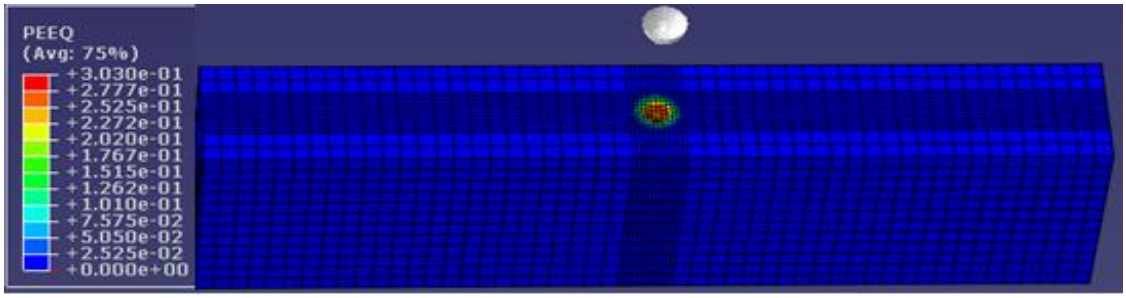

(b) Equivalent plastic strain distribution

Figure 9.8: Deformed shape showing longitudinal axial stress (MPa) and equivalent plastic strain distributions at an applied displacement of 0.18mm.

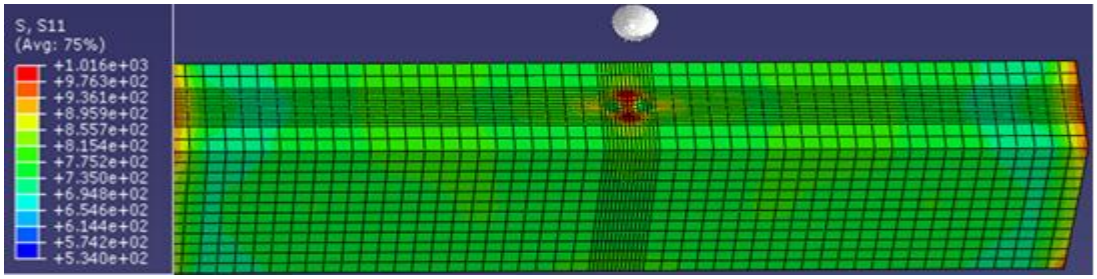

(a) Longitudinal axial stress (MPa) distribution

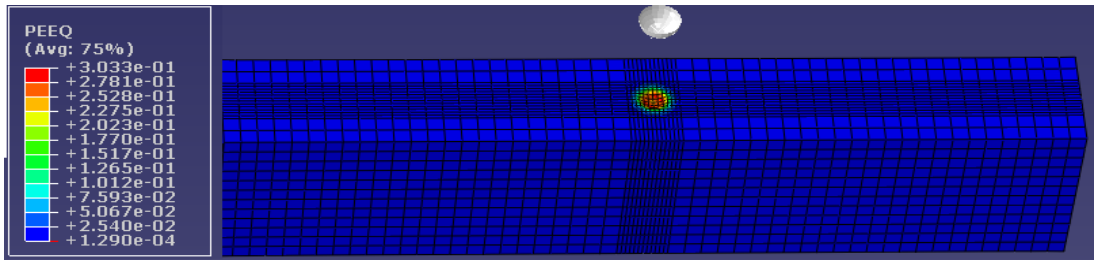

(b) Equivalent plastic strain distribution

Figure 9.9: Deformed shapes showing longitudinal axial stress (MPa) and equivalent plastic strain distributions at an applied displacement of 2.80mm.

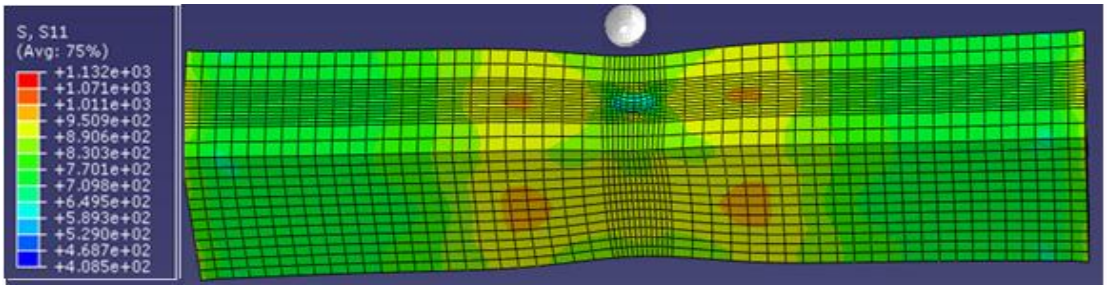

(a) Longitudinal axial stress (MPa) distribution

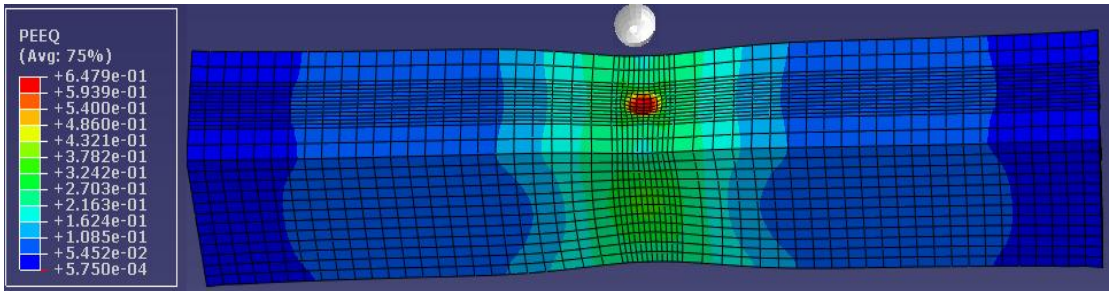

(b) Equivalent plastic strain distribution

Figure 9.10: Deformed shapes showing longitudinal axial stress (MPa) and equivalent plastic strain distributions at an applied displacement of 3.68mm.

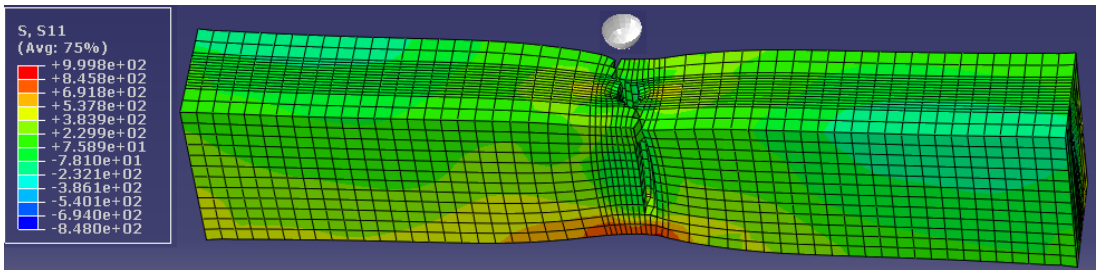

(a) Longitudinal axial stress (MPa) distribution

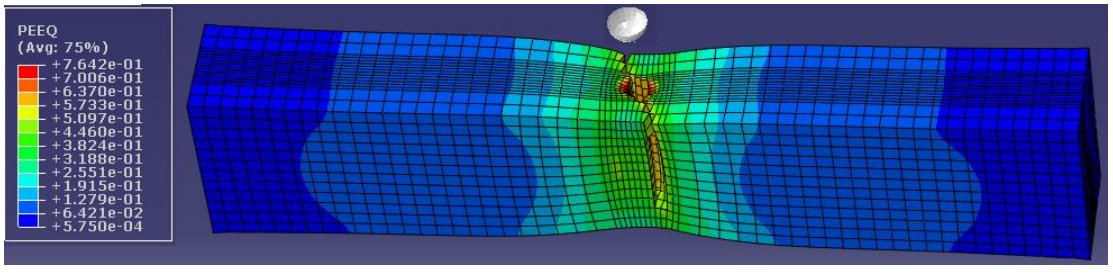

(b) Equivalent plastic strain distribution

Figure 9.11: Deformed shapes showing longitudinal axial stress (MPa) and equivalent plastic strain distributions at an applied displacement of 5.78mm.

The completely fractured dented specimen with the longitudinal axial stress and equivalent plastic strain distributions are shown in Figures 9.12 (a) and (b) respectively. The shaped of

the fractured dented specimen from the FE is similar to the shaped of the fractured dented specimen obtained from the laboratory tensile test shown in Figure 9.12(c).

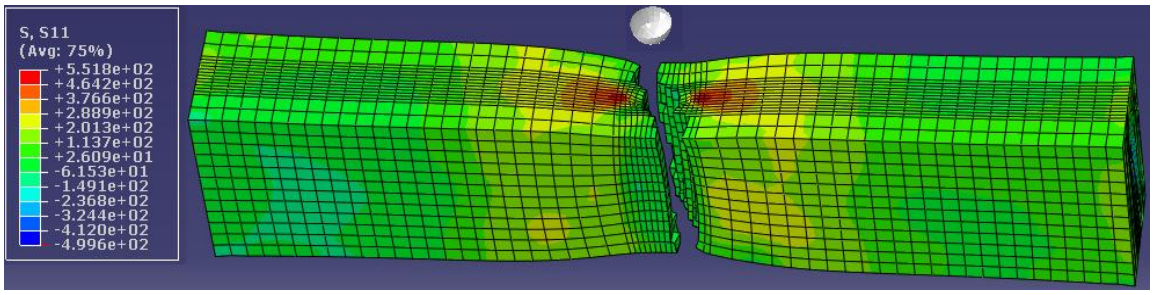

(a) Longitudinal axial stress (MPa) distribution

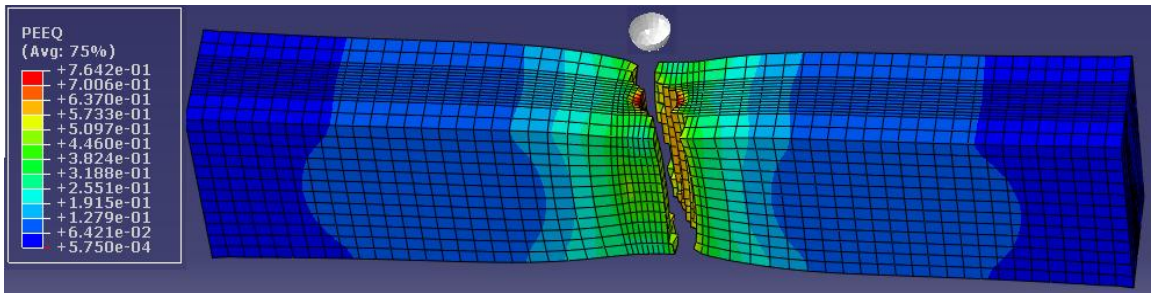

(b) Equivalent plastic strain distribution

(c) Completely fractured dented wire from experiment

Figure 9.12: Completely fractured dented specimen from FE and Experiment.

The longitudinal axial stress and the equivalent plastic strain profiles throughout the tensile testing simulations obtained from the dent-depth node are shown in Figures 9.13 and 9.14 respectively. The dent-depth node is the node that is directly under the spherical indenter tip node, at the centre of the location of indentation and at the bottom centre of the dent. It is the deepest point in the spherical dent.

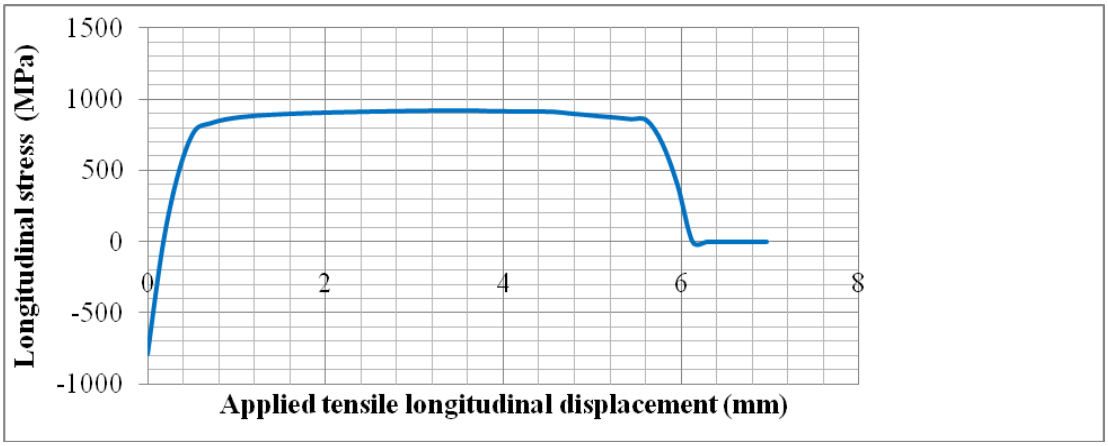

Figure 9.13: Longitudinal axial stress profile of the dent-depth node.

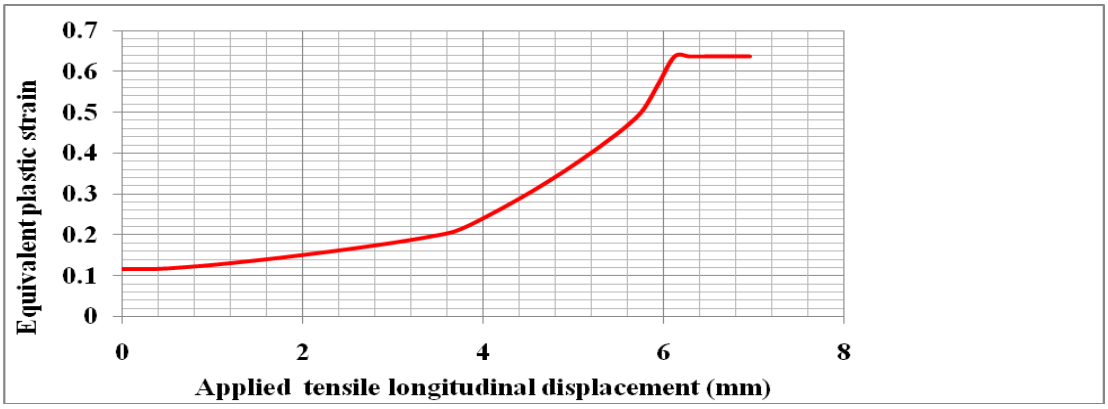

Figure 9.14: Equivalent plastic strain profile of the dent-depth node.

At an applied tensile displacement of 0.2mm, the residual compressive stress of 787MPa induced in the wire specimen by the indentation was neutralized by the tensile stress induced during the tensile testing simulation. Stretching the wire beyond 0.2mm, the stress turned tensile, reaches its maximum value at an applied displacement of 3.68mm and became zero at an applied displacement of 6.13mm. At the beginning of the tensile testing simulation, the equivalent plastic strain at the bottom of the dent is 0.12 and it increases throughout the tensile testing simulation.

9.4.1 Mesh convergence and refinement

To obtain the optimum mesh density for the FE simulation of the tensile testing of the dented tensile armour wires, the mesh around the location of indentation was successively refined with 0.5mm, 0.25mm and 0.1mm elements. The deformed shapes showing the stress distributions after the indentation, indenter removal and tensile testing predicted by the

simulations with successive mesh refinements around the locations of the indentation are shown in Figures 9.15, 9.16 and 9.17 (a) to (c) respectively.

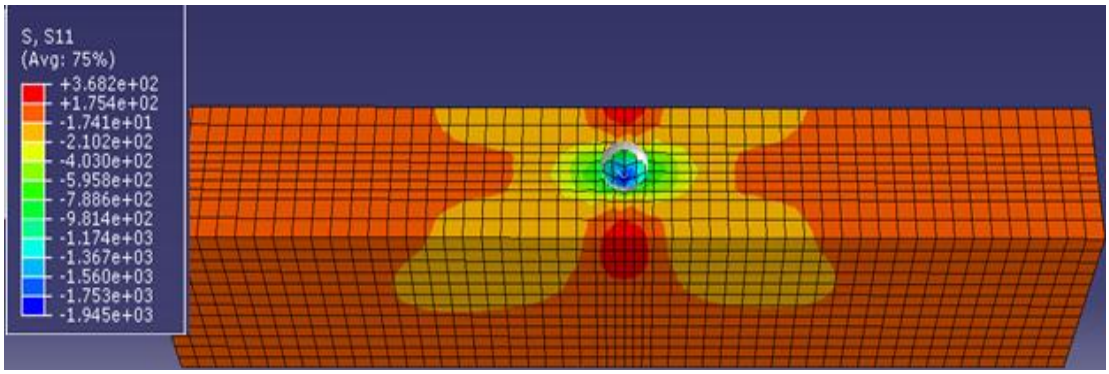

(a) 0.5mm elements around location of indentation

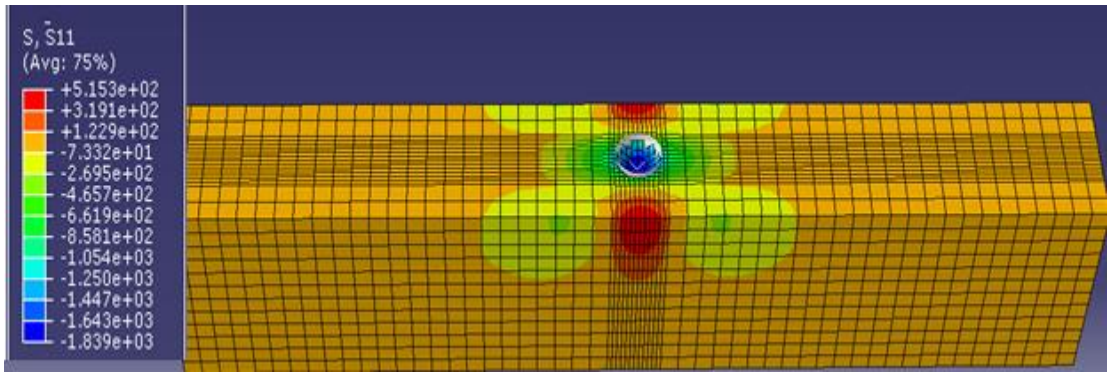

(b) 0.25mm elements around location of indentation

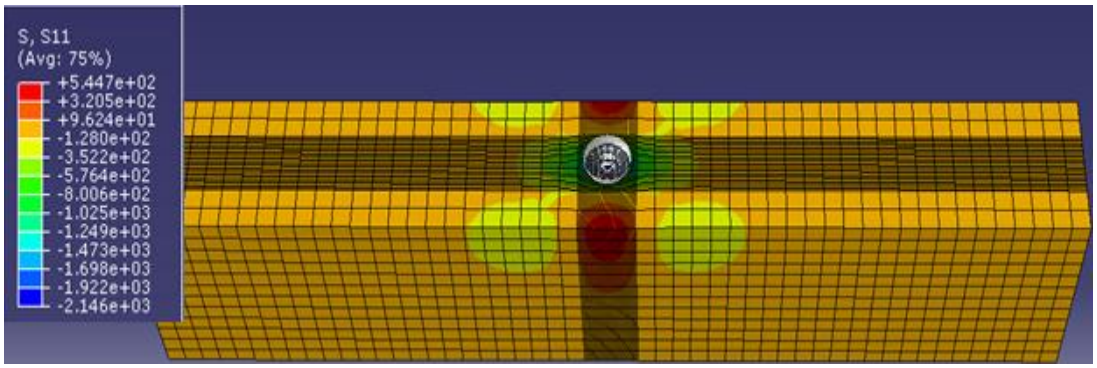

(c) 0.1mm elements around location of indentation

Figure 9.15: Deformed shapes showing longitudinal axial stress (MPa) distributions after indentation from simulations with successive mesh refinements.

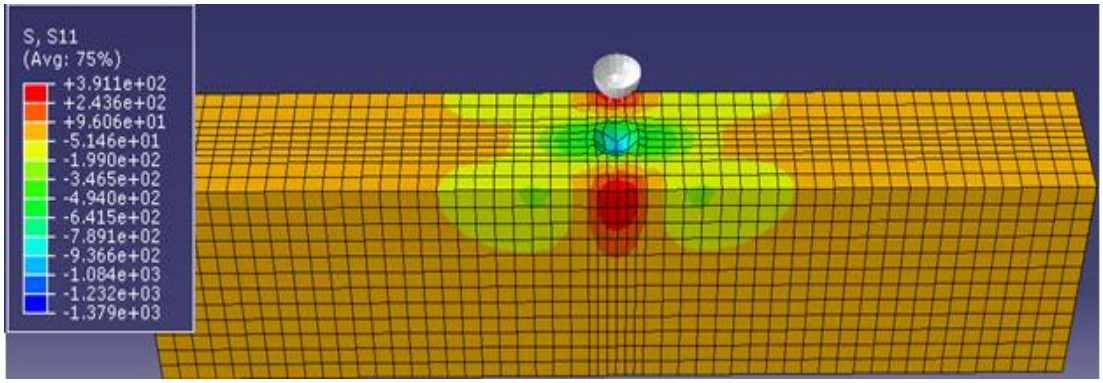

(a) 0.5mm elements around location of indentation

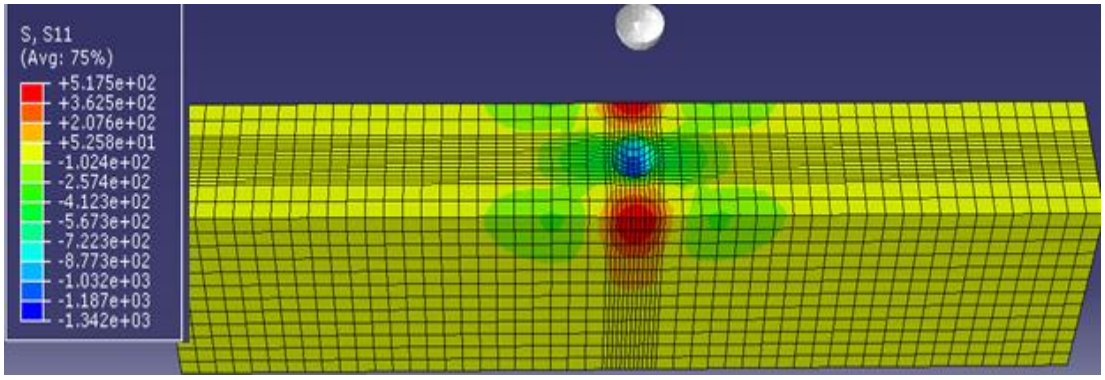

(b) 0.25mm elements around location of indentation

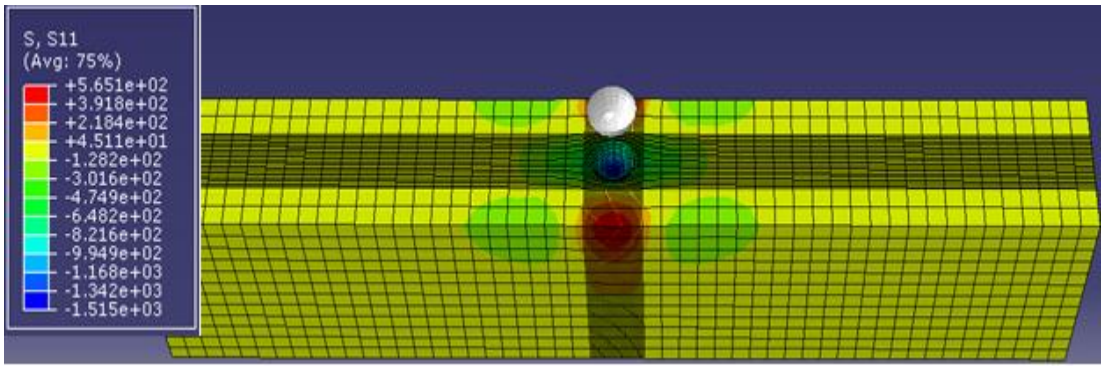

(c) 0.1mm elements around location of indentation

Figure 9.16: Deformed shapes showing longitudinal axial stress (MPa) distributions after indenter removal from simulations with successive mesh refinements.

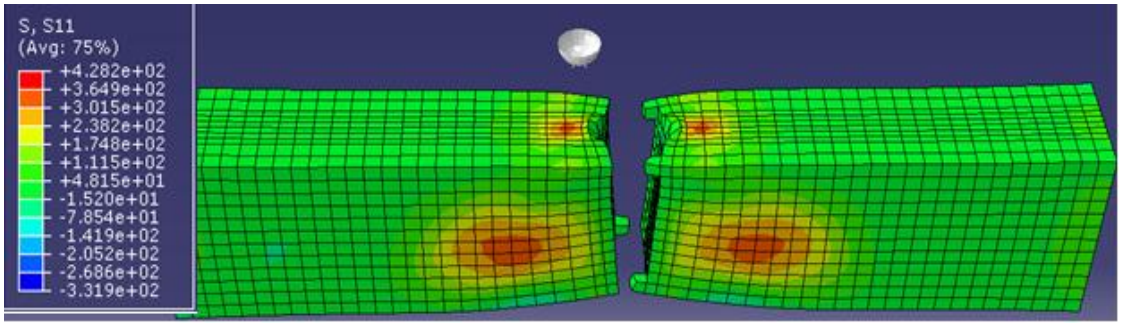

(a) 0.5mm elements around location of indentation

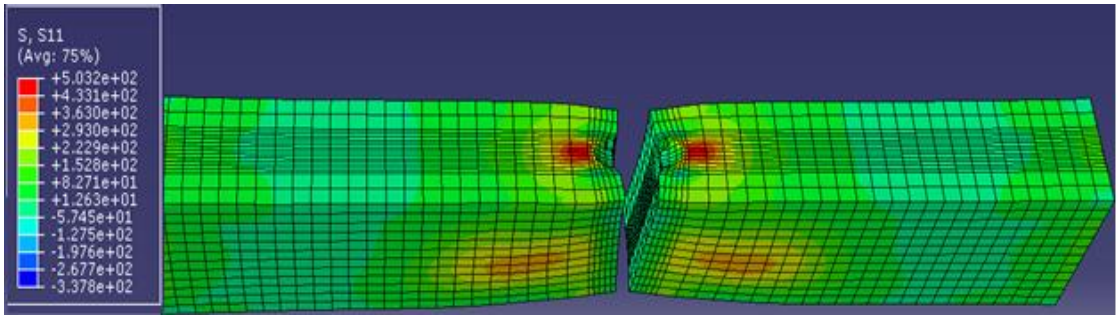

(b) 0.25mm elements around location of indentation

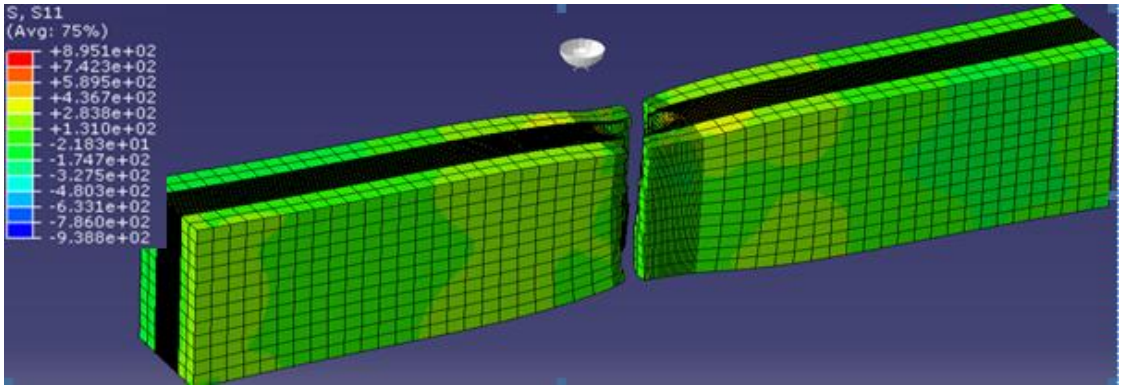

(c) 0.1mm elements around location of indentation

Figure 9.17: Deformed shapes showing longitudinal axial stress (MPa) distributions after tensile testing from simulations with successive mesh refinements.

The force-displacement curves predicted by the simulations of the tensile testing of the dented tensile armour wires carried out with 0.5mm, 0.25mm and 0.1mm refined elements around the location of the indentation are shown in Figure 9.18. The negligible percentage differences (maximum of 1.08%) in the mechanical properties predicted by the FE simulations with 0.5mm, 0.25mm and 0.1mm elements around the location of indentation presented in Table 9.2 show that the mesh has converged. Consequently, subsequent simulations were carried out with 0.25mm elements around the location of the indentation as this level of mesh refinement produces sufficiently accurate results coupled with the fact that

the output from this mesh size has been validated with the experimental results. Also carrying out the simulation with 0.25mm instead of 0.1mm elements around the location of the indentation minimizes the output file capacity and optimizes the computation time without any loss of accuracy.

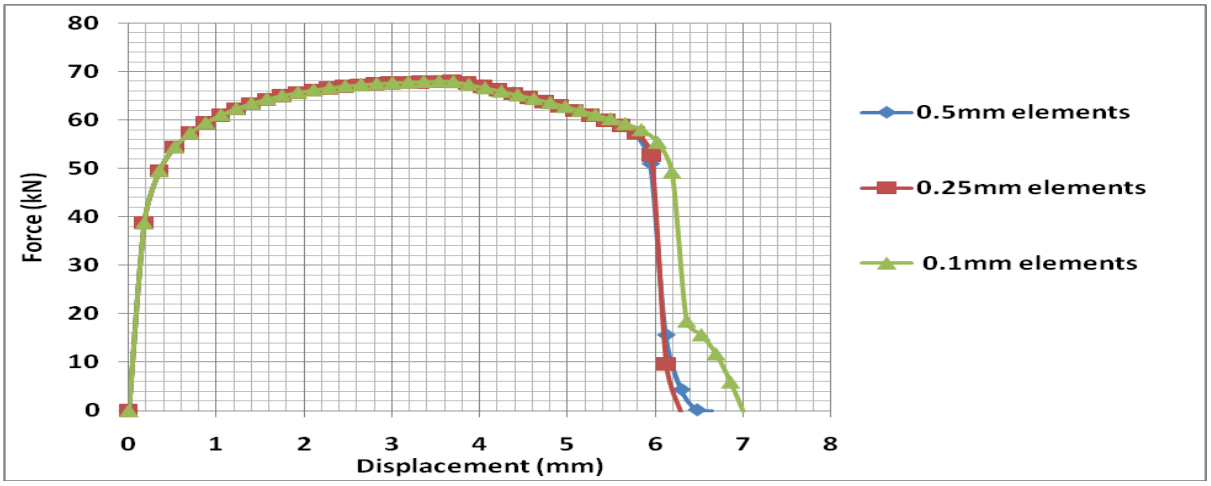

Figure 9.18: Force-displacement curves with successive mesh refinements around the location of indentation of a 12mmx7mm, 50mm gauge length wire specimen.

Table 9.2: Mechanical properties predicted by simulations with successive mesh refinements

Ultimate load point parameters					
Elements size at indentation location	Yield load (kN)	Percentage difference		Ultimate load (kN)	Percentage difference
0.5mm	49.49	-		67.97	-
0.25mm	49.50	0.03		67.98	0.008
0.1mm	49.49	0.03		67.96	0.020
Fracture point parameters					
Elements size at indentation location	Fracture load (kN)	Percentage difference		Displacement at fracture (mm)	Percentage difference
0.5mm	57.24	-		5.77	-
0.25mm	57.33	0.14		5.78	0.19
0.1mm	57.95	1.08		5.84	1.08

9. 4.2 Validation of the simulation of the tensile testing of dented tensile armour wires

The force-displacement curves obtained from the laboratory and numerical tensile testing of the dented tensile armour wire specimens are shown in Figure 9.19. As shown in Figure 9.19 and Table 9.3. The force-dispacement curves from the laboratory and numerical tensile testing agree well with 0.24% and 1.38% differences in the values of their ultimate and fracture loads respectively. As stated earlier, the FE curve represents the actual tensile behaviour of the wire since its displacements are the actual displacement within the 50mm wire specimen alone and it agrees with the experimental curve with the corrected displacements as shown in Figures 9.19.

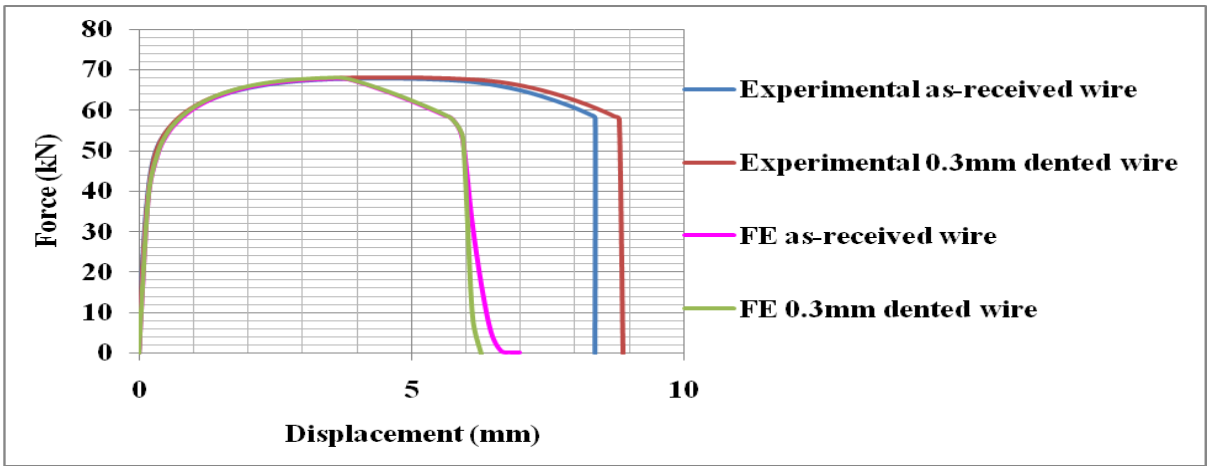

Figure 9.19: Force-displacement curves from laboratory and FE tensile testing of 12mmx7mm 50mm gauge length dented wire specimen.

Table 9.3: Mechanical properties of dented wire from laboratory test and FEA analysis

Parameters	Experimental	FE simulation	Percentage difference (%)
Ultimate load (kN)	67.82	67.98	0.24
Fracture load (kN)	58.13	57.33	1.38
Displacement at fracture (mm)	8.37	5.78	30.94

9.5 Effects of dent size and locations on tensile properties of tensile armour wires.

The effects of the location of the dents and the dent sizes on the tensile properties of the tensile armour wires was investigated by carrying out FE simulations of the tensile testing of the tensile armour wire specimens dented along their thickness, width and edge to dent depths

varying from 0.1mm to 1mm by 10mm, 5mm and 2.5mm spherical indenters. The deformed shapes after the indentation simulation showing the stress distributions in the specimens subjected to indentation along its thickness, width and edge hereinafter referred to as the: along-the-thickness dent, along-the-width dent and edge dent respectively are shown in Figures 9.20 (a), (b) and (c) respectively. Each indentation at the three locations shown in Figures 9.20 (a), (b) and (c) was made with 2.5mm diameter indenters placed 1mm above the wire and subjected to 1.8mm displacement.

Generally, the compressive stresses (indicated by the deepest blue to yellow colours in the specimen and the contour plots) in the specimen dented along its width is higher than that of the specimen dented along its thickness, which is equally higher than that of the specimen dented along its edge with the maximum values of 2038MPa, 1939MPa and 993MPa respectively. This is because there is no compressive stress relaxation in the specimen dented along its width as the compressive stresses were completely contained within the specimen without extending to its edges due to the presence of materials with sufficient dimensions around the indentation that provided the constraint that contained the compressive stress within the specimen. On the other hand, the compressive stresses in the specimen dented along its thickness and the specimen dented along its edge were not contained completely within these specimens as the compressive stresses extended to the edges of the specimens leading to compressive stress relaxations. The compressive stress relaxation is even greater in the specimen dented along its edge, which explains why it has the lowest value of compressive stress.

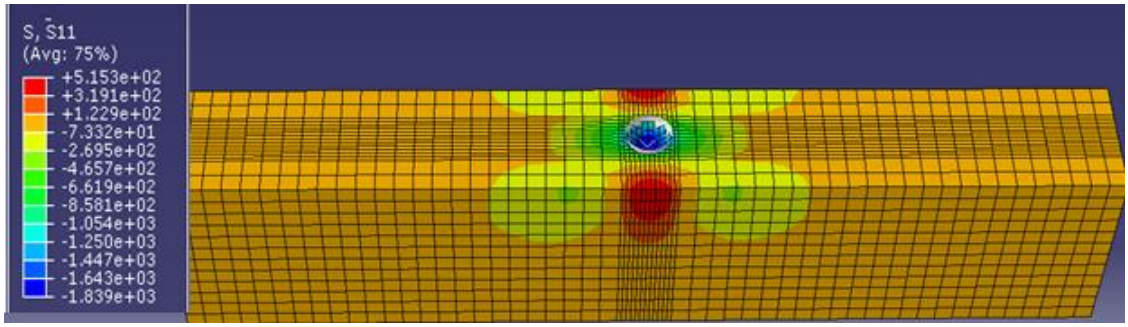

(a) Indentation along wire thickness

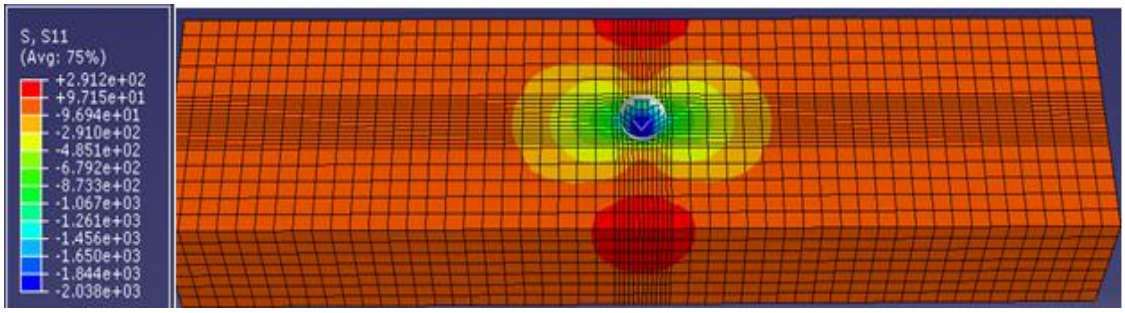

(b) Indentation along wire width

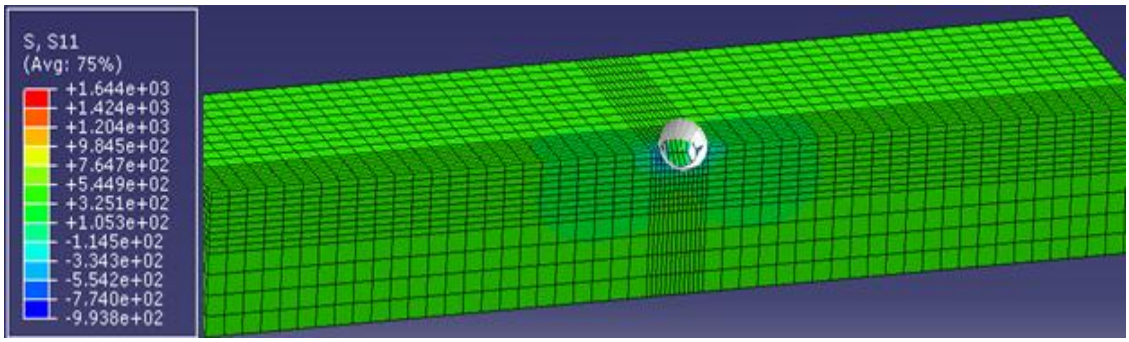

(c) Indentation on wire edge

Figure 9.20: Deformed shapes and longitudinal axial stress (MPa) distributions for specimens dented along its thickness, width and edge after indentation simulation.

The deformed shapes showing the stress distributions in the specimens dented along their thickness, width and edge after the indenter removal simulation are shown in Figures 9.21 (a), (b) and (c) respectively.

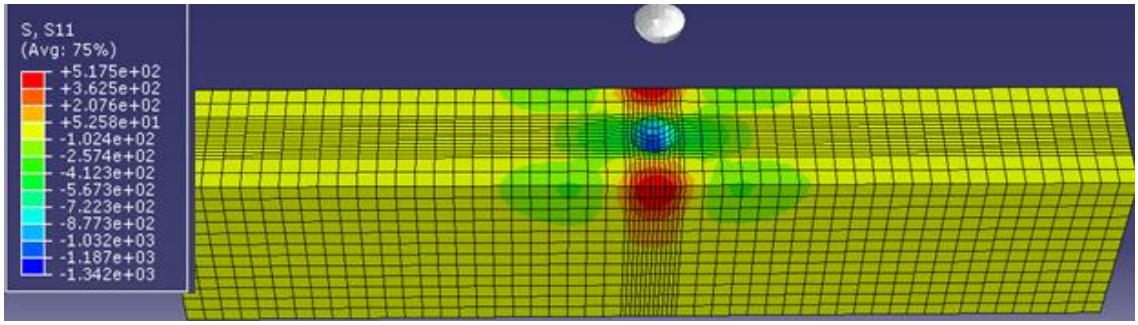

(a) Specimen with the along-the-thickness dent

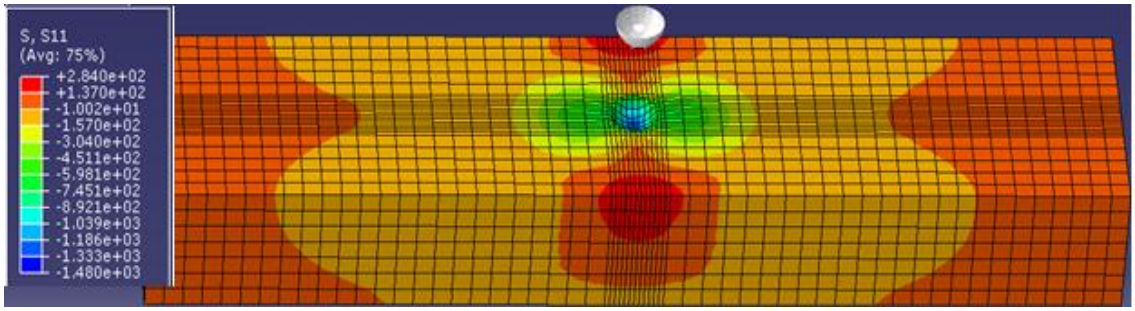

(b) Specimen with the along-the-width dent

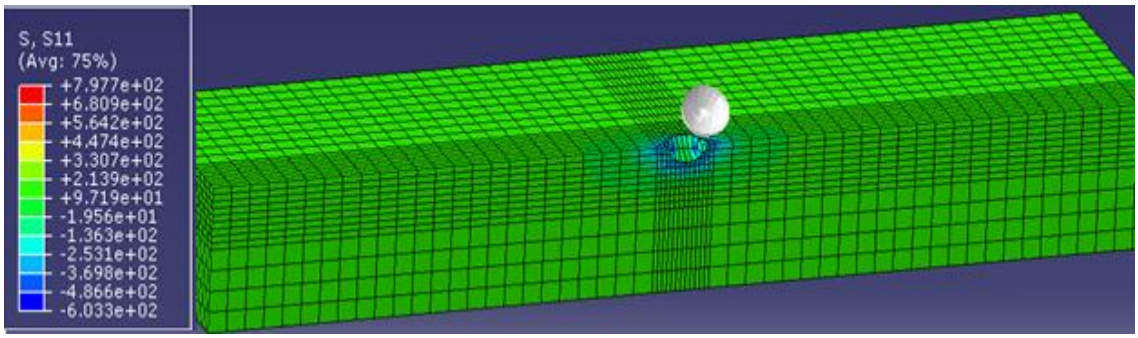

(c) Specimen with the edge dent

Figure 9.21: Deformed shapes and longitudinal axial stress (MPa) distributions for specimens dented along its thickness, width and edge after indenter removal simulation.

The deformed shapes showing the maximum tensile stresses occurring at the bottom of the along-the-thickness, along-the-width and edge dents at an applied displacement of 0.35mm are shown in Figures 9.22 (a), (b) and (c) respectively. As stated earlier, the maximum tensile stresses occurred at the bottom of the dents at the beginning of the tensile testing simulation due to the stress concentration effect of the dent geometry.

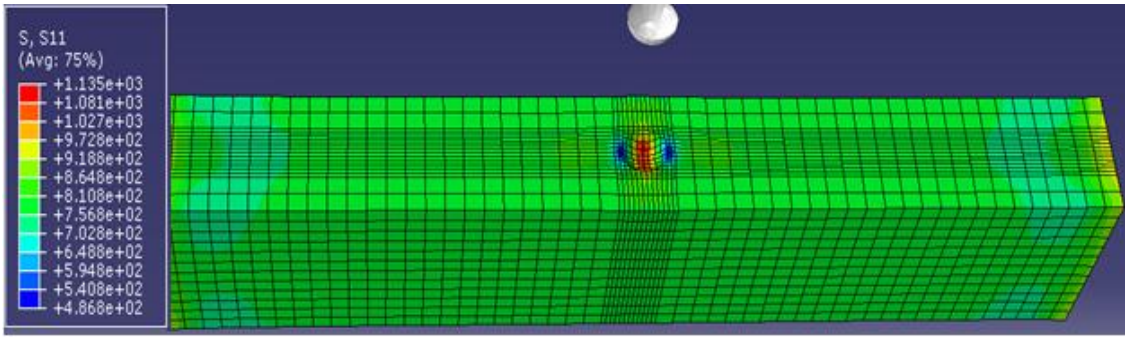

(a) Specimen with the along-the-thickness dent

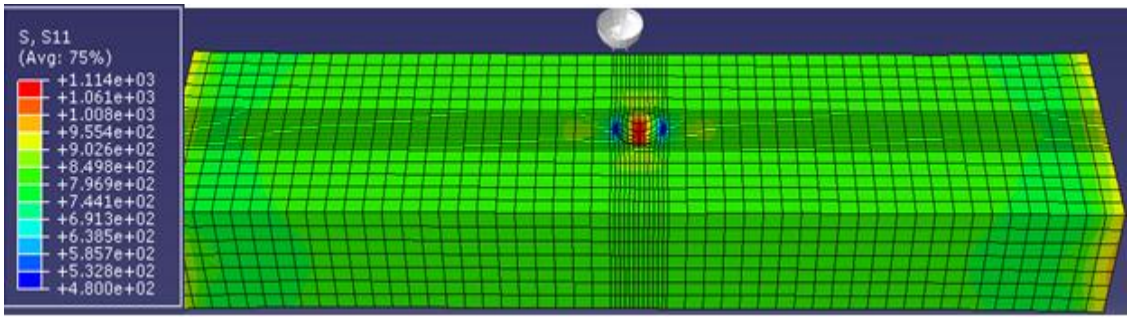

(b) Specimen with the along-the-width dent

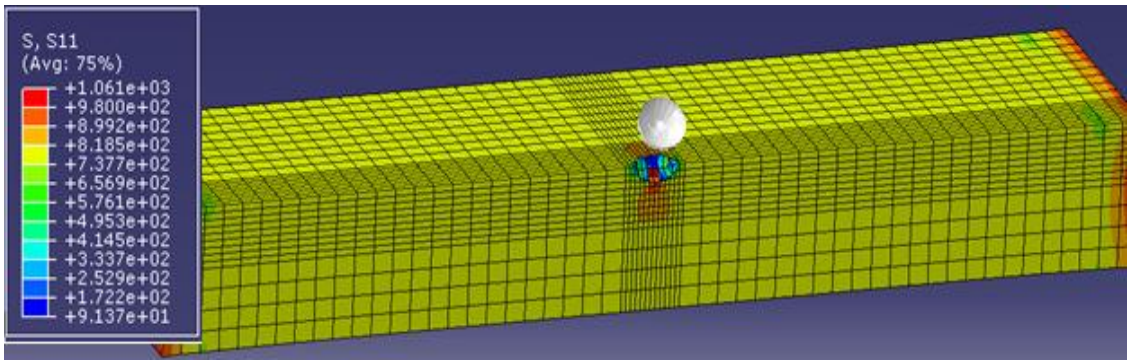

(c) Specimen with the edge dent

Figure 9.22: Deformed shapes and longitudinal axial stress (MPa) distributions for specimens dented along its thickness, width and edge at an applied displacement of 0.35mm.

The deformed shapes showing the fracture initiation in the specimens with the along-the-thickness, along-the-width and edge dents at an applied displacement of 5.80mm are shown in Figures 9.23 (a), (b) and (c) respectively. The fractured shapes of the specimens with the along-the-thickness, along-the-width and edge dents after tensile testing simulation at an applied displacement of 6.31mm are shown in Figures 9.24 (a), (b) and (c) respectively.

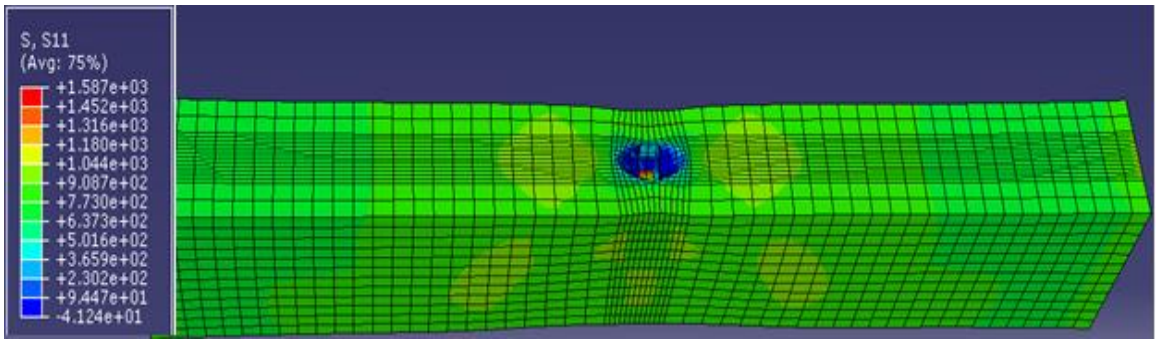

(a) Specimen with the along-the-thickness dent

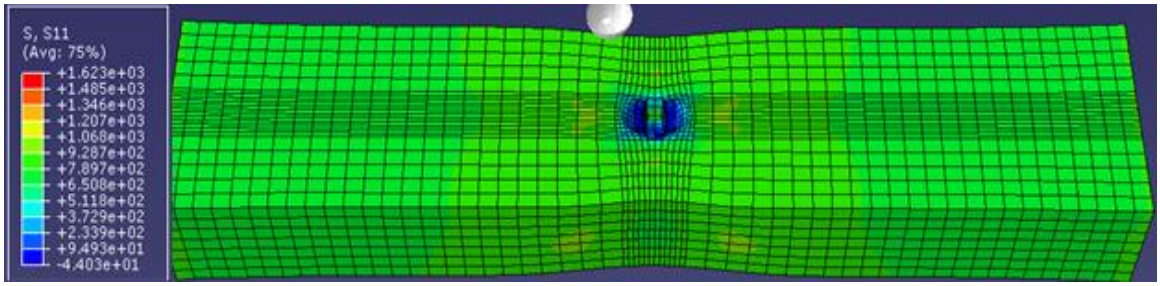

(b) Specimen with the along-the-width dent

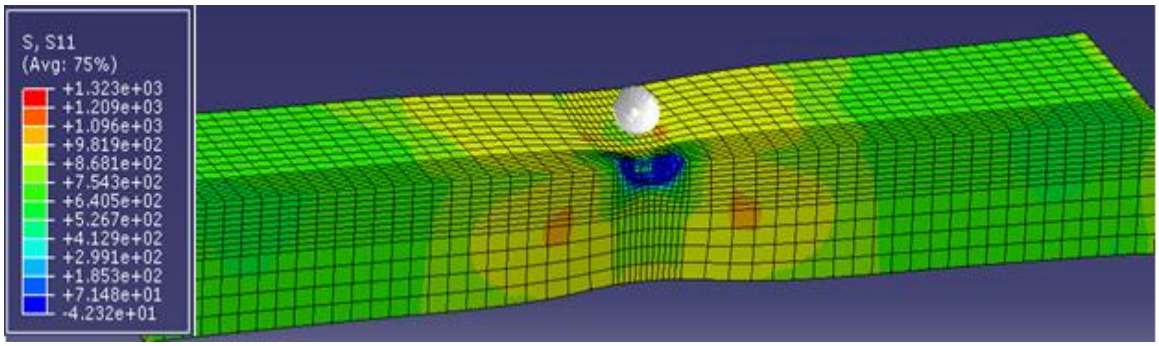

(c) Specimen with the edge dent

Figure 9.23: Deformed shapes and longitudinal axial stress (MPa) distributions for specimens dented along their thickness, width and edge during fracture initiation at an applied displacement of 5.80mm.

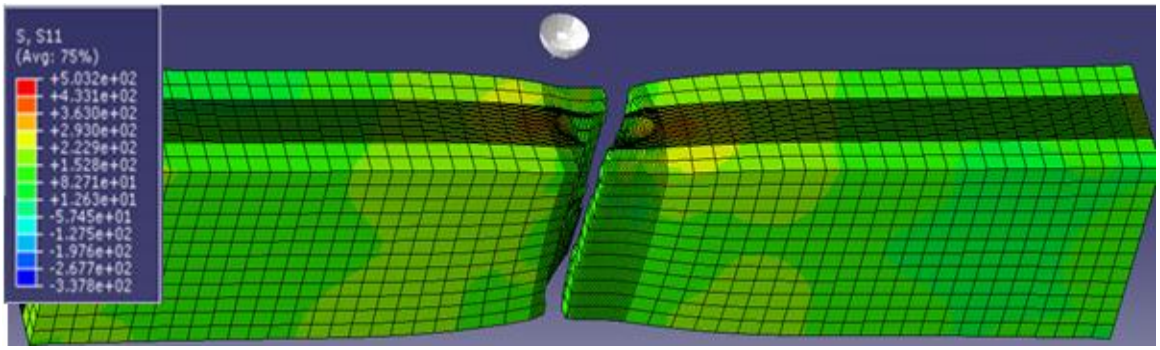

(a) Specimen with the along-the-thickness dent

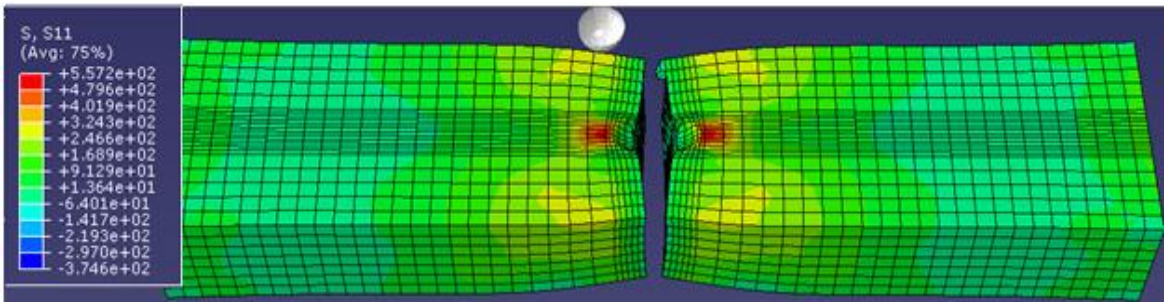

(b) Specimen with the along-the-width dent

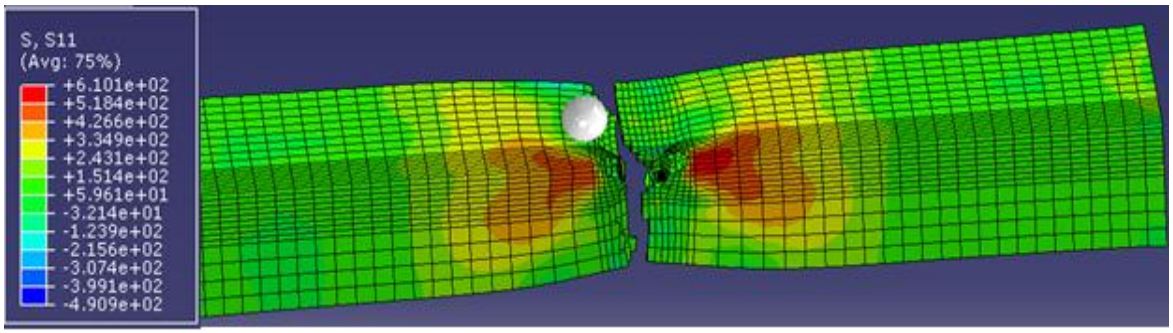

(c) Specimen with the edge dent

Figure 9.24: Fractured shapes and longitudinal axial stress (MPa) distributions for specimens dented along their thickness, width and edge after tensile testing simulation at an applied displacement of 6.31mm.

The variations of the yield loads, the ultimate loads and the fracture displacements with the dent depths and the dent diameters obtained from the specimens with the dent along their thickness, width and edge are shown in Figures 9.25, 9.26 and 9.27 respectively.

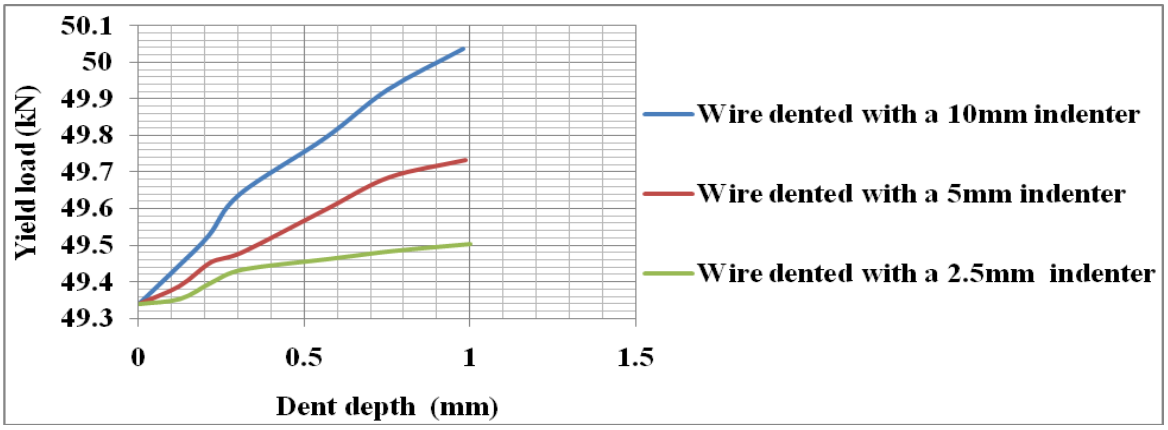

(a) From wire specimen with the along-the thickness dent

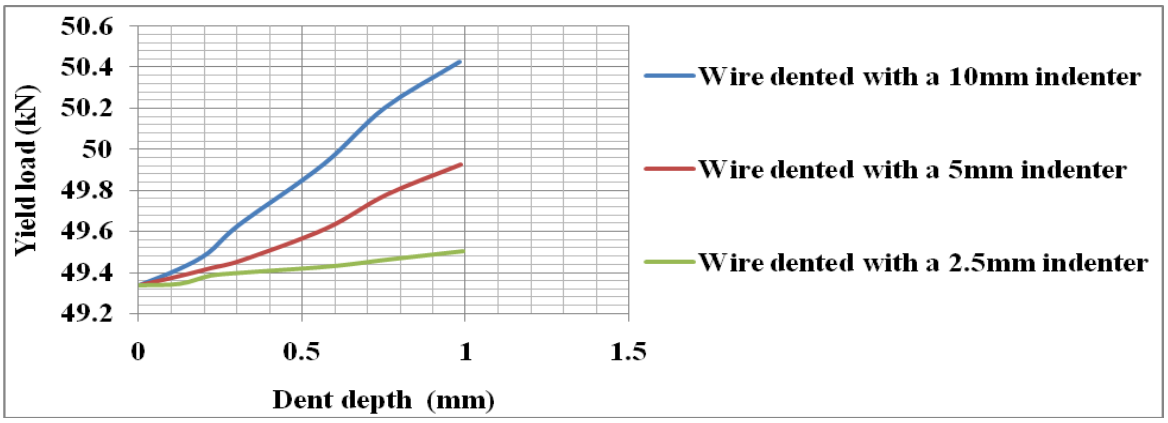

(a) From wire specimen with the along-the width dent

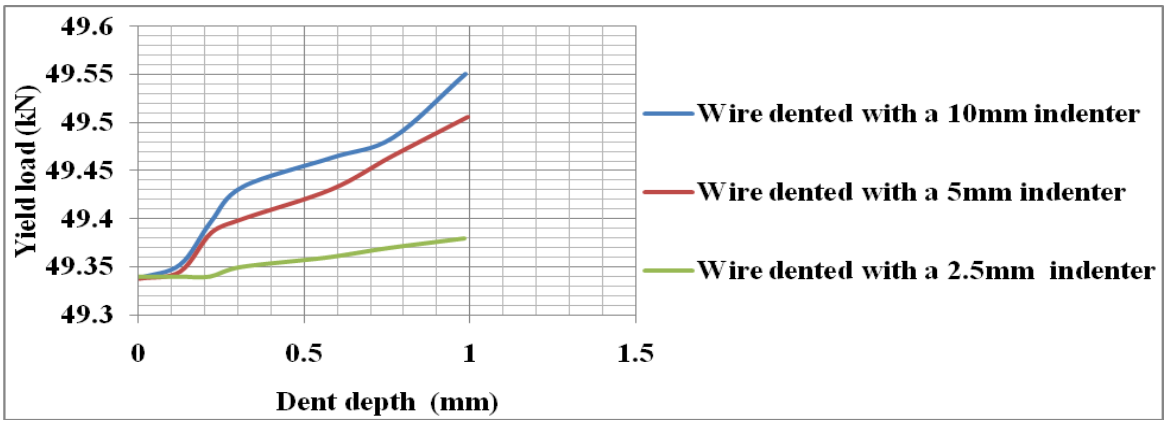

(c) From wire specimen with the edge dent

Figure 9.25: Variations of yield load with dent depths, dent diameters and dent locations.

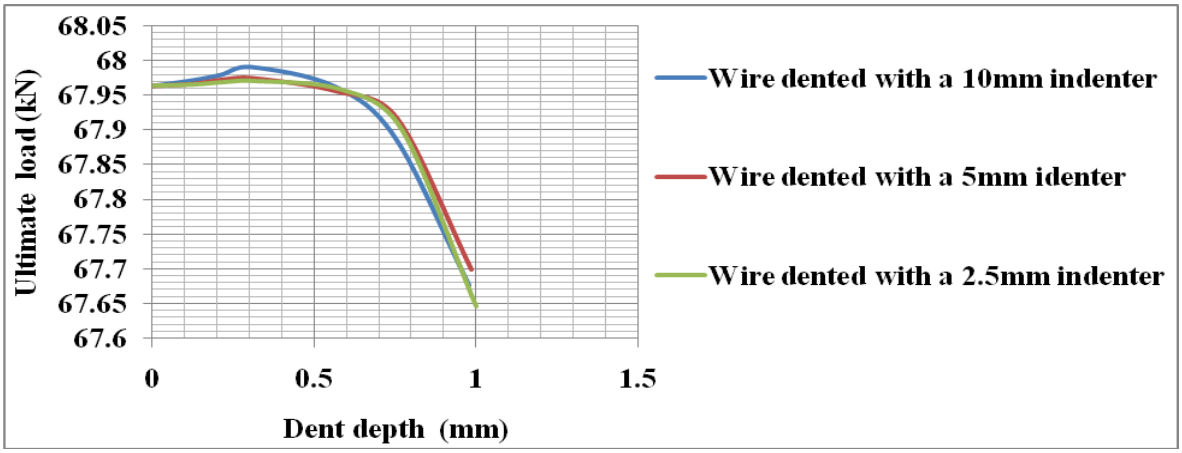

(a) From wire specimen with the along-the thickness dent

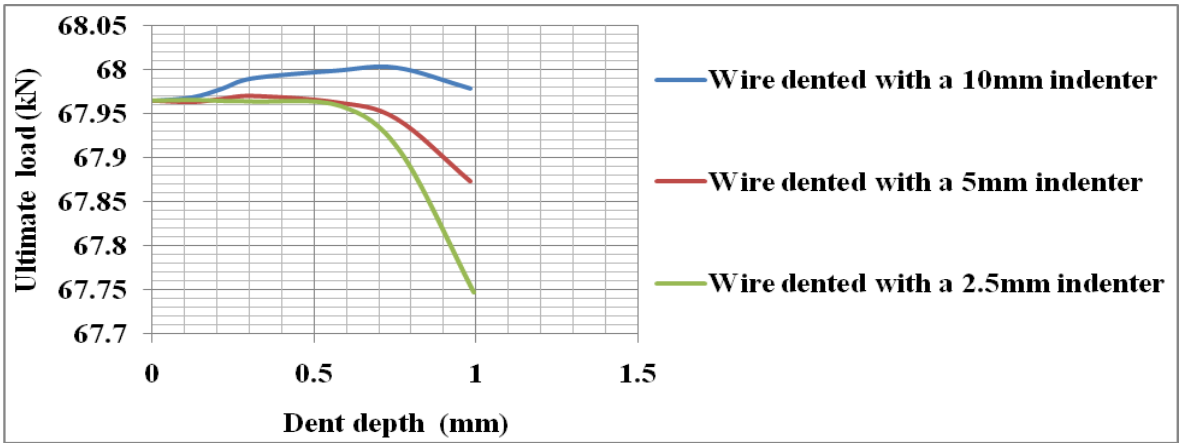

(b) From wire specimen with the along-the width dent

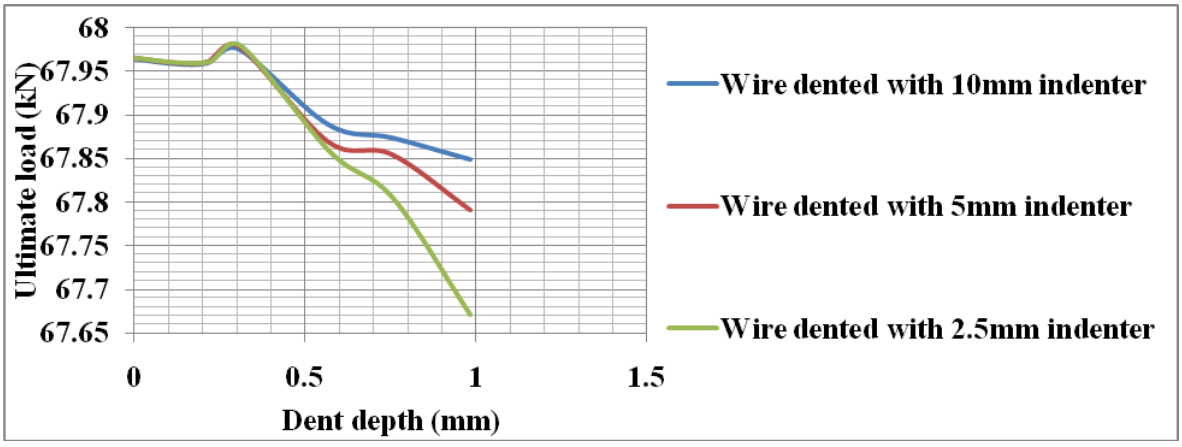

(c) From wire specimen with the edge dent

Figure 9.26: Variation of ultimate load with dent depths, dent diameters and dent locations.

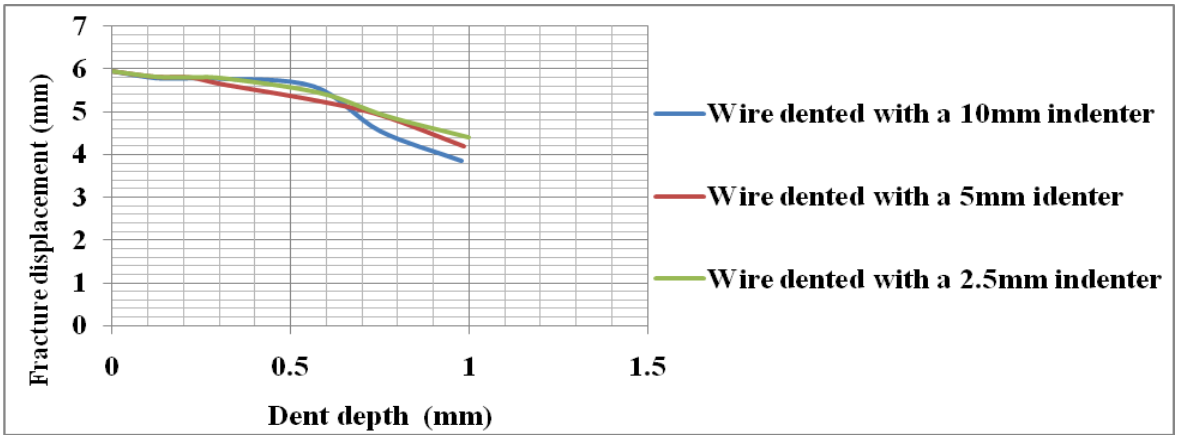

(a) From wire specimen with the along-the thickness dent

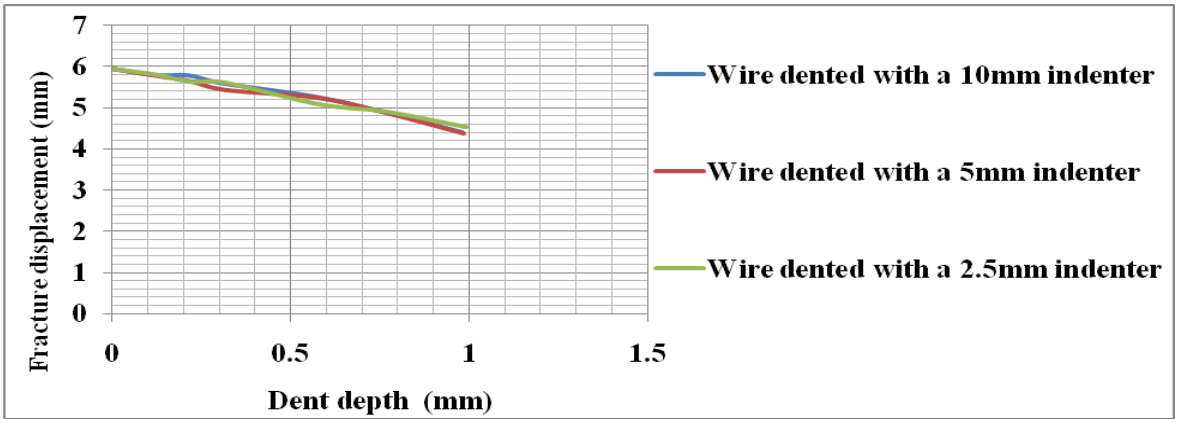

(b) From wire specimen with the along-the width dent

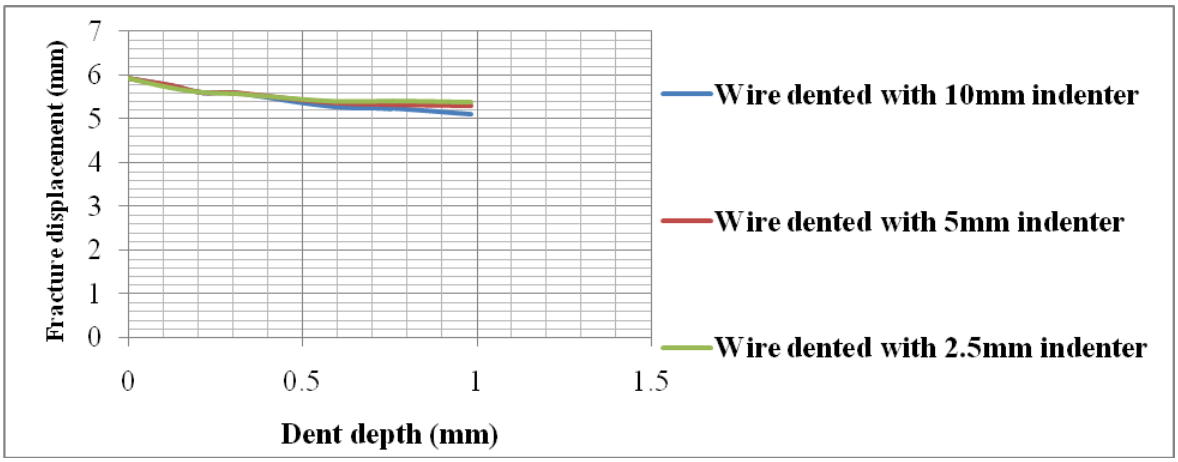

(c) From wire specimen with the edge dent

Figure 9.27: Variation of fracture displacement with dent depths, dent diameters and dent locations.

9.6 Analysis of results

Generally, irrespective of the location of the dent, the indentation of the wire increases its yield load. The result agrees with what is reported by Harsono, et al, 2010 and the increase in the yield load is due to the work hardening associated with the plastic deformation of the wire during indentation. The increase in the yield load increases with both dent diameter and dent depth as shown in Figure 9.38 and Tables 9.4, 9.5 and 9.6. There is no substantial difference in the increase in the yield loads of the specimens dented along their thicknesses and the specimens dented along their widths. However, the increases in the yield loads of both are substantially higher than that of the specimens dented along their edges. This is because there is more stress relaxation in the specimens with the edge dent than the specimens with the across-the-thickness and across-the-width dents as there is less constraint in these specimens as earlier stated.

Similarly, irrespective of the location of the dent, the indentation of the wire up to approximately 0.3mm deep increases the ultimate load of the wire. Beyond 0.3mm dent depth, the ultimate load of the wires reduces as shown in Figure 9.39 and Tables 9.4, 9.5 and 9.6. The change in the effects of the dent on the ultimate strength of the wire at approximately 0.3mm dent depth could be due to a trade-off between the work hardening effects of the indentation, which increases the wire's ultimate load, and the stress concentration effects of the dent which reduces the ultimate load of the wire. Thus, it can be said that below 0.3mm dent depth, the work hardening effect of the indentation is dominant while above 0.3mm dent depth the stress concentration effect of the dent is dominant.

As shown in Figure 9.40 and Tables 9.4, 9.5 and 9.6, irrespective of the location of the dent, the indentation of the wire reduces the displacement at fracture and invariably the ductility of the wire. The reduction in the displacement at fracture (and invariably, the ductility) increases with increases in the dent depth and the dent diameter. Indentation along the edge of the wire causes a smaller reduction in the fracture displacement (ductility) than indentation along the thickness and width of the wire. This is because the highest stress relaxation that occurred in the specimen with the edge dent leaved the specimen with the lowest amount of plastic deformation. Consequently, the lowest portion of the total amount of available/allowed plastic deformation for the wire specimen was used up during the plastic deformation

associated with of the specimen with the edge dent, leaving it with the highest ductility; since ductility depends on the total amount of available/allowed plastic deformation.

Table 9.4: Variations in mechanical properties of specimens dented along their thickness, width and edge with depth of dents made with a 10mm diameter indenter

	Specimen with the along-the-thickness dent							
Dent depth (mm)	Yield load (kN)	% increase in yield load		Ultimate load (kN)	% reduction in ultimate load		Fracture displacement	% reduction in fracture displacement
0	49.34	-		67.9649	-		5.93	-
0.12	49.44	0.21		67.9727	0.011		5.78	2.63
0.21	49.53	0.38		67.9807	0.023		5.77	2.73
0.30	49.64	0.61		67.992	0.039		5.76	2.87
0.56	49.79	0.92		67.9638	0.002		5.58	5.88
0.75	49.93	1.19		67.8898	0.110		4.55	23.33
0.97	50.04	1.42		67.6777	0.423		3.86	34.96
	Specimen with the along-the-width dent							
Dent depth (mm)	Yield load (kN)	% increase in yield load		Ultimate load (kN)	% reduction in ultimate load		Fracture displacement	% reduction in fracture displacement
0	49.34			67.96			5.93	
0.12	49.42	0.16		67.97	0.006		5.78	2.60
0.21	49.50	0.32		67.98	0.020		5.78	2.66
0.31	49.63	0.59		67.99	0.037		5.59	5.84
0.57	49.93	1.19		68.00	0.050		5.26	11.27
0.75	50.20	1.75		68.00	0.055		4.91	17.27
0.98	50.42	2.20		67.98	0.021		4.40	25.82
	Specimen with the edge dent							
Dent depth (mm)	Yield load (kN)	% increase in yield load		Ultimate load (kN)	% reduction in ultimate load		Fracture displacement	% reduction in fracture displacement
0	49.34			67.96			5.93	
0.12	49.33	0.009		67.96	0.007		5.75	3.09
0.21	49.33	0.000		67.96	0.006		5.60	5.60
0.31	49.35	0.015		67.96	0.009		5.59	5.74
0.57	49.36	0.053		67.86	0.158		5.29	10.90
0.75	49.35	0.011		67.80	0.236		5.23	11.77
0.98	49.35	0.000		67.67	0.432		5.09	14.10

Table 9.5: Variations in mechanical properties of specimens dented along their thickness, width and edge with depth of dents made with a 5mm diameter indenter.

	Specimen with the along-the-thickness dent							
Dent depth (mm)	Yield load (kN)	% increase in yield load		Ultimate load (kN)	% reduction in ultimate load		Fracture displacement	% reduction in fracture displacement
0	49.34	-		67.96			5.93	
0.12	49.39	0.01		67.97	0.004		5.80	2.19
0.22	49.45	0.23		67.97	0.014		5.79	2.39
0.31	49.48	0.29		67.97	0.016		5.63	5.13
0.57	49.60	0.53		67.96	0.011		5.25	11.43
0.76	49.68	0.70		67.92	0.069		4.90	17.40
0.99	49.73	0.80		67.70	0.390		4.19	29.42
	Specimen with the along-the-width dent							
Dent depth (mm)	Yield load (kN)	% increase in yield load		Ultimate load (kN)	% reduction in ultimate load		Fracture displacement	% reduction in fracture displacement
0	49.34			67.96			5.93	
0.12	49.38	0.092		67.96	0.002		5.77	2.83
0.22	49.42	0.171		67.97	0.003		5.63	5.08
0.31	49.46	0.247		67.97	0.008		5.43	8.48
0.57	49.62	0.562		67.96	0.003		5.24	11.70
0.76	49.78	0.870		67.94	0.035		4.90	17.47
0.98	49.93	1.193		67.87	0.135		4.38	26.13
	Specimen with the edge dent							
Dent depth (mm)	Yield load (kN)	% increase in yield load		Ultimate load (kN)	% reduction in ultimate load		Fracture displacement	% reduction in fracture displacement
0	49.34			67.96			5.93	
0.12	49.34	0.015		67.96	0.000		5.76	2.85
0.22	49.39	0.096		67.96	0.000		5.60	5.66
0.31	49.40	0.125		67.98	0.019		5.59	5.71
0.58	49.43	0.187		67.87	0.141		5.39	9.22
0.76	49.47	0.258		67.85	0.163		5.33	10.09
0.99	49.51	0.339		67.79	0.256		5.30	10.56

Table 9.6: Variations in mechanical properties of specimens dented along their thickness, width and edge with depth of dents made with a 2.5mm diameter indenter

	Specimen with the along-the-thickness dent							
Dent depth (mm)	Yield load (kN)	% increase in yield load		Ultimate load (kN)	% reduction in ultimate load		Fracture displacement	% reduction in fracture displacement
0	49.34	-		67.96	-		5.93	-
0.12	49.35	0.029		67.97	0.003		5.8	2.187
0.22	49.4	0.119		67.97	0.008		5.79	2.347
0.31	49.43	0.192		67.97	0.01		5.77	2.747
0.58	49.46	0.253		67.96	0.008		5.44	8.366
0.77	49.48	0.296		67.9	0.091		4.89	17.429
0.99	49.50	0.334		67.65	0.469		4.23	28.78
	Specimen with the along-the-width dent							
Dent depth (mm)	Yield load (kN)	% increase in yield load		Ultimate load (kN)	% reduction in ultimate load		Fracture displacement	% reduction in fracture displacement
0	49.34			67.96			5.93	
0.12	49.35	0.015		67.97	0.002		5.79	2.42
0.22	49.39	0.097		67.96	0.0004		5.62	5.31
0.31	49.40	0.125		67.96	0.002		5.60	5.54
0.58	49.43	0.187		67.96	0.009		5.08	14.45
0.77	49.47	0.258		67.91	0.085		4.90	17.38
0.99	49.51	0.339		67.75	0.320		4.53	23.67
	Specimen with the edge dent							
Dent depth (mm)	Yield load (kN)	% increase in yield load		Ultimate load (kN)	% reduction in ultimate load		Fracture displacement	% reduction in fracture displacement
0	49.34			67.96			5.93	
0.12	49.34	0.000		67.96	0.000		5.71	3.72
0.21	49.34	0.000		67.96	0.000		5.61	5.50
0.31	49.35	0.024		67.98	0.020		5.57	6.18
0.57	49.36	0.044		67.86	0.158		5.42	8.70
0.75	49.37	0.064		67.84	0.236		5.41	8.78
0.98	49.38	0.085		67.67	0.432		5.38	9.38

9.7 Conclusion

It can be concluded that irrespective of the location of the dent, denting of the tensile armour wires increases its yield load and invariably its yield strength. Denting of the tensile armour also increases the ultimate load (and invariably the ultimate strength) of the wire if the dent depth is less or equal to 0.3mm, beyond which it reduces the wire's ultimate load. Furthermore, denting of the tensile armour wires reduces the fracture displacement/ductility of the wire. Hence for elastic design, the presence of dent(s) in the wire is not a cause for concern, but for elastic-plastic design and for situations in which the wire is subjected to large strain, then denting of the tensile armour wires can cause the wire to fail at a lower load (especially, if the dent depth is greater than 0.3mm) and/or a lower fracture displacement (ductility). The reductions in the ultimate load and the displacement at fracture of the tensile armour wires increase with dent depth and dent diameter. The worst effects of the presence of dents with depth and/or diameter less than the 0.2mm which cannot be detected by the inline eddy current detector are 2.73% reduction in the displacement at fracture of the wire.

Having presented the investigation of the effects of scratches and dents on the tensile properties of tensile armour wires, the next chapter introduces the investigation of the effect of the reverse bending and straightening operations on the tensile properties of tensile armour wires and on tensile armour wire defects

Chapter 10 Effects reverse bending on defects and tensile properties of tensile armour wires.

As stated in section 2.22.3, tensile armour wires are supplied coiled around reels and are also subjected to routine reverse bending tests to detect lamination(s) in the wires. Typically during the manufacturing of flexible pipes, tensile armour wires are unwound from the reel on which they are supplied and wound round a smaller reel. Tensile armour wires from the smaller reel are subjected to bending over a 100mm diameter roller, reverse bending over another 100mm diameter roller and finally straightened over the third 100mm roller as shown in Figure 10.1(a). Bending the tensile armour wires over the big and small reels and bending and reverse bending of the wires over the 100mm rollers subject the wires to bending stresses. The wires are subjected to the highest bending stresses during the bending and reverse bending over the 100mm rollers. These high bending stresses could affect their tensile properties and consequently, their performance in service. The effects of the reverse bending and straightening processes on laminations and scratches as well as the tensile properties of tensile armour wires were investigated using laboratory and numerical experiments.

The laboratory experiments on the reverse bending, straightening and tensile testing of the tensile armour wire, and on the determination of the through thickness microstructure and hardness profiles of the unbent reverse bent, reverse bent and straightened (RBS), and RBS wire that have been subjected to tensile testing are presented in sections 10.1 and 10.2 respectively. The finite element simulations of the reverse bending, straightening and tensile testing of as-received tensile armour wire, and the validation of the simulation of the tensile testing of the RBS wire specimens are presented in section 10.3. The simulations of the effect of bending, reverse bending and straightening of the tensile armour wire on the mid-thickness lamination, near surface lamination and channel shaped scratches in the wire are presented in section 10.4. Section 10.5 presents the summary of the effect of the reverse bending and straightening operations on the tensile armour wire and on the defects in the wire.

10.1: Laboratory experimental reverse bending, straightening and tensile testing of tensile armour wires.

A length of tensile armour wire was wound round a 100mm roller as shown in Figure 10.1(b). The wire was released, allowed to spring back and reverse bent (bent in the opposite

direction) over the same 100mm roller. The wire length was straightened and cut into tensile test specimens. These reverse bent and straightened specimens, which are hereinafter referred to as RBS specimens and the unbent wires tensile test specimens cut from the same wire as the RBS specimens, were subjected to tensile testing. The force-displacement curves and the mechanical properties obtained from the laboratory tensile testing of three as-received/unbent and three RBS wire are shown in Figure 10.2 and Table10.1 respectively. The tensile properties of the experimental unbent specimen 3 was used for the FE material input and the FE result was validated with the experimental RBS specimen 1 curve as their properties are the closest to the average values.

(a) Industrial reverse bending (b) Experimental bending

Figure 10.1: Bending and reverse bending of tensile armour wire round 100mm diameter rollers.

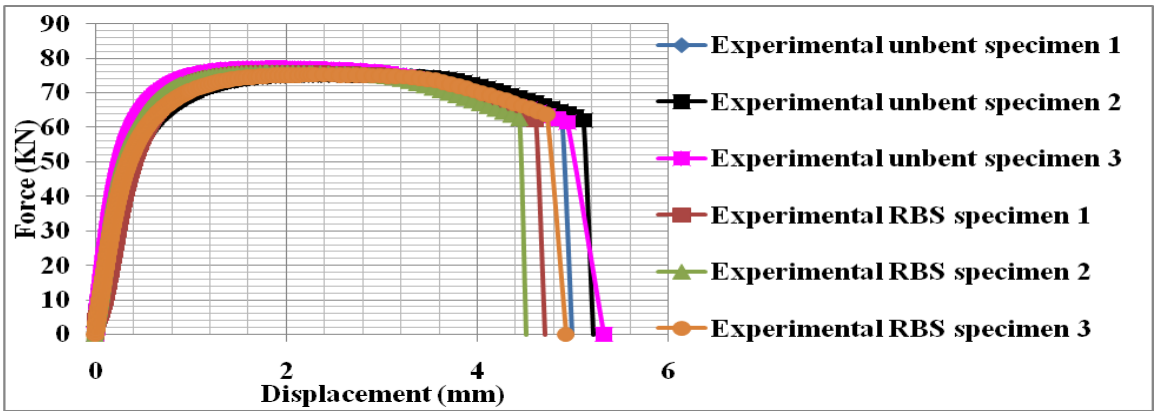

Figure 10.2: Force-displacement curves from laboratory tensile testing of unbent and RBS 12mmx5mm, 50mm gauge length tensile armour wire specimens.

Table 10.1: Mechanical properties from experimental tensile testing of unbent and RBS 12mmx5mm tensile armour wire specimens

Experimental as-received/unbent				
Parameters	Specimen 1	Specimen 2	Specimen 3	Reported value
Ultimate load (kN)	77.6	77.1	77.19	77.30 ± 0.27
Fracture load (kN)	61.92	61.06	61.43	61.47 ± 0.43
Displacement at fracture (mm)	4.88	5.01	4.94	4.94 ± 0.07
Experimental RBS				
Parameters	Specimen 1	Specimen 2	Specimen 3	Reported value
Ultimate load (kN)	75.2	75.89	75.19	75.43 ± 0.40
Fracture load (kN)	62.87	62.7	63.76	63.11 ± 0.57
Displacement at fracture (mm)	4.81	4.44	4.92	4.72 ± 0.25

The reverse bending and straightening processes reduce the ultimate load and displacement at fracture (ductility) by 2.58% and 2.71% respectively as shown in Table 10.1. The reduction in the ultimate load could be due to a reduction in thickness of the wire as a result of necking-down of the wire caused by high back tension and stretching of the fibres on the outer surfaces of the wire during bending and reverse bending. The reduction in the ductility of the wire is due to the work hardening of the wire during bending and reverse bending operations.

10.2 Microstructure and hardness profiles of unbent wires and RBS wires

The effect of the reverse bending, straightening and tensile testing processes on the microstructure and hardness of the tensile armour wires was investigated by taking through thickness micrographs and microhardness profiles with an optical microscope and a microhardness tester respectively. The through thickness micrographs obtained from the unbent wires, reverse bent wires, RBS wires and RBS wires that have been subjected to tensile testing are presented in Figures 10.3, 10.4, 10.5 and 10.6 respectively.

From the micrographs, there is no noticeable difference in the microstructure of the unbent wires specimen and the microstructure of reverse bent, RBS and tensile tested RBS specimens. The micrographs show that the upper and lower surfaces of the wire contain mostly ferrite, which are the white areas of the micrographs, while below the surfaces and

throughout the middle of the wire, the wires contain mostly pearlite which are the dark areas of the micrographs. The grains in the middle of the wire are elongated in the rolling/drawing direction. From the predominant presence of pearlite across the wire thickness except at the upper and lower surfaces, which contains mainly ferrite, the wire can be described as pearlitic with decarburised (loss of carbon from pearlite leaving ferrite) surface layers.

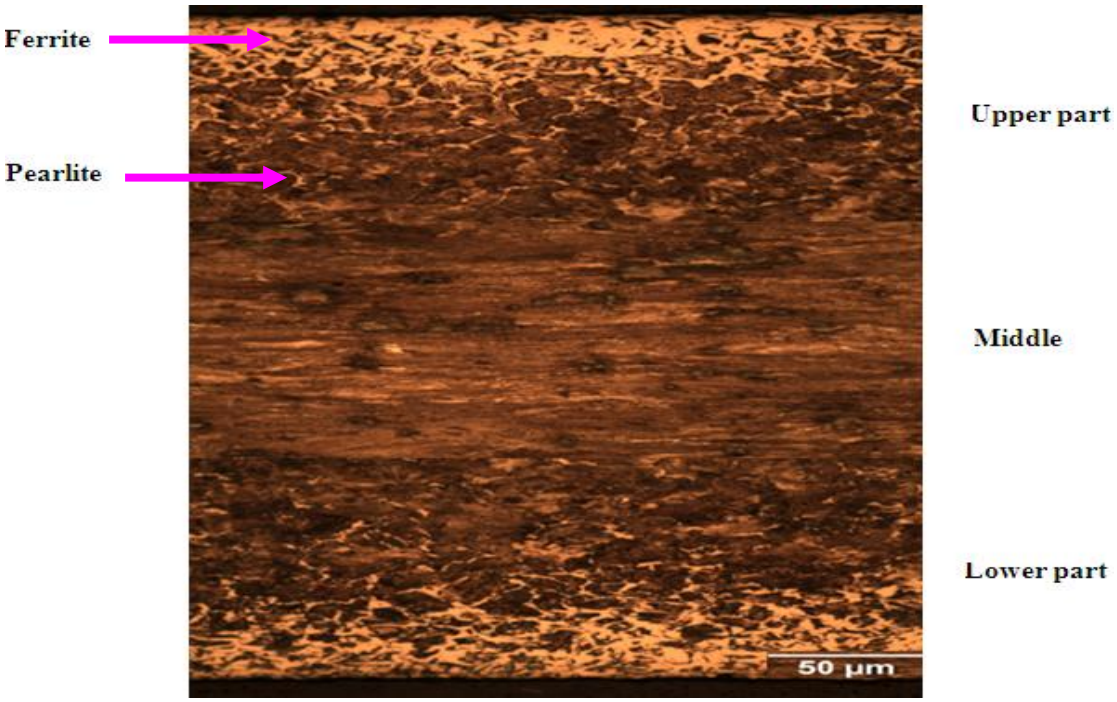

Figure 10.3: Through thickness micrograph of unbent wire.

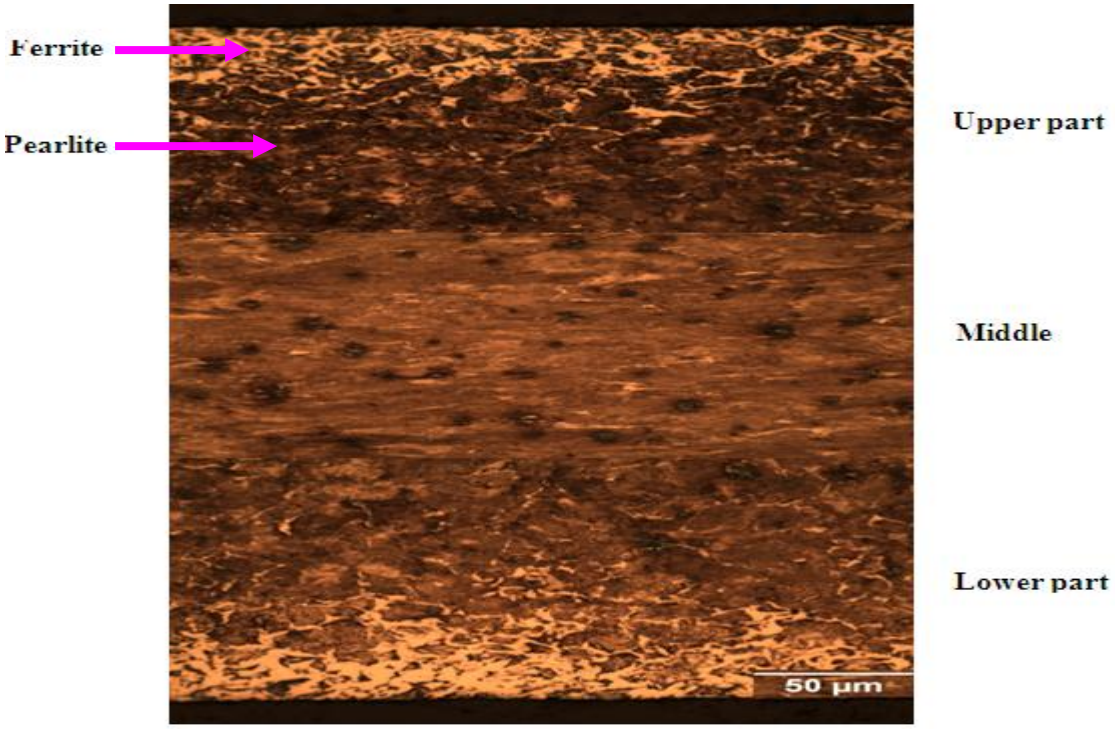

Figure 10.4: Through thickness micrograph of wire subjected to reverse bending.

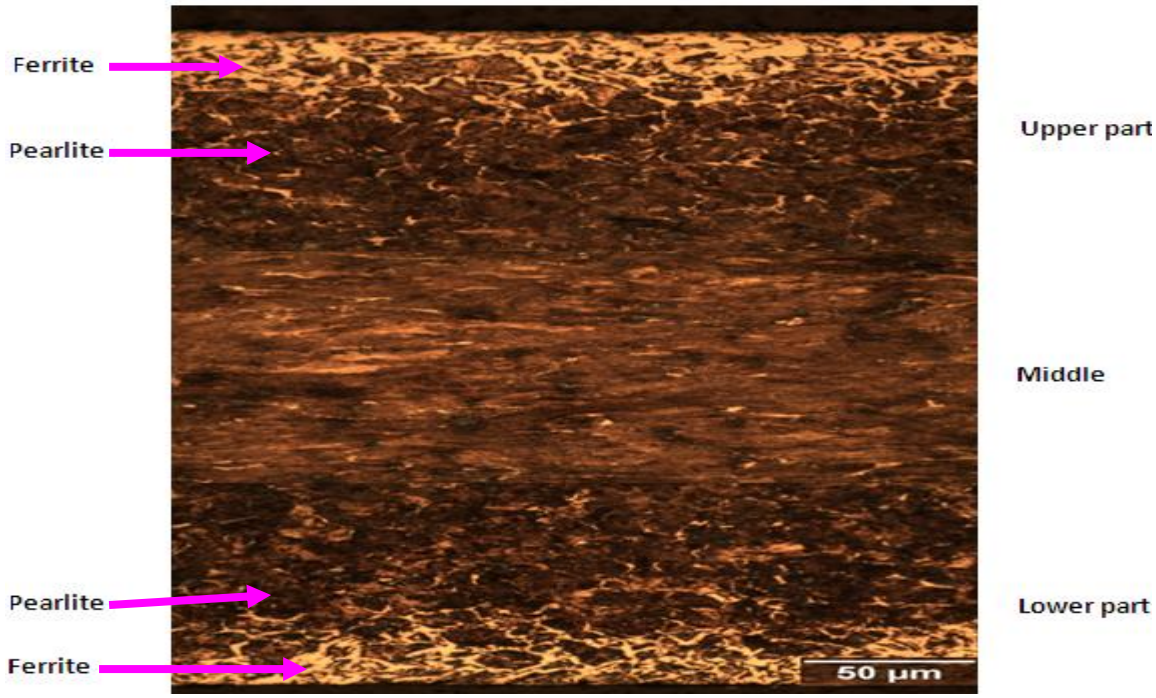

Figure 10.5: Through thickness micrograph of wire subjected to reverse bending and straightening.

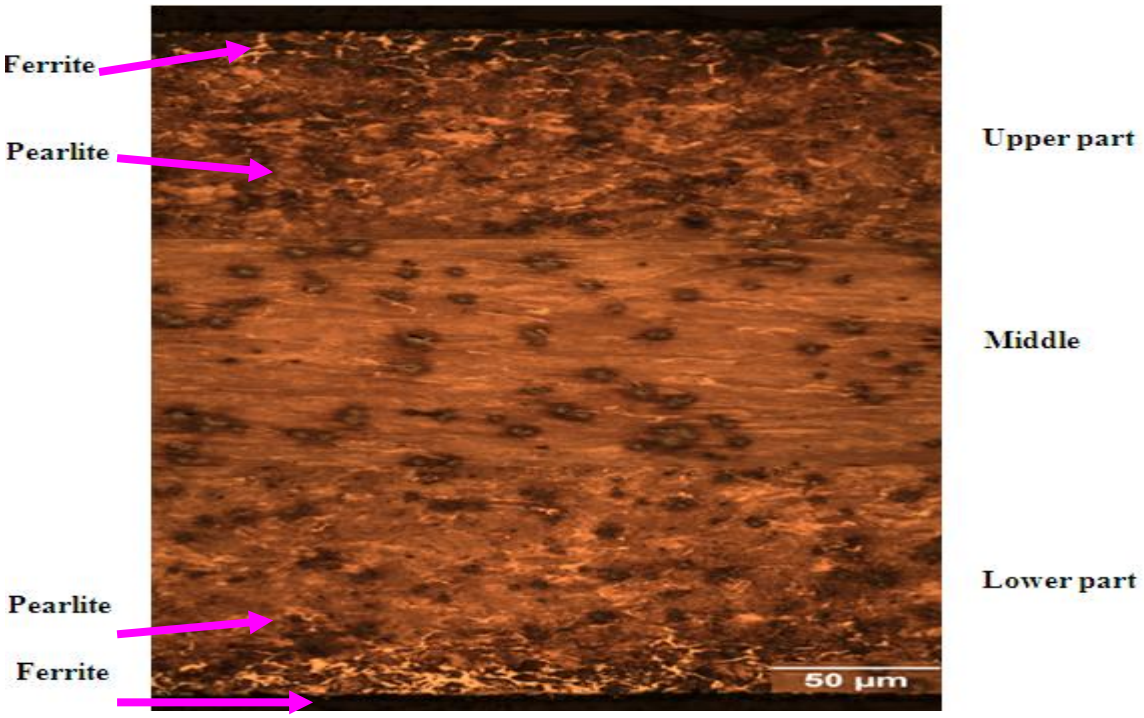

Figure 10.6: Through thickness micrograph of wire subjected to reverse bending, straightening and tensile testing.

The through thickness microhardness profiles shown in Figures 10.7 show that there is no noticeable difference in the through thickness microhardness of the unbent wire, reverse bent, RBS and RBS tensile tested wire specimens. It also shows that the hardness of the wire is not uniform across its thickness with a $57HV_{0.3}$, $61HV_{0.3}$, $83HV_{0.3}$ and $52HV_{0.3}$ difference in the hardness values between the softest and the hardest parts of the unbent wire, reverse bent, RBS and RBS tensile tested wire specimens respectively.

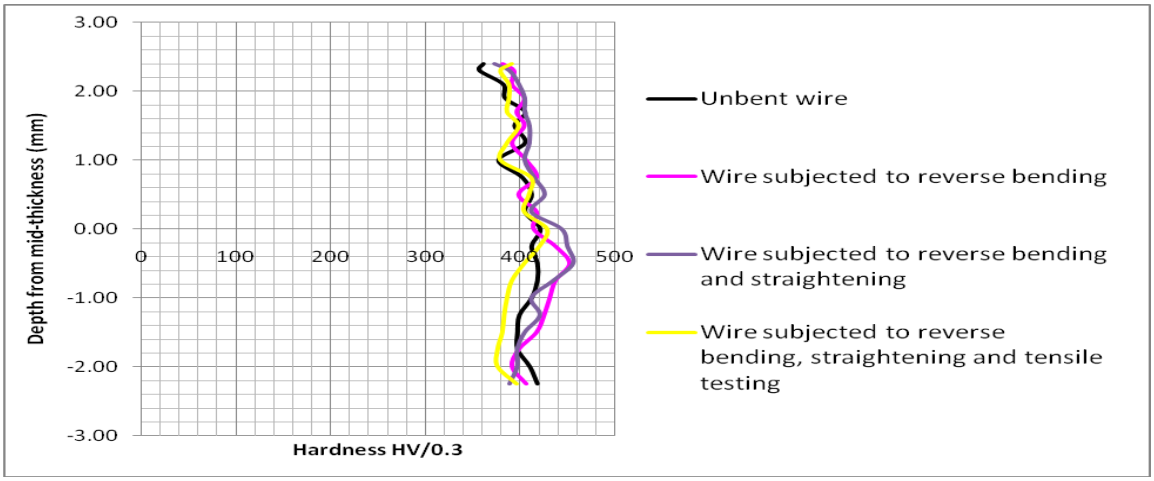

Figure 10.7: Through the thickness hardness profiles of unbent and tensile tested RBS wires.

10.3: Numerical experiments on reverse bending, straightening and tensile testing of as-received tensile armour wires.

The simulations of bending, reverse bending, straightening and tensile testing of the RBS as-received 12mmx5mm tensile armour wires were carried out using the arrangement shown in Figure 10.8. The arrangement consists of a 305mm long tensile armour wire length between the 100mm diameter left roller (roller 1) and the100mm diameter right roller (roller 2), and a guide plate. The 305mm length of tensile armour wire consists of the 50mm long tensile testing specimen in the middle the equal length left and right attachments.

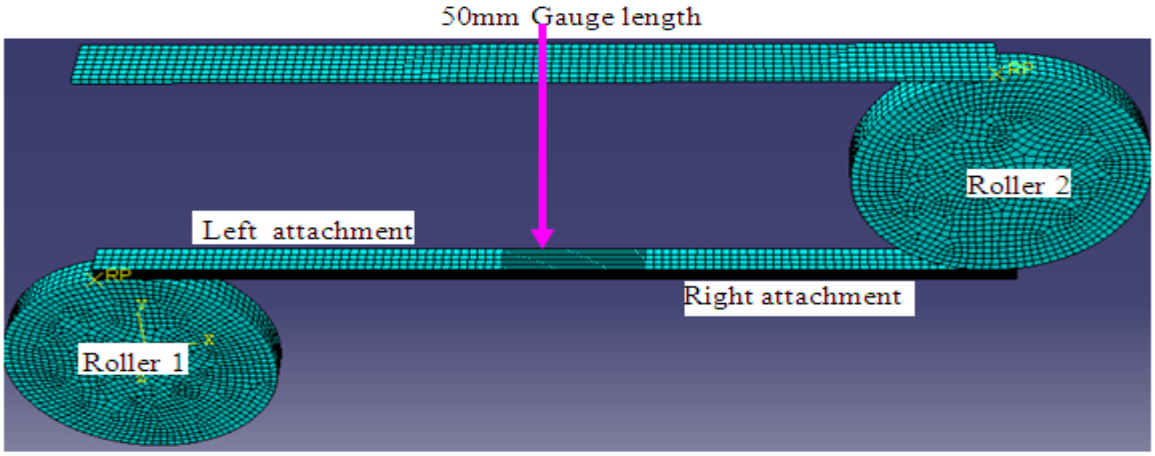

Figure 10.8: Assembly of specimen, attachments, rollers and guide plate.

The simulations were carried out with the attachments to prevent local deformations of the ends of the 50mm long tensile test specimen which occurred when the reverse bending and straightening simulations were carried out without the attachments (i.e. with the ends of the specimen directly attached to the rollers) as shown in Figures 10.9 (a) and (b). The localised specimen end deformation made it impossible to carry out the tensile testing simulation as the boundary conditions for the tensile testing simulation which follows the straightening simulation could not be applied to the badly deformed specimen ends.

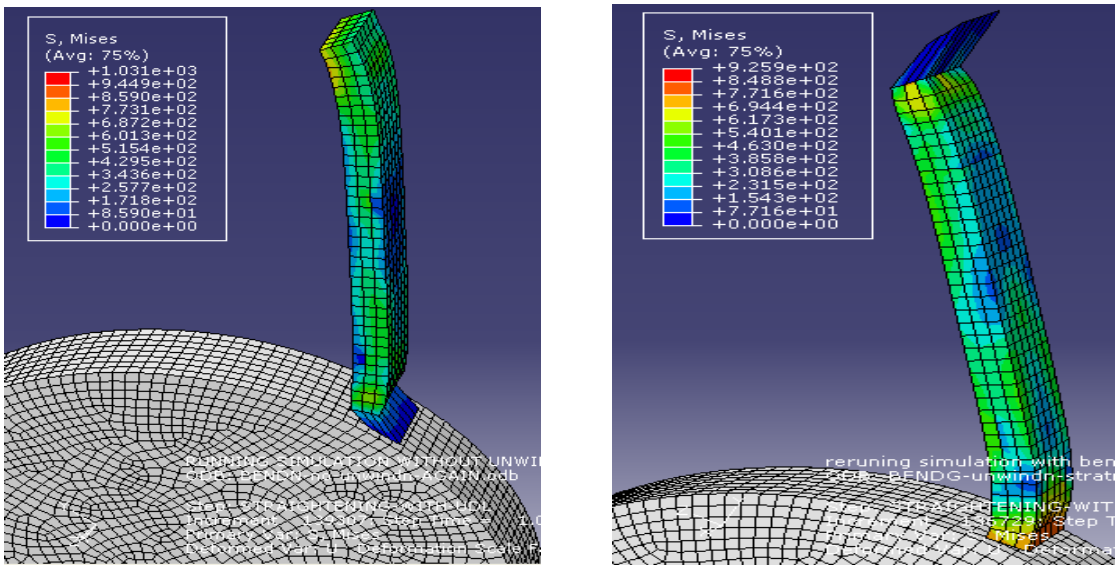

(a) End deformation during bending (b) End deformation during straightening

Figure 10.9: Localised specimen ends deformation and Mises stress (MPa) distribution from simulations without attachments.

The whole model was meshed with C3D8R elements (8-node hexahedral linear brick reduced integration elements with hourglass control). The rollers and the guide plate were meshed with 3mmx3mmx3mm elements while the attachments and the specimen were meshed with elements having 3mmx3mmx0.5mm and 3mmx1mmx0.5mm dimensions. The 1mm dimension is along the specimen length and the 0.5mm dimension is along the wire thickness. With 0.5mm element thickness, there are 10 elements along the wire thickness. The specimen was meshed with the finest mesh in order to obtain accurate results as the tensile testing simulation was carried out on the 50mm long specimen alone. The rollers, the guide plate and the attachments (which were only introduced to prevent localised deformation of the ends of the specimen) were meshed with a coarse mesh to reduce the output file size and computation time. Attempts to use smaller element sizes were not successful as the ends of the attachments meshed with smaller elements deformed excessively as shown in Figure 10.10, making subsequent straightening and tensile testing simulation steps impossible.

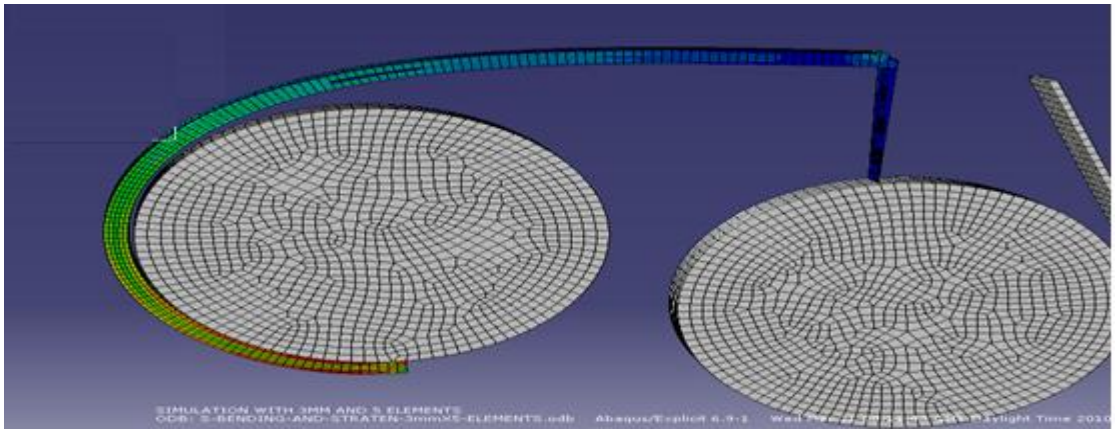

Figure 10.10: Excessive deformation of ends of attachments meshed with finer mesh.

Two elastic-plastic simulations were carried out; one with an isotropic hardening model and the other with a combined hardening model in order to determine which one would predict the behaviour of the tensile armour wires more accurately since the simulation involves strain reversal. The material input data used for the simulation with isotropic hardening were the post yield true stress and plastic strain obtained from the laboratory tensile test results while the material input data used for the simulation with combined hardening were obtained from laboratory tensile test results and numerical experiments detailed in section 10.3.1.

10.3.1 Determination of combined hardness modelling parameter values

The appropriate parameter combinations for the combined hardening model were obtained through laboratory and numerical testing, parametric study and correlation with experimental curve as stated in section 3.7.4.1. The yield stress at zero plastic strain was obtained from the laboratory tensile test results as the true yield stress at the absolute yield point of the wire. The numerical testing and parametric study involved simulating tensile testing of unbent/as-received wire specimens with varying combined hardening modelling parameters until the FE force-displacement curve agreed with the experimental curve. The parameter sensitivity analysis carried out revealed that the extent of the work hardening and the ultimate load value are chiefly determined by the value of the kinematic hardening parameter, γ, while the displacement at fracture is chiefly determined by the value of the isotropic hardening parameter, b. The force-displacement curve is less sensitive to other parameters
Various simulations were carried out with various combinations of the isotropic hardening parameters b and Q infinity (Q_∞), and the kinematic hardening parameters, $C1$, and Gamma(γ), until the force-displacement curve predicted by the FE had ultimate load and

displacement at fracture values that are close to the experimental values. Some of the parameter combinations are presented in Table 10.2.

Table 10.2: Combined hardening parameter combinations

	Parameter combination A	Parameter combination B	Parameter combination C	Parameter combination D
Yield stress at zero plastic strain (MPa)	754.850	754.850	754.850	754.850
Kinematic hardening parameter $C1$	15300	15300	15300	15300
Gamma γ	240	280	275	275
Q infinity	12000	12000	12000	12000
Hardening parameter b	0.01	0.014	0.04	0.05

A simulation of the tensile testing was also carried out with the isotropic hardening model for comparison. Figure 10.11 shows the experimental force-displacement curve and the force-displacement curves predicted by the simulations with the isotropic hardening model and combined hardening model with parameter combinations A, B, C and D.

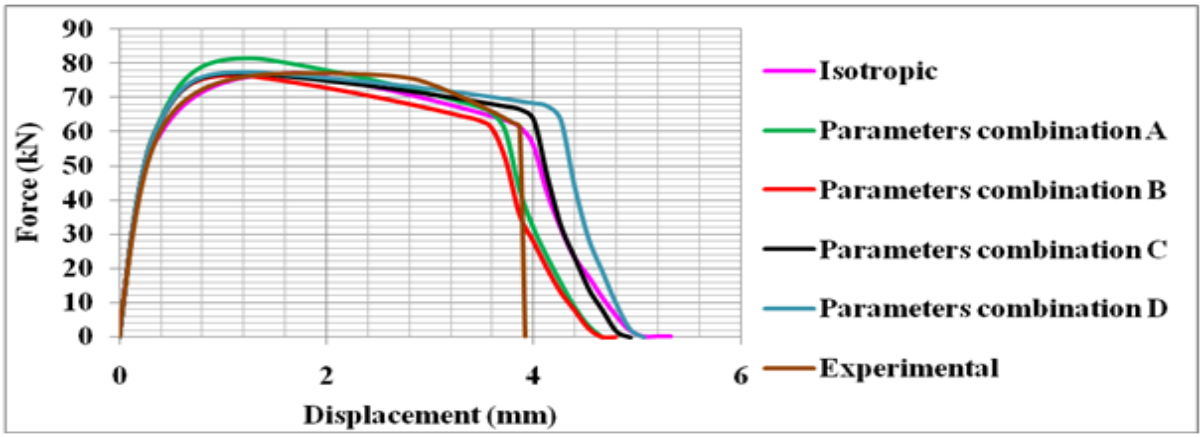

Figure 10.11: Experimental and FE with isotropic and combined hardening models force-displacement curves for 12mmx5mm wire with 50mm gauge length.

As shown in Figure 10.12, the force-displacement curve predicted by the simulation with combined hardening parameter combination C agrees best with the experimental force-displacement curve with only 0.059% and 0.093% differences between their ultimate load and their displacement at fracture values respectively as shown in Table 10.3. All the curves in figure 10.11 have the same elastic response. Consequently, subsequent simulations were carried out with combined hardening parameters combination C.

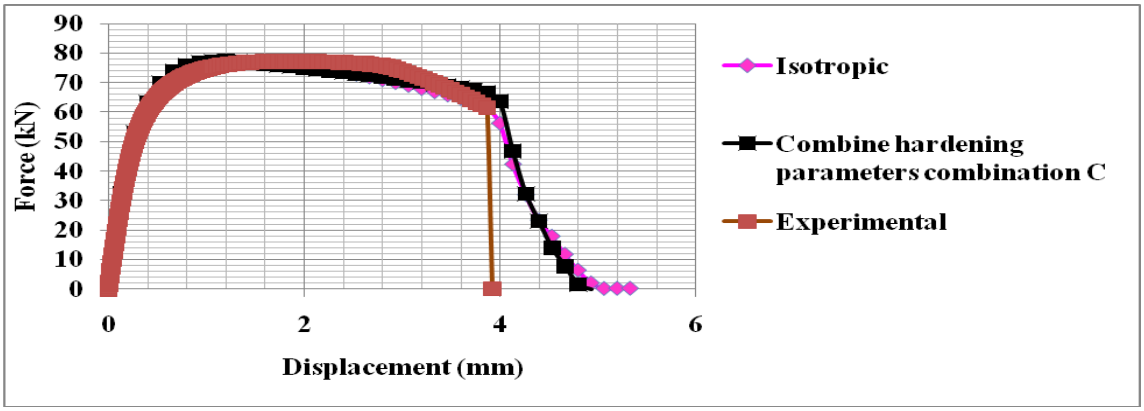

Figure 10.12: Experimental, FE with isotropic and combined hardening parameter combination C force-displacement curves.

Table 10.3: Mechanical parameters from experiment and FE simulations with isotropic and combined hardening models

Parameters	Experiment	FE with isotropic hardening	FE with combined hardening	% difference between isotropic hardening and experimental values	% difference between combined hardening and experimental values
Ultimate load (kN)	77.19	77.19	77.23	0.00	0.06
Fracture load (kN)	61.43	61.55	63.57	0.21	3.49
Displacement at fracture (mm)	3.86	3.86	3.86	0.00	0.00

10.3.2 Simulations of bending, reverse bending, straightening and tensile testing of tensile armour wires

Having obtained the combined hardening parameters combination where the force-displacement curve predicted by the FE simulation agrees with the experimental curve, simulations of bending, reverse bending, straightening and tensile testing were carried out with isotropic hardening and combined hardening models. Throughout the bending, reverse bending, straightening and tensile testing simulations, the deformed shapes predicted by the simulations carried out with isotropic hardening and combined hardening are exactly the same except for the difference in the shapes of the fractured specimens after the tensile testing simulation. However, there are slight differences in the values of the stress and strain across the thickness of the wire predicted by the simulations with the two hardening models. Consequently, only the deformed shapes obtained from the simulation with isotropic hardening alone are presented to conserve space while the through the thickness stress and strain profiles predicted by the simulations with the two hardening models are presented.

10.3.2.1 Bending simulation

The bending simulation was carried out by rotating the left roller (roller 1) in an anticlockwise direction. The deformed shape of the whole 320mm wire length showing the longitudinal axial stress (S11) distribution during the bending simulation is shown in Figure 10.13(a). The through thickness longitudinal axial stress and Mises stress distributions in the 50mm long tensile test specimen during bending simulation are shown in Figures 10.13(b) and (c) respectively. Positive axial stresses in the S_{11}contour plot represent tensile axial stresses while negative axial stresses represent compressive axial stresses. The highest tensile stress is indicated at the top of the contour plot with the deepest red colour while the highest compressive stress is indicated at the bottom of the contour plot with the deepest blue colour. From Figure 10.13 (b), the upper and the lower parts of the wire are subjected to tensile and compressive axial stresses respectively while the middle of the specimen has zero equivalent/Mises stress as shown in Figure 10.13(c).

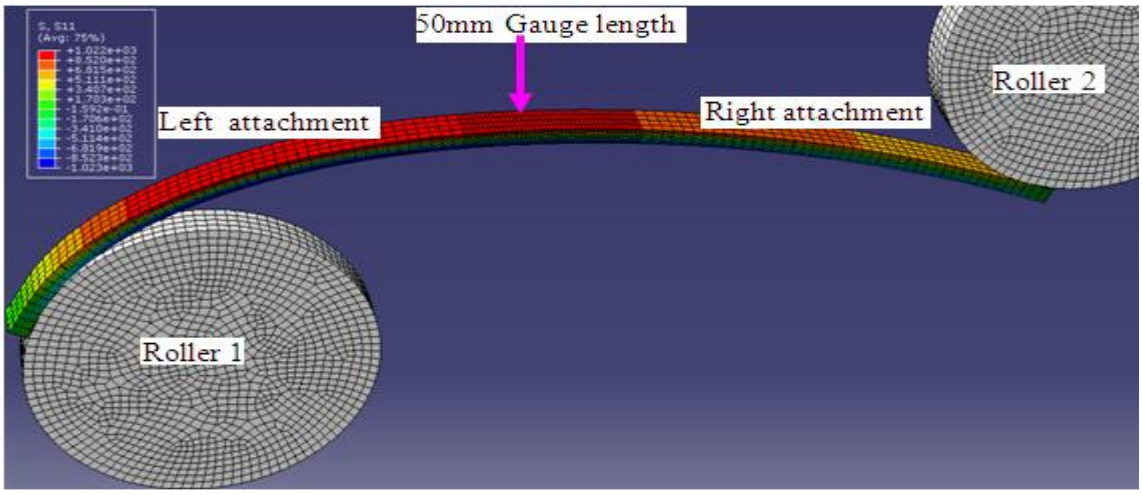

(a) Deformed shape and longitudinal axial stress distribution in whole wire length

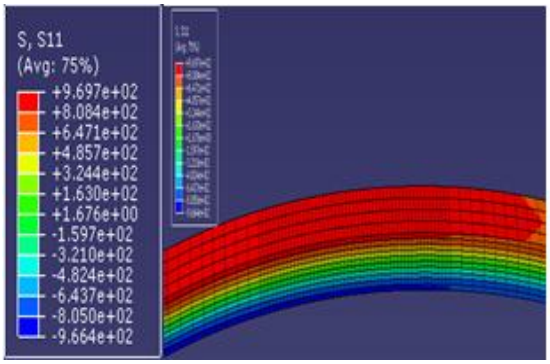

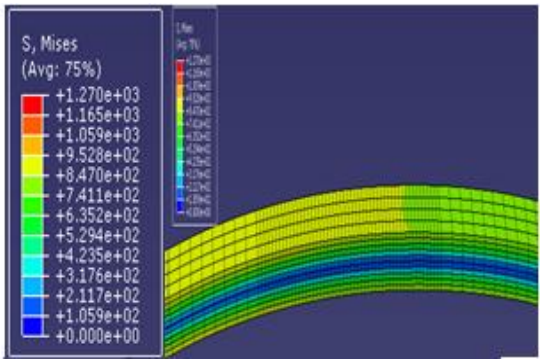

(b) Specimen longitudinal axial stress distribution (c) Specimen Mises stress distribution

Figure 10.13: Axial stress (MPa) and plastic strain distributions in wire during bending simulation.

The deformed shape of the whole 320mm wire length showing the longitudinal axial stress distribution after bending simulation is shown in Figure 10.14(a) while the through thickness longitudinal axial stress and equivalent plastic strain distributions in the test specimen are shown in Figures 10.14 (b) and (c) respectively.

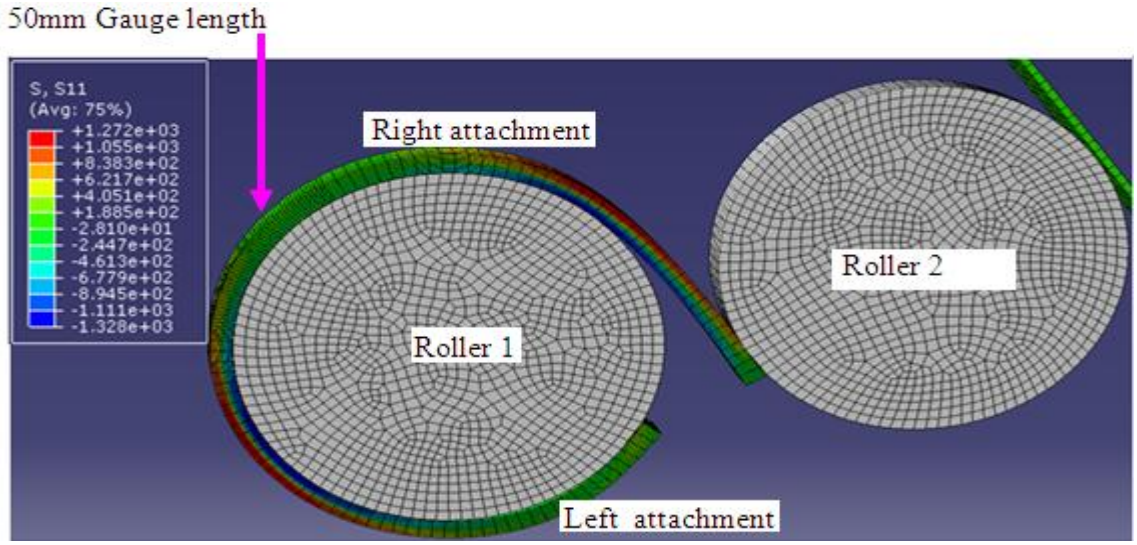

(a) Deformed shape and longitudinal axial stress distribution in whole wire length

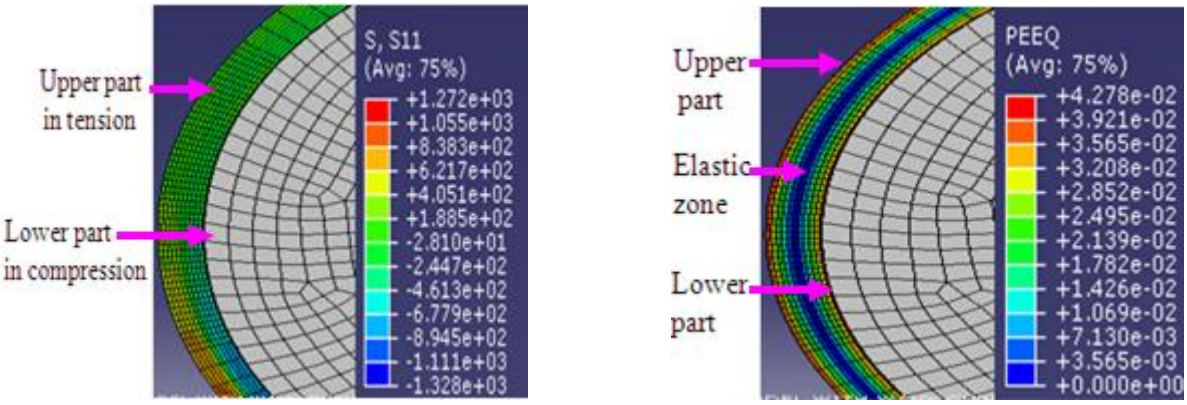

b) Specimen longitudinal axial stress distribution (c) Equivalent plastic strain distribution

Figure 10.14: Axial stress (MPa) and plastic strain distributions in specimen after bending simulation.

The maximum longitudinal axial stress and plastic strain across the thickness of the wire hereafter referred to as the through thickness axial stress profile and through thickness plastic strain profile respectively in the 50mm long specimen due to bending are shown in Figures 10.15 and 10.16 respectively. The stress and strain in the upper half thickness and the lower half thickness of the wire are plotted with 0 to 2.5mm and 0 to -2.5mm Y-axis coordinates respectively. As shown in Figures 10.15 and 10.16, there is a stress-strain gradient across the thickness of the wire with the peak stress and strain occurring at the surfaces of the wire. This result agrees with what is reported by Tvergaard, (1987) and is due to the fact that the fibres at the surfaces of the wire experience the highest stress and strain. Also the predicted through thickness longitudinal axial stress profile in the bent wire in Figure 10.19 agrees with the

through thickness axial stress profile after bending shown in Figure 4.11 reported by Gau and Kinzel, (2001). As shown in Figure 10.16, the strain profile is linear as expected since the deformation or straining of the wire is imposed by the curvature during bending.

Calculating the maximum strain in the wire with a thickness (T) of 5mm, bent over a roller of diameter (D_r) of 100mm with the expression given in equation 4.8, the maximum strain in the wire is calculated as 0.048 as shown in equation 10.1. The 0.048 maximum strain obtained with the analytical expression agrees well with the 0.043 predicted by the bending simulation as shown in the equivalent strain contour plot in Figure 10.14(c). This shows the accuracy of the bending simulation.

$$e = \frac{T}{T + D_r} = \frac{5}{5 + 100} = 0.048 \tag{10.1}$$

From Figures 10.15, and 10.16, the 5mm thick wire is subjected to tensile and compressive stresses at its upper and lower parts respectively. The neutral axis/zone occurs approximately at a depth of 0.0148mm below the geometric mid-thickness of the wire and not at the mid-thickness/depth which occurs in elastic and/or pure bending because the simulation involves plastic bending and frictional contact between the lower part of the wire and the roller. As shown by the elastic zone (zero plastic strain) in Figure 10.14(c) and the linear portion of the axial stress profile in Figure 10.15, approximately the middle 20% of the wire thickness with tensile/compressive stresses less or equal to 754MPa (the axial yield strength of the wire) remains elastic after bending. The remaining outer portions of the wire have been plastically deformed to varying degrees with the highest plastic deformation (typified by the highest axial stress and plastic strain) occurring at the top of the upper half and bottom of the lower half of the wire.
(Gau and Kinzel, 2001).

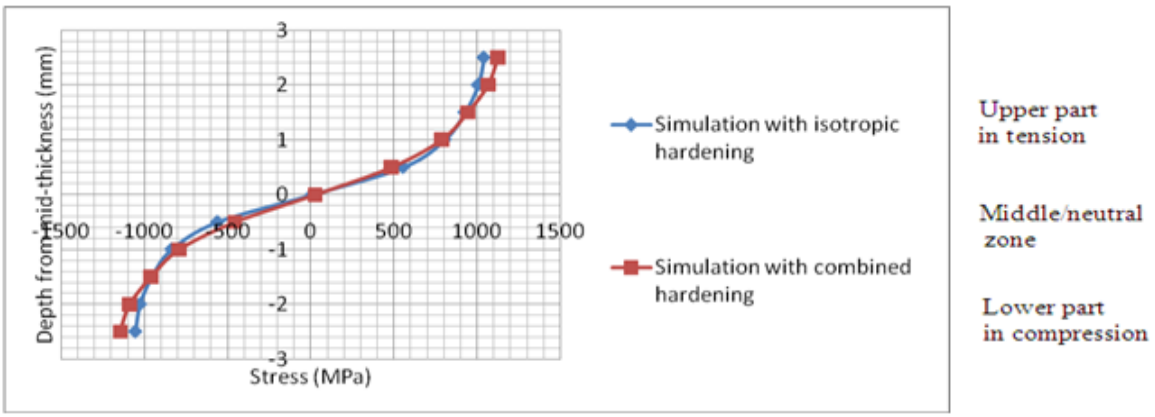

Figure 10.15: Through thickness longitudinal axial stress profile in specimen after bending.

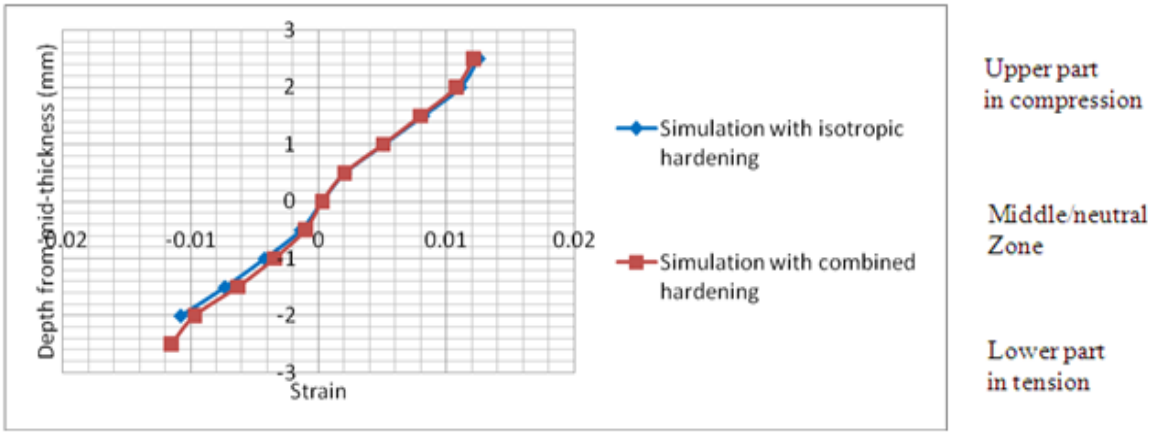

Figure 10.16: Through thickness longitudinal axial plastic strain profile in test specimen after bending.

10.3.2.2 Reverse bending simulation

The reverse bending simulation was carried out by rotating the right roller (roller 2) in an anticlockwise direction. The deformed shape of the whole 320mm wire length showing the longitudinal axial stress distribution during reverse bending over the second 100mm roller (reel 2) is given in Figure 10.17(a).

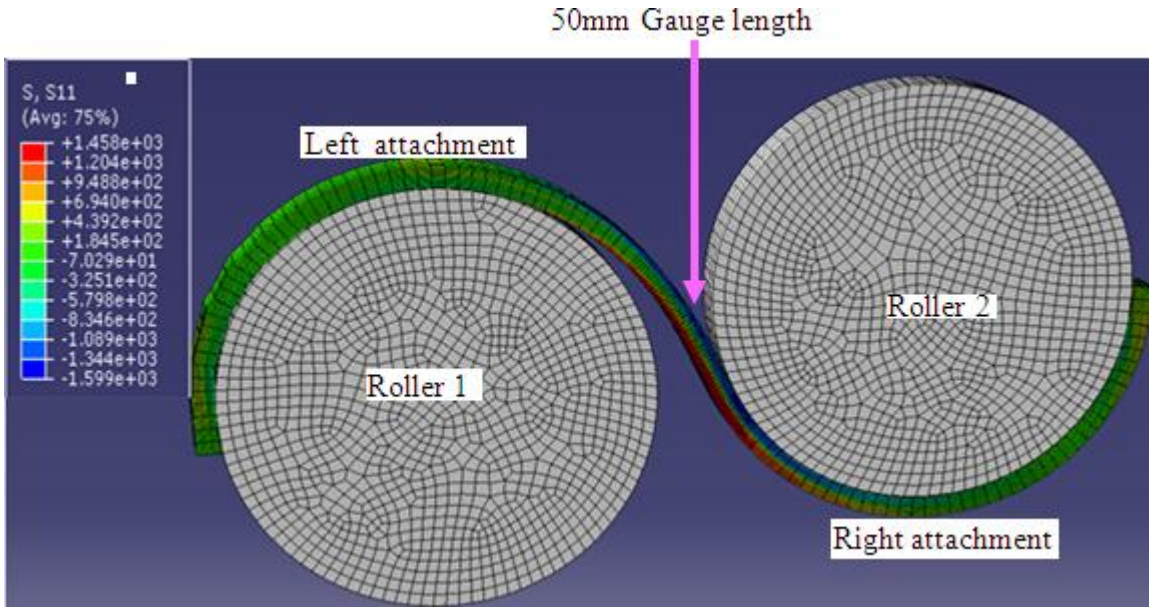

Figure 10.17: Axial stress (MPa) and plastic strain distributions in specimen during reverse bending simulation.

The deformed shape of the whole 320mm wire length showing the longitudinal axial stress distribution after the reverse bending simulation is shown in Figure 10.18 (a) and the through thickness longitudinal axial stress and equivalent plastic strain distributions in the specimen are shown in Figures 10.18 (b) and (c) respectively.

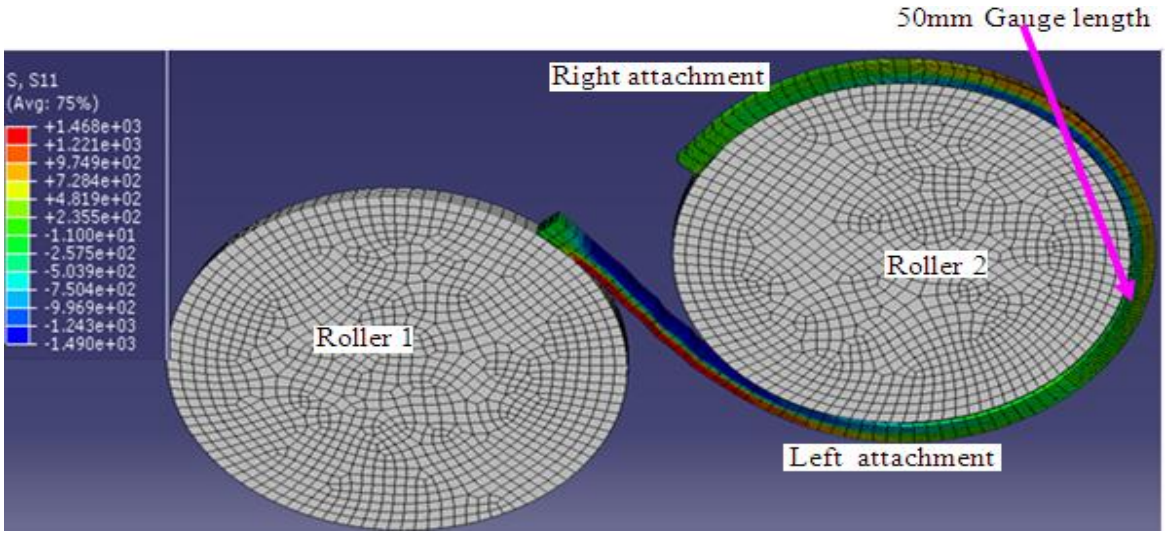

(a) Deformed shape and longitudinal axial stress distribution in whole wire length

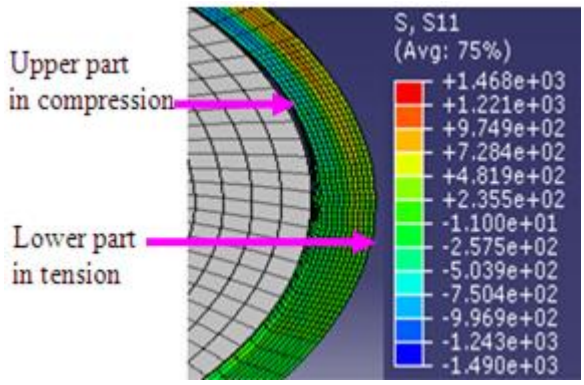

(b) Longitudinal axial stress distribution

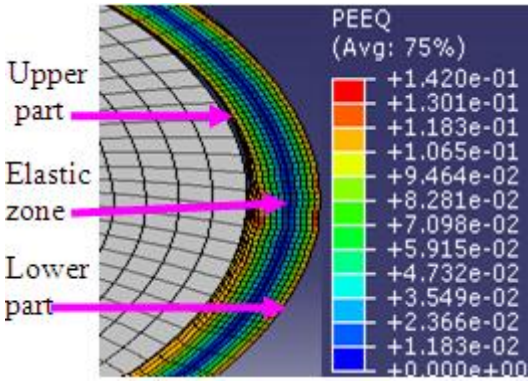

(c) Equivalent plastic strain distribution

Figure 10.18: Axial stress (MPa) and plastic strain distributions in specimen after reverse bending simulation.

The through thickness maximum longitudinal axial stress and plastic strain profiles of the test specimen after reverse bending simulation are presented in Figures 10.19 and 10.20 respectively. Again, the predicted through thickness longitudinal axial stress profile in the reverse bent wire in Figure 10.19 agrees with the through thickness stress profile after reverse bending shown in Figure 4.11 reported by Gau and Kinzel, (2001). As shown in Figure 10.20, the strain profile predicted by the simulation with the combined hardening model is linear as expected for a bending induced straining, whereas the strain profile predicted by the simulation with the isotropic hardening model is not linear. Now, a difference between the hardening models is observed. Unlike the bending simulation which subjected the upper and

lower halves of the wire to tension and compression respectively, the upper half of the wire is now subjected to compression and the lower half is subjected to tension after reverse bending simulation as shown in Figures 10.18, 10.19 and 10.20.

As shown by the elastic zone (zero plastic strain) in Figure 10.18(c) and the linear portion of the longitudinal axial stress profile in Figure 10.19, approximately the middle 20% of the wire thickness with tensile/compressive stresses less or equal to 754MPa (the axial yield strength of the wire) remains elastic after reverse bending while the remaining outer portions of the wire have been plastically deformed.

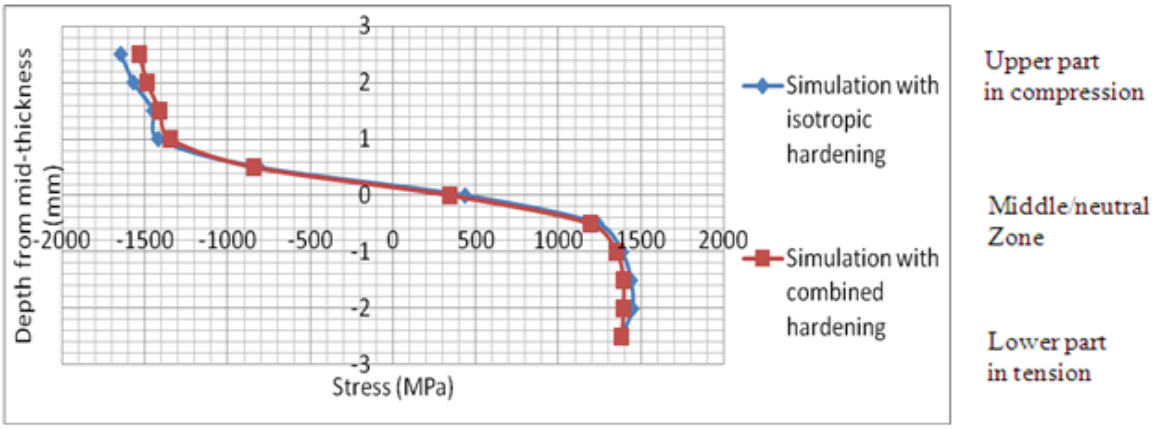

Figure 10.19: Through thickness axial stress profile in specimen after reverse bending.

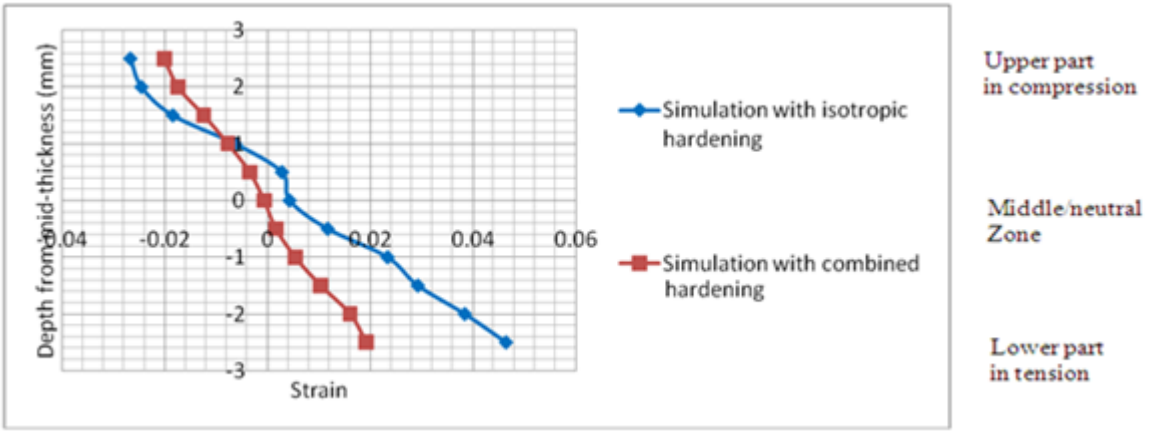

Figure 10.20: Through thickness axial plastic strain profile in test specimen after reverse bending.

10.3.2.3 Straightening simulation

The straightening simulation was carried out by rotating roller 2 in a clockwise direction to unwind the tensile armour wire and by pulling roller 1 longitudinally and vertically until the attachments and test specimen was straightened. The deformed shape of the whole 320mm wire length showing the longitudinal axial stress distribution after the straightening simulation is shown in Figure 10.21(a). The through thickness longitudinal axial stress and equivalent plastic strain distributions in the test specimen are shown in Figures 10.21 (b) and (c) respectively.

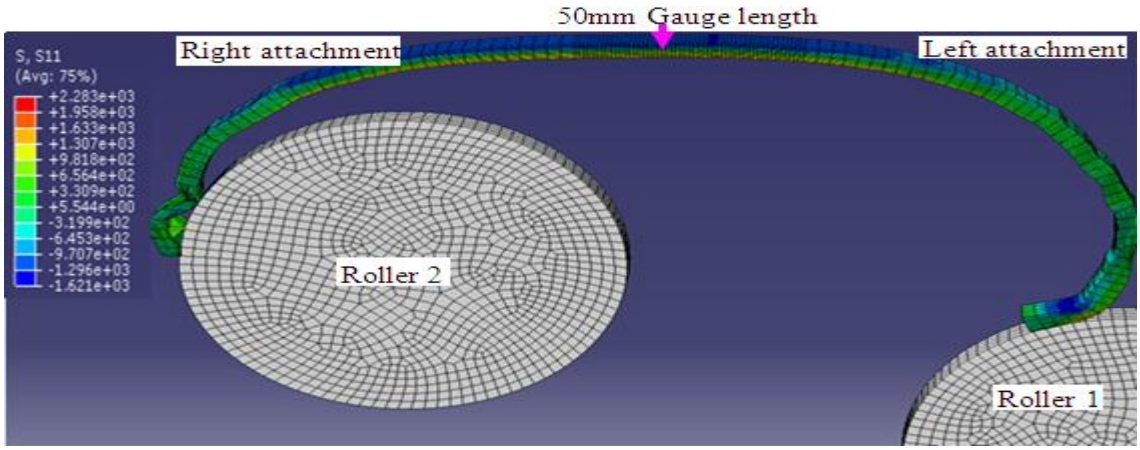

(a) Deformed shape and stress distribution in whole wire length

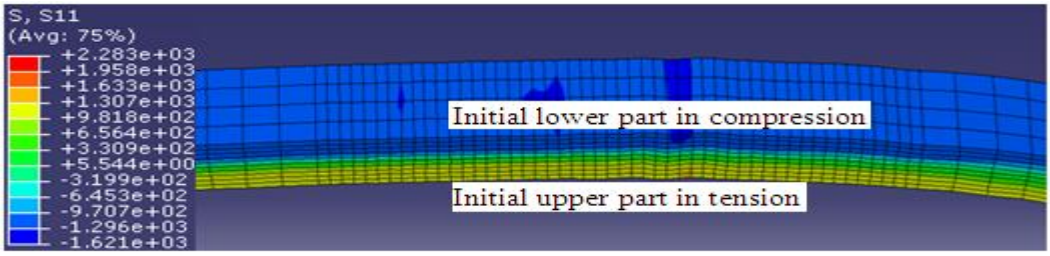

(b) Longitudinal axial stress distribution

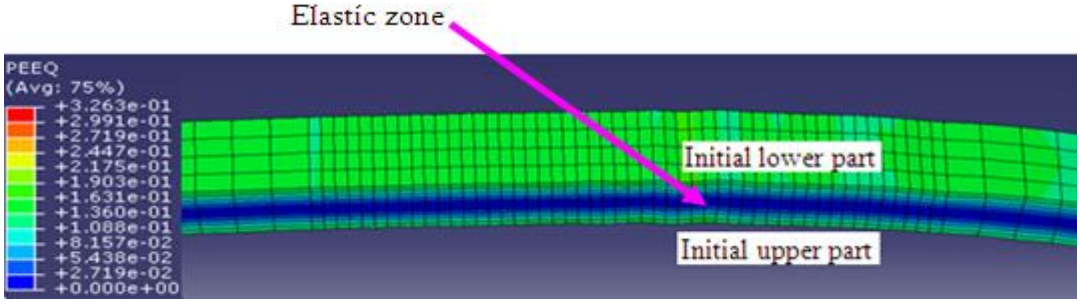

(c) Equivalent plastic strain distribution

Figure 10.21: Axial stress (MPa) and plastic strain distributions in specimen after straightening simulation.

The through thickness maximum longitudinal axial stress profile and the maximum longitudinal axial plastic strain profile in the test specimen after straightening simulation are presented in Figures 10.22 and 10.23 respectively. The strain profiles predicted by the two hardening models shown in Figure 10.23 are no longer linear after straightening due to the tensile induced plastic straining involved in the straightening process. As shown in Figures 10.21(a), (b) and (c), the initial upper part of the wire at the beginning of the simulation is now the lower part after the wire has undergone bending, reverse bending and straightening simulations and is in tension. As shown by the elastic zone (zero plastic strain) in Figure 10.21(c) and the linear portion of the longitudinal axial stress profile in Figure 10.22, approximately the middle 20% of the wire thickness with tensile/compressive stresses less or equal to 754MPa (the axial yield strength of the wire) remains elastic after straightening while the remaining outer portions of the wire have been plastically deformed.

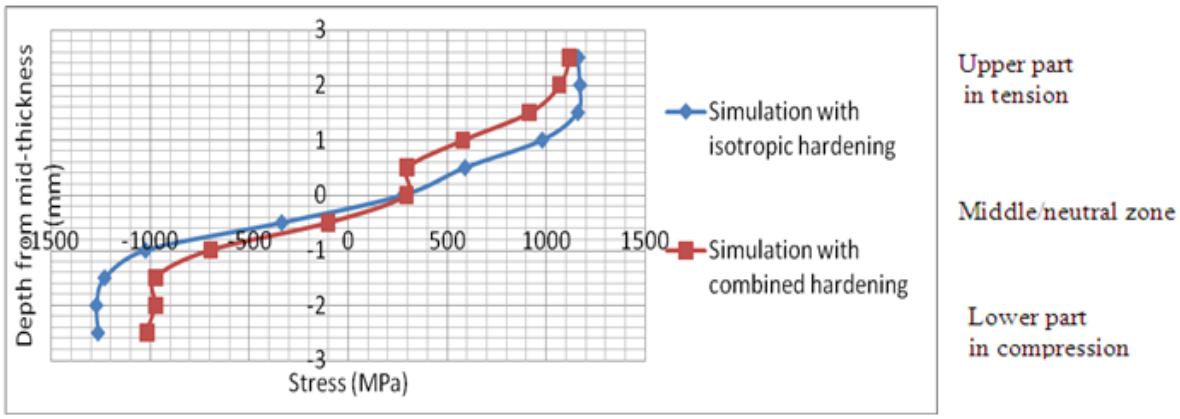

Figure 10.22: Through thickness longitudinal axial stress profile in specimen after straightening.

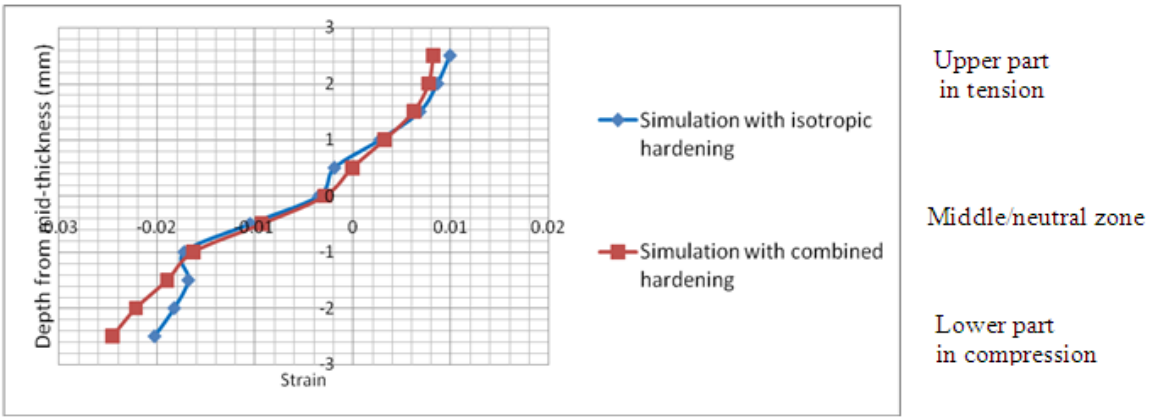

Figure 10.23: Through thickness longitudinal axial plastic strain profile in specimen after straightening.

10.3.2.4 Tensile testing simulation

The combined longitudinal axial stress histories showing the stress reversals that the upper, the middle and the lower parts of the wire have undergone during the bending, reverse bending and straightening simulations are shown in Figure 10.24. The combined stress histories were obtained from nodes at the topmost part, the mid-thickness and the bottom of the lower part of the wire. In Figure 10.24, the bending, reverse bending and straightening simulations occurred at 0-1s, 1-2s, and 2-3s analysis step times respectively. As stated earlier, and as evidenced in Figure 10.24, throughout the bending, reverse bending and straightening simulations, the middle of the wire remains elastic as it was never stressed beyond its yield stress of 754MPa, while the upper and lower parts of the wire underwent cyclic tensile and compressive plastic deformations.

The stress at the end of the straightening simulation represents the residual stress in the 50mm tensile test specimen at the beginning of the tensile testing simulation. Consequently, the upper and the lower parts of the tensile test specimen (which were initially the lower and upper part at the beginning of the bending simulation respectively) have residual compressive and residual tensile stresses respectively at the beginning of tensile testing simulation. Thus the residual stress across the wire thickness at the beginning of the tensile testing simulation is not uniform leaving the RBS wire test specimen with an unbalanced stress distribution. Also the upper and the lower parts of the wire specimen subjected to the tensile testing simulation have been plastically deformed and work hardened while the middle 20% (approximately) of its thickness remained elastic.

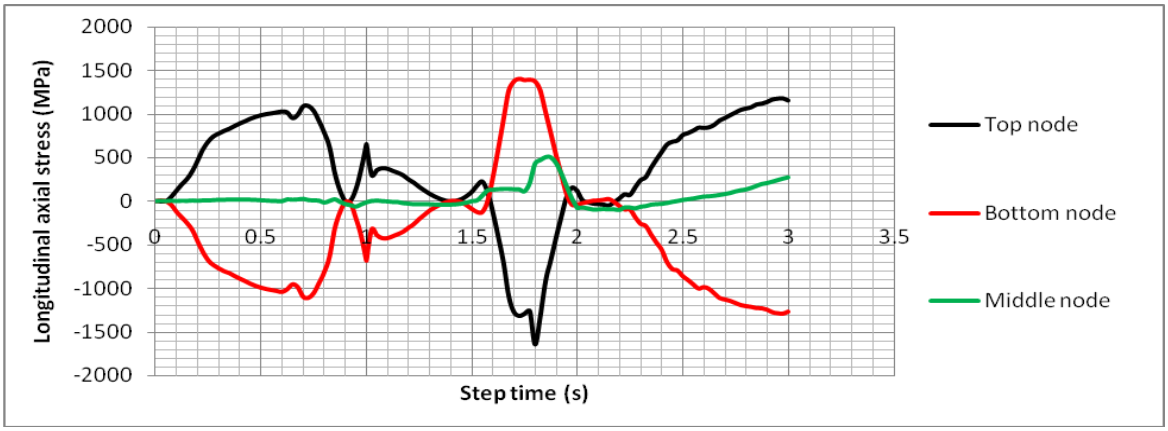

Figure 10.24: Stress histories of upper, middle and lower parts of RBS wire test specimen.

10.3.2.5 Boundary conditions during tensile testing simulation

During the tensile testing simulation step, the left roller, the left attachment and the left end of the specimen were fixed while the right roller, the right attachment and the right end of the specimen that are free to move only in the longitudinal direction were subjected to longitudinal axial displacement. To ascertain whether these boundary conditions are appropriate, a tensile testing simulation alone without the bending, reverse bending and straightening simulations was carried out on the unbent wire in the rollers-attachments-specimen assembly with these boundary conditions as shown in Figure 10.25(a). The result of the simulation was compared with the result of a tensile testing simulation carried out on unbent wire alone (i.e. not in the rollers-attachments-specimen assembly) with the same boundary conditions as shown in Figures 10.25(b).

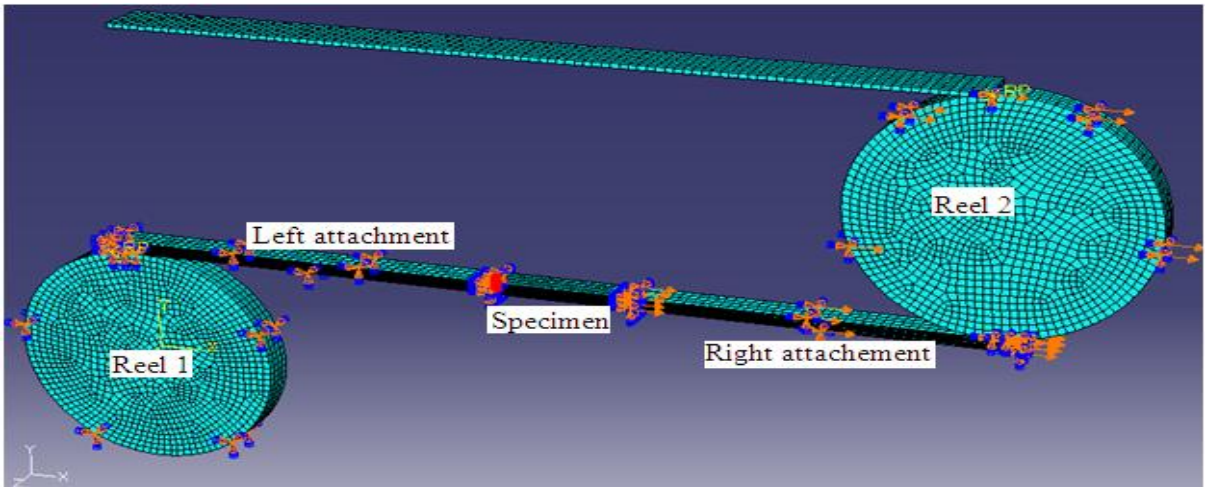

(a) Unbent wire in rollers-attachments-specimen assembly

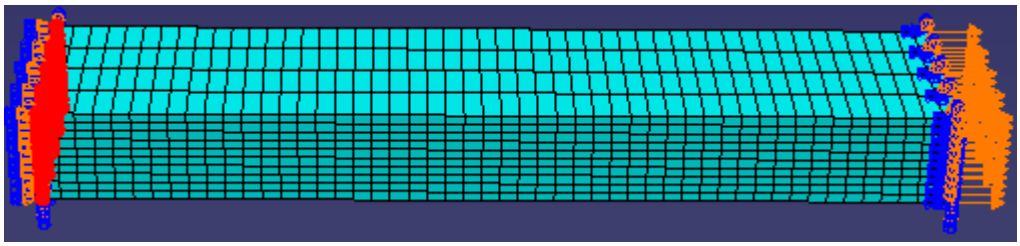

(b) Unbent wire alone

Figure 10.25: Boundary conditions on unbent wire alone and unbent wire in rollers-attachments-specimen assembly during tensile testing simulation.

The fracture shapes predicted by the simulations carried out with the unbent wire alone and with the unbent wire in the rollers-attachments-specimen assembly are shown in Figure

10.26. The force-displacement curves predicted by the simulations with the unbent wire alone and the unbent wire in the rollers-attachments-specimen assembly shown in Figures 10.27 agrees well with a maximum of 0.19% difference between the mechanical properties predicted by the two simulations as shown in Table 10.4. This shows that the boundary conditions applied to the reels, attachments and specimen during the tensile testing simulation step are appropriate as they have negligible impact on the tensile response of the 50mm tensile test specimen. The 0.19 percentage difference is within the variation that occurs in FE computations and could be due to the differences in the computation of the nodal force and displacement values as a result of the differences in the number of nodes involved in the computations for the simulations with the unbent wire alone and the unbent wire in the rollers-attachments-specimen assembly.

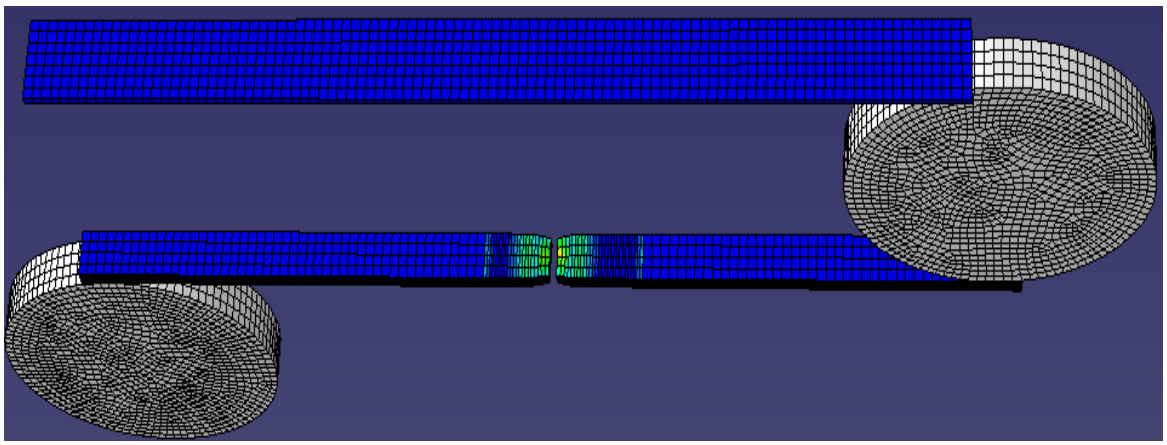

(a) Unbent specimen in reels-attachments-specimen assembly

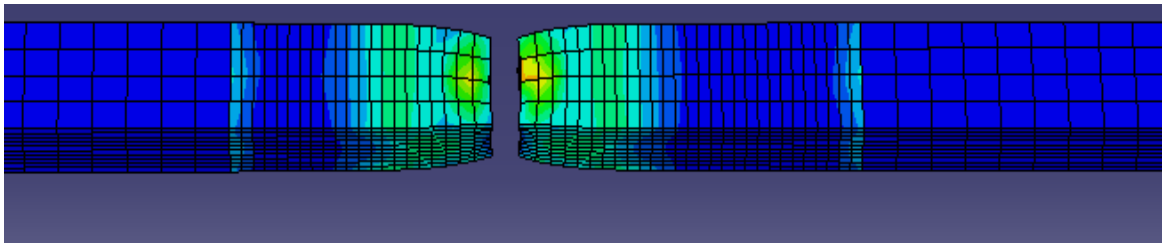

(b) Fractured specimen between attachments

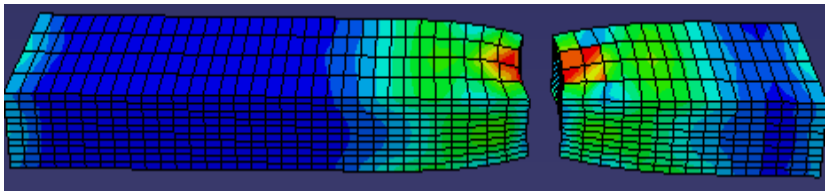

(c) Unbent specimen alone

Figure 10.26: Fracture shapes of unbent wire specimen alone and unbent wire specimen in reels-attachments-specimen assembly.

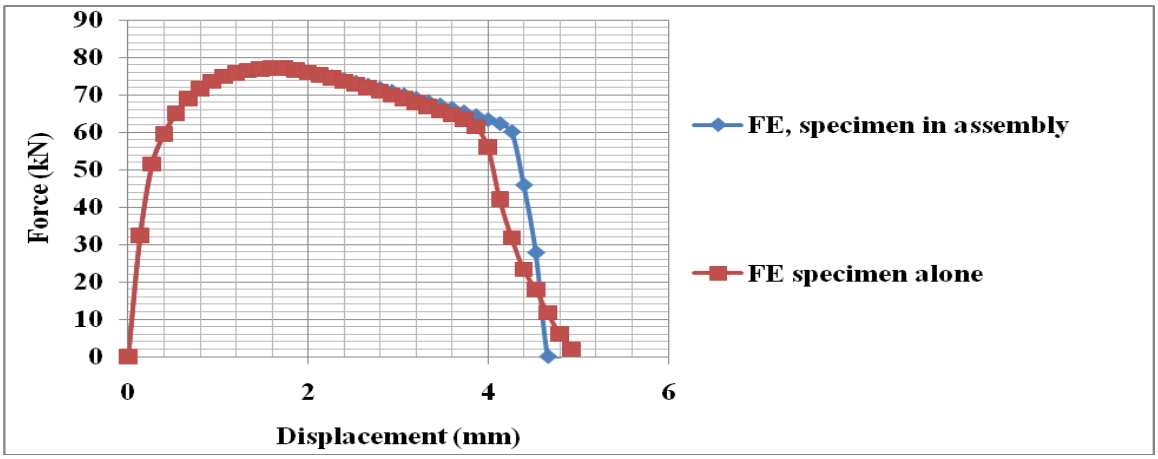

Figure 10.27: Force-displacement curves from simulations with 12mmx5mm, 50mm gauge length unbent specimen alone and unbent specimen in rollers-attachments-specimen assembly.

Table 10.4 Mechanical properties wire predicted by simulations with specimen alone and specimen in rollers-attachments-specimen assembly

Parameters	Simulation with specimen alone	Simulation with specimen in specimen-rollers-attachments assembly	Percentage difference
Yield load (kN)	53.14	53.13	0.0131
Ultimate load (kN)	77.24	77.23	0.0003
Fracture load (kN)	66.48	66.35	0.1897
Yield point displacement (mm)	0.27	0.27	5.26E-05
Ultimate load displacement (mm)	1.20	1.20	0.0004
Fracture displacement (mm)	3.99	4.26	0.0684

10.3.2.6 Deformed shapes and stress distributions during tensile testing simulation

The deformed shape of the whole 320mm wire length showing the longitudinal axial stress distributions, the residual longitudinal axial stress distributions in the RBS test specimen and the undeformed stress-free unbent specimen before tensile testing are shown in Figures 10.28 (a), (b) and (c) respectively.

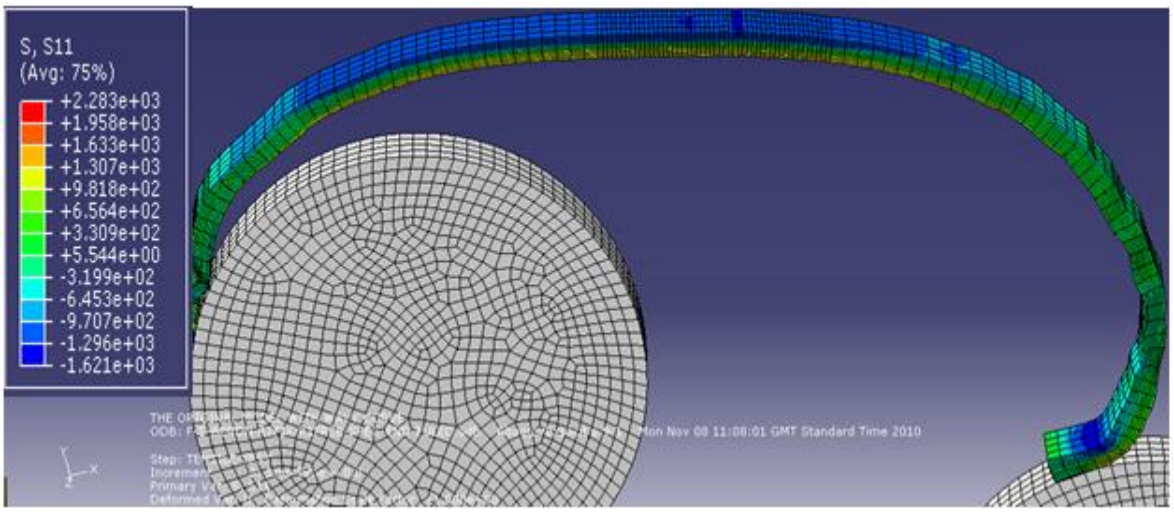

(a) Stress distributions in the whole wire length

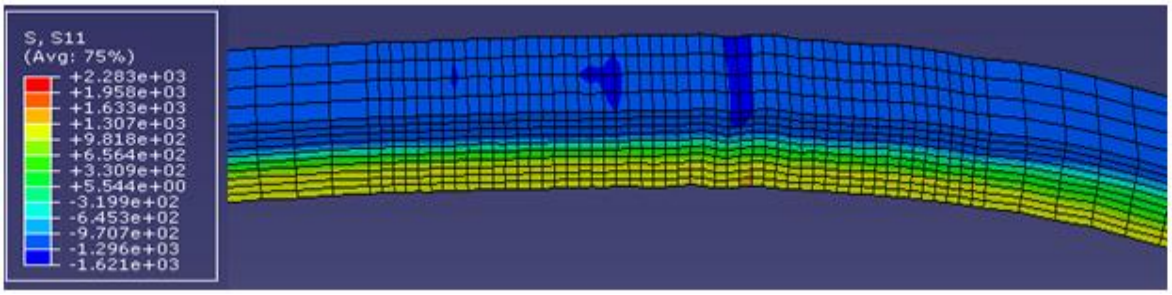

(b) Stress distributions in RBS specimen

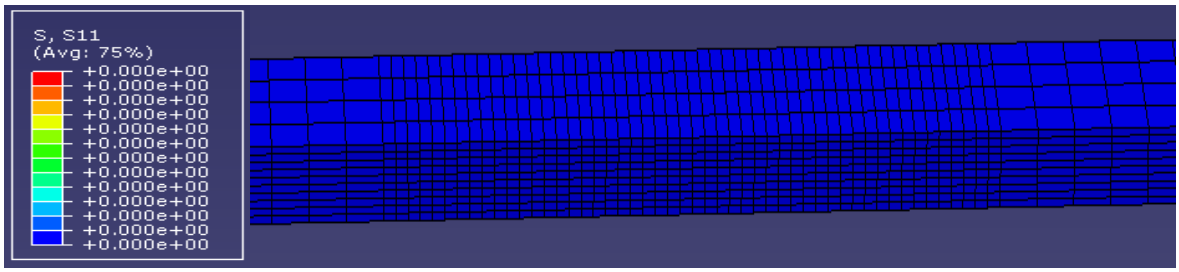

(c) Unbent stress free specimen

Figure 10.28: Residual longitudinal axial stress (MPa) distributions in whole wire length, unbent, and RBS specimens before tensile testing.

The deformed shape of the whole 320mm wire length showing the longitudinal axial stress distributions, and the longitudinal axial stress distributions in the RBS and unbent specimens at the beginning of tensile testing are shown Figure 10.29 (a), (b) and (c) respectively. As shown in Figures 10.29 (a) and (b), at the beginning of the tensile testing simulation, the displacement applied to the specimens produced a uniform tensile stress across the thickness of the unbent specimen while the stress across the thickness of the RBS specimen is not uniform. The stress is not uniform because of the unbalanced residual stress distribution in

the RBS specimen and because the outer parts of the specimen has been plastically deformed while its middle part remains elastic.

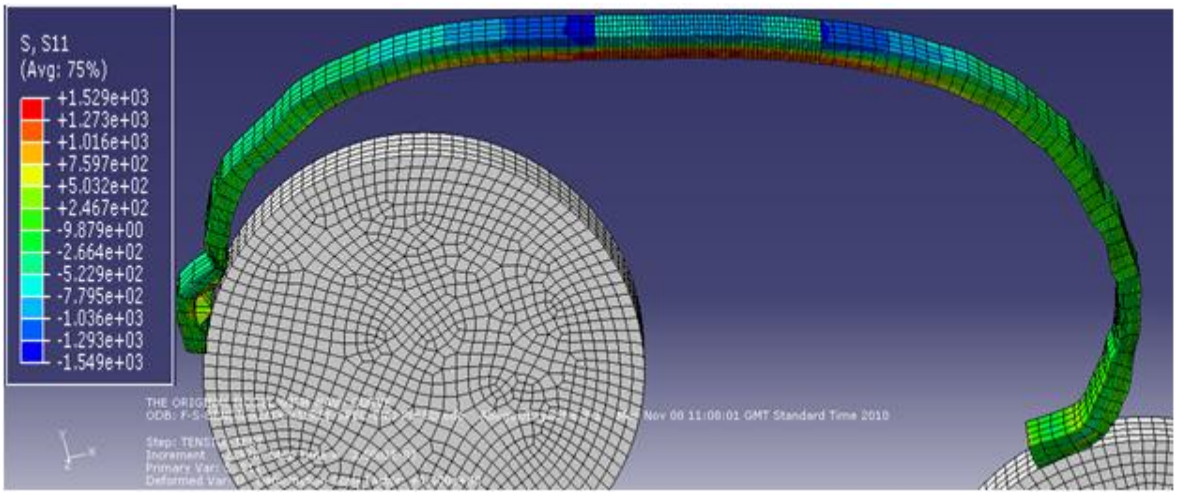

(a) Stress distributions in the whole wire length

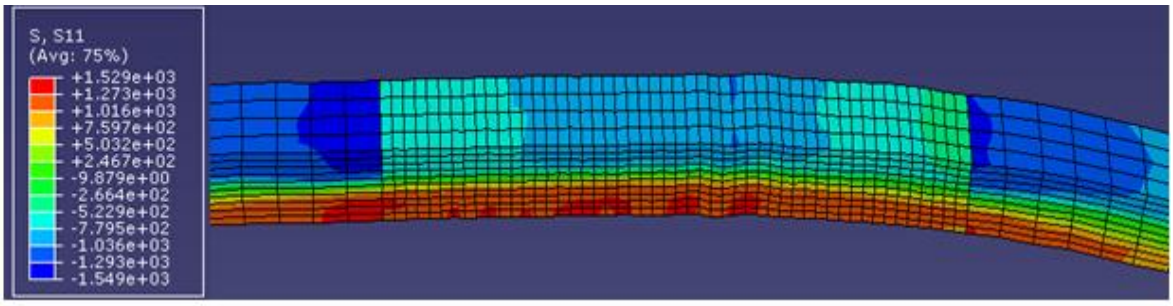

(b) Stress distributions in RBS specimen

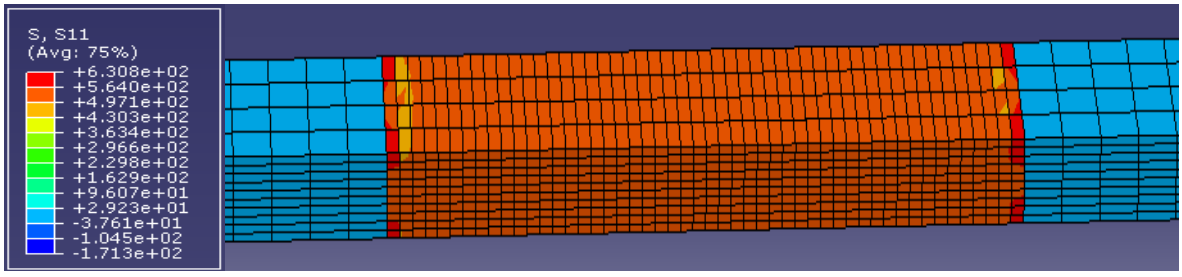

(c) Stress distributions in unbent specimen

Figure 10.29: Longitudinal axial stress (MPa) distributions in unbent and RBS specimens at an applied displacement of 0.16mm.

The deformed shape of the whole 320mm wire length showing the longitudinal axial stress distributions and the longitudinal axial stress distribution in the RBS and unbent specimens before necking are shown Figures 10.30(a), (b) and (c) respectively. At this stage, the stress across the thickness of the RBS specimen is purely tensile and approximately uniform.

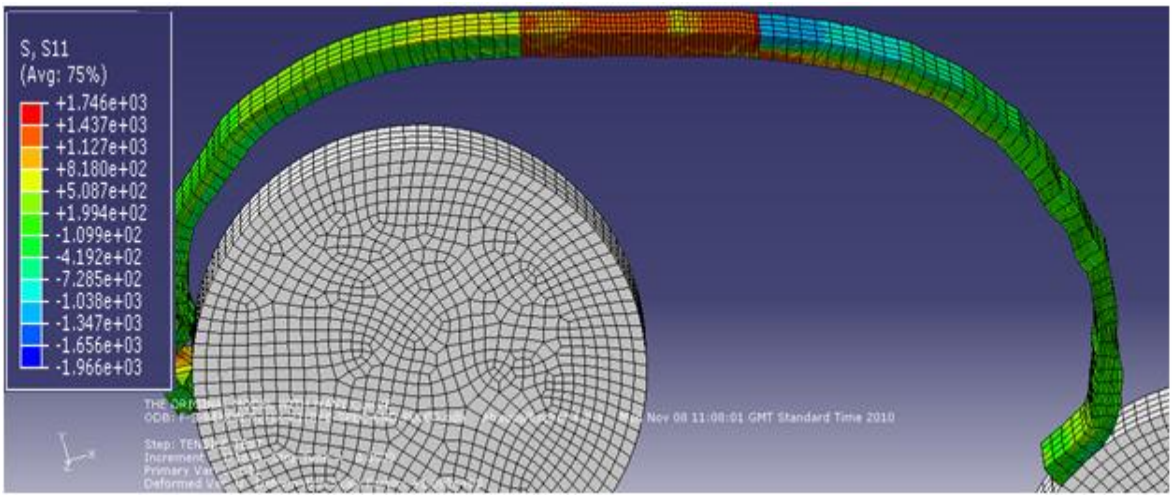

(a) Stress distributions in the whole wire length

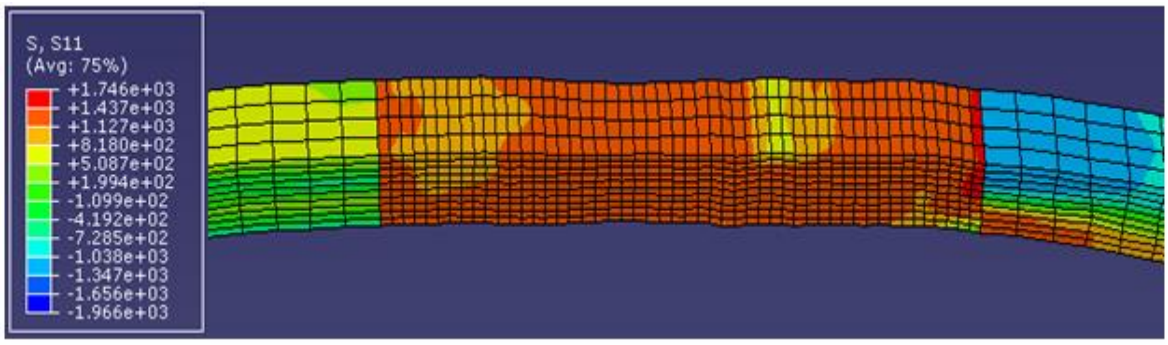

(b) Stress distribution in RBS specimen

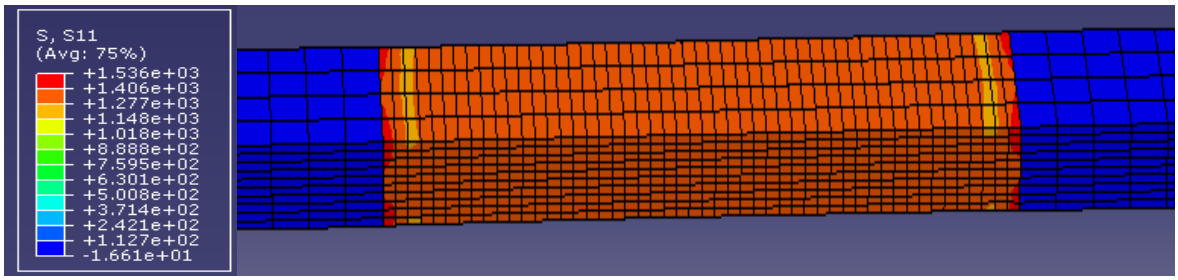

(c) Stress distribution in unbent specimen

Figure 10.30: Longitudinal axial stress (MPa) distributions in unbent and RBS specimens before necking.

The deformed shape of the whole 320mm wire length showing the longitudinal axial stress distributions and the longitudinal axial stress distributions in the RBS and unbent specimens during necking are shown Figures 10.31(a), (b) and (c) respectively.

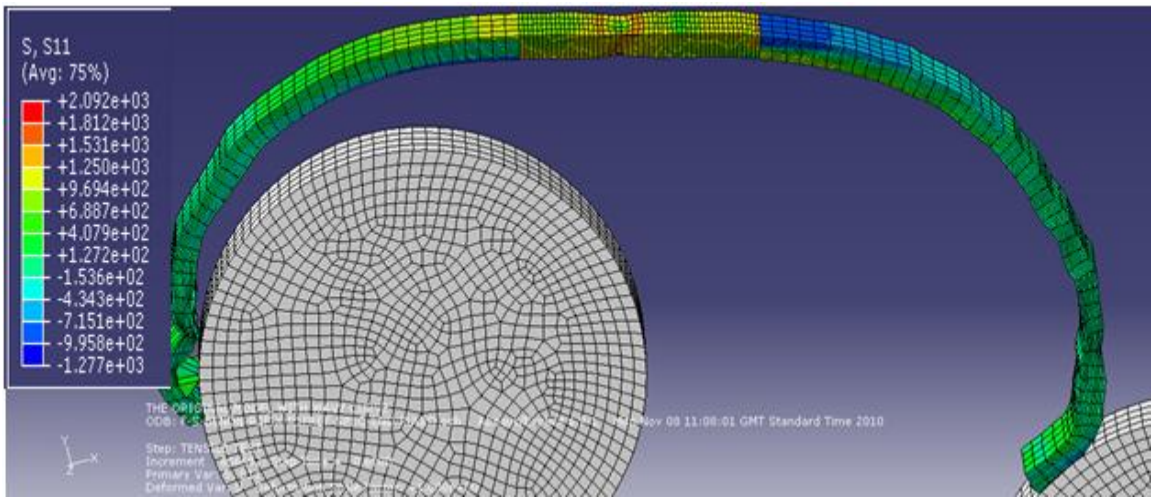

(a) Stress distributions in the whole wire length

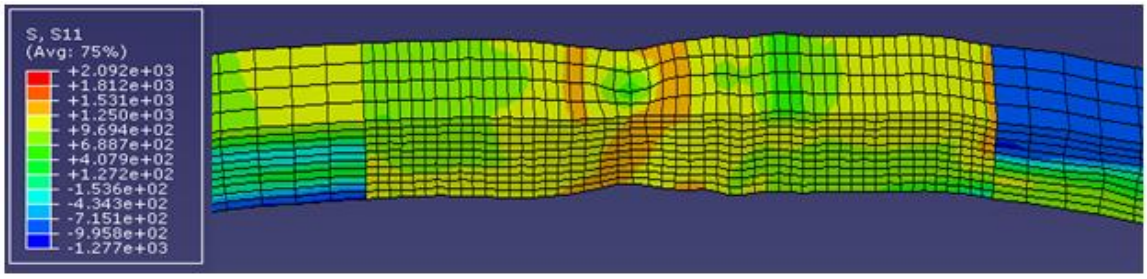

(b) Stress distribution in RBS specimen

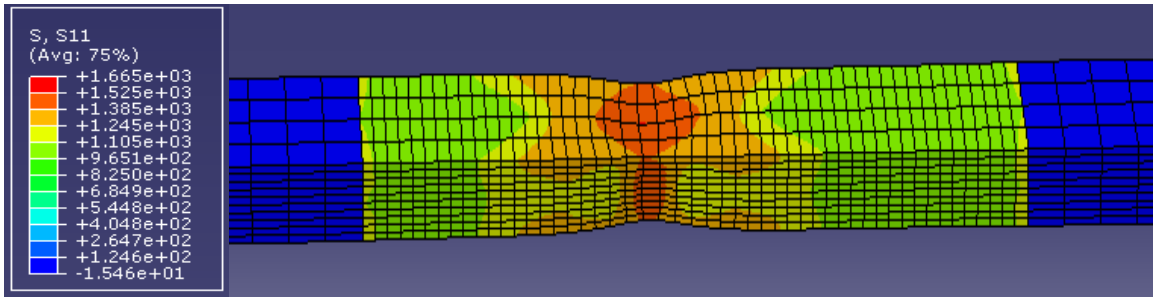

(c) Stress distribution in unbent specimen

Figure 10.31: Longitudinal axial stress (MPa) distributions in whole wire length, unbent, and RBS specimens during necking.

The deformed shapes showing the fractured RBS specimen within the whole 320mm length of wire is shown in Figures 10.32 while the deformed shapes of the unbent and RBS specimens alone are shown in Figure 10.33.

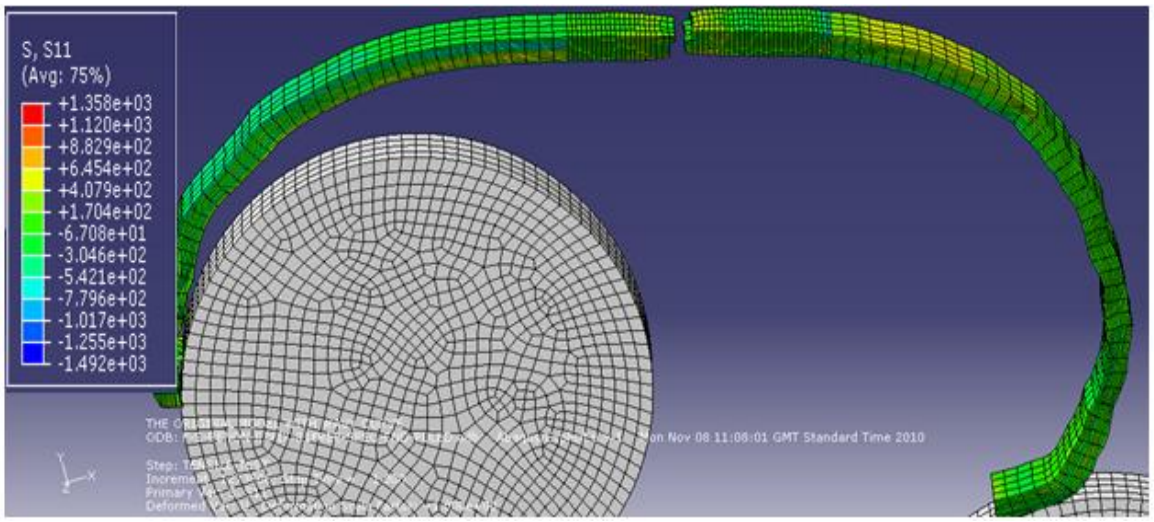

Figure 10.32: Fracture RBS specimen within the whole length of wire showing longitudinal axial stress (MPa) distribution.

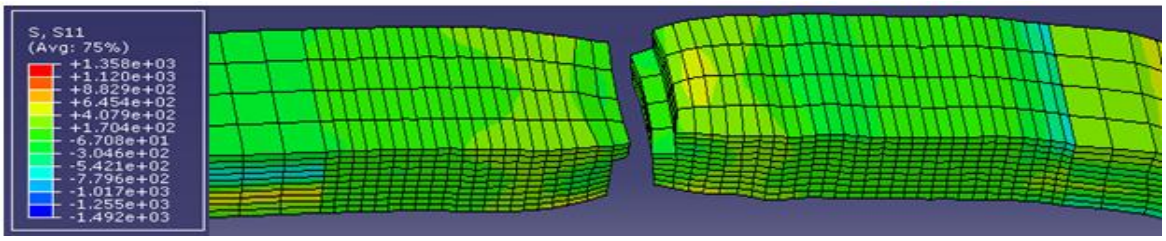

(a) Fractured RBS specimen

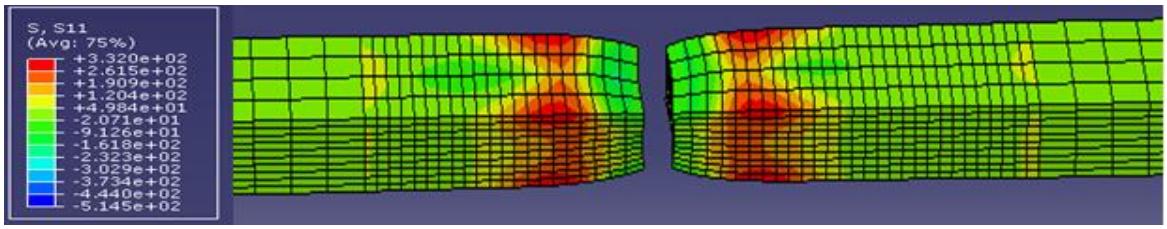

(c) Fractured unbent specimen

Figure 10.33: Fractured RBS and unbent specimens showing longitudinal axial stress (MPa) distribution.

10.3.2.7 Analysis of results of FE simulation of tensile testing of RBS specimens

The force-displacement curves obtained from experimental and numerical tensile testing of RBS specimens, and from experimental and numerical tensile testing of unbent and RBS specimens with isotropic and combined hardening models are shown the Figures 10.34 and 10.35. The force-displacement curve predicted by the simulation of bending, reverse bending, straightening and tensile testing carried out with combined hardening agrees very well with the experimental curve throughout the elastic region, and fairly well in the plastic region and

fracture region. Conversely, the force-displacement curve predicted by the simulation with isotropic hardening does not agree with the experimental curve throughout the elastic region as it shows that the wire has been work hardened which is not evident in the experimental curve. It also predicted that the RBS specimen has a higher fracture displacement than the unbent specimen as shown in Figure 10.35 (a) which is contrary to the lower fracture displacement value for the RBS specimen obtained from the experiment and from the simulation with kinematic hardening shown in Figures 10.35 (b) and (c) respectively.

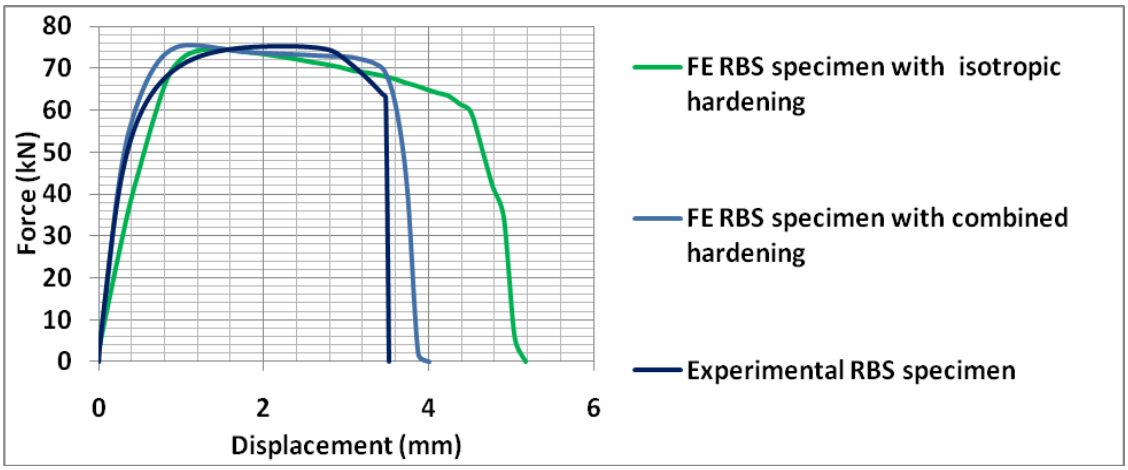

Figure 10.34: Force-displacement curves from experimental and numerical tensile testing of 12mmx5mm, 50mm gauge length RBS specimens.

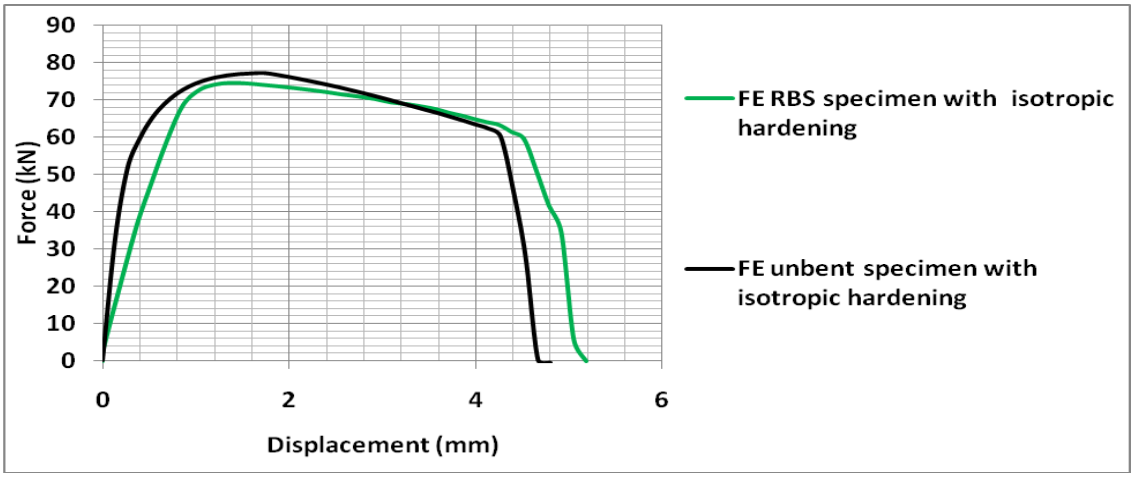

(a) Simulation with isotropic hardening

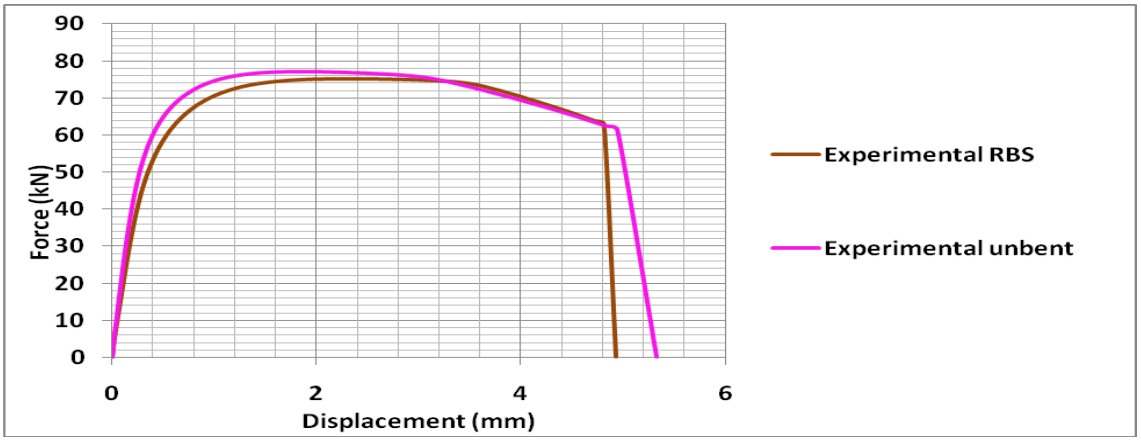

(b) Experimental curves

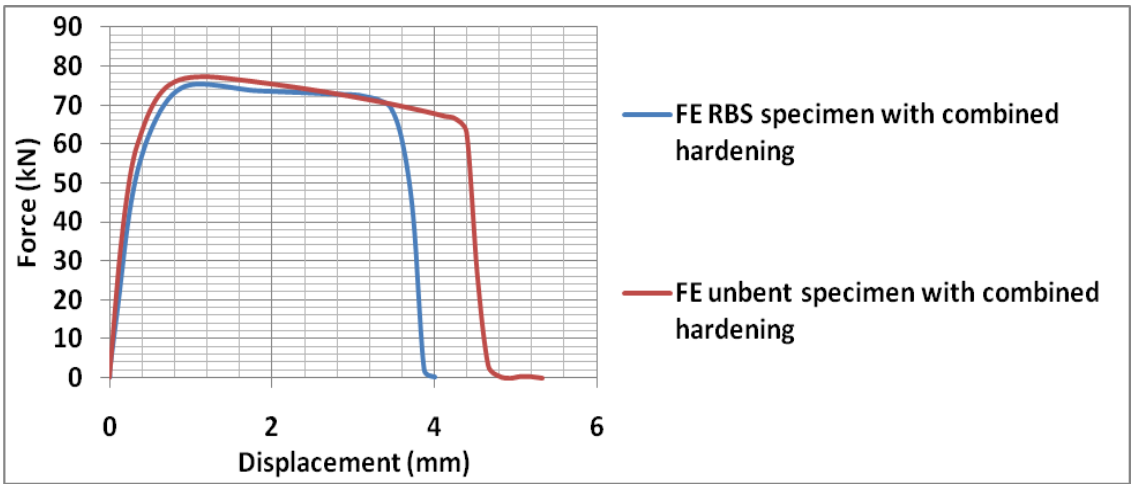

(c) Simulation with combined hardening

Figure 10.35: Force-displacement curves from experimental and numerical tensile testing of 12mmx5mm, 50mm gauge length unbent and RBS specimens.

Consequently, the combined hardening model is more appropriate for the simulation of bending, reverse bending, and straightening of tensile armour wires which involves strain reversal as it captures the behaviour of the wire better than the simulation with isotropic hardening. The simulation with isotropic hardening merely captured the work hardening during bending, reverse bending, and straightening simulations and not the reduction in yield (softening) of the wire due to the Bauchinger effect which results from the strain reversal involved in the simulation. Therefore, subsequent simulations were carried out with the combined hardening model.

The mechanical properties predicted by the simulations of tensile testing of unbent and RBS wire specimens with combined hardening models are presented in Table 10.5. From Table 10.5, the bending, reverse bending and straightening simulations or operations reduced the yield load, ultimate load and fracture displacement by 4.22%, 2.18% and 18.62% respectively. This reduction in the yield load agrees with what is reported by Fukuda et al, (2005) and is due to the Bauschinger effect. As with the experimental tensile testing of RBS specimen which reduced the ultimate load, fracture load and fracture displacement by 2.58%, 2.38% and 2.71% respectively (earlier presented in Table 10.1), the largest effect (18.62% reduction) of the reverse bending and straightening predicted by the FE simulation is observed in the fracture displacement results.

Table 10.5: Mechanical properties predicted by simulation of tensile testing of unbent and RBS wire specimens with combined hardening models

Parameters	Unbent wire specimen	RBS wire specimen	Percentage difference
Yield load (kN)	53.14	50.87	4.27
Ultimate load (kN)	77.24	75.55	2.18
Fracture load (kN)	66.36	69.05	4.05
Yield point displacement (mm)	0.27	0.31	17
Ultimate load point displacement (mm)	1.19	1.12	6.18
Fracture displacement (mm)	4.26	3.47	18.62

The differences between the percentage reductions in these mechanical properties obtained from experiments and FE simulations could be because the spring back, elastic recovery and

stress relaxation in the wire between the bending and reverse bending simulation which occurred in the experimental simulations did not occur in the numerical simulation. Also, as the rollers are rotated during bending and reverse bending, the FE simulation ensures a complete contact between every part of the wire surface and the rollers. A complete contact between the wire and the roller may not have been achieved in the experimental simulation as the wires were manually wound round the roller. Consequently, there could be differences in the radius of curvature of the wires during the experimental and numerical simulations which could affect the degree of stress and the degree of work hardening to which the wires were subjected during the experimental and numerical simulations. The FE simulation of the bending and reverse bending of the wires can therefore be said to replicate the real life process in the industry better than the experimental simulation and its results in this context can be said to be more reliable than the experimental results.

The drop in the yield stress and the ultimate loads of the RBS wires can be attributed to the possible necking and consequent reduction in thickness of the wire due to the high tensile stresses to which the outermost layers of the wires were subjected during bending, reverse bending and straightening operations as stated in sections 10.3.2, 10.3.3 and 10.3.4. Also the reduction in the yield and the ultimate loads could be due to the presence of some residual tensile stresses which make it easier for subsequent plastic deformation to occur and which may override the work hardening effects of plastic deformation. Furthermore, the drop in the yield stress may also be due to the softening effect of the Bauchinger effect. The drop in the fracture displacement and invariably the ductility of the RBS wire specimens is due to the accumulated plastic straining from the bending, reverse bending and straightening processes which has work hardened the specimen and used part of the wires total plastic deformation(ductility) due to previous dislocation motions in the RBS specimen.

10.4 Effects of bending, reverse bending and straightening on tensile armour wire defects

The effects of bending, reverse bending and straightening on tensile armour wire defects were investigated by carrying out FE simulations of tensile armour wire specimens with defects subjected to bending, reverse bending, straightening and tensile testing. The defects considered were laminations and surface scratches.

10.4.1 Effects of the combination of lamination and reverse bending and straightening on tensile armour wires

The effects of laminations alone on the tensile properties of tensile armour wires and the effects of bending, reverse bending and straightening operations on laminations in tensile armour wire, as well as the effects of the combination of laminations and bending, reverse bending and straightening operations on the tensile properties of tensile armour wires were investigated using finite element simulations. Finite element simulations alone were used for the investigation as it is not practicable to introduce laminations into the laboratory wire specimens due to the infinite width of laminations.

10.4.1.1 Effects of lamination on tensile properties of tensile armour wires

The effect of laminations on the tensile properties of tensile armour wires was investigated by comparing the force-displacement curves and the mechanical properties predicted by FE simulation of tensile testing of lamination free wire and wires with laminations. The simulations of the tensile testing of lamination free wire and wires with laminations were carried out with the tensile test specimens within the same specimen-rollers-attachment assembly used for the reverse bending and straightening simulations shown in Figures 10.36. This was conducted to provide a good basis for comparison of the results from this arrangement with the result of the simulations involving bending, reverse bending and straightening of a wire specimen with laminations used for investigating the effects of a combination of laminations and bending, reverse bending and straightening operations which was carried out with this same arrangement.

The 50mm long tensile armour wire tensile test specimen in Figure 10.36 has a 20mm long lamination. The lamination is not visible in the meshed image in Figure 10.36(a) because it was modelled as a partition line with a seam as this is the only way to make the width of the lamination infinite. A seam in Abaqus is used to model faces that are originally closed but open during analyses. The lamination in the specimen can be seen in the wire framed image in Figure 10.36(b).

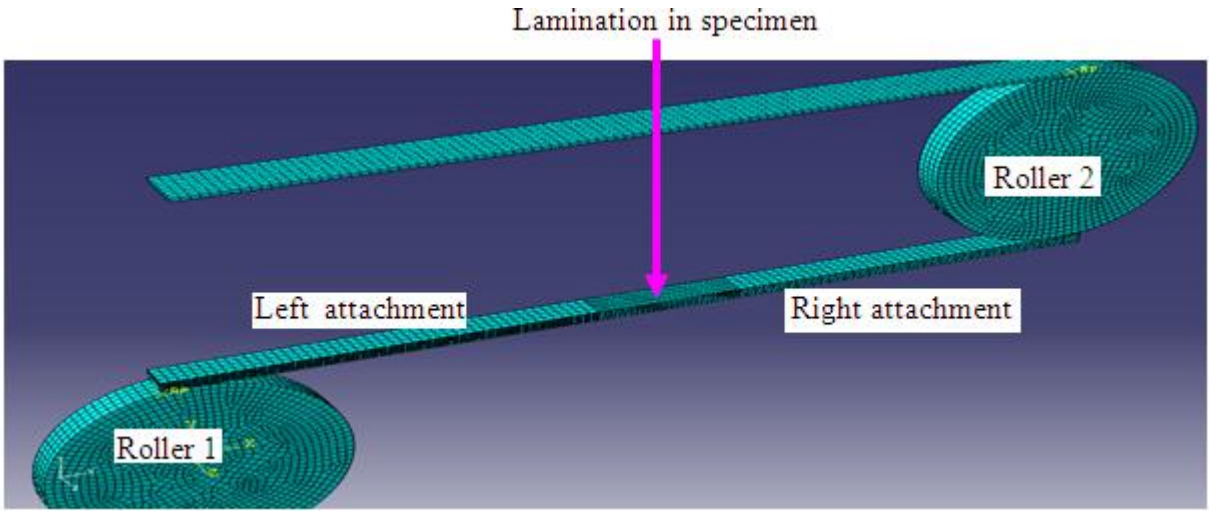

(a) Meshed specimen-rollers-attachments assembly

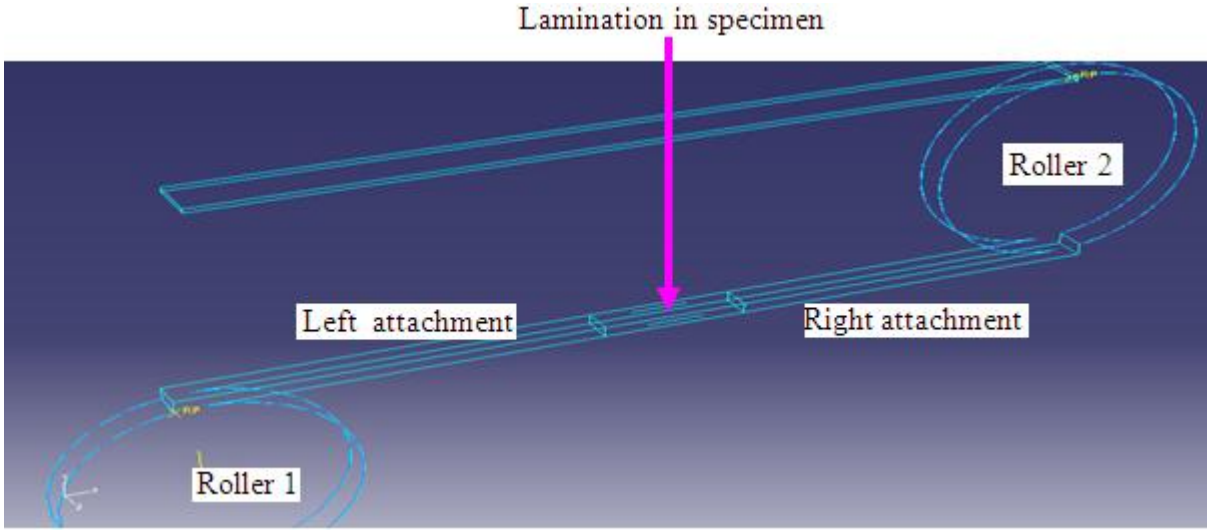

(b) Assembly of specimen-rollers-attachments in wire frame

Figure 10.36: Specimen with lamination in specimen-rollers-attachments assembly.

The tensile testing simulations was carried out on wire specimens with a lamination at the middle of its thickness hereinafter referred to as mid-thickness lamination, and with a lamination 1mm below the top surface of the wire hereinafter referred to as near-surface-lamination shown in Figures 10.37(a) and (b) respectively.

.

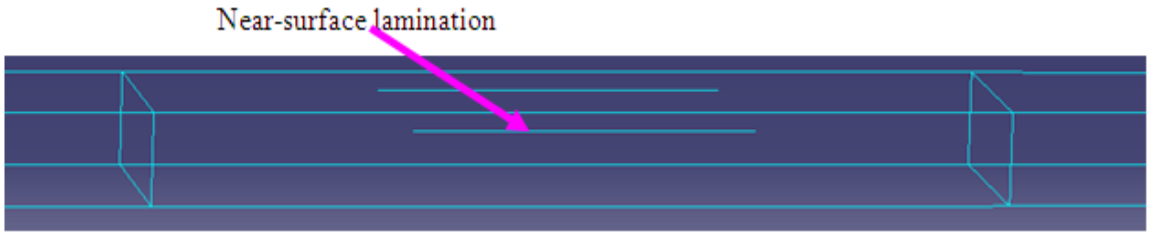

(a) Specimen with a mid-thickness lamination.

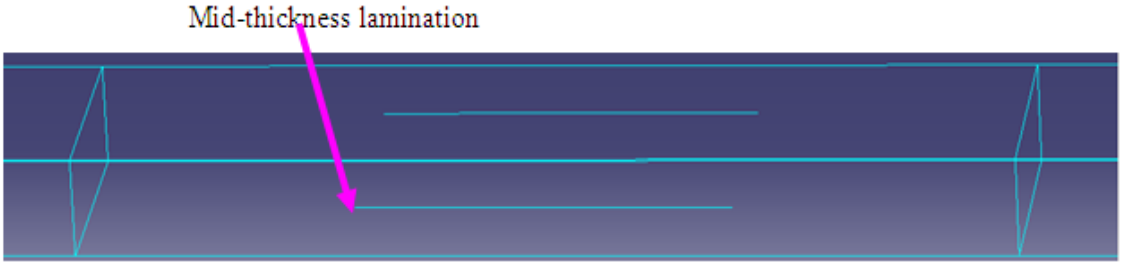

(b) Specimen with a near-surface lamination.

Figure 10.37: Tensile test specimens with mid-thickness and near-surface laminations.

There is no difference in the deformed shapes and stress distribution of the lamination free specimen and the specimens with a near-surface lamination or mid-thickness lamination at the beginning of the tensile testing simulation and the deformed shape of one of them is shown in Figure 10.38.

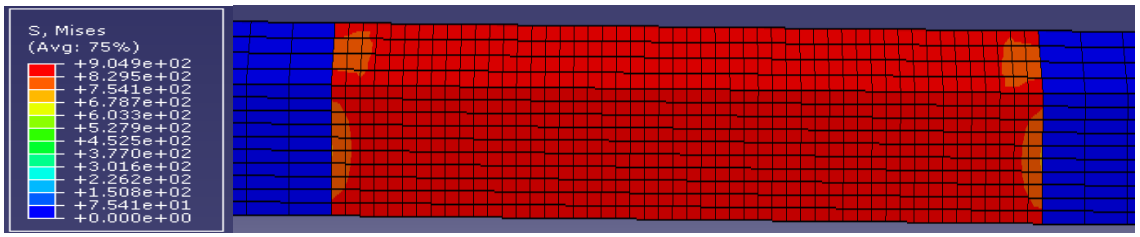

Figure 10.38: Deformed shapes and Mises stress (MPa) distribution for lamination free specimen and specimens with laminations at the beginning of tensile testing simulation.

During necking, the entire cross section of the lamination free specimen necked down as a single unit as shown in Figure 10.39(a). For the specimens with laminations, the presence of the lamination divides the wire specimen into two ligaments along its thickness with each ligament necking separately thereby creating a space between the two ligaments as they shrink in opposite vertical directions as shown in Figure 10.39(b) and (c).

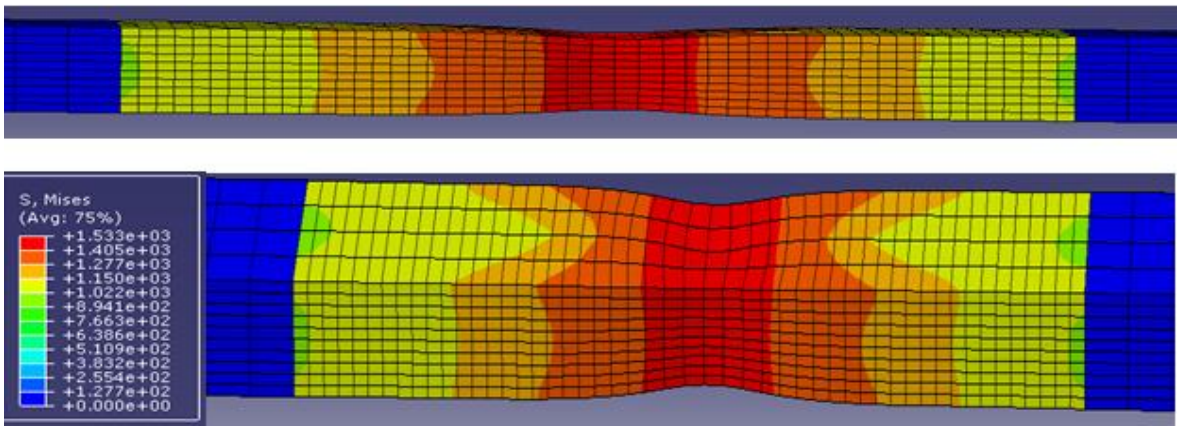

(a) Lamination free wire specimen

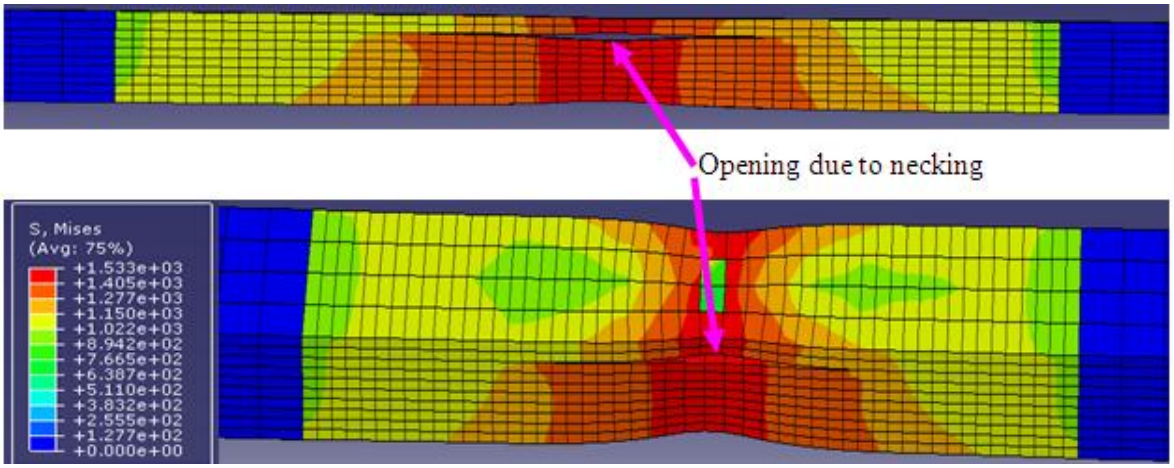

(b) Wire specimen with near-surface lamination

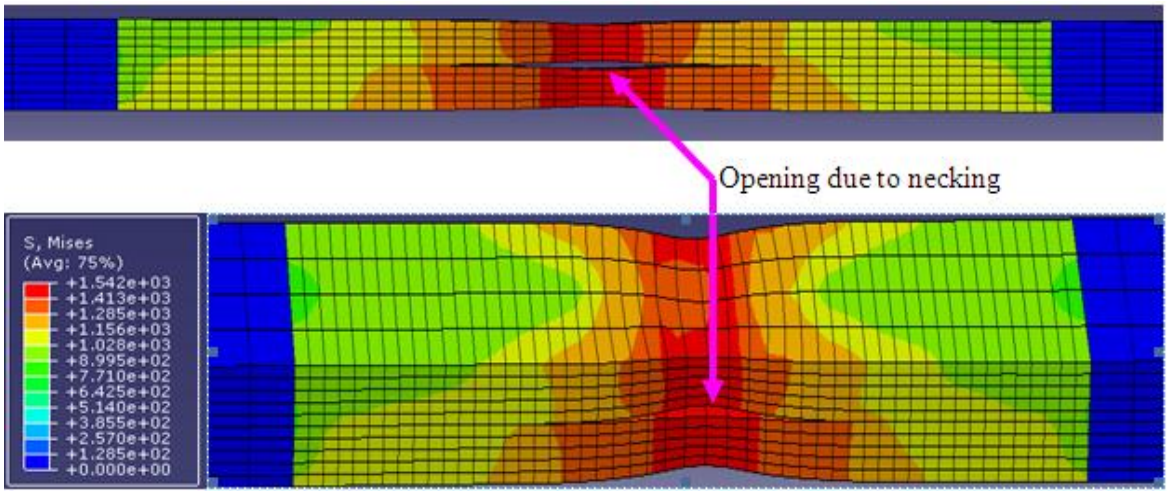

(c) Wire specimen with mid-thickness lamination

Figure 10.39: Deformed shapes and Mises stress (MPa) distribution for lamination free specimen, and specimens with laminations during necking.

As shown in Figure 10.40(a), fracture initiation, indicated by elements removal, occurred across the entire thickness of the lamination free specimen at once. Fracture initiation also occurred in the two ligaments of the specimen with the mid-thickness lamination at the same time because of their equal size whilst fracture occurred first in the thin ligament of the specimen with the near-surface lamination as shown in Figures 10.40(b) and 10.40(c) respectively. Fracture initiation occurred first in the thin ligament of the specimen with near-surface lamination because the stress and strain in this ligament is higher than that in the thick ligament.

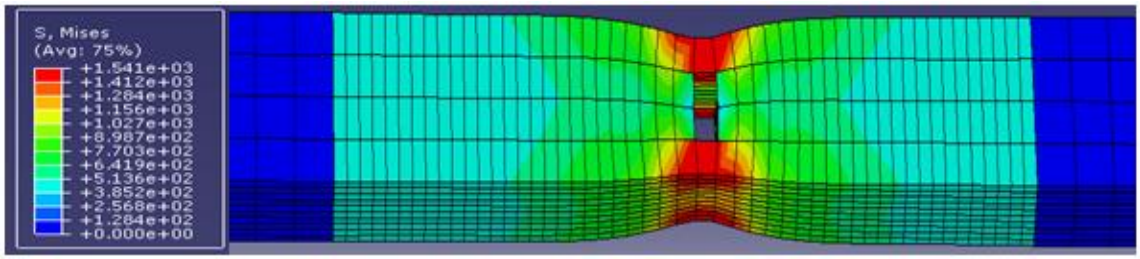

(a) Lamination free specimen

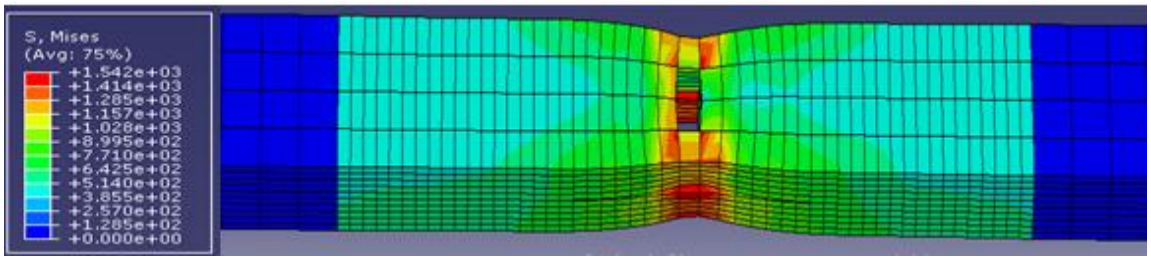

(b) Specimen with mid-thickness lamination

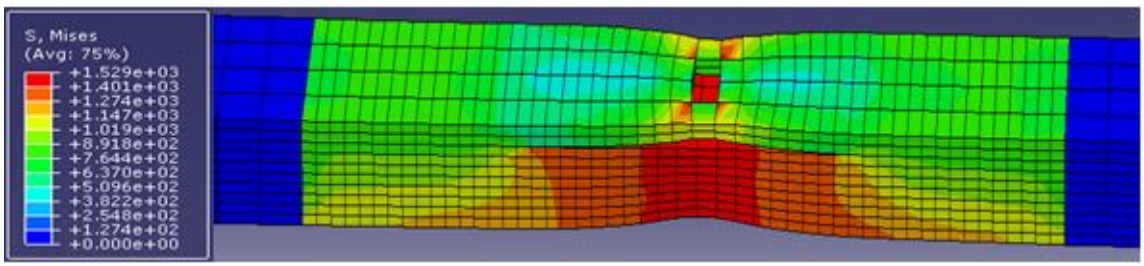

(c) Specimen with near-surface lamination

Figure 10.40: Deformed shapes showing Mises stress (MPa) distribution during fracture initiation in lamination free specimen and in specimens with laminations.

As shown in Figure 10.41(a), the entire cross section of the lamination free specimen fractured as a single unit. The two ligaments of the specimen with mid-thickness lamination also fractured at the same time because of their size, while the thin ligament of the specimen with near-surface lamination fractured first as shown in Figures 10.41(b) and (c) 10.41(c) respectively. The completely fractured specimen with near-surface lamination is shown Figure 10.41(d).

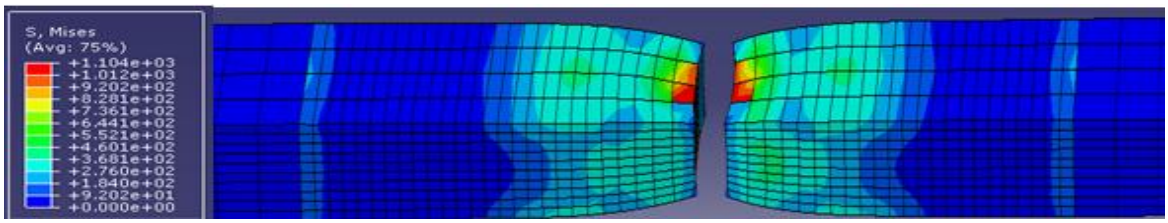

(a) Completely fractured lamination free specimen.

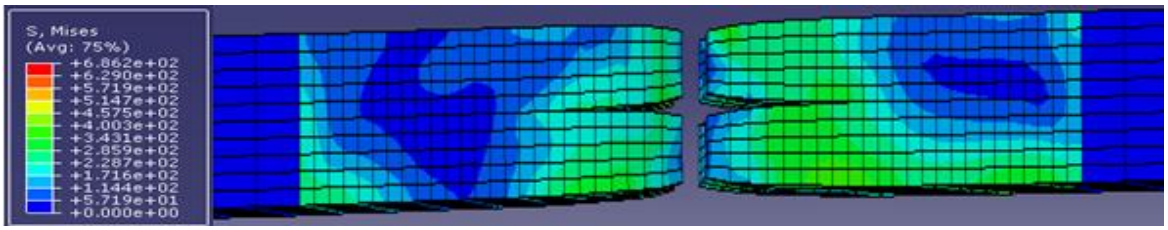

(b) Completely fractured specimen

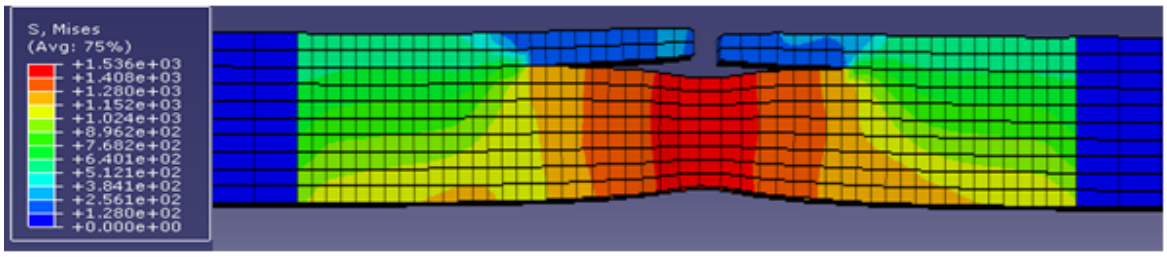

(c) Fractured thin ligament

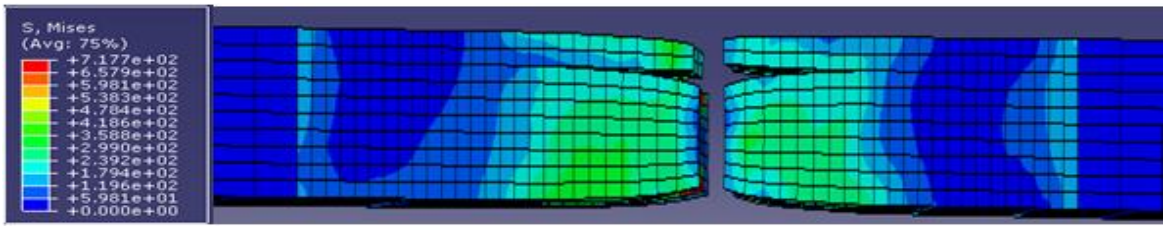

(d) Completely fractured specimen

Figure 10.41: Completely fractured lamination free specimen and specimen with laminations showing Mises stress (MPa) distribution.

The force-displacement curves and the mechanical properties obtained from the simulations of the tensile testing of the lamination free wire and wires with mid-thickness and near-surface laminations are shown in Figures 10.42 and Table 10.6 respectively.

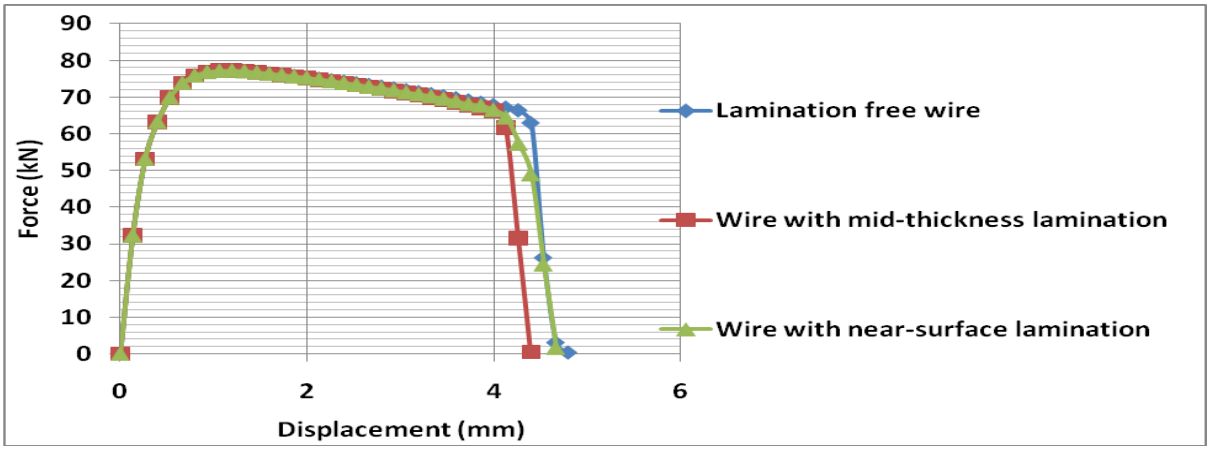

Figure 10.42: Force-displacement curves for lamination free 12mmx5mm, 50mm gauge length wire and wires with laminations.

Table 10.6: Mechanical properties predicted for lamination free wire and wires with laminations

Parameters	Lamination free wire	Wire with mid-thickness lamination	Wire with near-surface lamination	Percentage difference between lamination free wire and wires with lamination	
				Mid-thickness lamination	Near-surface lamination
Yield load (kN)	53.14	53.14	53.14	0.00	0.00
Ultimate load (kN)	77.24	77.24	77.24	0.00	0.00
Fracture load (kN)	66.35	66.27	66.52	0.12	0.25
Yield point displacement (mm)	0.26	0.26	0.26	0.00	0.00
UTL displacement (mm)	1.19	1.19	1.19	0.00	0.00
Fracture displacement (mm)	4.26	3.99	3.99	6.25	6.25

From Figures 10.4 and Table 10.6, both mid-thickness and near-surface laminations have negligible effects (0.0079% and 0.0053% reductions respectively) on the yield load and also negligible effects (0.0003% reductions for both) on the ultimate loads of the wire**.** However both mid-thickness and near-surface laminations have a worse effect on the fracture displacement and invariably the ductility of the wire which both reduced by 6.25%.

10.4.1.2 The effects of bending, reverse bending and straightening operations on laminations in tensile armour wire

The effects of bending, reverse bending and straightening operations on laminations in tensile armour wires were investigated by carrying out FE simulations of bending, reverse bending and straightening of tensile armour wire specimens with mid-thickness and near-surface laminations. Throughout the bending simulation, the deformed shapes of the specimen with mid-thickness and the specimen with near-surface lamination are the same. Hence, the deformed shape of only one of them is presented in Figure 10.43. Throughout the bending simulation, there was no noticeable effect of bending on both mid-thickness and near-surface laminations as shown in Figures 10.43 and (b). Consequently, the lamination is not visible in the meshed image in Figure 10.43(a) and is therefore shown in the wire framed image in Figure 10.43(b).

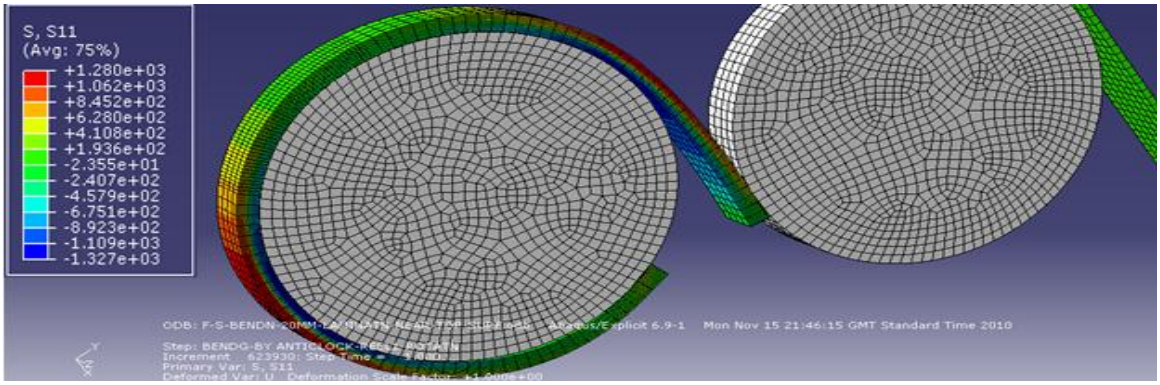

(a) Meshed image of wire with lamination bent round roller

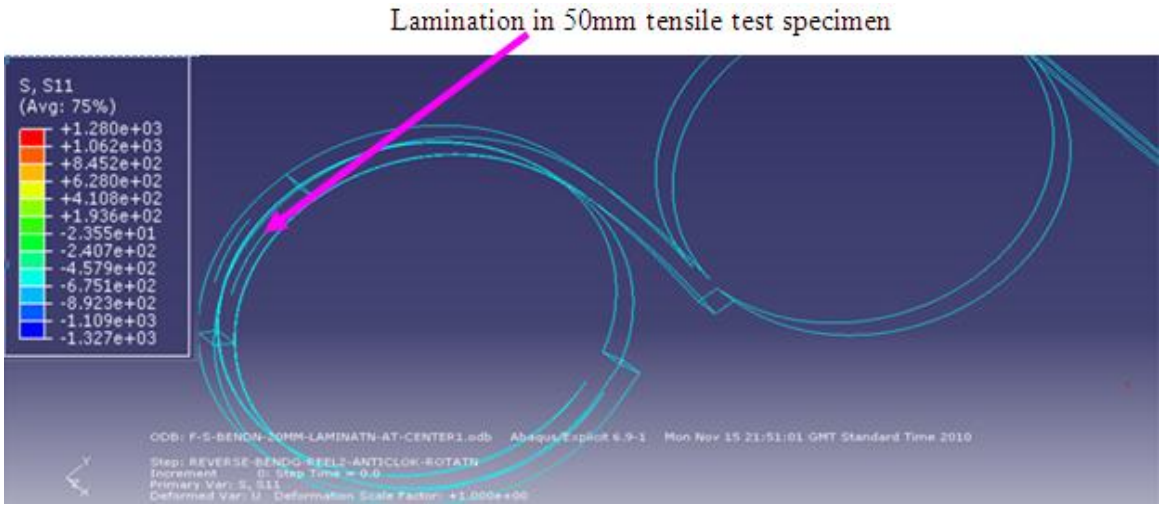

(b) Wire framed image of wire with lamination bent round roller.

Figure 10.43: Deformed shapes and longitudinal stress (MPa) distribution for specimens with laminations after bending simulation.

During bending, the upper part of the wire which is above the mid-thickness lamination and within which the near-surface lamination lies is subjected to tensile stresses while the lower part of the wire is subjected to compressive stresses. During reverse bending, the specimen opened up at the locations of the laminations. The specimen with the mid-thickness laminations opens up slightly as shown in Figures 10.44(a) while the specimen with the near-surface lamination opened up considerably as shown in Figures 10.44(b). The deformed shapes of the specimens with mid-thickness and near surface laminations during the reverse bending simulation have openings at the locations of the laminations as shown in Figure 10.45.

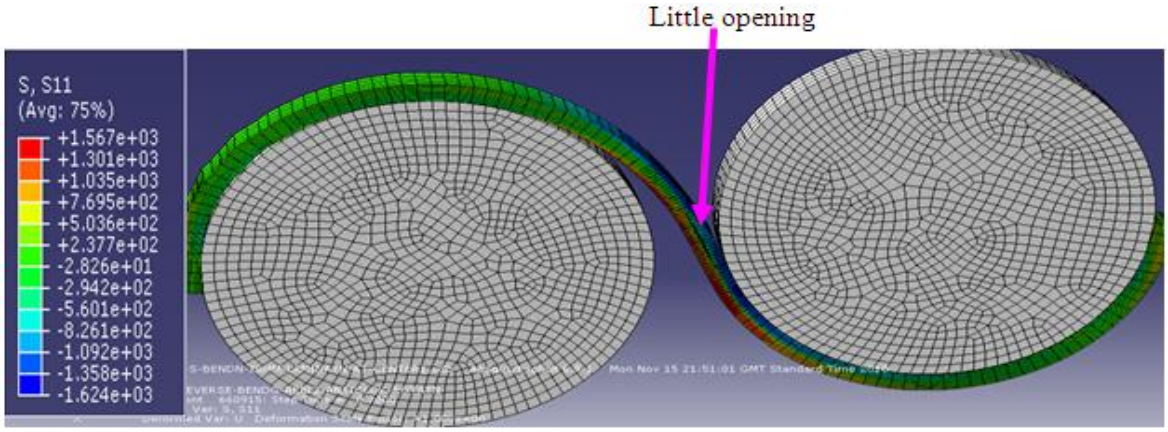

(a) Opening at the location of mid-thickness lamination

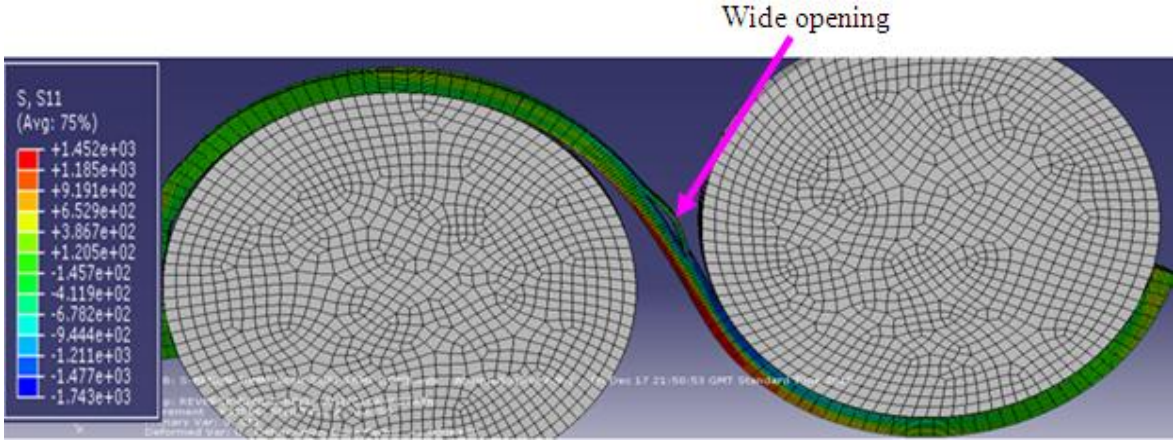

(b) Opening at the location of near-surface lamination

Figure 10.44: Deformed shapes and longitudinal stress (MPa) distribution for of specimens with laminations during reverse bending.

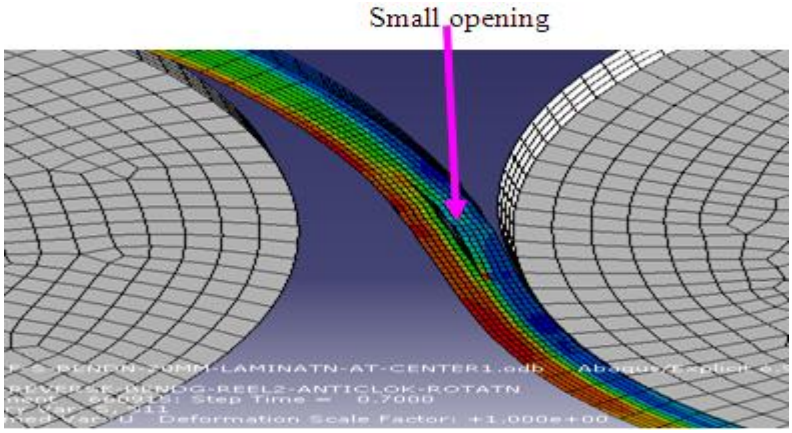

(a) Opening at mid-thickness lamination location

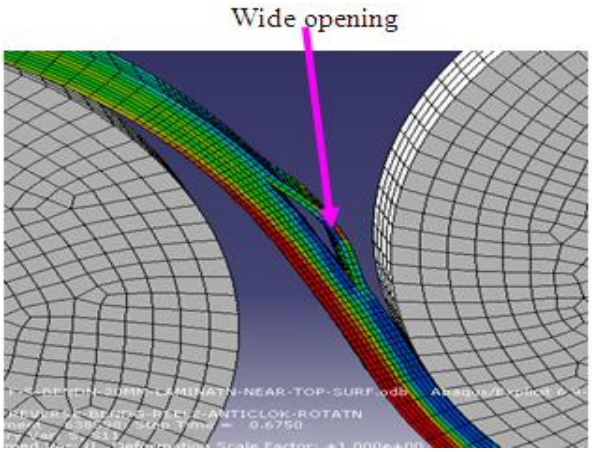

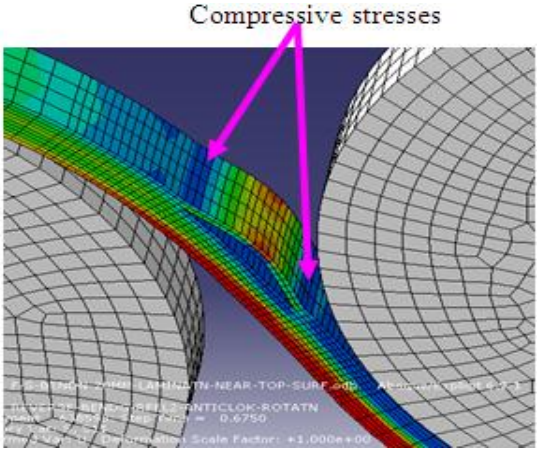

(b) Opening at near-surface lamination location (c) Buckling under compressive stresses

Figure 10.45: Opening at locations of laminations during reverse bending.

The presence of a lamination in the wire divided the wire into two ligaments, with the ligament above the lamination buckling/bowing under the compressive longitudinal axial stresses to which the upper part of the wire is subjected during reverse bending as shown in Figure 10.45(c). The blue colour represents a compressive stress while the red represents tensile stress as stated earlier. The ligaments buckled and caused the wire to open up at the location of the laminations because they are thinner than the remaining parts of the specimen and the attachments without lamination or divided ligaments (with a full wire thickness) which did not buckle throughout the reverse bending. The thin ligament of the specimen with near-surface lamination buckled more than the ligament of the specimen with mid-thickness lamination because it is thinner. This explains why the opening in the specimen with near-

surface lamination as shown in Figure 10.45 (b) is larger than the opening in the specimen with mid-thickness lamination shown in Figures 10.45(a).

At the end of the reverse bending simulation, the opening at the location of the near-surface lamination remains as shown in Figures 10.46(a) and 10.47(a) as the roller was unable to flatten out the buckled thin ligament due to its high degree of curvature. On the other hand, the opening at the location of the mid-thickness lamination is closed up as shown in Figures 10.46 (b) because the buckled ligament was flattened by the roller due to its gentle curvature. Hence the mid-thickness lamination is not visible in the meshed image in Figure 10.46 (b) and is shown in the wire framed image in Figure 10.46(c).

Large opening Opening closed up Lamination

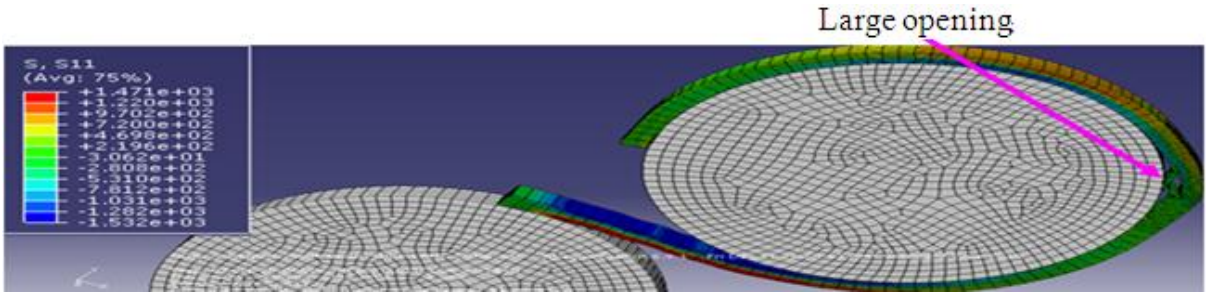

(a) Specimens with near-surface lamination

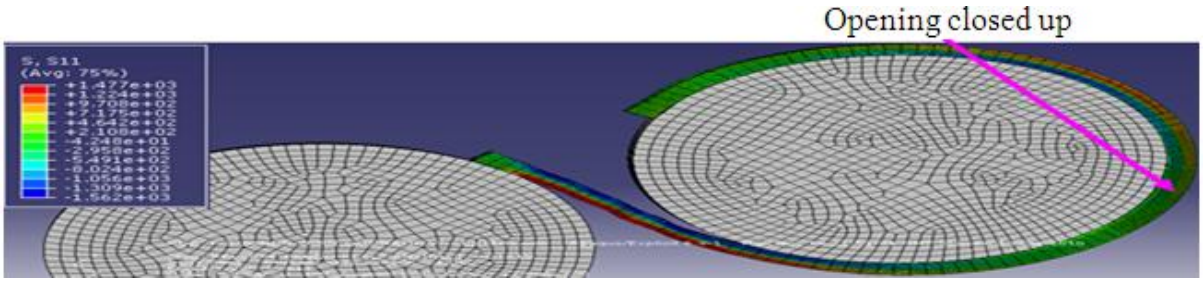

(b) Meshed image of specimens with mid-thickness lamination

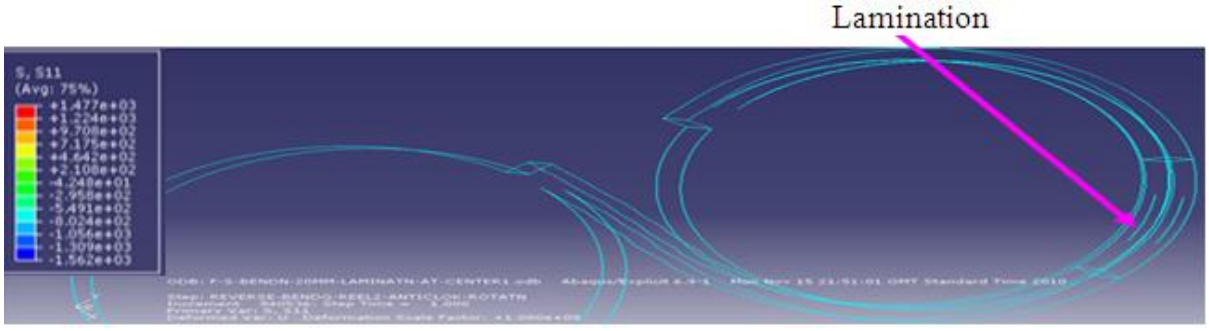

(c) Specimens with mid-thickness lamination in wire frame.

Figure 10.46: Deformed shapes and longitudinal stress (MPa) distribution for specimens with laminations after reverse bending simulation.

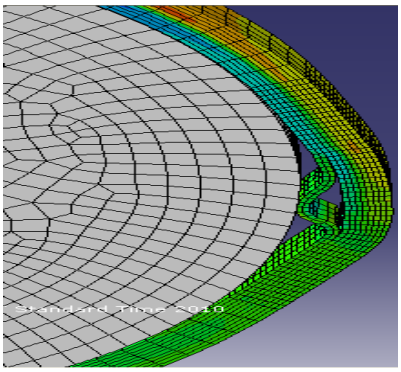

Opening at near-surface lamination location

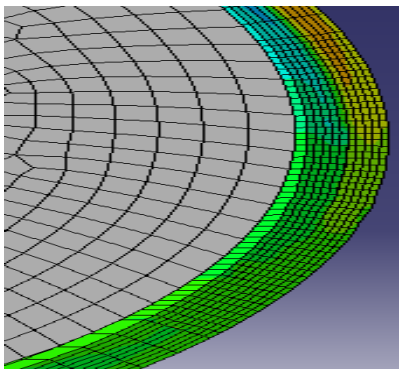

(b) Mid-thickness lamination location without opening

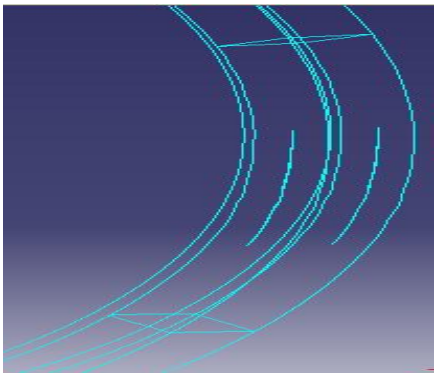

(c) Lamination in wire framed image

Figure 10.47: Deformed shapes at locations of laminations after reverse bending simulation.

During the straightening simulation, the upper and lower parts of the wire specimen are subjected to compressive stresses and tensile stresses respectively as shown in Figures 10.48(a) and (b). Consequently, the buckled/bowed thin ligament of the specimen with near-surface lamination is subjected to tensile stresses which straightens it and reduces its degree of curvature. Conversely, the ligament that is above the mid-thickness lamination buckles/bows under compressive stresses during straightening, leading to an opening up of the specimen at the location of the mid-thickness lamination shown in Figures 10.48(b) and 10.49(b).

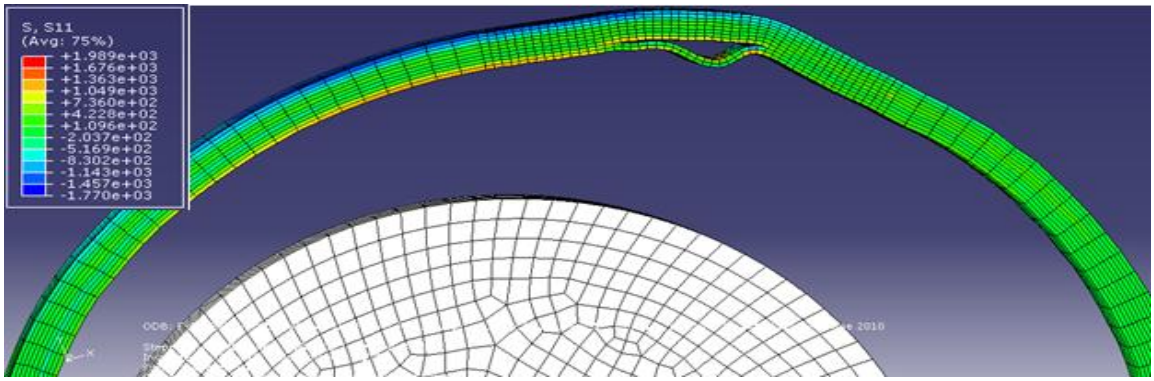

(a) Specimens with near surface lamination

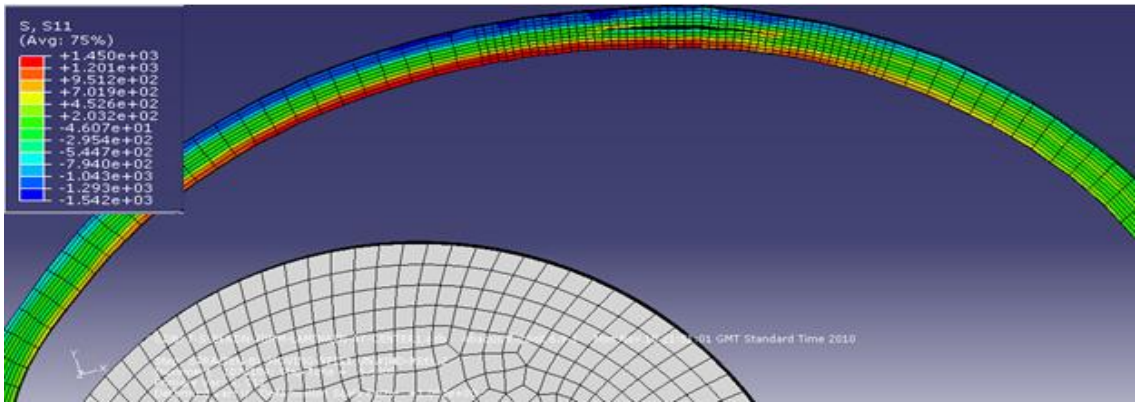

(a) Specimens with mid-thickness lamination

Figure 10.48: Deformed shapes and longitudinal stress (MPa) distribution for specimens with laminations during straightening simulation.

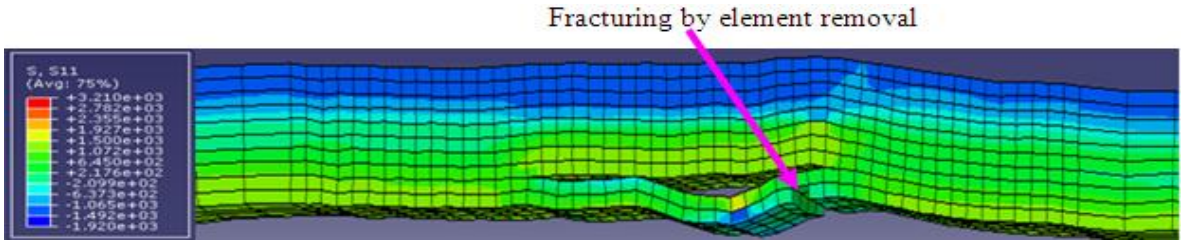

(a) Specimen with near-surface lamination

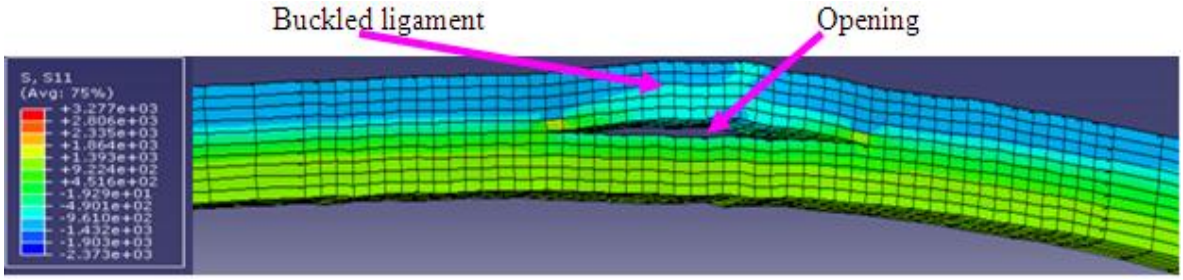

(b) Specimen with mid-thickness lamination

Figure 10.49: Deformed shapes at locations of laminations toward end of straightening simulation.

Towards the end of the straightening simulation, the thin ligament of the specimen with near-surface lamination started fracturing as indicated by the removal of one of the two layers of the thin ligament elements, shown in Figures 10.49(a), whilst there was no fracture initiation in the ligaments of the specimen with mid-thickness lamination as shown in Figures 10.49 (b). The thin ligament started fracturing before the end of the straightening simulation while the thick ligament did not because the tensile stress/strain in the thin ligament is considerably higher than the tensile stress/strain in the thick ligament due to its thinner dimension.

The deformed shapes of the specimens with near-surface and mid-thickness laminations within the specimen-rollers-attachments assembly at the end of the straightening simulation are shown in Figure 10.50 (a) and (b) respectively. The deformed shapes of the specimens alone are shown in Figures 10.50 (c) and (d) respectively. As shown in Figure 10.5c (c) and (d), the partially fractured thin ligament of the specimen with near-surface lamination fractured completely at the end of the straightening simulation while none of the ligaments of the specimen with mid-thickness lamination fractured. The partially fractured thin ligament completely fractured due to its thin dimension which was made even thinner by its partial fracture during the straightening simulation.

At the end of the straightening simulation, the opening at the location of the mid-thickness lamination eventually closed up as shown in Figure 10.53(d) due to the straightening of the buckled ligament by the tensile stress to which it was subjected during the straightening simulation. Thus, it can be inferred that bending, reverse bending and straightening of tensile armour wires can only reveal near-surface laminations in the wire as wires with mid-thickness laminations will pass through the reverse bending and straightening without fracturing. Also the mid-thickness lamination in the wire may be undetected with the naked eye as the opening at the location of the mid-thickness lamination closes up after straightening which may make the laminations invisible.

Hence the reverse bending operation may not be an effective test to detect mid-thickness laminations in the tensile armour wires and other in-line non destructive testing (NDT) methods might have to be used to detect mid-thickness laminations. This is because the presence of laminations does not only reduce the strength and ductility of the wire but can make the wire suffer rapid corrosion failure rate when the wires are in service.

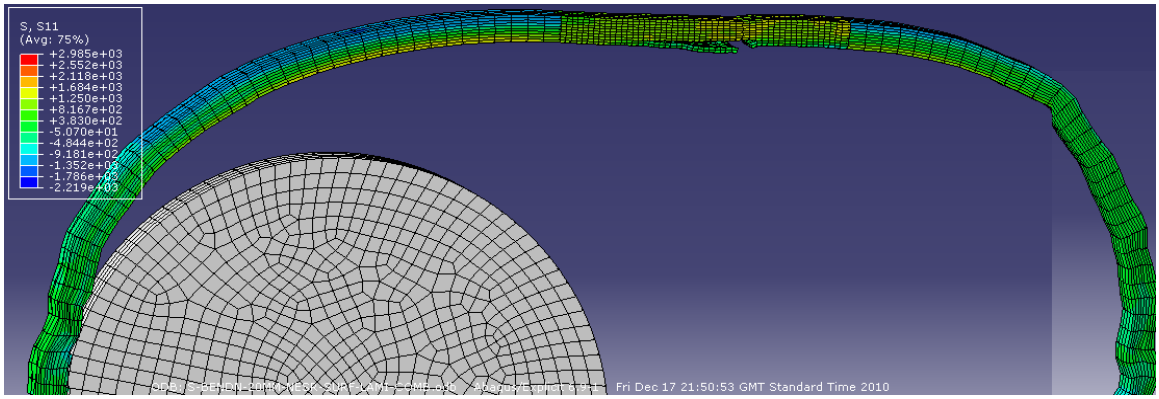

(a) Specimen with near-surface lamination within the specimen-rollers-attachment assembly

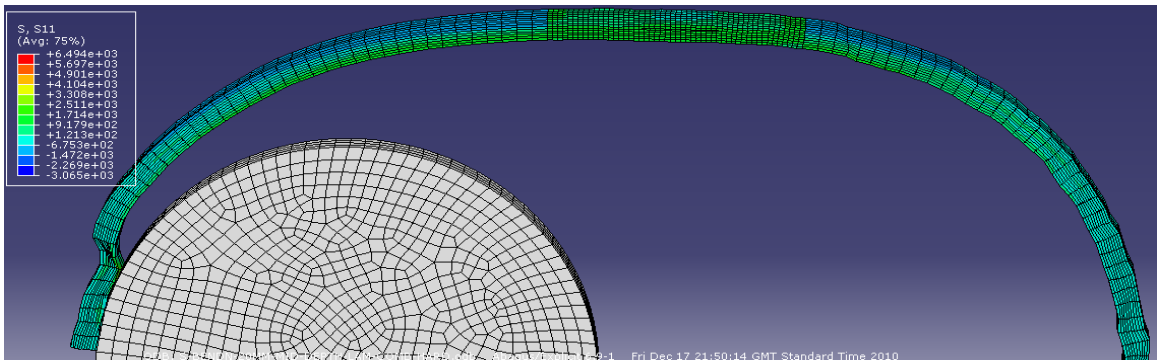

(b) Specimen with mid-thickness lamination within the specimen-rollers-attachment assembly

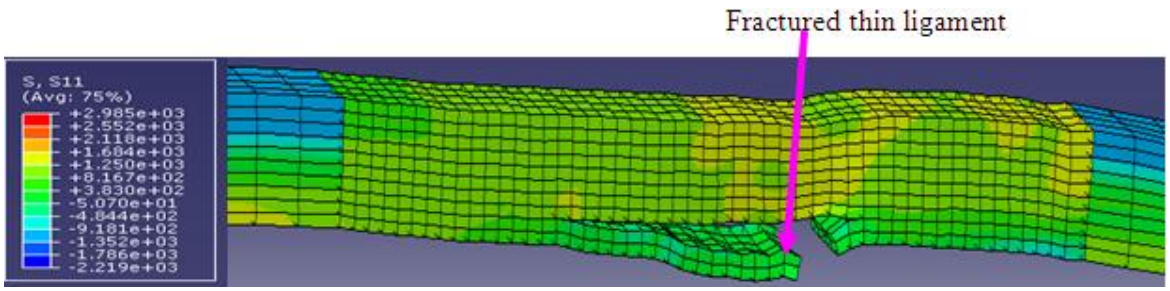

(c) Specimen with near-surface lamination alone

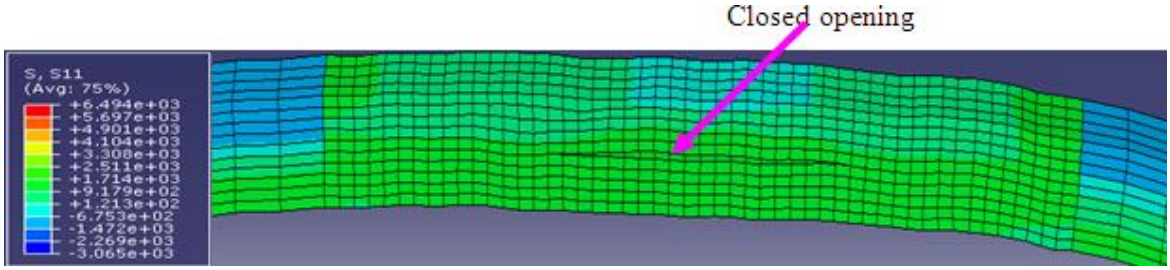

(d) Specimen with mid-thickness lamination alone

Figure 10.50: Deformed shapes and longitudinal stress (MPa) distribution for specimens with mid-thickness and near surface laminations after straightening simulation.

10.4.1.3 Effects of combination of lamination and reverse bending and straightening on tensile armour wires.

The investigation of the effects of a combination of laminations, and bending, reverse bending and straightening operations on the tensile properties of tensile armour wires was conducted by carrying out finite element simulation of the tensile testing of wire specimens with laminations that have been subjected to bending, reverse bending and straightening. The results of the RBS wire specimens with near-surface and mid-thickness laminations were compared with the results of RBS wire specimens without laminations and with the result of the unbent wire specimens with laminations.

The deformed shapes and Mises stress distributions in the RBS specimens with the near-surface and mid-thickness laminations alone at various stages of the tensile testing simulation are shown in Figures 10.51 (a) to (d) and Figures 10.52 (a) to (d) respectively. To conserve space, only the deformed shapes of the RBS specimen with near-surface and mid-thickness laminations within the specimen-rollers-attachments assembly at the end of tensile testing simulations alone are shown in Figures 10.51 (e) and 10.52(e). As shown in Figure 10.51(a), since the thin ligament has fractured, the applied tensile load was carried by the thick ligament until fracture is initiated in this ligament as shown in Figure 10.53 (b), and until it completely fractured as shown in Figure 10.51(c). In contrast, the two equal ligaments of the specimen with mid-thickness lamination carried the applied tensile load throughout the tensile testing simulation. Fracture initiation occurred in the two ligaments as shown in Figure 10.53(b) and both ligaments fractured at approximately the same time as shown in Figure 10.53(c).

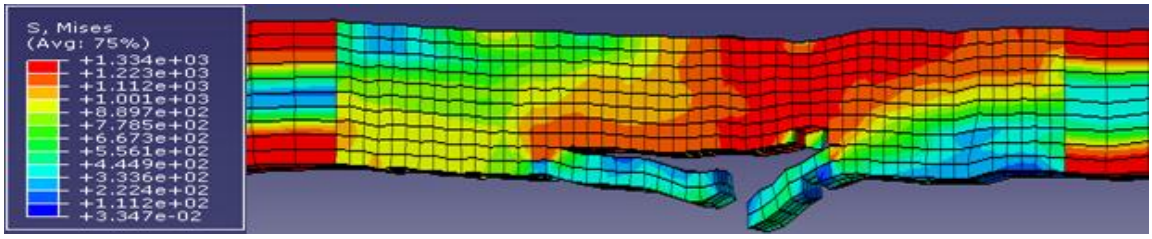

(a) At the beginning of tensile testing

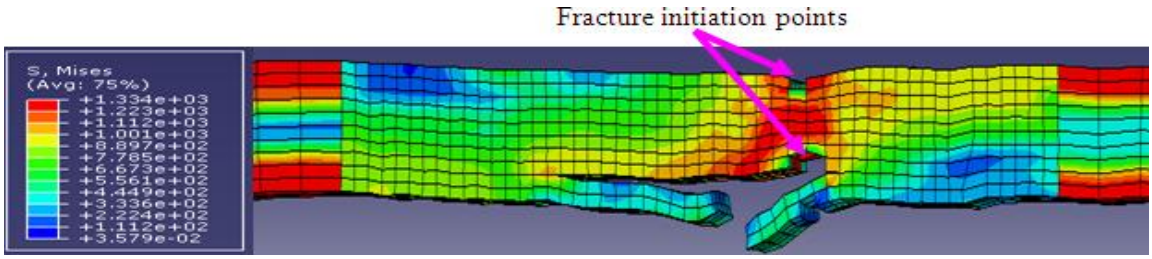

(b) Fracture initiation in thicker ligament

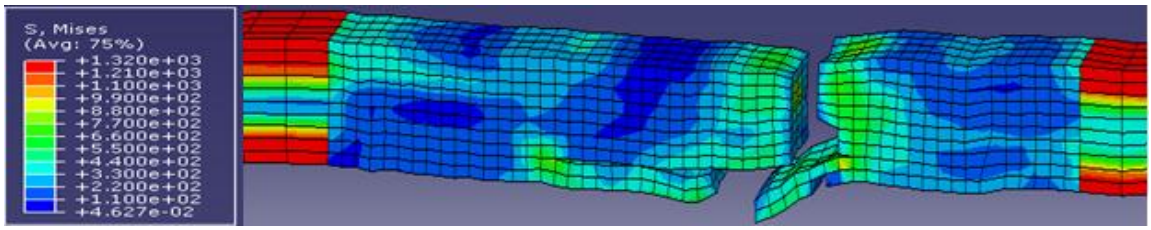

(c) Completely fractured specimen isotropic

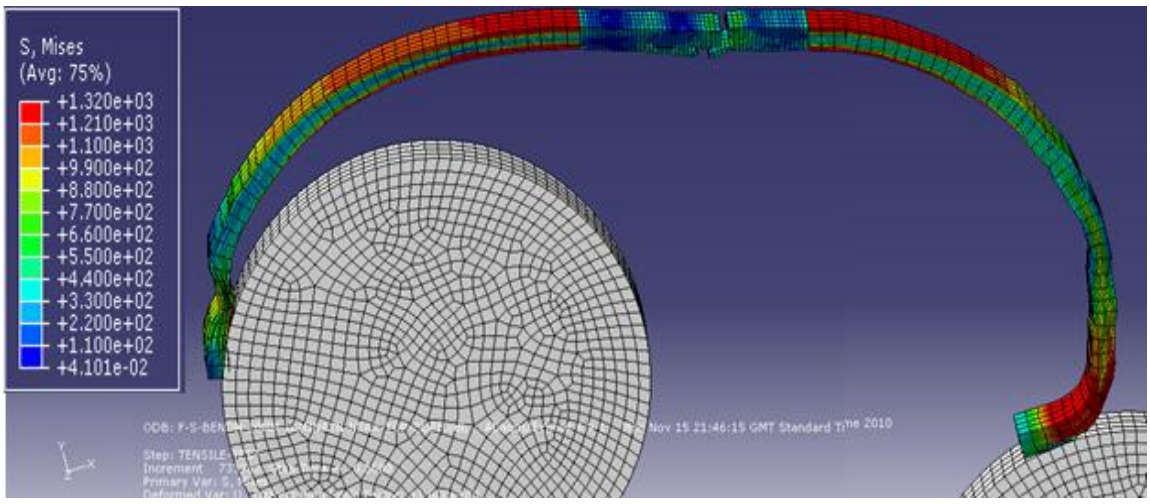

(d) Completely fractured specimen within specimen-rollers-attachments assembly.

Figure 10.51: Deformed shapes and Mises stress (MPa) distribution from simulation of tensile testing of RBS specimen with near-surface lamination.

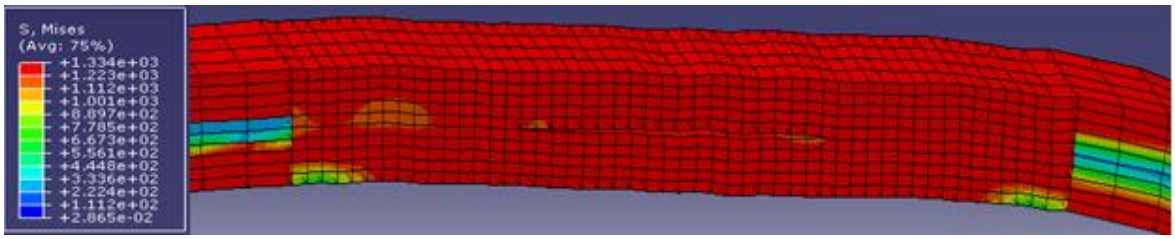

(a) At the beginning of tensile testing simulation

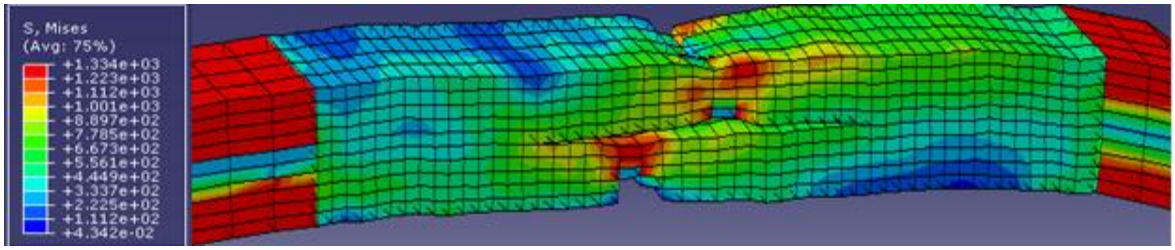

(b) During fracture initiation

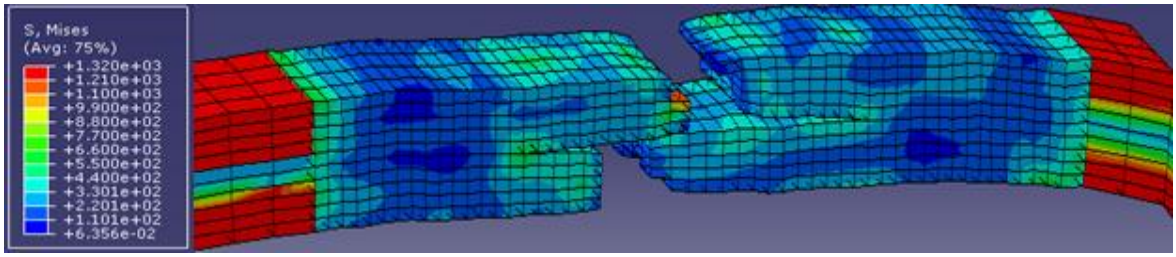

(c) Completely fractured specimen

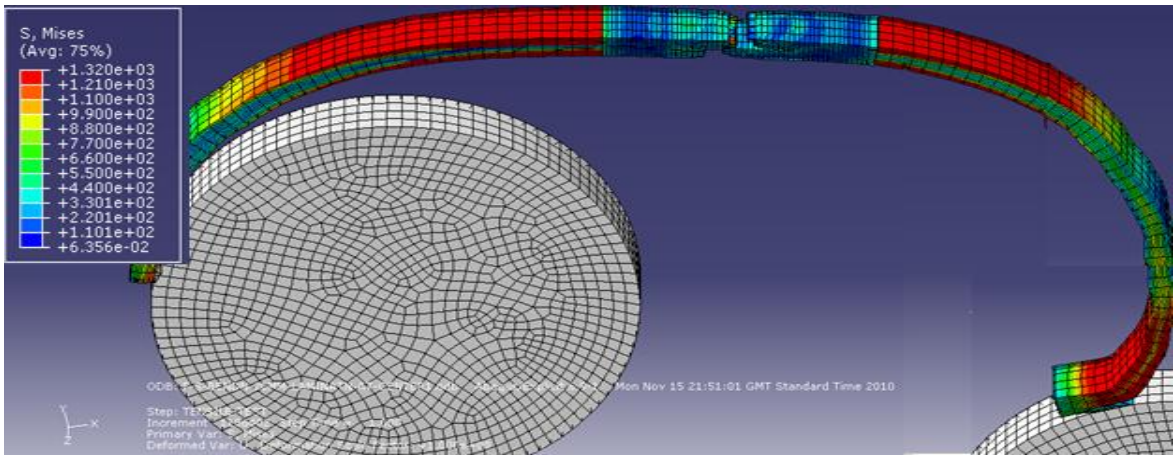

(d) Completely fractured specimen within specimen-rollers-attachments assembly.

Figure 10.52: Deformed shapes and Mises stress (MPa) distribution from simulation of tensile testing of RBS specimen with mid-thickness lamination.

The force-displacement curves and the mechanical properties of the tensile armour wires predicted by the simulations of the tensile testing of the unbent lamination free specimen, RBS lamination free specimen and RBS specimen with near-surface and mid-thickness laminations are shown in Figures 10.53(a) and (b), and Table 10.7 respectively. From Table 10.7, for both near-surface and mid-thickness laminations, the combination of reverse bending and lamination has the worse effect on the wire as it reduces the yield load, the ultimate load and the fracture displacement of the wire more than the presence of the lamination alone or reverse bending and straightening alone.

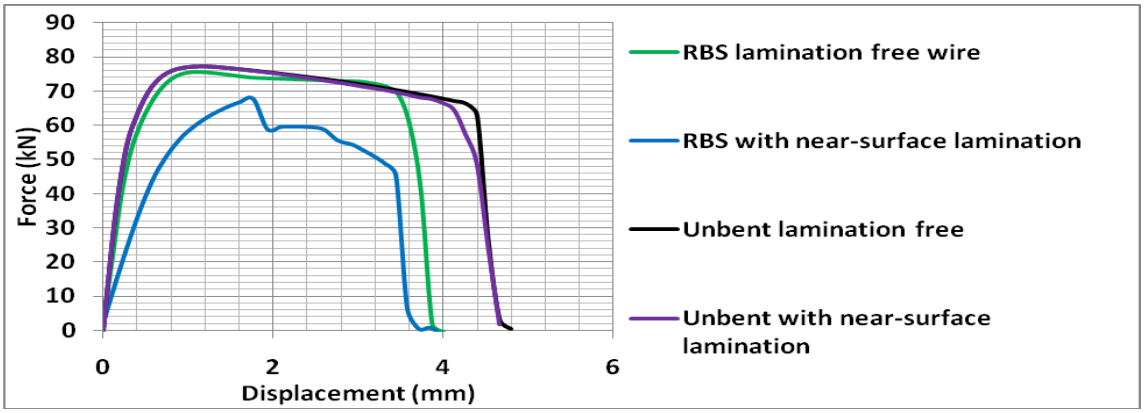

(a) Curves from specimen with near-surface lamination

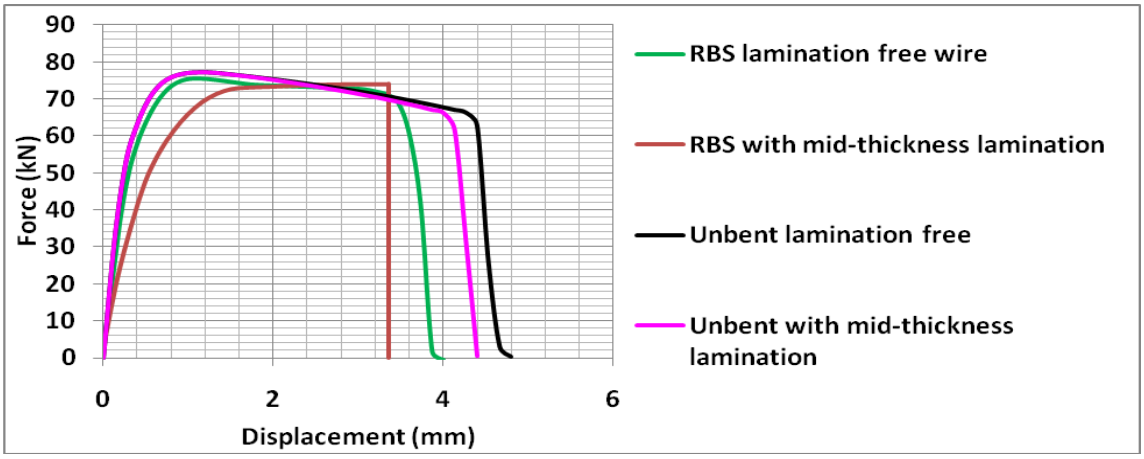

(b) Curves from specimen with mid-thickness lamination

Figure 10.53: Force-displacement curves from 12mmx5mm, 50mm gauge length unbent and RBS lamination free wires and unbent and RBS wires with laminations.

Tables 10.7: Mechanical properties of lamination free wire and RBS wires with laminations

Parameters	Lamination free wire	RBS wire with mid-thickness lamination	RBS wire with near-surface lamination	Percentage difference between lamination free wire and RBS wires with lamination	
				Mid-thickness lamination	Near-surface lamination
Yield load (kN)	53.14	47.69	36.65	10.26	31.03
Ultimate load (kN)	77.24	74.05	67.70	4.12	12.34
Fracture load (kN)	66.35	66.46	58.81	0.17	11.37
Yield point displacement (mm)	0.26	0.50	0.4586	88.03	72.21
UTL displacement (mm)	1.19	3.84	1.769	220.7	47.74
Displacement at fracture (mm)	4.26	3.36	2.599	21.22	39.05

The effects of the combination of the near-surface lamination with reverse bending and straightening on the tensile armour wire is worse than that of the combination of mid-thickness laminations with reverse bending and straightening as shown in Figure 10.54 and Table 10.7. However, near-surface laminations can readily be detected by the reverse bending and straightening procedures and do not constitute a cause for concern. The combination of mid-thickness laminations with reverse bending and straightening reduced the yield load, ultimate load and fracture displacement by 10.26%, 4.12% and 21.22% respectively, and therefore constitutes a cause for concern as it may go undetected by the reverse bending and straightening procedures.

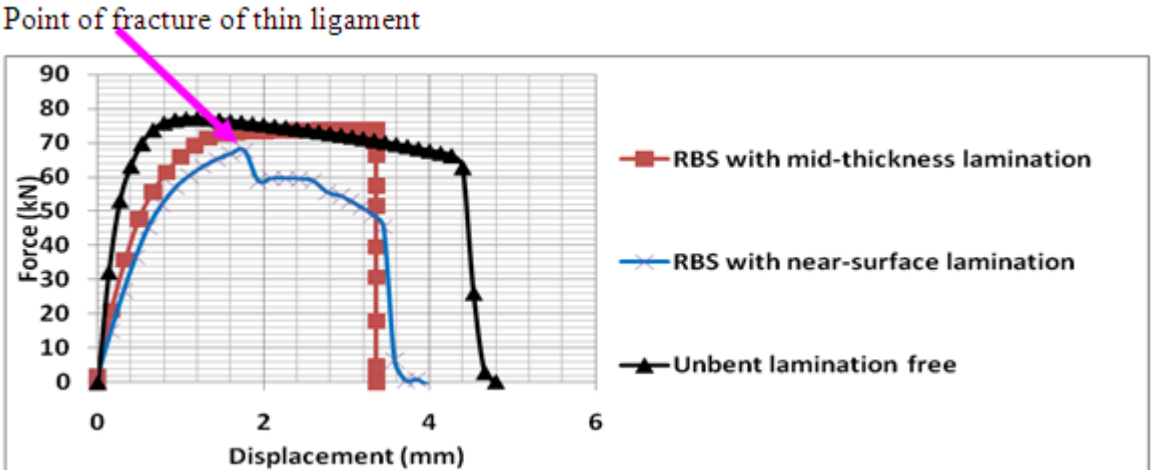

Figure 10.54: Force-displacement curves from lamination free 12mmx5mm, 50mm gauge length wire and RBS wires with mid-thickness and near-surface laminations.

10.4.2 Effects of reverse bending and straightening operations on tensile armour wires surface scratches

The effect of bending, reverse bending and straightening operations on tensile armour wire surface scratches was investigated by carrying out FE simulation of tensile armour wire specimens with a flat bottom scratch hereinafter referred to as a groove or channel subjected to bending, reverse bending and straightening. The simulation was carried out using the same specimen-rollers-attachments assembly shown in Figure 10.55(a). The simulations were carried out with wire specimens having a channel cut across the entire wire width on the upper and lower faces of the wire as well as across the entire wire thickness as shown in Figures 10.5b(b), (c) and (d) respectively. The elements around the channel were refined as shown in Figures 10.56 (a) to (c) to capture the stress concentration around the grooves. The

grooves considered have a width of 0.2mm (0.2mm being the detection limit of the eddy current detector) with depth varying from 0.1mm to 1mm. The across-the-width channels have a length of 7mm and the across-the-thickness channel has a length of 5mm.

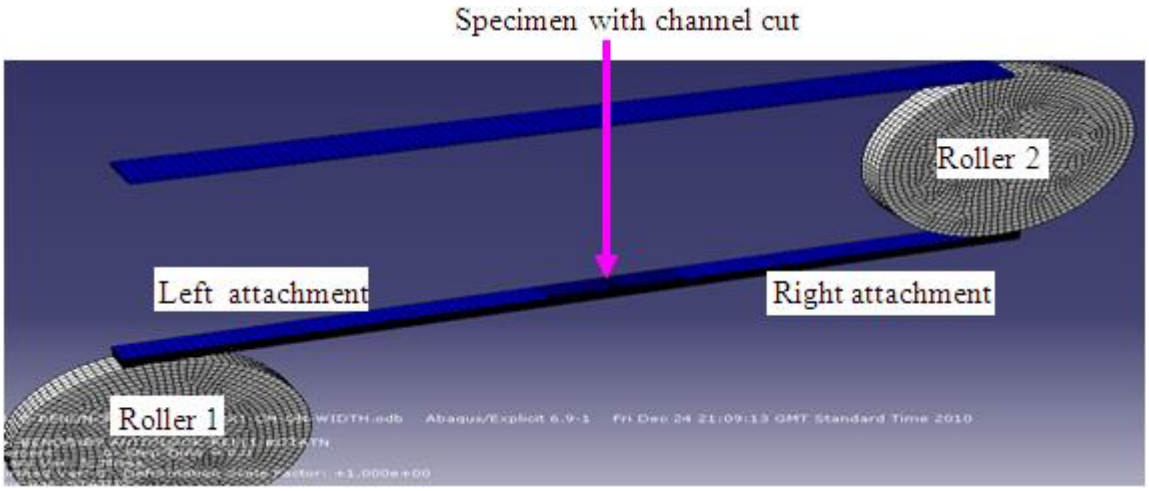

(a) Specimen with groove in specimen-rollers-attachment assembly

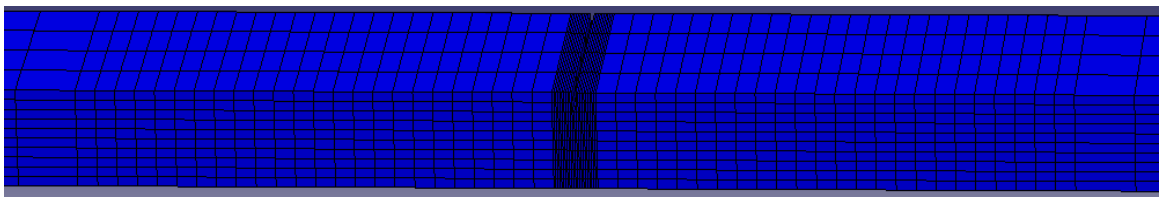

(b) Specimen with across-the-width groove on its upper face

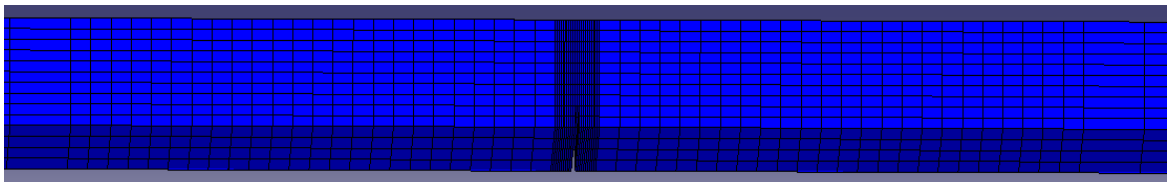

(c) Specimen with across-the-width groove on its lower face

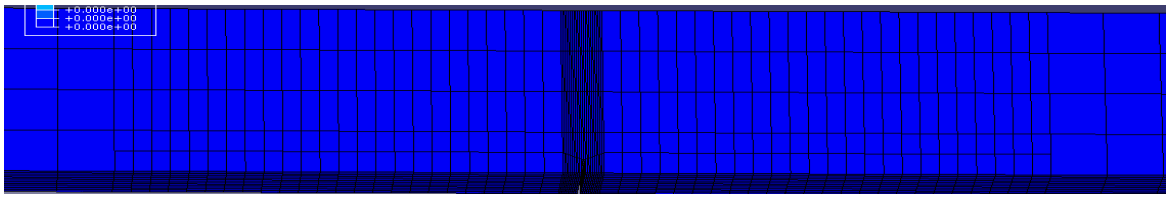

(d) Specimens with across-the thickness groove

Figure 10.55: Specimens with groove at various locations

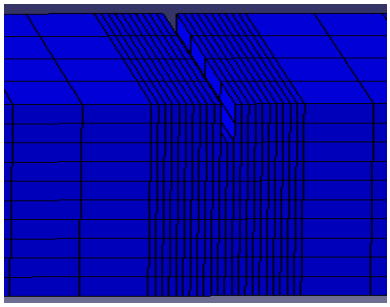

(a) Channel on upper part thickness

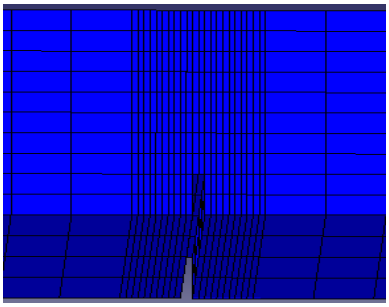

(b) Channel on upper part

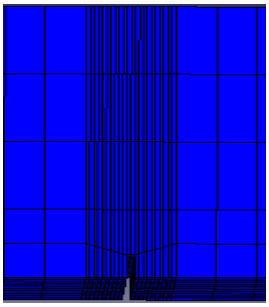

(c) Channel across

Figure 10.56: Mesh refinement around the across-the-width and across-the-thickness channels.

To conserve space, only the deformed shapes predicted by the simulation carried out with the wire specimen having across-the-width channel on its upper part within the specimen-rollers-attachments assembly at the various stages of the bending, reverse bending and straightening simulations are presented. The deformed shapes of the specimens with the across-the-width channel and the specimen with the across-the-thickness channel at the various stages of the simulations are presented. Also only the deformed shapes of the specimens with the 1mm deep channel are presented, except where the deformed shapes of the specimen with the other channel depths differ from that of the specimen with the 1mm deep channel. The deformed shape and longitudinal axial stress distribution in the specimen with across-the-width groove on its upper part within the specimen-rollers-attachment assembly at the beginning of bending simulation is shown in Figure 10.57. The deformed shapes of the specimens section at the beginning of bending simulation are shown in Figures 10.58 and the deformed shapes of the specimens around the grooves are shown in Figure 10.59.

The across-the-width grooves on the upper and lower parts of the specimens amplified the tensile and compressive stresses to which the upper and lower parts of the wire are subjected as shown in Figures 10.58 and 10.59 respectively. The across-the-thickness groove also amplified the tensile and compressive stresses in its upper and lower parts respectively as shown in Figures 10.58 and 10.59.

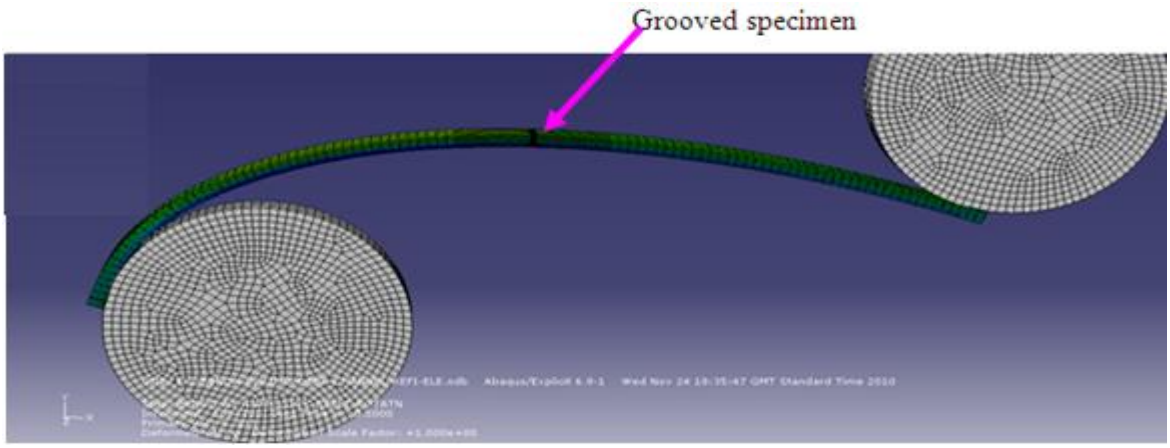

Figure 10.57: Deformed shape of grooved specimen within specimen-rollers-attachments assembly at the beginning of bending simulation.

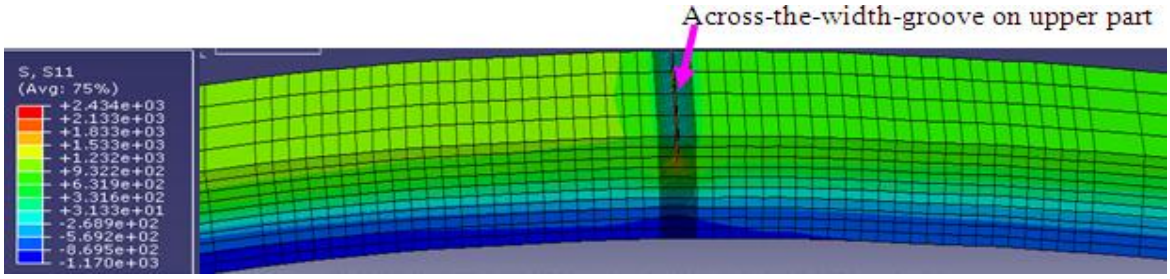

(a) Specimen with across the width groove on its upper face

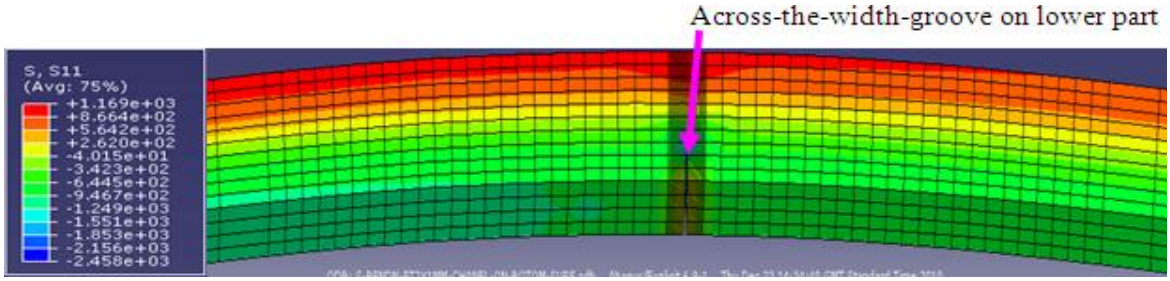

(b) Specimen with across the width groove on its lower face

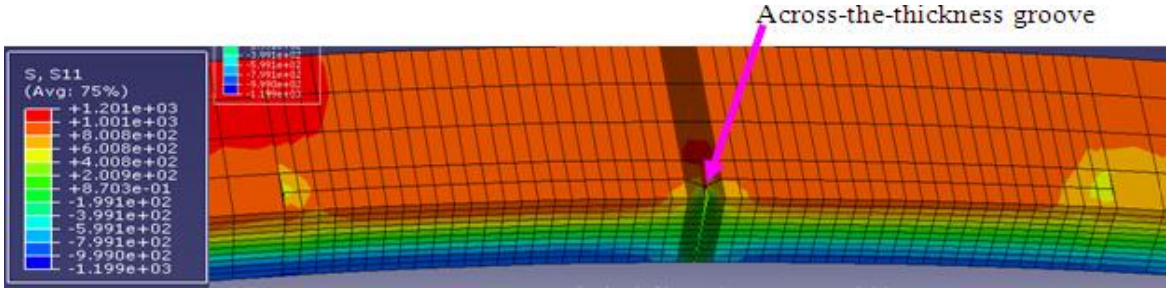

(c) Specimen with across the thickness groove

Figure 10.58: Deformed shapes and longitudinal axial stress (MPa) distribution in grooved specimens at the beginning of bending simulation

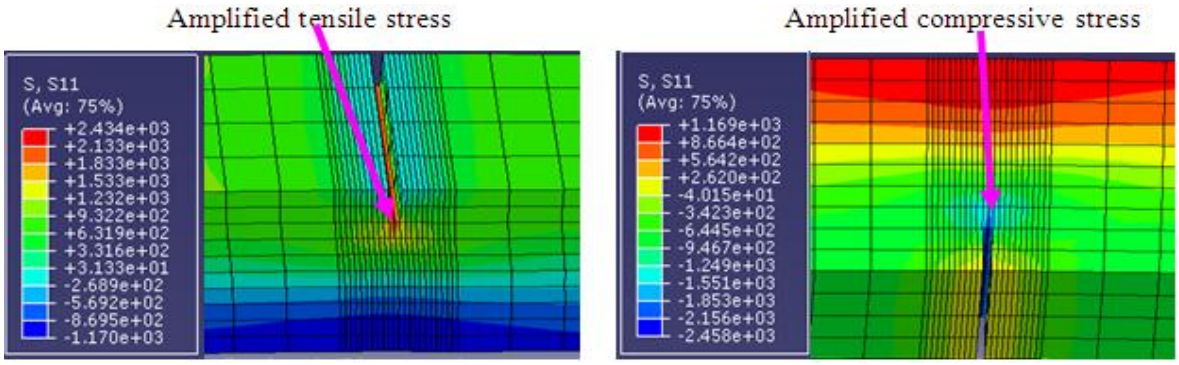

(a) Across the width groove on upper face (b) Across the width groove on lower face

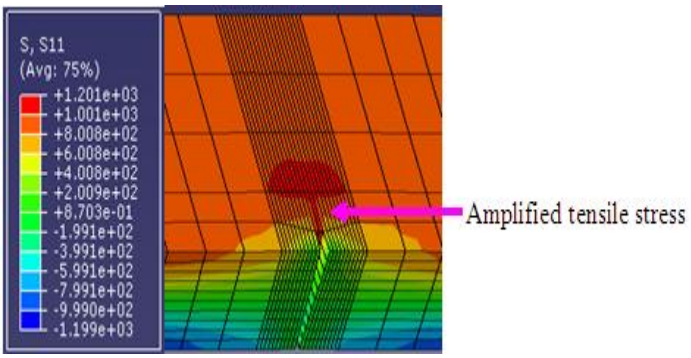

(c) Across the thickness groove

Figure 10.59: Deformed shapes and longitudinal axial stress (MPa) distribution around grooves at the beginning of bending simulation.

As the wire bent more and assumed the curvature of the roller as shown Figures 10.60, the tensile stress in the upper part of the wire became high enough to initiate fracture in the wire specimen with the across-the-width channel on its upper part as shown Figures 10.61(a) and 10.62(a). At this stage of the bending simulation, the compressive stress in the lower part of the wire was equally high enough to partially close the across-the-width groove on the lower part of the specimen as shown in Figures 10.61(b) and 10.62(b). Similarly, at this stage of the bending simulation, the tensile stresses in the upper of the specimen with the across-the-thickness channel opened the upper part of the groove and the compressive in its lower parts closed the lower part of the groove as shown in Figures 10.61(c) and 10.62(c). There was no fracture initiation in the specimen with the across-the-width groove on the lower part and the specimen with across-the-thickness groove at this stage of the bending simulation.

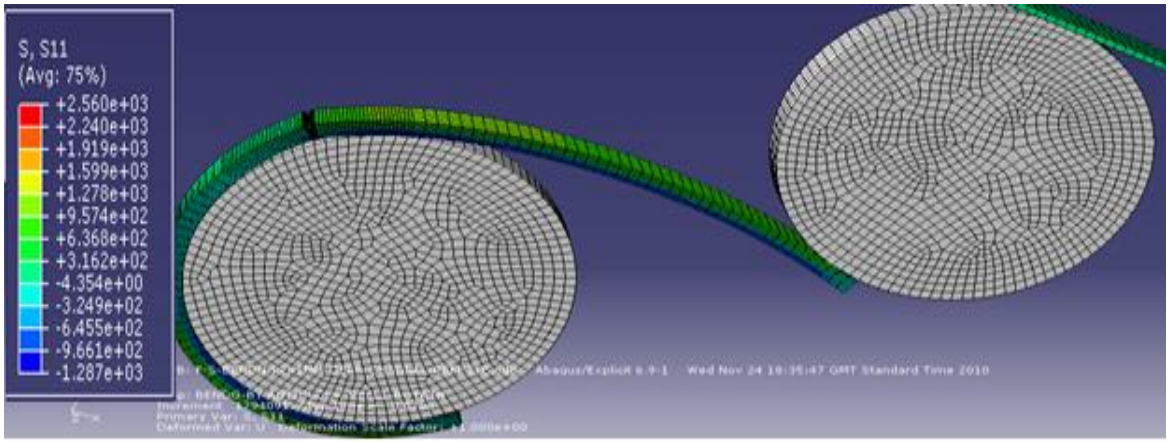

Figure 10.60: Deformed shape and longitudinal axial stress (MPa) distribution in grooved specimen within specimen-rollers-attachment assembly during bending simulation.

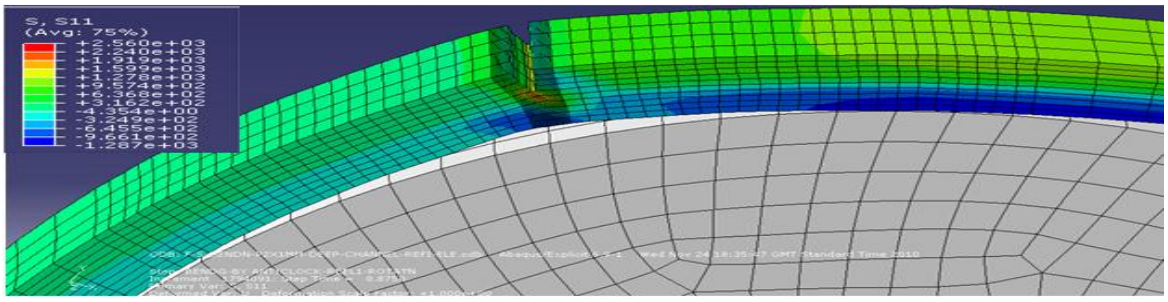

(b) Specimen with across the width groove on its upper face

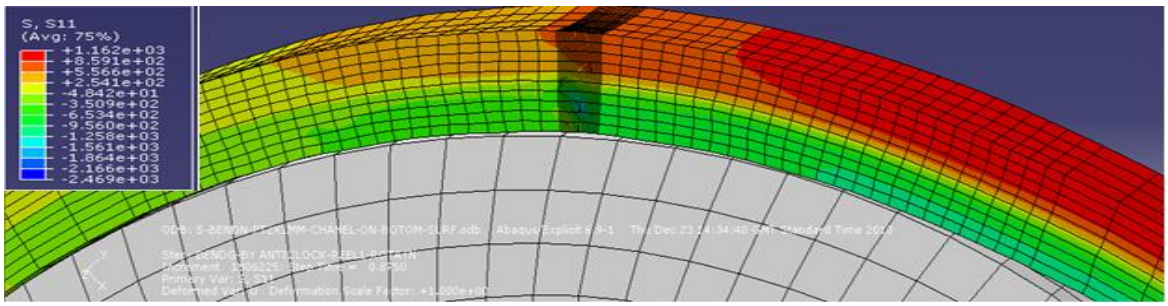

(c) Specimen with across the width groove on its lower face

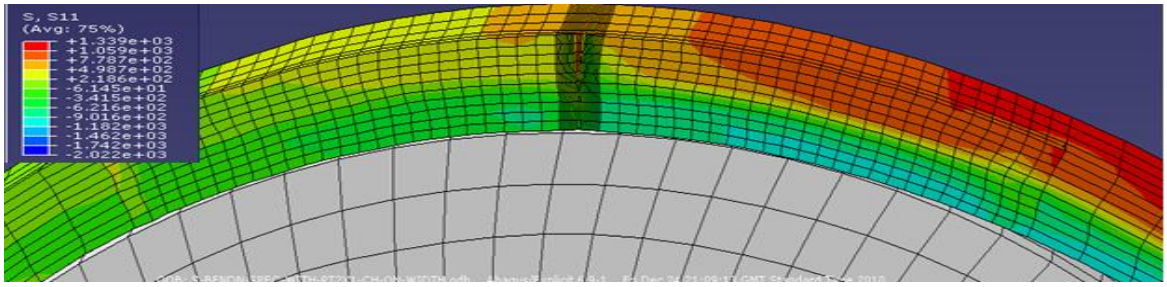

(d) Specimen with across the thickness groove

Figure 10.61: Deformed shapes and longitudinal axial stress (MPa) distribution in the grooved specimens during bending simulation

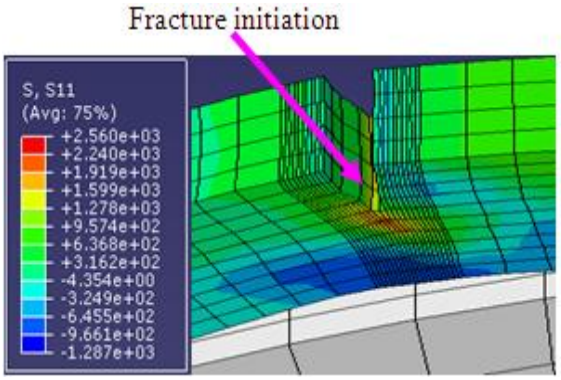

(a) Across the width groove on upper face

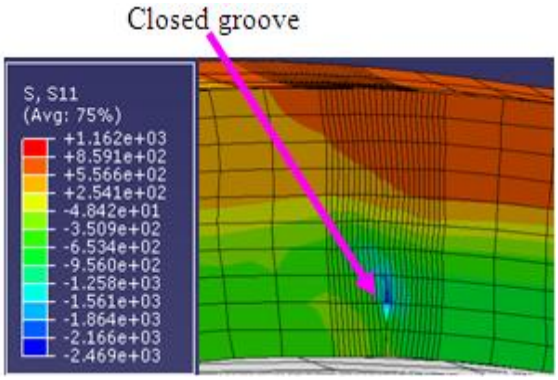

(b) Across the width groove on lower face

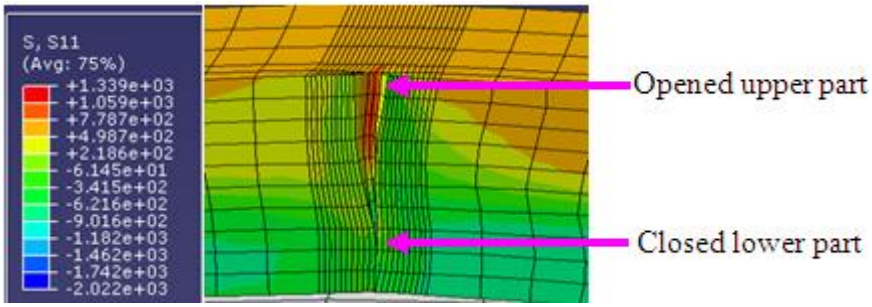

(c) Across the thickness groove

Figure 10.62: Deformed shapes and longitudinal axial stress (MPa) distribution around grooves during bending simulation

The deformed shape of the grooved specimen within the specimen-rollers-attachments assembly at the end of bending simulation is shown in Figure10.63. At the end of the bending simulation, the fracture in the specimen with the across-the-width channel on its upper part has propagated slightly while the specimen with across-the-width groove on its lower part and the specimen with across-the-thickness groove are yet to begin fracturing as shown in Figures 10.64 and 10.65. The specimen with across-the-width groove on its lower part is yet to start fracturing because the stress in its lower part is compressive and does not promote fracture initiation. The specimen with the across-the-thickness groove is yet to begin fracturing because the groove is not located in the plane of bending of the wire and consequently, the tensile stress at the tip of the groove is not high enough to initiate a fracture.

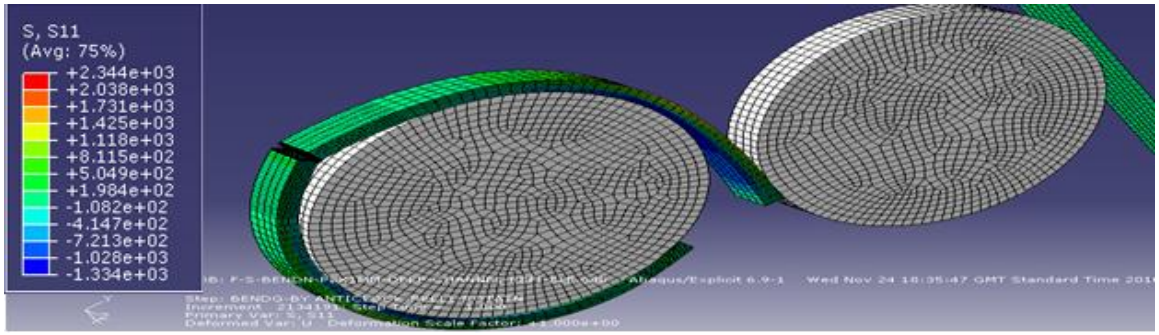

Figure10.63: Deformed shape and longitudinal axial stress (MPa) distribution in grooved specimen within specimen-rollers-attachment assembly at the end of bending simulation.

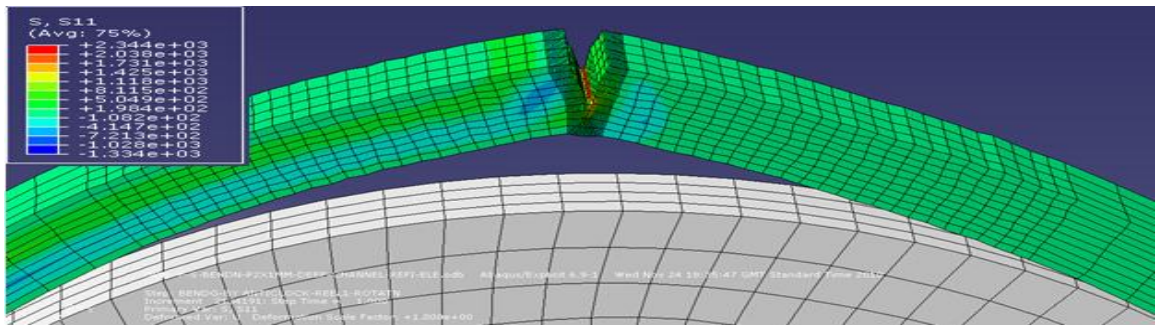

(a) Specimen with across the width groove on its upper face

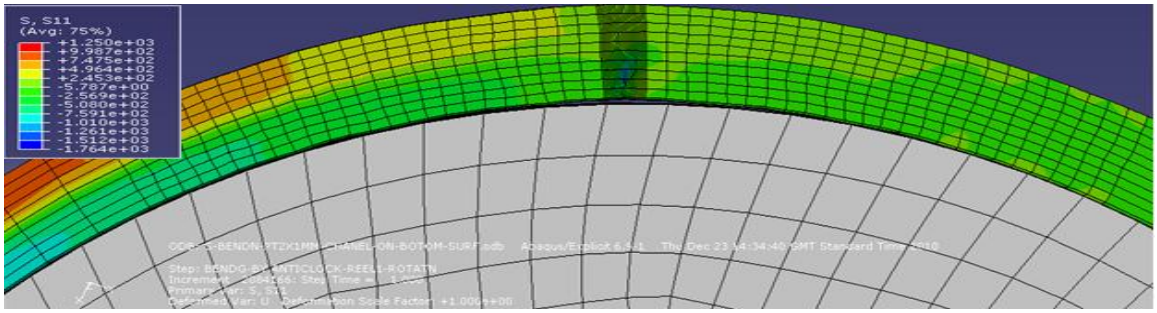

(b) Specimen with across the width groove on its lower face

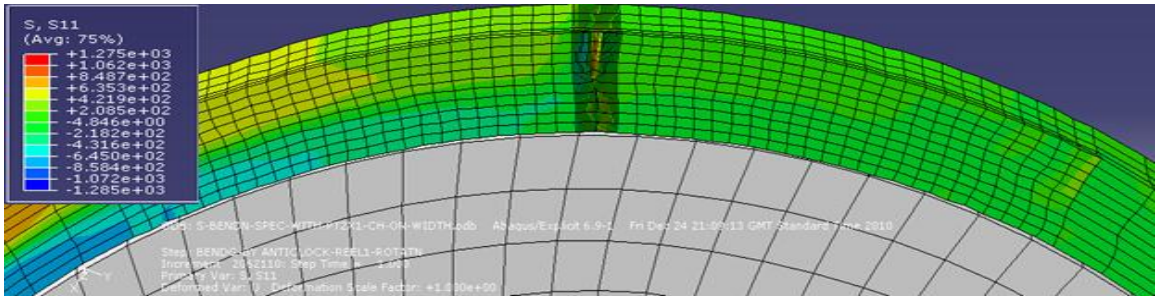

(c) Specimen with across the thickness groove

Figure 10.64: Deformed shapes and longitudinal axial stress (MPa) distribution in the grooved specimens after bending simulation

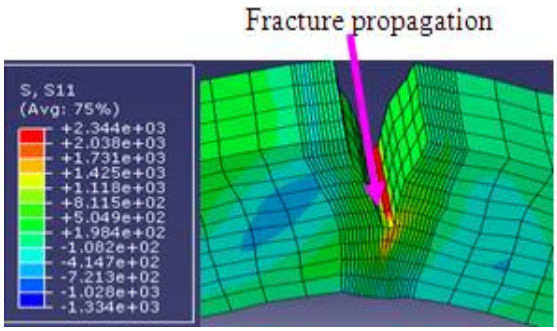

(a) Across the width groove on upper face

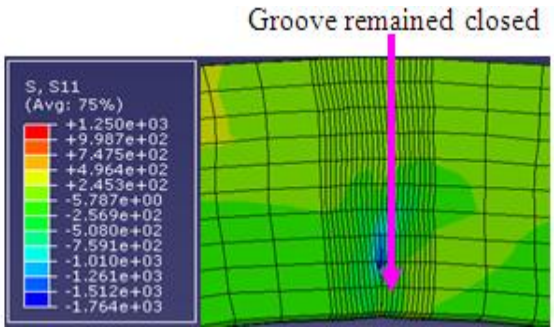

(b) Across the width groove on lower face

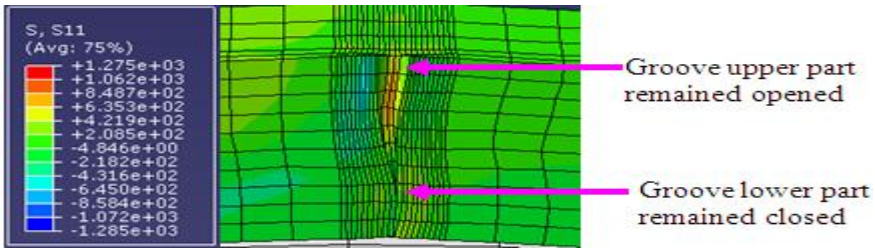

(c) Across the thickness groove

Figure 10.65: Deformed shapes and longitudinal axial stress (MPa) distribution around grooves after bending simulation

The deformed shape of the grooved specimen within the specimen-rollers-attachments assembly during the reverse bending simulation is shown in Figure 10.66. The deformed shapes of the specimen alone and the deformed shapes of the specimens around the grooves are shown in Figures 10.67 and 10.68 respectively. During reverse bending, the upper and lower parts of the wire are now subjected to compressive and tensile stress respectively. Consequently, the remaining ligament of the specimen with an across-the-width groove on its upper part is now subjected to a tensile stress. Due to the thickness of the remaining ligament, the tensile stress was high enough to initiate fracturing early during the reverse bending as shown in Figures 10.67 and 10.68(a). At this same stage of the reverse bending simulation, the groove in the specimen with the across-the-width groove on its lower part that was closed at the end of bending simulation opened up and started fracturing as shown in Figures 10.67 and 10.68(b) due to the tensile stress now in the lower part of the specimen. No fracture initiation was observed in the specimen with the across-the-thickness channel as shown in Figures 10.67 and 10.68(c). However, the lower part of the across-the-thickness channel that was closed at the end of bending simulation opened up due to the tensile stress now in the lower part of the specimen.

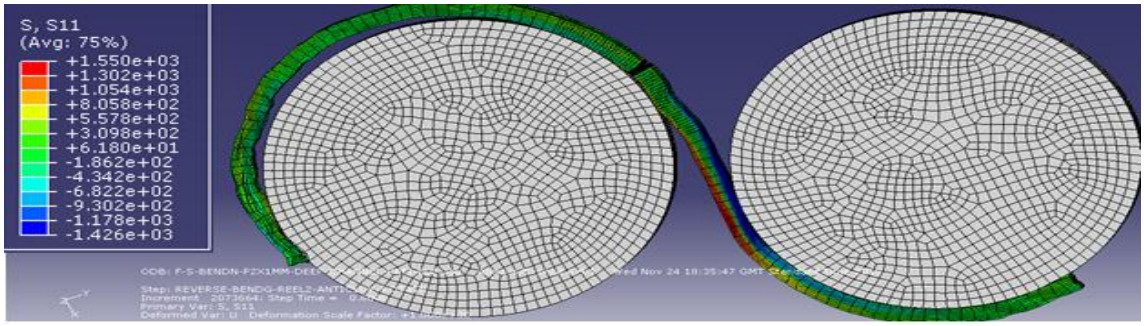

Figure10.66: Deformed shape and longitudinal axial stress (MPa) distribution in grooved specimen within specimen-rollers-attachment assembly at the end of bending simulation.

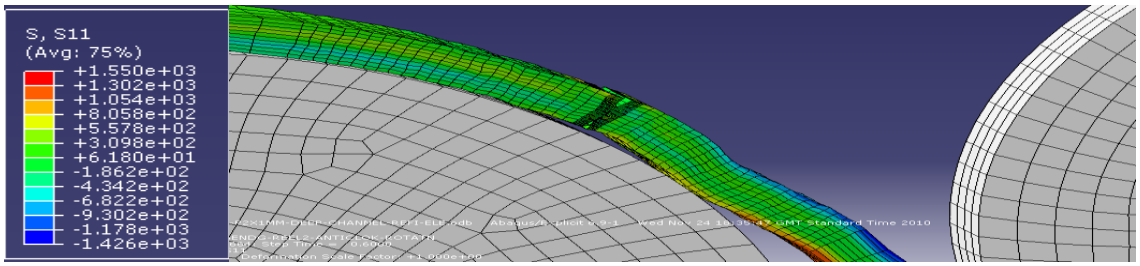

(a)Specimen with across-the-width groove on its upper face

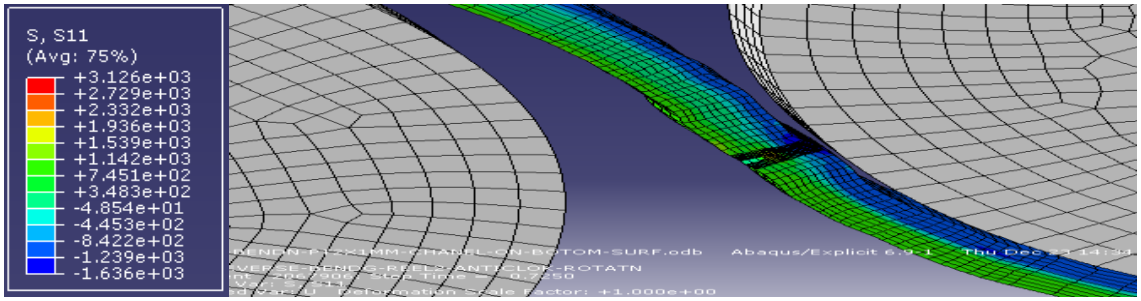

(b) Specimen with across-the-width groove on its lower face

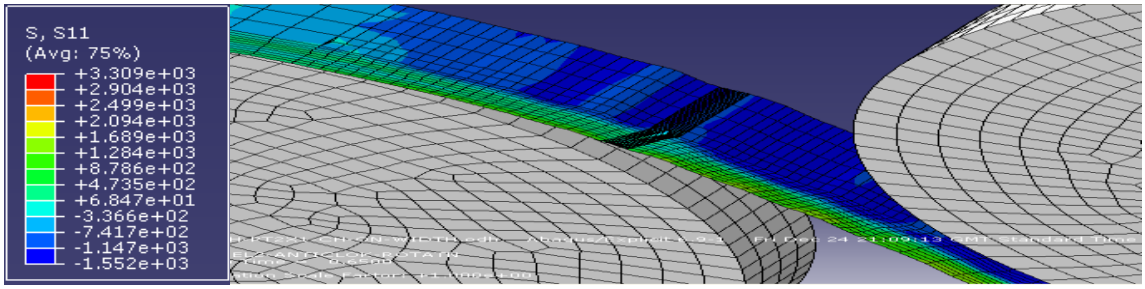

(c) Specimen with across-the-thickness groove

Figure 10.67: Deformed shapes and longitudinal axial stress (MPa) distribution in grooved specimens during reverse bending simulation.

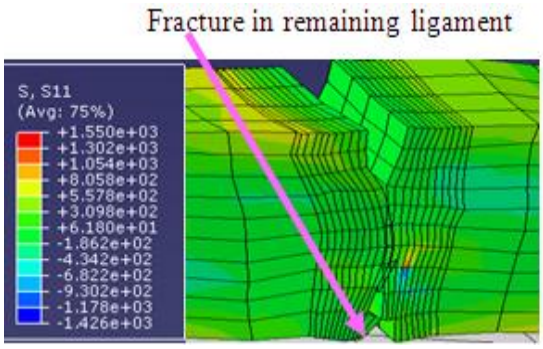

(a) Across the width groove on upper face

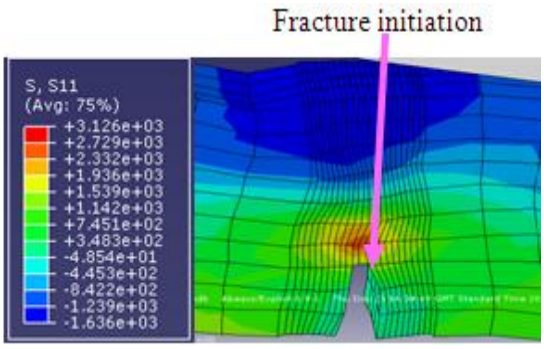

(b) Across the width groove on lower face

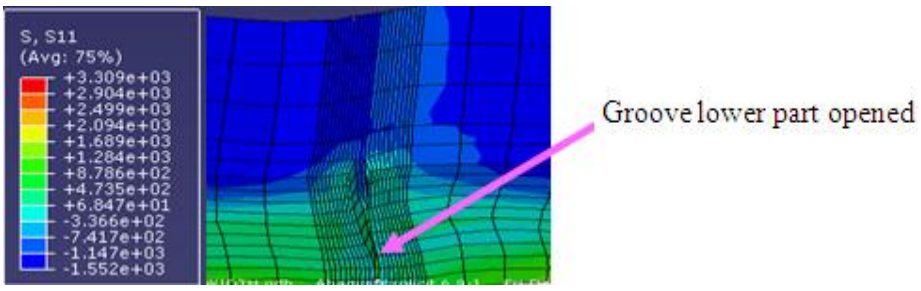

(c) Across the thickness groove

Figure 10.68: Deformed shapes and longitudinal axial stress (MPa) distribution around grooves during reverse bending simulation.

As the reverse bending simulations continued, the specimen with the 1mm deep across-the-width groove on its upper part, and the specimen with the1mm deep across-the-width groove on its lower part fractured completely as shown in Figures 10.69(a) and (b) respectively. No fracture initiation was observed on the specimen with the across-the-thickness groove as shown in Figure 10.69(c). While the specimens with the 1mm deep across-the-width groove on its upper part fractured completely during the reverse bending, the specimen with the 0.75mm deep across-the-width groove on its upper part passed through the reverse bending but started fracturing during the straightening as shown in Figure 10.69 (d). As shown in Figure 10.70(a), the specimens with 0.5mm deep across-the-width channel and the specimen with up to 1mm deep across-the-thickness channel passed through the reverse bending and straightening without fracturing. The deformed shapes of the specimens with the 0.5mm deep across-the-width channel and the specimen with up to 1mm deep across-the-thickness channel after the straightening simulations are shown in Figures 10.70 (b) and (c) respectively. The completely fractured specimen is shown in Figure 10.71.

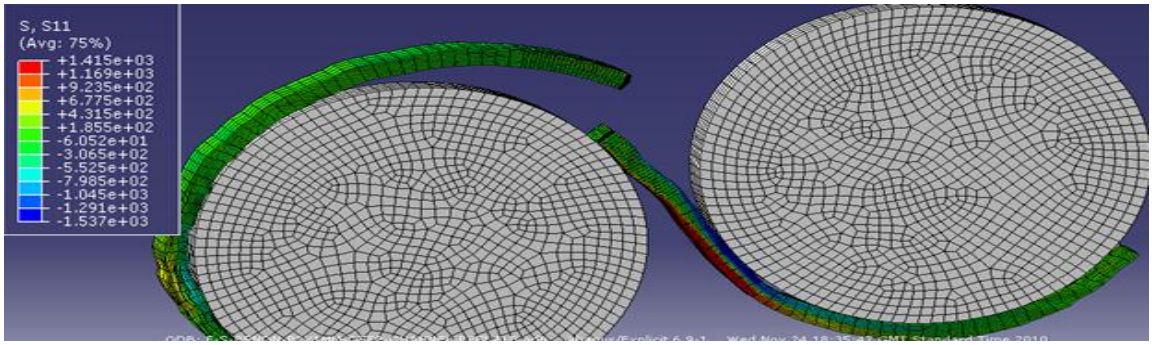

(a) Specimen with 1mm deep across-the-width groove on upper face

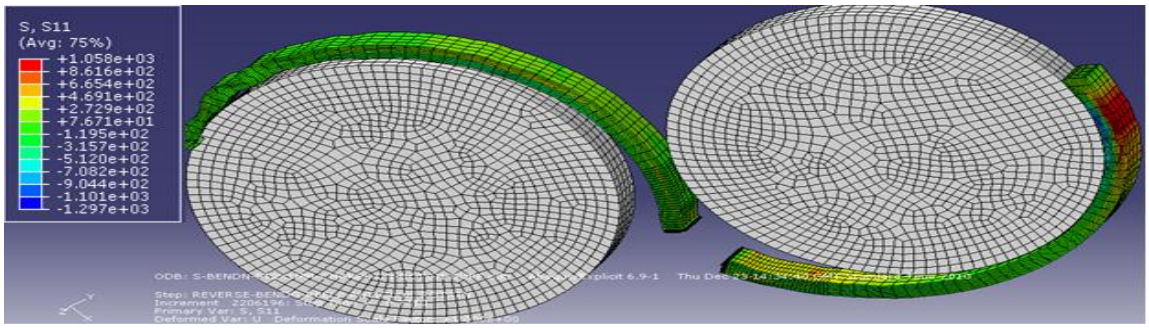

(b) Specimen with 1mm deep across the-width-groove on lower face

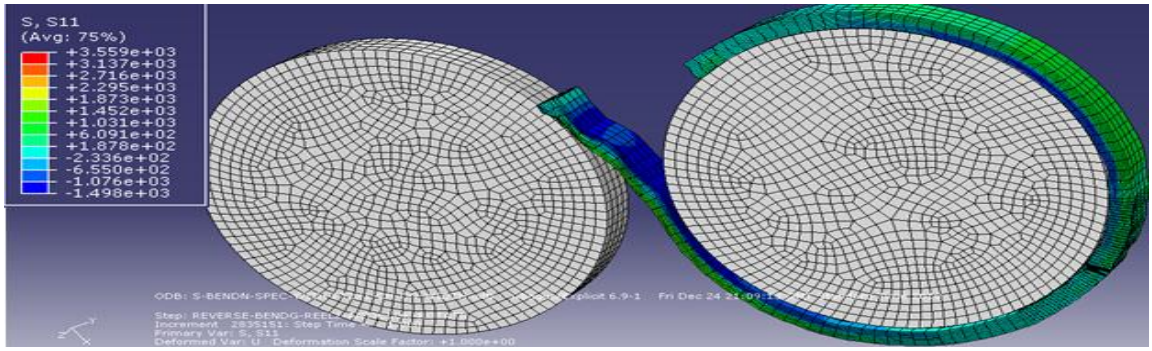

(c) Specimen with 1mm deep across-the-thickness groove

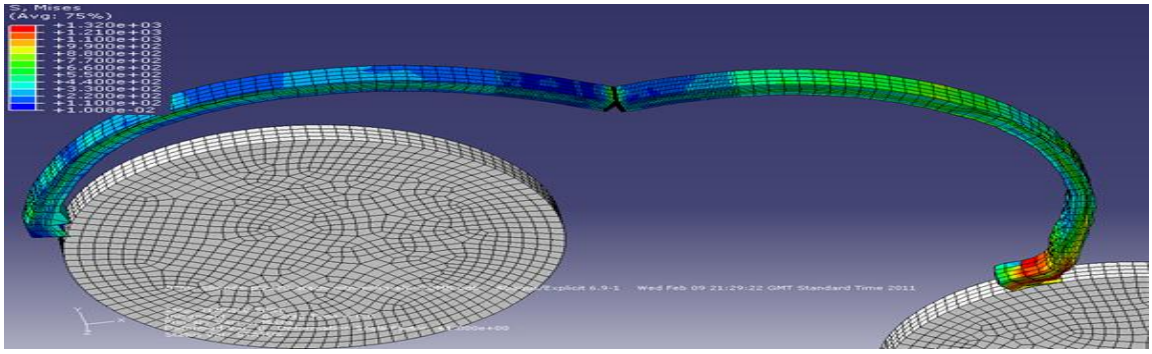

(d) Specimen with 0.75mm deep across-the-thickness groove

Figure10.69: Deformed shapes and longitudinal axial stress (MPa) distribution in specimen with varying channel depths after reverse bending and straightening simulations.

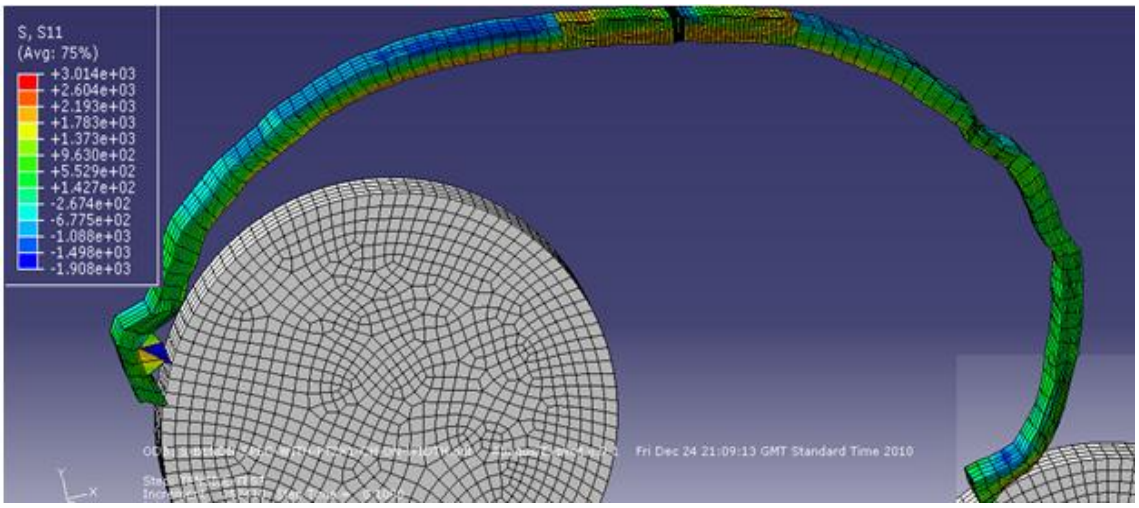

(a) Specimen within the specimen-rollers-attachment assembly

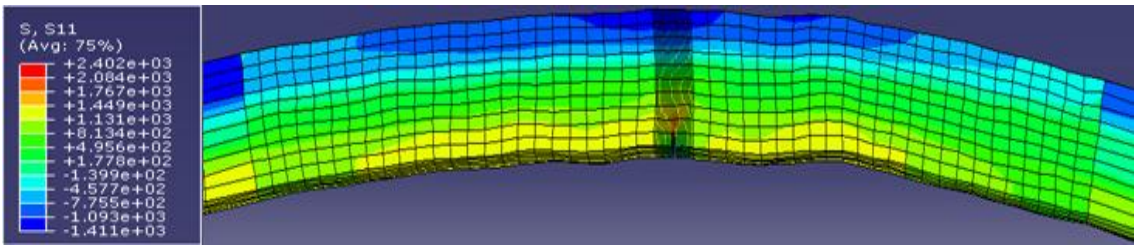

(b) Specimen with 0.5mm deep across-the-width channel

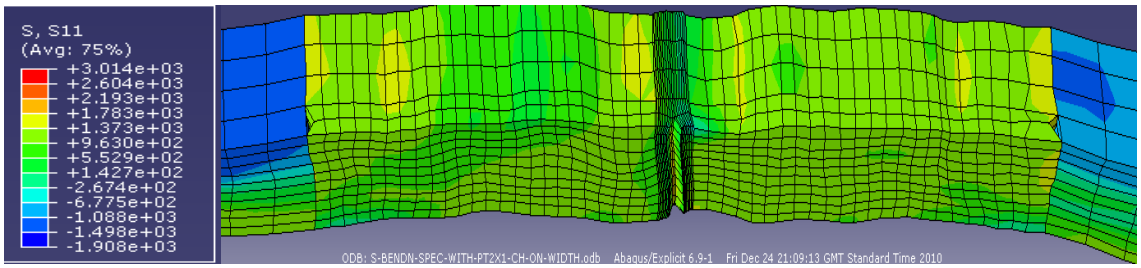

(c) Specimen with 1mm deep across-the-thickness channel

Figure 10.70: Deformed shape and longitudinal axial stress (MPa) distribution in specimens with 0.5mm deep across-the-thickness and 1mm deep across-the-width channel after straightening simulation.

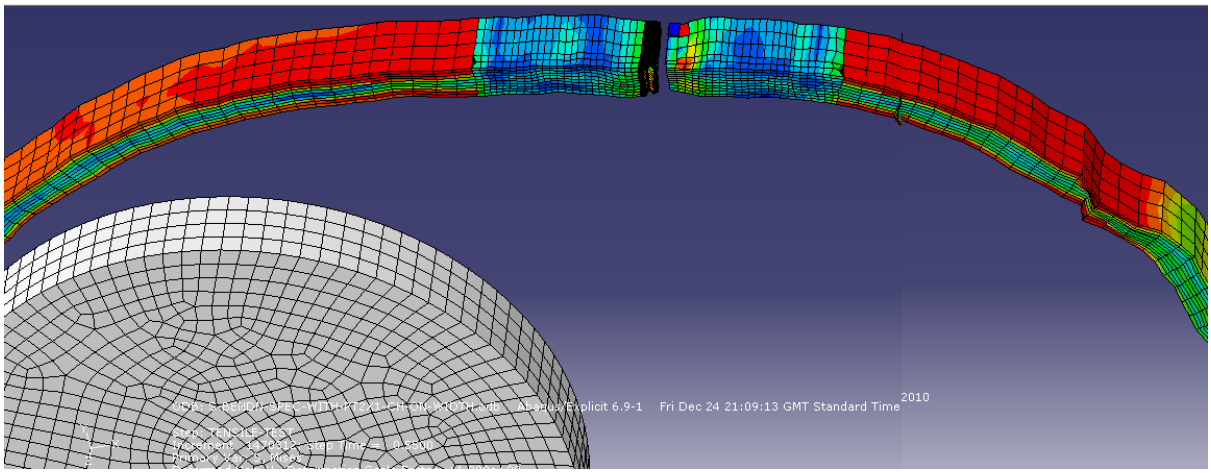

(a) Specimen within the specimen-rollers-attachment assembly

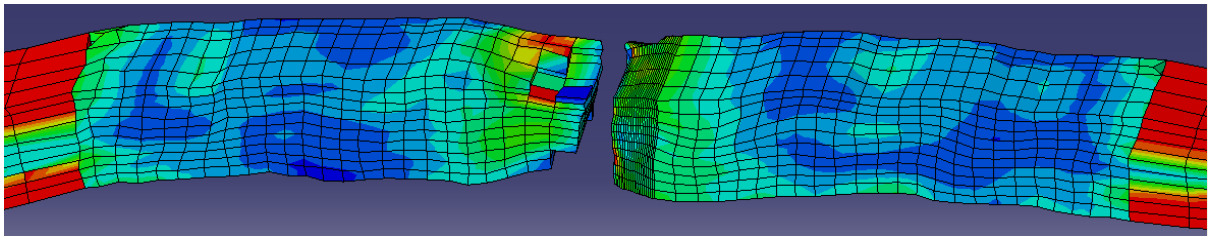

(b) Specimen with 0.5mm deep across-the-width channel

Figure 10.71: Completely fractured specimen of wire with channel cut subjected to reverse bending and straightening

The force-displacement curves obtained from the simulations of the tensile testing of the wire specimen with 0.2mmx0.5mm channel and the wire specimen with 0.2mmx0.5mm channel that was subjected to reverse bending and straightening are shown in Figure 10.72. The force-displacement curves and the tensile properties obtained from the tensile testing simulation of the: as-received wire, as-received wire subjected to reverse bending and straightening, wire specimen with 0.2mmx0.5mm channel and wire specimen with 0.2mmx0.5mm channel subjected to reverse bending and straightening simulations are shown in Figure 10.73 and Table 10.8 respectively.

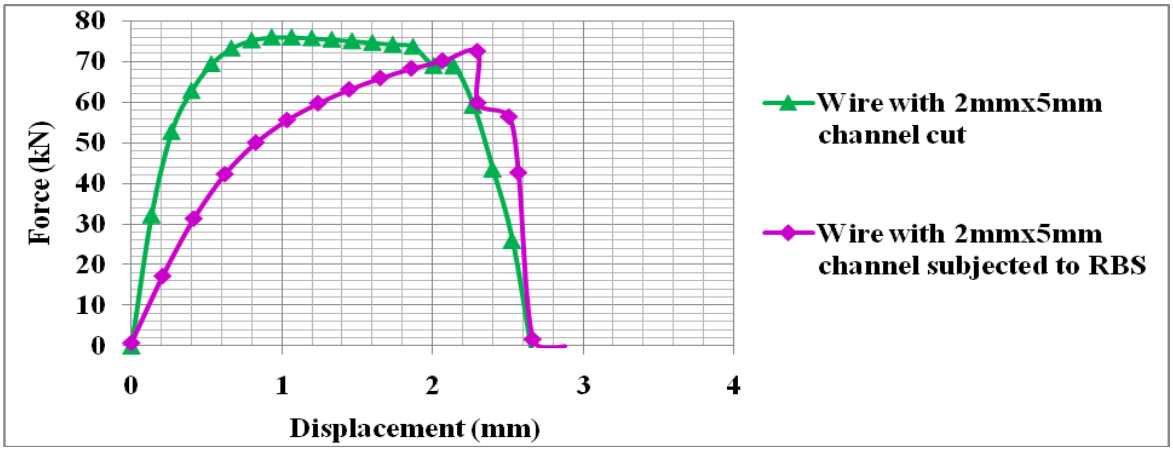

Figure 10.72: Force-displacement curves for 12mmx5mm, 50mm gauge length unbent and RBS specimens with 0.2mmx0.5mm across-the-width channel

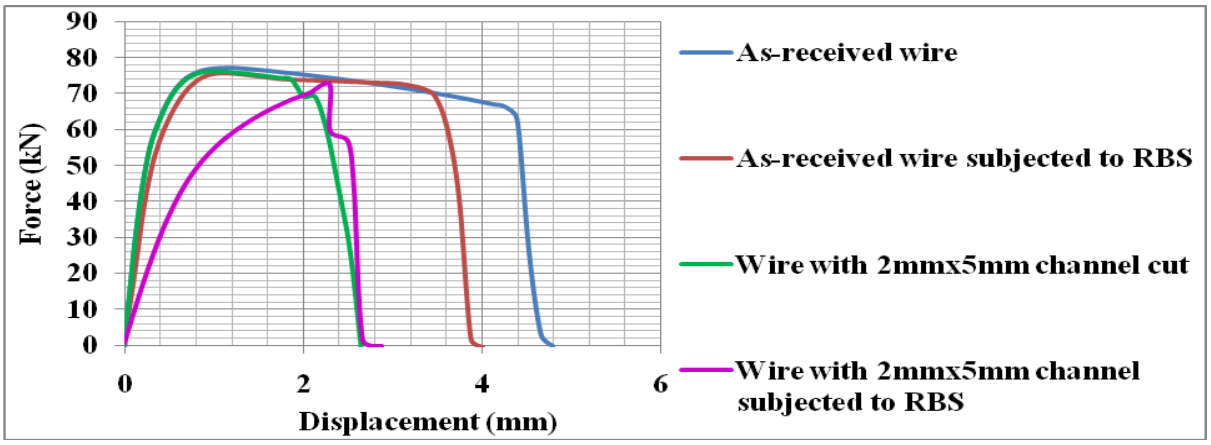

Figure 10.73: Force-displacement curves for 12mmx5mm, 50mm gauge length unbent and RBS as-received and unbent and RBS specimens with 0.2mmx0.5mm across-the-width channel.

Table 10.8: Tensile properties from unbent and RBS as-received, and Unbent and RBS specimens with 0.2mmx0.5mm across-the-width channel.

Parameters	As-received wire	As received wire subjected to RBS	Wire with 0.2mmx0.5mm channel	Wire with 0.2mmx0.5mm channel subjected to RBS
Yield load (kN)	53.14	50.87	52.77	42.31
Ultimate load (kN)	77.24	75.55	76.04	72.55
Displacement at fracture (mm)	4.13	3.47	2.15	2.09

From Figures 10.72, 10.73 and Table 10.8, the combination of the presence of the 0.2mmx0.5mm channel and RBS reduced the yield load, the ultimate load and the displacement at fracture by 20.38%, 6.07 and 49.345 respectively compared to the 0.70%, 1.55% and 47.94% reductions in the yield load, the ultimate load and the displacement at fracture of the wire by the presence of the 0.2mmx0.5mm channel, and the 4.2%, 2.18% and 15.98% reductions in the yield load, the ultimate load and the displacement at fracture of the wire by the reverse bending and straightening operations. Thus it can be concluded that the combination of the presence of scratches and RBS operations causes a higher reduction in the tensile properties of the tensile armour wires than the reduction in the tensile properties due to either the presence of scratches or the reverse bending and straightening operations.

Attempts to simulate the bending, reverse bending, straightening and tensile testing of the tensile armour wire with channel depth less than 0.5mm were not successful as the wire broke from the roller as shown in Figure 10.74 during the reverse bending, which made the reverse bending, straightening and tensile testing simulation impossible. The wire broke from the roller because the elements that connected the wire to the roller, which are less than 0.5mm (the lowest dimension in the thickness direction with which the reverse bending and straightening simulation could be carried out) as shown in Figure 10.75 could not withstand the excessive strain they are subjected to during the reverse bending simulations. The element needed to be of the same dimension as the depth of the channel cut (which is less than 0.5mm) so as to have adequate node to node contact between the elements of the specimen and the elements of the left and right attachments, without which the nodes connecting the specimen to the attachments broke during the simulation.

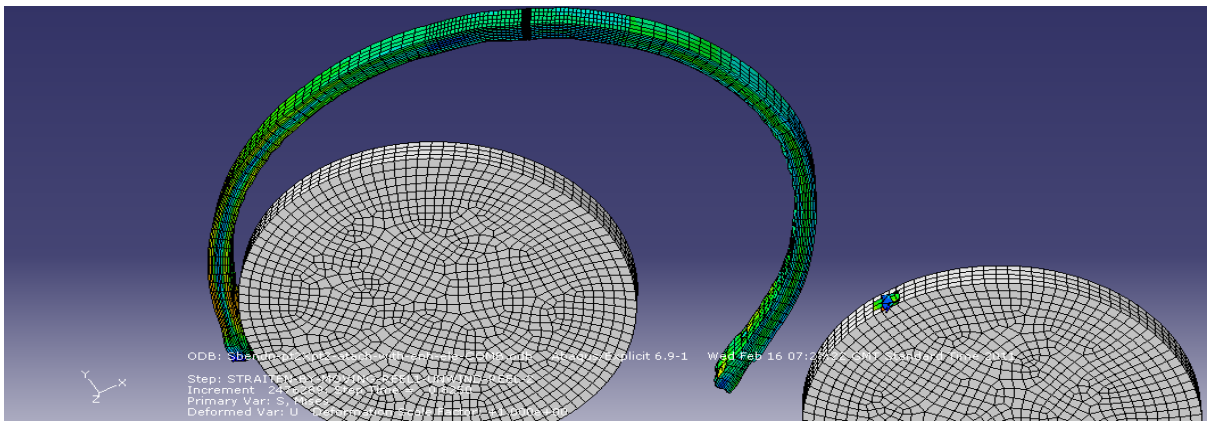

Figure 10.74: Disconnection of wire with channel depth less than 5mm from roller during reverse bending simulation.

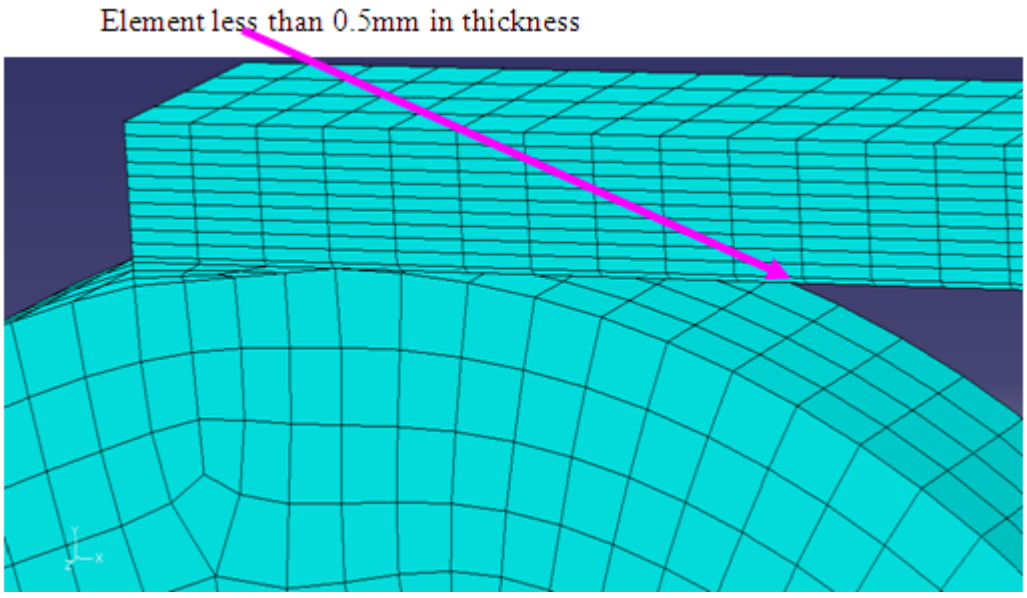

Figure 10.75: Thin element connecting attachment to roller

10.5 Conclusion

From both laboratory and numerical experiments, it can be concluded that bending, reverse bending and straightening of tensile armour wires reduces the yield load, the ultimate load and the displacement at fracture of the wires by at least 4.27%, 2.58% and 18.62% respectively. The presence of either near-surface or mid-thickness lamination has negligible effects on the tensile properties of the tensile armour wires with only a 6.25% reduction in the displacement at fracture of the wires. However, if tensile armour wires with either near-surface or mid-thickness lamination are subjected to bending, reverse bending and straightening, the yield load, the ultimate load and the displacement at fracture of the wires are reduced considerably. The combination of reverse bending and straightening with near-surface lamination has the worse effects of reducing the yield load, the ultimate load and the displacement at fracture of the wire by 31.03%, 12.34% and 39.05% respectively.

The reverse bending and straightening test is only effective in revealing or detecting near-surface laminations and may not be an effective test to detect mid-thickness lamination in tensile armour as wires with the mid-thickness laminations will pass through the reverse bending and straightening procedures without fracturing and with the mid-thickness laminations undetected. Consequently, other in-line non destructive testing methods might have to be used to detect mid-thickness laminations as tensile armour wires with mid-thickness laminations subjected to bending, reverse bending and straightening may have their

yield load, ultimate load and fracture displacement reduced by 10.26%, 4.12% and 21.22% respectively.

The reverse bending and straightening test can also reveal scratches with a depth greater than 0.5mm as the wires will breaks during the reverse bending operation. The combination of the presence of 0.5mm deep scratch and the RBS operations reduced the yield load, the ultimate load and the displacement at fracture by 20.38%, 6.07 and 49.345 respectively. The reduction in the tensile properties due to the combination of the presence of scratches and RBS operations is higher than the reduction in the tensile properties of the tensile armour wires due to either the presence of scratches or the reverse bending and straightening operations.

Having presented the investigations of the effects of scratches, dents, laminations as well as bending, reverse bending and straightening operations on the tensile properties of tensile armour wires, the summary and conclusions of the overall findings of this research as well as the further works are presented in the next chapter.

Chapter 11 Conclusions and further work

In this chapter, the conclusions drawn from the analyses of the results obtained from both laboratory and numerical or virtual experiments carried out to investigate the effects of miniature flat bottom scratches, miniature pointed end scratches, miniature dents, and laminations on the tensile properties of the tensile armour wires are presented. Also presented in this chapter, are the conclusions drawn from the analyses of the results obtained from both laboratory and virtual experiments carried out to investigate the effects of reverse bending and straightening, and the effects of the combinations of reverse bending and straightening operations with laminations and with scratches on the tensile properties of the tensile armour wires. In addition, further work is also suggested.

11.1 Conclusions

The following are the conclusions drawn from the outcome of this research:

a) The failure mechanism for both the as-received or "defect free" tensile armour wires and the defective tensile armour wires is the shear failure mechanism.

b) The maximum reductions in the yield load, the ultimate load and the fracture displacement of the tensile armour wires by flat bottom scratches with dimensions less than 0.2mm, which cannot be detected by the eddy current detector system, are 0.072%, 0.238% and 10.95% respectively.

c) The maximum reductions in the yield load, the ultimate load and the fracture displacement of the tensile armour wires by pointed end scratches with dimensions less than 0.2mm are 0.07%, 0.09% and 2.92% respectively.

d) Denting of tensile armour wires to dent depths and less than 0.2mm increases the yield and the ultimate loads of the wire but reduces its displacement at fracture by no more than 5.66%. Denting only begins to cause reductions in the yield and the ultimate loads of the wire when the dent depth and/or diameter is greater than 0.3mm.

d) The extent of the reductions in the yield load, the ultimate load and the displacement at fracture of the tensile armour wires depends on the size rather than the location of both flat bottom and pointed end scratches. The extent of the effects of indentation on the tensile armour wires tensile properties also depends on the size rather than the location of the indentation.

e) The worst effect of the pointed end or flat bottom scratches is on the displacement at fracture and invariably the ductility of the wire, followed by the ultimate load, with the least effect on the yield load of the tensile armour wires. The worst effect of denting is also on the displacement at fracture of the tensile armour wires.

f) The 0.2mm defect detection limit of the eddy current defect detection system seems adequate as the reduction in the yield load, the ultimate load and displacement at fracture of the tensile armour wires by scratches and dents are minimal and are within the range of what the factor of safety applied to material properties can conveniently accommodate.

g) Bending, reverse bending and straightening of tensile armour wires reduce the yield load, the ultimate load and the displacement at fracture (i.e. the ductility) of the wires by at least 4.27%, 2.58% and 18.62% respectively.

h) Near-surface or mid-thickness laminations on their own have negligible effects on the tensile properties of the tensile armour wires with little or no reduction in the yield and ultimate loads of the wires, and only a 6.25% reduction in the displacement at fracture of the wires. However, if tensile armour wires with either near-surface or mid-thickness lamination are subjected to bending, reverse bending and straightening, the combination of the reverse bending and straightening, and laminations considerably reduces the yield load, the ultimate load and the displacement at fracture of the wires. The combination of reverse bending and straightening with near-surface lamination has the worse effect, reducing the yield load, the ultimate load and the displacement at fracture of the wires by 31.03%, 12.34% and 39.05% respectively.

i) The reverse bending and straightening test is only effective in revealing or detecting near-surface laminations, and may not be an effective test to detect mid-thickness

laminations in tensile armour wires. This is because wires with mid-thickness laminations will pass through the reverse bending and straightening procedures without fracturing and with the mid-thickness laminations undetected. Consequently, other in-line non destructive testing methods might have to be used to detect mid-thickness laminations, as tensile armour wires with mid-thickness laminations subjected to bending, reverse bending and straightening may have their yield load, ultimate load and fracture displacement reduced by 10.26%, 4.12% and 21.22% respectively.

j) With the present arrangement being used for the reverse bending and straightening test, in which the width of the wire is in contact with the rollers, the reverse bending and straightening test will fracture tensile armour wires with scratches across or along their width that are 0.75mm or more deep. Wires with shallower scratches across or along their width and wires with scratches deeper than 0.75mm across their thickness will pass through the reverse bending and straightening test without fracturing.

k) While wires with across-the-width scratches that are shallower than 0.75mm pass through the reverse bending and straightening operations unbroken, their yield load, ultimate load and displacement at fracture reduce considerably when compared with wires with the same size of scratches that are not subjected to the reverse bending and straightening test. Confirm this statement from the FE

11.2 Further work

Further investigation of the effects of miniature scratches; dents, and laminations on the tensile properties of tensile armour wires can be carried out on a range of steel wires with different sizes and strengths from the wires covered by this research. Investigation of the effects of miniature scratches and dents, and laminations, as well as the bending, reverse bending and straightening operations on the fatigue properties or behaviour of the tensile armour wires needs to be carried out as flexible pipes and invariably tensile armour wires are subjected to cyclic loading during service. For such an investigation, more accurate kinematic hardening parameters need to be obtained from laboratory and/or numerical experiments. Furthermore, the effects of welding and as well as the effects of the inherent defects in welds on the tensile properties of the tensile armour wires needs to be investigated.

Appendix A

TableA1: Crosshead displacement correction values

Stiffness K (kN/mm)	Experimental		Machine correction $\Delta_E = P/K$ (mm)	Displacement corrected with Δ_E (mm)	Assumed grip end and plastic displacement (mm)	Final corrected displacement (mm)
	Force from UTL (kN)	Displacement from UTL point				
322.8	76.01	2.1	0.2441	1.864	0.03	1.83
322.4	75.99	2.27	0.2357	2.03	0.07	1.4
321.8	75.93	2.43	0.236	2.19	0.1	1.24
316.8	75.83	2.6	0.2394	2.36	0.14	2.22
308.2	75.68	2.76	0.2456	2.52	0.17	2.35
300.9	75.42	2.93	0.2507	2.68	0.2	2.47
293.7	74.91	3.09	0.2551	2.84	0.24	2.6
289	73.98	3.26	0.2559	3	0.27	2.73
285.2	72.76	3.42	0.2551	3.17	0.3	2.86
276.7	71.44	3.59	0.2582	3.33	0.34	2.99
272	70.02	3.75	0.2574	3.5	0.37	3.12
269.5	69.27	3.84	0.257	3.58	0.41	3.18
261.3	67.72	4.01	0.2591	3.75	0.44	3.31
255.1	66.08	4.18	0.2591	3.92	0.47	3.45
251.6	64.37	4.35	0.2558	4.09	0.51	3.59
247.8	62.55	4.52	0.2524	4.27	0.54	3.73
247.8	0	4.66	0.2524	4.41	0.54	3.87

Appendix B

Table B1: Data for tensile test FEA simulation with absolute yield strength

Data point	Displacement (mm)	Force (N)	Nominal Strain (%)	Nominal Stress (Mpa)	True Strain (%)	True stress (MPa)	Plastic strain (%)
256	0.193599	39.99804	0.387198	666.634	0.003864503	669.2152	1.79292E-10
257	0.194988	40.20145	0.389976	670.0242	0.003892176	672.6372	2.76726E-05
258	0.196452	40.40665	0.392904	673.4442	0.003921341	676.0902	5.68385E-05
259	0.197932	40.61255	0.395864	676.8758	0.003950825	679.5553	8.63222E-05
260	0.199253	40.8169	0.398506	680.2817	0.003977141	682.9927	0.000112638
261	0.200584	41.02167	0.401168	683.6945	0.004003655	686.4372	0.000139152
262	0.201927	41.22677	0.403854	687.1128	0.004030407	689.8877	0.000165904
263	0.203297	41.43241	0.406594	690.5402	0.004057696	693.3479	0.000193193
264	0.204652	41.63677	0.409304	693.9461	0.004084686	696.7865	0.000220183
265	0.20601	41.83977	0.41202	697.3295	0.004111735	700.2027	0.000247232
266	0.207364	42.04277	0.414728	700.7128	0.004138704	703.6188	0.000274201
267	0.208733	42.24651	0.417466	704.1085	0.00416597	707.0479	0.000301467
268	0.210128	42.45057	0.420256	707.5094	0.004193754	710.4828	0.000329251
269	0.211539	42.65541	0.423078	710.9235	0.004221855	713.9313	0.000357352
270	0.212959	42.86021	0.425918	714.3368	0.004250135	717.3793	0.000385632
271	0.214361	43.06389	0.428722	717.7315	0.004278056	720.8086	0.000413553
272	0.215767	43.26633	0.431534	721.1055	0.004306056	724.2173	0.000441553
273	0.217208	43.46916	0.434416	724.486	0.004334751	727.6332	0.000470248
274	0.218654	43.67193	0.437308	727.8655	0.004363546	731.0485	0.000499043
275	0.220091	43.87271	0.440182	731.2119	0.00439216	734.4305	0.000527657
276	0.22153	44.07295	0.44306	734.5491	0.004420814	737.8036	0.000556311
277	0.222962	44.27313	0.445924	737.8854	0.004449327	741.1758	0.000584824
278	0.224455	44.47416	0.44891	741.236	0.004479054	744.5635	0.000614551
279	0.225962	44.67519	0.451924	744.5864	0.004509059	747.9514	0.000644556
280	0.227466	44.87706	0.454932	747.9509	0.004539003	751.3536	0.0006745
281	0.228962	45.0789	0.457924	751.315	0.004568787	754.7554	0.000704284
282	0.230488	45.27959	0.460976	754.6599	0.004599168	758.1387	0.000734665
283	0.232002	45.47836	0.464004	757.9727	0.004629308	761.4897	0.000764805
284	0.233523	45.67646	0.467046	761.2744	0.004659587	764.8299	0.000795084
285	0.235066	45.87354	0.470132	764.5589	0.004690303	768.1534	0.0008258
286	0.236604	46.07039	0.473208	767.8399	0.004720919	771.4734	0.000856416
287	0.238141	46.26726	0.476282	771.121	0.004751514	774.7937	0.000887011
288	0.239698	46.46533	0.479396	774.4222	0.004782506	778.1347	0.000918003
289	0.241289	46.66377	0.482578	777.7295	0.004814173	781.4826	0.00094967
290	0.242895	46.86218	0.48579	781.0364	0.004846138	784.8306	0.000981635
291	0.244482	47.05901	0.488964	784.3169	0.004877725	788.1519	0.001013222
292	0.246099	47.25591	0.492198	787.5985	0.004909907	791.475	0.001045404
293	0.247734	47.45231	0.495468	790.8718	0.004942446	794.7903	0.001077943
294	0.249344	47.64734	0.498688	794.1223	0.004974487	798.0825	0.001109984
295	0.250945	47.8409	0.50189	797.3483	0.005006347	801.3501	0.001141844
296	0.252584	48.03487	0.505168	800.5812	0.005038963	804.6255	0.00117446
297	0.254254	48.23081	0.508508	803.8469	0.005072195	807.9345	0.001207692
298	0.255936	48.42763	0.511872	807.1272	0.005105664	811.2586	0.001241161
299	0.257651	48.6236	0.515302	810.3933	0.005139789	814.5693	0.001275286
300	0.259383	48.81646	0.518766	813.6076	0.00517425	817.8283	0.001309747

Table B1: Data for tensile test FEA simulation with absolute yield strength continued

Data point	Displacement (mm)	Force (N)	Nominal Strain (%)	Nominal Stress (Mpa)	True Strain (%)	True stress (MPa)	Plastic strain (%)
301	0.26469	49.39546	0.52938	823.2576	0.005279837	827.6158	0.001415334
302	0.266471	49.59049	0.532942	826.5081	0.005315269	830.9129	0.001450766
303	0.268253	49.7857	0.536506	829.7616	0.005350719	834.2134	0.001486216
304	0.270084	49.98037	0.540168	833.0062	0.005387143	837.5058	0.00152264
305	0.271922	50.17468	0.543844	836.2446	0.005423705	840.7924	0.001559202
306	0.273776	50.37017	0.547552	839.5028	0.005460584	844.0995	0.001596081
308	0.275648	50.56652	0.551296	842.7754	0.005497819	847.4215	0.001633316
310	0.277568	50.76328	0.555136	846.0546	0.005536008	850.7513	0.001671505
311	0.279488	50.95905	0.558976	849.3176	0.005574195	854.065	0.001709692
312	0.281424	51.15437	0.562848	852.5728	0.005612699	857.3715	0.001748196
313	0.283402	51.34932	0.566804	855.822	0.005652037	860.6728	0.001787534
314	0.285387	51.54377	0.570774	859.0629	0.005691513	863.9662	0.00182701
315	0.287389	51.7365	0.574778	862.2751	0.005731325	867.2312	0.001866822
316	0.289395	51.929	0.57879	865.4833	0.005771214	870.4926	0.001906711
317	0.291438	52.12104	0.582876	868.684	0.005811839	873.7473	0.001947336
318	0.293488	52.31398	0.586976	871.8997	0.0058526	877.0176	0.001988097
319	0.295604	52.50792	0.591208	875.132	0.005894672	880.3058	0.002030169
320	0.297746	52.70163	0.595492	878.3605	0.00593726	883.5911	0.002072757
321	0.299888	52.89509	0.599776	881.5849	0.005979845	886.8724	0.002115342
322	0.30206	53.08684	0.60412	884.7807	0.006023025	890.1258	0.002158522
323	0.304249	53.27715	0.608498	887.9524	0.006066541	893.3556	0.002202038
324	0.306462	53.46722	0.612924	891.1203	0.006110533	896.5822	0.00224603
325	0.308641	53.65564	0.617282	894.2607	0.006153846	899.7808	0.002289343
326	0.310849	53.84346	0.621698	897.3909	0.006197734	902.97	0.002333231
327	0.313107	54.03102	0.626214	900.517	0.006242614	906.1561	0.002378111
328	0.315395	54.21987	0.63079	903.6645	0.006288088	909.3648	0.002423585
329	0.317725	54.4077	0.63545	906.7949	0.006334395	912.5572	0.002469892
330	0.320089	54.59489	0.640178	909.9148	0.006381376	915.7399	0.002516873
331	0.322455	54.78062	0.64491	913.0104	0.006428394	918.8985	0.002563891
332	0.32484	54.9673	0.64968	916.1217	0.006475787	922.0735	0.002611284
333	0.327249	55.15257	0.654498	919.2095	0.006523655	925.2257	0.002659152
334	0.329658	55.33543	0.659316	922.2571	0.00657152	928.3377	0.002707017
335	0.332097	55.51681	0.664194	925.2801	0.00661998	931.4258	0.002755477
336	0.334558	55.69827	0.669116	928.3044	0.006668874	934.5159	0.002804371
337	0.337041	55.87891	0.674082	931.3151	0.006718202	937.5929	0.002853699
338	0.339539	56.05904	0.679078	934.3174	0.006767827	940.6621	0.002903324
339	0.342082	56.23805	0.684164	937.3008	0.006818342	943.7134	0.002953839
340	0.344629	56.41675	0.689258	940.2792	0.006868935	946.7601	0.003004432
341	0.347208	56.59469	0.694416	943.2448	0.00692016	949.7948	0.003055657
342	0.349791	56.77137	0.699582	946.1894	0.006971463	952.8088	0.00310696
343	0.352392	56.94661	0.704784	949.1102	0.00702312	955.7994	0.003158617
344	0.355013	57.12027	0.710026	952.0046	0.007075172	958.764	0.003210669
345	0.357622	57.29261	0.715244	954.8769	0.007126983	961.7066	0.00326248
346	0.360306	57.46391	0.720612	957.7318	0.00718028	964.6333	0.003315777
347	0.362993	57.63685	0.725986	960.6141	0.007233634	967.588	0.003369131
348	0.36574	57.81163	0.73148	963.5272	0.007288177	970.5752	0.003423674
349	0.368551	57.98602	0.737102	966.4337	0.007343987	973.5573	0.003479484

Table B1: Data for tensile test FEA simulation with absolute yield strength continued

Data point	Displacement (mm)	Force (N)	Nominal Strain (%)	Nominal Stress (Mpa)	True Strain (%)	True stress (MPa)	Plastic strain (%)
350	0.371398	58.15898	0.742796	969.3164	0.007400509	976.5164	0.003536006
351	0.374259	58.33114	0.748518	972.1856	0.007457305	979.4626	0.003592802
352	0.377147	58.50269	0.754294	975.0449	0.007514634	982.3996	0.003650131
353	0.380041	58.67304	0.760082	977.884	0.007572079	985.3168	0.003707576
354	0.382948	58.84145	0.765896	980.6908	0.007629779	988.2018	0.003765276
355	0.385883	59.00905	0.771766	983.4841	0.007688031	991.0743	0.003823528
356	0.388982	59.17596	0.777964	986.266	0.007749535	993.9387	0.003885032
357	0.392106	59.34256	0.784212	989.0426	0.00781153	996.7988	0.003947027
358	0.395231	59.51058	0.790462	991.843	0.007873542	999.6832	0.004009039
359	0.398303	59.67996	0.796606	994.666	0.007934498	1002.59	0.004069995
360	0.40142	59.84858	0.80284	997.4763	0.007996344	1005.484	0.004131841
361	0.404556	60.01573	0.809112	1000.262	0.008058562	1008.355	0.004194059
362	0.407748	60.18082	0.815496	1003.014	0.008121888	1011.193	0.004257385
363	0.410934	60.34454	0.821868	1005.742	0.008185091	1014.008	0.004320588
364	0.414166	60.50764	0.828332	1008.461	0.008249202	1016.814	0.004384699
365	0.417436	60.66916	0.834872	1011.153	0.008314062	1019.594	0.004449559
366	0.42071	60.83041	0.84142	1013.84	0.008378998	1022.371	0.004514495
367	0.424038	60.99236	0.848076	1016.539	0.008445	1025.16	0.004580497
368	0.42737	61.15494	0.85474	1019.249	0.008511078	1027.961	0.004646575
369	0.430787	61.31644	0.861574	1021.941	0.008578836	1030.745	0.004714333
370	0.434222	61.47748	0.868444	1024.625	0.008646947	1033.523	0.004782444
371	0.437713	61.63807	0.875426	1027.301	0.008716164	1036.294	0.004851661
372	0.441228	61.79749	0.882456	1029.958	0.008785851	1039.047	0.004921348
373	0.44479	61.95562	0.88958	1032.594	0.008856465	1041.779	0.004991962
374	0.448382	62.11196	0.896764	1035.199	0.008927669	1044.483	0.005063166
375	0.451997	62.26873	0.903994	1037.812	0.008999324	1047.194	0.005134821
376	0.455659	62.42499	0.911318	1040.416	0.009071906	1049.898	0.005207403
377	0.459351	62.58002	0.918702	1043	0.009145076	1052.582	0.005280573
378	0.463075	62.73425	0.92615	1045.571	0.009218875	1055.254	0.005354372
379	0.466816	62.88943	0.933632	1048.157	0.009293006	1057.943	0.005428503
380	0.470611	63.04364	0.941222	1050.727	0.009368201	1060.617	0.005503698
381	0.474438	63.19648	0.948876	1053.275	0.009444024	1063.269	0.005579521
382	0.478312	63.34839	0.956624	1055.807	0.009520773	1065.907	0.00565627
383	0.482241	63.50016	0.964482	1058.336	0.009598606	1068.543	0.005734103
384	0.486177	63.65036	0.972354	1060.839	0.009676571	1071.154	0.005812068
385	0.490122	63.79823	0.980244	1063.304	0.009754708	1073.727	0.005890205
386	0.494115	63.94417	0.98823	1065.736	0.009833789	1076.268	0.005969286
387	0.498093	64.09045	0.996186	1068.174	0.009912568	1078.815	0.006048065
388	0.502137	64.23714	1.004274	1070.619	0.009992647	1081.371	0.006128144
389	0.506215	64.38307	1.01243	1073.051	0.010073393	1083.915	0.00620889
390	0.510355	64.52893	1.02071	1075.482	0.010155359	1086.46	0.006290856
391	0.514514	64.67392	1.029028	1077.899	0.010237696	1088.991	0.006373193
392	0.518723	64.8169	1.037446	1080.282	0.010321015	1091.489	0.006456512
393	0.522944	64.95763	1.045888	1082.627	0.010404564	1093.95	0.006540061
394	0.527208	65.09776	1.054416	1084.963	0.010488958	1096.403	0.006624455
395	0.531518	65.23559	1.063036	1087.26	0.010574255	1098.818	0.006709752
396	0.535792	65.37141	1.071584	1089.524	0.010658832	1101.199	0.006794329

Table B1: Data for tensile test FEA simulation with absolute yield strength continued

Data point	Displacement (mm)	Force (N)	Nominal Strain (%)	Nominal Stress (Mpa)	True Strain (%)	True stress (MPa)	Plastic strain (%)
397	0.540108	65.50726	1.080216	1091.788	0.010744233	1103.581	0.00687973
398	0.545521	65.64256	1.091042	1094.043	0.010851331	1105.979	0.006986828
399	0.551864	65.77789	1.103728	1096.298	0.010976814	1108.398	0.007112311
400	0.558072	65.91235	1.116144	1098.539	0.011099611	1110.801	0.007235108
401	0.562522	66.04482	1.125044	1100.747	0.011187624	1113.131	0.007323121
402	0.567009	66.17643	1.134018	1102.941	0.011276362	1115.448	0.007411859
403	0.571531	66.30745	1.143062	1105.124	0.011365784	1117.756	0.007501281
404	0.576066	66.43575	1.152132	1107.263	0.011455455	1120.02	0.007590952
405	0.580605	66.5623	1.16121	1109.372	0.011545197	1122.254	0.007680694
406	0.585198	66.68712	1.170396	1111.452	0.011635998	1124.46	0.007771495
407	0.589802	66.81316	1.179604	1113.553	0.011727009	1126.688	0.007862506
408	0.594449	66.93929	1.188898	1115.655	0.011818861	1128.919	0.007954358
409	0.599131	67.06424	1.198262	1117.737	0.011911397	1131.131	0.008046894
410	0.603889	67.1894	1.207778	1119.823	0.012005426	1133.348	0.008140923
411	0.608647	67.31307	1.217294	1121.884	0.012099446	1135.541	0.008234943
412	0.613436	67.43401	1.226872	1123.9	0.012194069	1137.689	0.008329566
413	0.618256	67.55393	1.236512	1125.899	0.012289296	1139.821	0.008424793
414	0.623101	67.67258	1.246202	1127.876	0.012385008	1141.932	0.008520505
415	0.627997	67.79067	1.255994	1129.845	0.012481718	1144.035	0.008617215
416	0.632902	67.90766	1.265804	1131.794	0.012578597	1146.121	0.008714094
417	0.637852	68.02444	1.275704	1133.741	0.012676354	1148.204	0.008811851
418	0.642795	68.14047	1.28559	1135.675	0.012773964	1150.275	0.008909461
419	0.647803	68.25588	1.295606	1137.598	0.012872848	1152.337	0.009008345
420	0.652984	68.37066	1.305968	1139.511	0.012975138	1154.393	0.009110635
421	0.658398	68.48484	1.316796	1141.414	0.013082016	1156.444	0.009217513
422	0.663831	68.5985	1.327662	1143.308	0.013189258	1158.488	0.009324755
423	0.669037	68.7104	1.338074	1145.173	0.013292009	1160.497	0.009427506
424	0.674246	68.82156	1.348492	1147.026	0.013394808	1162.494	0.009530305
425	0.679479	68.9321	1.358958	1148.868	0.01349807	1164.481	0.009633567
426	0.68476	69.04159	1.36952	1150.693	0.013602268	1166.452	0.009737765
427	0.690069	69.15064	1.380138	1152.511	0.013707008	1168.417	0.009842505
428	0.695418	69.259	1.390836	1154.317	0.013812526	1170.371	0.009948023
429	0.70081	69.36634	1.40162	1156.106	0.013918881	1172.31	0.010054378
430	0.706239	69.47384	1.412478	1157.897	0.014025955	1174.252	0.010161452
431	0.711737	69.58021	1.423474	1159.67	0.014134377	1176.178	0.010269874
432	0.717331	69.68621	1.434662	1161.437	0.014244681	1178.1	0.010380178
433	0.723017	69.79086	1.446034	1163.181	0.014356786	1180.001	0.010492283
434	0.728733	69.89339	1.457466	1164.89	0.01446947	1181.868	0.010604967
435	0.734343	69.99383	1.468686	1166.564	0.014580053	1183.697	0.01071555
436	0.739953	70.09381	1.479906	1168.23	0.014690622	1185.519	0.010826119
437	0.745651	70.19439	1.491302	1169.906	0.014802914	1187.353	0.010938411
438	0.751377	70.29621	1.502754	1171.604	0.014915745	1189.21	0.011051242
439	0.757192	70.39615	1.514384	1173.269	0.015030317	1191.037	0.011165814
440	0.763042	70.49473	1.526084	1174.912	0.015145565	1192.842	0.011281062
441	0.768961	70.59273	1.537922	1176.545	0.015262158	1194.64	0.011397655
442	0.775031	70.68977	1.550062	1178.163	0.015381713	1196.425	0.01151721
443	0.781316	70.78552	1.562632	1179.759	0.015505486	1198.194	0.011640983

Table B1: Data for tensile test FEA simulation with absolute yield strength continued

Data point	Displacement (mm)	Force (N)	Nominal Strain (%)	Nominal Stress (Mpa)	True Strain (%)	True stress (MPa)	Plastic strain (%)
444	0.7878	70.87898	1.5756	1181.316	0.015633163	1199.929	0.01176866
445	0.79423	70.97043	1.58846	1182.84	0.01575976	1201.629	0.011895257
446	0.800283	71.06192	1.600566	1184.365	0.01587892	1203.322	0.012014417
447	0.806321	71.15273	1.612642	1185.879	0.015997771	1205.003	0.012133268
448	0.812432	71.24278	1.624864	1187.38	0.016118044	1206.673	0.012253541
449	0.818564	71.33373	1.637128	1188.895	0.016238715	1208.359	0.012374212
450	0.824718	71.42395	1.649436	1190.399	0.016359806	1210.034	0.012495303
451	0.830957	71.51216	1.661914	1191.869	0.016482553	1211.677	0.01261805
452	0.837202	71.5979	1.674404	1193.298	0.016605404	1213.279	0.012740901
453	0.843461	71.68245	1.686922	1194.707	0.016728515	1214.861	0.012864012
454	0.84974	71.76698	1.69948	1196.116	0.016852004	1216.444	0.012987501
455	0.85605	71.84891	1.7121	1197.482	0.016976087	1217.984	0.013111584
456	0.862374	71.92896	1.724748	1198.816	0.017100431	1219.492	0.013235928
457	0.868694	72.00832	1.737388	1200.139	0.01722468	1220.99	0.013360177
458	0.875036	72.08706	1.750072	1201.451	0.017349346	1222.477	0.013484843
459	0.8814	72.16581	1.7628	1202.764	0.017474429	1223.966	0.013609926
460	0.88782	72.24383	1.77564	1204.064	0.017600597	1225.444	0.013736094
461	0.894275	72.32161	1.78855	1205.36	0.017727436	1226.919	0.013862933
462	0.900779	72.39783	1.801558	1206.63	0.017855223	1228.369	0.01399072
463	0.907303	72.47224	1.814606	1207.871	0.017983385	1229.789	0.014118882
464	0.913835	72.54398	1.82767	1209.066	0.018111689	1231.164	0.014247186
465	0.920374	72.61558	1.840748	1210.26	0.018240113	1232.537	0.01437561
466	0.926934	72.68697	1.853868	1211.45	0.018368933	1233.908	0.01450443
467	0.933519	72.75689	1.867038	1212.615	0.018498228	1235.255	0.014633725
468	0.967123	73.10294	1.934246	1218.382	0.019157772	1241.949	0.015293269
469	1.001666	73.42188	2.003332	1223.698	0.019835293	1248.213	0.01597079
470	1.037464	73.72499	2.074928	1228.75	0.020536946	1254.246	0.016672443
471	1.074314	74.00223	2.148628	1233.37	0.021258704	1259.871	0.017394201
472	1.115779	74.26686	2.231558	1237.781	0.022070231	1265.403	0.018205728
473	1.154989	74.50449	2.309978	1241.741	0.022837019	1270.425	0.018972516
474	1.195246	74.72665	2.390492	1245.444	0.023623671	1275.216	0.019759168
475	1.2365	74.92358	2.473	1248.726	0.024429163	1279.607	0.02056466
476	1.278763	75.09852	2.557526	1251.642	0.025253684	1283.653	0.021389181
477	1.323943	75.25402	2.647886	1254.234	0.026134363	1287.444	0.02226986
478	1.368042	75.39058	2.736084	1256.51	0.026993223	1290.889	0.02312872
479	1.412695	75.50526	2.82539	1258.421	0.027862121	1293.976	0.023997618
480	1.458191	75.61279	2.916382	1260.213	0.028746647	1296.966	0.024882144
481	1.504514	75.70112	3.009028	1261.685	0.029646449	1299.65	0.025781946
482	1.521474	75.71838	3.042948	1261.973	0.029975686	1300.374	0.026111183
483	1.605194	75.80168	3.210388	1263.361	0.031599321	1303.92	0.027734818
484	1.689754	75.86313	3.379508	1264.385	0.033236575	1307.115	0.029372072
485	1.774234	75.91746	3.548468	1265.291	0.034869607	1310.189	0.031005104
486	1.859874	75.95519	3.719748	1265.92	0.036522345	1313.009	0.032657842
487	1.945834	75.98196	3.891668	1266.366	0.038178516	1315.649	0.034314013
488	2.030794	76.00005	4.061588	1266.667	0.03981273	1318.114	0.035948227
489	2.098754	76.01048	4.197508	1266.841	0.041118027	1320.017	0.037253524

Appendix C

Table C1: Mechanical properties variation with groove depths for wire specimens with 0.2mm wide across-the- thickness channel cut

Groove depth (mm)	Yield load (kN)	% reduction in yield load (kN)		Ultimate load (kN)	% reduction in ultimate load (kN)		Displacement at fracture (mm)	% reduction in displacement at fracture (mm)
0	50.31			67.97			5.93	
0.1	50.29	0.025		67.94	0.057		5.78	2.626
0.2	50.29	0.034		67.89	0.119		5.72	3.565
0.3	50.26	0.090		67.76	0.307		5.15	13.127
0.5	50.20	0.218		67.23	1.090		4.14	30.239
0.75	50.00	0.603		65.91	3.039		3.54	40.373
1	49.79	1.030		64.16	5.612		2.90	51.121

Table C2: Mechanical properties variation with groove depths for wire specimens with 0.2mm wide across-the- width channel cut

Groove depth (mm)	Yield load (kN)	% reduction in yield load (kN)		Ultimate load (kN)	% reduction in ultimate load (kN)		Displacement at fracture (mm)	% reduction in displacement at fracture (mm)
0	50.31			67.97			5.93	
0.1	50.28	0.044		67.93	0.065		5.71	3.837
0.2	50.27	0.072		67.81	0.238		5.28	10.946
0.3	50.23	0.159		67.64	0.494		4.75	19.867
0.5	50.10	0.418		66.86	1.633		3.74	36.905
0.75	49.86	0.898		65.01	4.361		3.17	46.641
1	49.51	1.591		62.40	8.199		2.42	59.202

Table C3: Mechanical properties variation with groove depths for wire specimens with 0.1mm wide across-the- thickness groove.

Groove depth (mm)	Yield load (kN)	% reduction in yield load (kN)		Ultimate load (kN)	% reduction in ultimate load (kN)		Displacement at fracture (mm)	% reduction in displacement at fracture (mm)
	50.31			67.97			5.93	
0.1	50.31	0.002		67.93	0.066		5.89	0.556
0.2	50.3	0.022		67.91	0.092		5.65	4.735
0.3	50.27	0.078		67.8	0.255		5.5	7.231
0.5	50.19	0.238		67.5	0.698		4.52	23.869
0.75	50.04	0.54		66.57	2.059		3.77	36.447
1	49.81	0.996		65.19	4.102		3.19	46.083

Table C4: Mechanical properties variation with groove depths for wire specimens with 0.2mm wide across-the- thickness groove.

Groove depth (mm)	Yield load (kN)	% reduction in yield load (kN)		Ultimate load (kN)	% reduction in ultimate load (kN)		Displacement at fracture (mm)	% reduction in displacement at fracture (mm)
	50.31			67.97			5.93	
0.1	50.29	0.025		67.94	0.057		5.89	0.64
0.2	50.29	0.034		67.89	0.119		5.6	5.576
0.3	50.26	0.09		67.76	0.307		5.23	11.802
0.5	50.2	0.218		67.23	1.09		4.15	29.985
0.75	50	0.603		65.91	3.039		3.21	45.921
1	49.79	1.03		64.16	5.612		2.9	51.121

Table C5: Mechanical properties variation with groove depths for wire specimens with 0.3mm wide across-the- thickness groove.

Groove depth (mm)	Yield load (kN)	% reduction in yield load (kN)		Ultimate load (kN)	% reduction in ultimate load (kN)		Displacement at fracture (mm)	% reduction in displacement at fracture (mm)
0	50.31			67.97			5.93	
0.1	50.28	0.039		67.92	0.072		5.89	0.734
0.2	50.27	0.072		67.88	0.131		5.54	6.622
0.3	50.25	0.113		67.76	0.313		5.15	13.127
0.5	50.18	0.241		67.29	1.001		4.14	30.239
0.75	50.01	0.592		66.12	2.731		3.54	40.373
1	49.76	1.081		64.39	5.264		2.61	55.988

References:

1 Abdel-Nasser, Y.A., Masaoka, K., and Okada, H., 2006. Ultimate strength of dented tubular. Alexandria Engineering Journal, Volume 45, Issue 1, January 2006, pages 37-46.

2 Anderson T.L., 2005. Fracture mechanics fundamentals and applications, Third edition. CRC press, Taylor and Francis Group, ISBN -10:0-8493-1656-1.

3 Askeland, D.R., and Phule, P.P., 2006. The science and engineering of materials. Fifth edition. Thomson Canada Limited, ISBN 0 534 55396 6.

4 ASTM E8M, 2009. Standard Test Method for Tension Testing of Metallic Materials. American Society for Testing of Materials.

5 Atzori B., Lazzarin P., and Filippi, S., 2001. Cracks and notches: analogies and differences of the relevant stress distributions and practical consequences in fatigue limit predictions. International Journal of Fatigue, Vol 23 pages 355-362.

6 Bai, Y., and Bai, Q., 2005. Subsea pipelines and risers. Elsevier Incorporation, ISBN 0-080-4456-67.

7 Balart, M.J., and Knott, J.F., 2006. Effects of geometry and flow properties on the fracture toughness of a C-Mn reactor pressure vessel steel in the lower shelf region, International Journal of Pressure Vessels and Piping, Vol. 83, pages 205-215.

8 Bayram, A., Uguz, A., and Ula, Murat., 1999. Effects of Microstructure and Notches on the Mechanical Properties of Dual-Phase Steels. Material characterisation, Vol. 43, pages 259-269.

9 Beghini, M., Bertini, L., and Fontanari V., 2006. Evaluation of the stress–strain curve of metallic materials by spherical indentation, International Journal of Solids and Structures, Volume 43, Issue 7-8, April 2006, pages 2441-2459.

10 Bernauer G., and Brocks, W., 2002. Micro-mechanical modelling of ductile damage and tearing–results of a European numerical round robin. Fatigue and Fracture of Engineering Materials & Structures, 2002, Volume 25, Issue 4, pages 363 – 384.

11 Besson, J., Steglich, D., and Brocks, W., 2003. Modeling of plane strain ductile rupture, International Journal of Plasticity, Vol. 19, Pages 1517-1541.

12 Braestrup, M.W., Andersen, J.B., Andersen, L.W., and Christensen, C., 2005. Design and Installation of Marine Pipelines. Blackwell Science Ltd, ISBN-13: 978-0632-05984-3, page 278.

13 Broek, D., 1997. The Practical Use of Fracture Mechanics. Kluwer Academics Publishers, ISBN-90-247-3707-9.

14 Bruehl, R., 1984. Defects in steel wires and its routine testing. Wire, Volume 34, Issue 2, March 1984, Pages 43-46.

15 BS 7448-1, 1991. Fracture mechanics toughness tests - Part 1: Method for determination of *K*Ic, critical CTOD and critical *J* values of metallic materials. British Standards Institute.

16 BS EN ISO 9513, (2002). Metallic materials, Calibration of extensometers used in uniaxial testing, British standards institutes.

17 BS EN ISO13628-2, (2006). Petroleum and natural gas industries - Design and operation of subsea production systems - Unbonded flexible pipe systems for subsea and marine applications. British Standards Institute.

18 Burks, B.M., Armentrout, D.L., Baldwin, M., Buckley, J. and Kumosa, M., 2009. Hybrid composite rods subjected to excessive bending loads. Composites Science and Technology, 2009, pages 2625-2632.

19 Burks, B., Middleton, J., Armentrout ,D. and Kumosa, M., 2010. Effect of excessive bending on residual tensile strength of hybrid composite rods. Composites Science and Technology, Vol 70, (2010) pages 1490–1496.

20 Cabezas, E.E., and Celentano, D.J., 2004. Experimental and numerical analysis of the tensile test using sheet specimens. Finite Elements in Analysis and Design, Vol 40, 2004, pages 555-575.

21 Callister, W.D. Jr., 2007. Materials Science and Engineering-An Introduction. 7th edition, John Wiley & Sons Inc, ISBN-13: 978-0-471-73696-7.

22 Cao, Y.P., and Lu, Jian., 2004. A new method to extract the plastic properties of metal materials from an instrumented spherical indentation loading curve. Walled Structures, Volume 43, Issue 9, September 2005, Pages 1475-14.

23 Carbonnie, J., Thuillier, S., Sabourin, F., Brunet, M., and Manach, P.Y., 2008. Comparison of the work hardening of metallic sheets in bending–unbending and simple shear. International Journal of Mechanical Sciences, Vol. 51, pages 122-130.

24 Celentano, D.J., and Chaboche, J., 2007. Experimental and numerical characterization of damage evolution in steels. International Journal of Plasticity, 2007, Vol 23 pages 1739-1762.

25 Chakrabarty, J., 2006. Theory of Plasticity. Elsvier Butterworth Heinemann, ISBN 10: 0-7506-6638-2.

26 Chao, Y.J., Liu, S., and Broviak, B.J., 2001. Brittle fracture: variation of fracture toughness with constraints and crack curving under mode I condition. Experimental mechanics, Vol. 41, Issue 3, pages 232-241.

27 Chen, F.K., and Ko, S., 2006. Deformation analysis of springback in L-bending of sheet metal. Journal of Achievements in Materials and Manufacturing Engineering Vol. 18 Issue 1-2.

28 Chun, T.B., and Nho, I.S., 2005. Ultimate strength analysis of dented tubular members, Proceedings of the International Offshore and Polar Engineering Conference Vol. 2005, 2005, pages 293-299.

29 Coutarel, A., 2001. Light weight flexible pipes for ultra deepwater developments. Offshore pipeline technology conference, Amsterdam.

30 Davis, J.R., 2004. Tensile Testing. Second edition, ASM International, ISBN-0-87170-806-X.

31 Dieter, G.E., 1998. Mechanical metallurgy. McGraw-Hill Book Company, ISBN 0-07-084187-X, page 659.

32 Duan, L., Chen, W.F., and Loh, J.T., 1993. Analysis of dented tubular members using moment curvature approach. Thin-Walled Structures, Volume 15, Issue 1, 1993, pages 15-41.

33 Duan, L., Chen, W. F., and Loh, J. T., 1994. Ultimate Strength of Damaged Tubular Members. International Journal of Offshore and Polar Engineering, Vol. 4, No.2, June 1994.

34 Dunand, M., and Mohr, D., 2009. Hybrid experimental-numerical analysis of basic ductile fracture experiments for sheet metals. International Journal of Solids and Structures , Vol 47, Issue 9, May 2010, pages 1130-1143.

35 Escoe, K.A., 2006. Piping and pipeline assessment guide, Gulf Professional Publishing. ISBN 13: 978-0-7506-7880-3.

36 BS EN ISO 6892-1:2009. Metallic materials -Tensile testing -Part 1: Method of test at ambient temperature, British Standards Institute.

37 BS EN ISO13628-2:2006. Petroleum and natural gas industries- Design and operation of subsea production systems - Unbonded flexible pipe systems for subsea and marine applications. British Standards Institute.

38 Fleck, N.A., Muller, G.M., Ashby, M.F., and Hutchinson, J.W., 1994. Strain gradient plasticity: theory and experiment, Acta Metallurgica, Vol 42, Issue 2, pages 475-487.

39 Fukuda, N., Hagiwara, N., and Masuda, T., 2005. Effect of Prestrain on Tensile and Fracture Toughness Properties of Line Pipes. Journal of Offshore Mechanics and Arctic Engineering, Vol. 127, pages 263-268.

40 Firat M., 2007. U-channel forming analysis with an emphasis on springback deformation. Materials and Design, Volume 28, pages 147-154.

41 Garrell, M.G., Shi, A.J., Edgar, L., and Scattergood, R.O., 2003. Finite-Element Analysis of Stress Concentration in ASTM D 638 Tension Specimens, Journal of Testing and Evaluation, Vol. 31, No.1.

42 Gau, J., and Kinzel, G.L., 2001. A new model for springback prediction in which the Bauschinger effect is considered. International Journal of Mechanical Sciences, 2001,Vol 43, Issue 8, pages 1813-1832.

43 Gillstrom, P., and Jarl, M., 2006. Mechanical descaling of wire rod using reverse bending and brushing, Journal of Materials Processing Technology, Volume 172, Issue 3, 10 March 2006, pages 332-34.

44 Gliha, V., and Rojko, D., 2003. The pre-cracking of wide plate specimens, International Journal of Pressure Vessels and Piping, Volume 80, Issue 6, June 2003, Pages 351-360.

45 Harkegard, G., and Mann, T., 2003. Neuber prediction of elastic plastic strain concentration in notched tensile specimens under large-scale yielding. The Journal of Strain Analysis for Engineering Design, Vol. 38, pages 79-94

46 Harsono, E., Swaddiwudhipong, S., Liu, Z.S., and Shen, L., 2010. Numerical and experimental indentation tests considering size effects. International Journal of Solids and Structures, Vol. 48, pages 972-978.

47 Health and Safety Executive, 1998. Guidelines for integrity monitoring of unbonded flexible pipes. Offshore technical report, OTO 98 019, May, 1998.

48 Health and Safety Executive, 2009. www.hse.gov.uk/pipelines/htm. Assessed 06/02/2009

49 Hooputra, H., Gese, H., Dell, H., and Werner, H., 2004. A comprehensive failure model for crashworthiness simulation of Aluminium extrusions, international, Journal of Crashworthiness, Vol. 9, pages 449- 464.

50 Huang, H., and Xue, L., 2009. Prediction of slant ductile fracture using damage plasticity theory. International Journal of Pressure Vessels and Piping, Vol. 86 pages 319-328

51 Huratlt, L.T., Sallo, R.L., and Stricker, C.D., 1970. Mechanical descaling of steel wire and rod. Wire Industry, Volume 37, Issue 441, September 1970, pages 843, 845-846.

52 Ifergane, S., Barkay, Z., Beeri, O and Eliaz, N., 2010. Study of fracture evolution in copper sheets by in situ tensile test and EBSD analysis. Journal of Material Science, Vol. 45, pages 6345-6352.

53 Instron, 2003. 2518/2525-100 Series Load Cells. Catalog number 2525-108/112, www.instron.us/wa/acccatalog, assessed on 12/02/2011.

54 Instron, 2004. 2630 Series Strain Gauge Extensometers. Catalog Number 2630-100, www.instron.us/wa/acccatalog, assessed on 12/02/2011.

55 Johnson, K.L., 1987. Contact Mechanics. Cambridge University Press, ISBN 0 521 34796 3.

56 Kato, A., 1992. Design equation for stress concentration factors of notched strips and grooved shafts, Journal of Strain Analysis, Vol. 26, pages 21-28.

57 Ken-ichiro, M., 2001. Simulation of materials processing: theory, methods and applications: proceedings of the 7th International Conference on Numerical Methods in Industrial Forming Processes--NUMIFORM 2001, pages 711-721. Paper presented by Cedric Xia, Z.

58 Kim, J., Zhang, G., Gao, X., 2006. Modelling of ductile fracture: Application of the mechanism-based concepts. International Journal of Solids and Structures, Vol. 44, pages 1844-1862.

59 Kim, Y., and Chao Y.J., 2008. Numerical simulation of cup-cone fracture in a round tensile bar, Proceedings of PVP2008, 2008 ASME pressure vessel and piping division conference, July 28-3, 2008, Chicago, Illinois, USA.

60 Kossakowski, P.G, 2010. An analysis of the load-carrying capacity of elements subjected to complex stress states with a focus on the microstructural failure. Archive of civil and mechanical engineering, Vol. 10, no 2, pages 15-39.

61 Krishnadev, M., Maude, L., Lakshmanan, I., and Sridhar, R., 2008. Metallurgical failure analysis of a Guy rope assembly, Engineering Failure Analysis, Volume 15, Issue 7, pages 894-902.

62 Kut, S., 2010. The application of the formability utilization indicator for finite element modelling the ductile fracture during the material blanking process. Materials & Design, Vol. 31, Issue 7, August, pages 3244-3252.

63 Lhermet, G., Vessiere, G., and Bahuaud, J., 1987. Determination of stress intensity factors from stress concentration factors for V-notched beams. Engineering Fracture Mechanics, Vol. 28, Issue 3, Pages 331-343.

64 Ling, Y., 1996. Uniaxial True Stress-Strain after Necking. AMP Journal of Technology Vol. 5 June, 1996, pages 37-48.

65 Li, Z., and Guo, W., 2001. Three-dimensional elastic stress fields ahead of blunt V-notches in finite thickness plates. International Journal of Fracture, Vol.107, pages 53-71.

66 Liu, S., and Chao, Y.J., 2003.Variation of fracture toughness with constraint. International Journal of Fracture, Vol.124, pages 13-117.

67 Livieri, P., 2003. A new path independent integral applied to notched components under mode I loadings. International Journal of Fracture, Vol. 123, Pages 107-12.

68 Lothian, E., Hermann, K., Stewart, M., 1981. An Atlas of Metal Damage. Wolf Publishing Limited, ISBN 0 7234 07509.

69 Mahmoud, K.M., 2007. Fracture strength for a high strength steel bridge cable wire with a surface crack. Theoretical and Applied Fracture Mechanics, Vol. 48, Issue 2, Pages 152-160.

70 Mahmudi, R., Mohammadia, R., and Sepehrband, P., 2003. Determination of tearing energy from uniaxial tension tests of aluminum alloy sheet. Journal of Materials Processing Technology, Vol. 147, pages 185-190.

71 Mapelli, C., and Barella, S., 2009. Failure analysis of a cableway rope, Engineering Failure Analysis, Volume 16, Issue 5, July 2009, pages 1734-1739.

72 Meneghetti, G., and Lazzarin, P., 2006. Significance of the elastic peak stress evaluated by FE analyses at the point of singularity of sharp V-notched components, Fatigue Fracture of Engineering Materials and Structures, Volume 30, pages 95-106.

73 Mesarovic, S.D., and Fleck, N.A., 1999. Spherical indentation of elastic-plastic solids. Procedure of the Royal Society, London, volume 455, pages 2707-2728.

74 Moir, Stephen., and Preston, J., 2002. Surface defects- evolution and behaviour from cast slab to coated strip. Journal of material processing technology, Vol-125-126, pages 720-724.

75 Montmitonnet, P., Edlinger, M.L. and Felder, E., 1993. Finite element analysis of elastoplastic indentation: part 1-homogeneous media. Jounal of Tribology, Transaction of the ASME 115, 10-14.

76 Murakami, Y., Noda, N., and Nishitani, H., 1981. The analysis of stress concentration of a cylindrical bar with a semi-elliptical circumferential notch under tension. Transactions of the Japan Society of Mechanical Engineers, pages 1194-1203.

77 Narasaiah, N., Tarafder, S., and Sivaprasad, S., 2010. Effect of crack depth on fracture toughness of 20MnMoNi55 pressure vessel steel. Materials Science and Engineering A, Vol. 527, Pages 2408–2411.

78 Nayebi, A., El Abd, R., Bartier, O., and Mauvoisin, G., 2002. New procedure to determine steel mechanical parameters from the spherical indentation technique. Mechanics of Materials, Vol. 34, pages 243-254.

79 Neimitz, A., and Galkiewicz, J., 2006. Fracture toughness of structural components: influence of constraint. International Journal of Pressure Vessels and Piping, Vol. 83 pages 42–54.

80 Noda, N.A., Sera, M., and Takase, Y., 1995. Stress concentration factors for round and flat test specimens with notches, International Journal of Fatigue, Vol. 17, No. 3, pages 163-178.

81 Noda, N., and Takase, Y., 2006. Stress concentration formula useful for all notch shape in a round bar (comparison between torsion, tension and bending), International Journal of Fatigue, Vol. 28, pages 151–163.

82 Oberkampf, W.L., Trucano, T.G., Hirsch, C., 2004. Verification, validation, and predictive capability in computational engineering and physics, Applied Mechanics Rev. Vol 57, Issue 5, pages 345-384.

83 Oberkampf, W.L., and Trucano, T.G., 2008. Verification and validation benchmarks. Nuclear Engineering and Design, Vol. 238, pages 716-743.

84 Paik, J. K., Lee, J.M., and Lee, D.H., 2003. Ultimate strength of dented steel plates under axial compressive loads, International Journal of Mechanical Sciences, Vol. 45, pages 433–448.

85 Paik, J.K., 2005. Ultimate strength of dented steel plates under edge shear loads, Thin-Walled Structures, Vol. 43, Issue 9, September 2005, Pages 1475-1492.

86 Pardoen, T., Scheyvaertsa, F., Simara, A., Tekoglu, C., and Onck, P., 2010. Multiscale modeling of ductile failure in metallic alloys. Comptes Rendus Physique, Vol. 11, Issues 3-4, April-May 2010, Pages 326-345.

87 Petti, J.P., and Dodds, R.H., 2004. Constraint comparisons for common fracture specimens: C(T)s and SE(B)s. Engineering Fracture Mechanics, Vol 71, pages 2677–2683.

88 Pipa, D., Morikawa, S., Pires, G., Camerini, C., and Marcio, S., 2010. Flexible Riser Monitoring Using Hybrid Magnetic/Optical Strain Gage Techniques through RLS Adaptive Filtering. EURASIP Journal on Advances in Signal Processing, Volume 2010, Article ID 176203, 14 pages.

89 Qingfen, Li., Shenghai, Hu., and Xinji, Pan., 1990. Effects of crack depth and shape on fracture toughness in a spring steel. Engineering Fracture Mechanics, Vol. 36, Issue 1, Pages 1-7

90 Ragab, A.R., 2004. A model for ductile fracture based on internal necking of spheroidal voids. Acta Materialia, Vol 52, pages 3997-4009.

91 Rakin, M., Cvijovic, Z., Grabulov, V., Putic, S., and Sedmak, A., 2004. Prediction of ductile fracture initiation using micromechanical analysis. Engineering Fracture Mechanics, Vol 71, pages 813-827.

92 Savruk, M., and Kazberuk, A., 2010. Two-dimensional fracture mechanics problems for solids with sharp and rounded V-notches. International Journal of Fracture, Vol. 161, pages 79-95.

93 Schrems, K., and Maclaren, D., 1996. Failure analysis of a mine hoist rope. Engineering failure analysis, Vol 4, No 1, pages 25-38.

94 Shen, J., Mao, J., Reyes, G., Chow, C., Boileau, J., Su, X., and Wells, J., 2009. A Multiresolution Transformation Rule of Material Defects. International Journal of Damage Mechanics, Vol. 18, November 2009, pages 739-758.

95 Shigley, J.E., Mischke, C.R., and Budynas, R.G., 2004. Mechanical Engineering Design. Seventh Edition, Mc Graw Hill Higher Education, ISBN 0-07-252036-1.

96 Simulia, 2007. Abaqus documentation, Abaqus Incorporation, Dassault Systemes.

97 Smith, B. O., Jenning, A. P., and Grimshaw, A. G., 1957. A portable lamination detector for steel sheet, The British Iron and Steel Research Association, Battersea Park Road, London

98 Smith, C.S., and Dow, R.S., 1981. Residual strength of damaged steel ships and offshore structure, Journal of Constructional Steel Research, Volume 1, Issue 4, September 1981, Pages 2-15.

99 Smith, G.D.W., and Easterling, K.E., 1993. Handbook of cases of histories in failure analysis, Vol 2, ASM International, ISBN: 0-87170-495-1.

100 Soboyejo, W. O., Mechanical properties of engineered materials. Marcel Dekker incorporation, ISBN 0-8247-8900-0.

101 Springmann, M., and Kuna, M., 2004. Identification of material parameters of the Gurson-Tvergaard-Needleman model by combined experimental and numerical techniques. Computational Material Science, 2005, Vol 32, pages 544-552.

102 Strandberg, Morten., 1999. A numerical study of the elastic stress field arising from sharp and blunt V -notches in a SENT-specimen. International Journal of Fracture, volume 100, pages 329-342.

103 Takeda, T., and Chen, Z., 1999. Yield Behavior of a Mild Steel after Prestraining and Agingunder Reversed Stress. Metallurgical and Materials Transactions A, Vol 30A, pages 411-416.

104 Tlilan, H. M., Shyyab, A. S., Al- Jawarneh, A. M., and Ababneh, A. K., 2008. Strain concentration factor of circumferentially V-notched cylindrical bars under static tension. Journal of Mechanics, Vol. 24, No. 4, December 2008, pages 419-427.

105 Toribio, J., and Valiente, A., 2004. Approximate evaluation of directional toughness in heavily drawn pearlitic steels. Materials Letters, Volume 58, Issues 27-28, pages 3514-3517.

106 Toribio, J., and Valiente, A., 2006. Failure analysis of cold drawn eutectoid steel wires for prestressed concrete. Engineering Failure Analysis, Volume 13, Issue 3 pages 301-311.

107 Troina, L.M.B., Rosa, L.F.L., Viero, P.F., Magluta, C., and Roitman, N., 2003. An Experimental Investigation on the Bending Behaviour of Flexible Pipes. Proceedings of the International Conference on Offshore Mechanics and Arctic Engineering - OMAE Volume 2, 2003, pages 637-645.

108 Tvergaard, V., and Needleman, A., 1984. Analysis of the cup-cone fracture in a round tensile bar, Acta Metallurgica, Vol 32, Issue 1, pages 157-169

109 Tvergaard, V., (1987). Ductile shear failure at the surface of a bent specimen. Mechanics of materials, Vol 6, pages 53-69.

110 Ueda, Y., 1991. Modern Method of Ultimate Strength Analysis of Offshore Structures, International Journal of Offshore and Polar Engineering, Vol. 1, No. 1, March 1991 (lSSN 1053-5381).